JOINT INSTITUTE FOR NUCLEAR RESEARCH

The XX International Scientific Conference of Young Scientists and Specialists (AYSS-2016)

dedicated to the 60th anniversary of the Joint Institute for Nuclear Research

Dubna, 14-18 March 2016

PROCEEDINGS

Dubna 2016

The XX International Scientific Conference of Young Scientists and Specialists (AYSS-2016) dedicated to the 60th anniversary of the Joint Institute for Nuclear Research (Dubna, 14-18 March 2016): Proceedings - Dubna: JINR 2016, 300 pp.

This collection of papers includes the contributions of participants from Russia, Poland, Bulgaria, Romania, India, Kazakhstan, Belarus, Egypt, the Czech Republic, South Africa, and other countries. These papers are interesting for specialists which deal with theoretical and experimental nuclear physics, physics of elementary particles and high energy physics, condensed matter physics, mathematical modelling and information technology, radiobiology and applied research.

Programme Committee:

Chairman: G.D. Shirkov (JINR)
D.V. Peshekhonov (VBLHEP JINR)
A.V. Guskov (DLNP JINR)
S.N. Nedelko (BLTP JINR)
O. Culicov (FLNP JINR)
A.V. Karpov (FLNR JINR)
D.V. Podgainy (LIT JINR)
I.V. Koshlan (LRB JINR)

Organizing Committee:

Co-chairman: A. V. Friesen
Co-chairman: V. Chudoba
A. Baimukhanova
A. A. Bezbakh
I. Chuprakov
L. Ježková
E. I. Krupko
O. N. Matyukhina
S.H. Tanyldz
Yu.S. Severukhin
. V. Shumeyko
T. N. Zaikina

PREFACE

This issue comprises proceedings of the XX International Scientific Conference of Young Scientists and Specialists (AYSS-2016). The Conference AYSS-2016, dedicated to the 60th anniversary of the Joint Institute for Nuclear Research, was held on 14-18 March 2016 at the Bogoliubov Laboratory of Theoretical Physics (JINR, Dubna). AYSS-2016 brought together more than 270 participants from Russia, Poland, Bulgaria, Romania, India, Kazakhstan, Belarus, Egypt, the Czech Republic, South Africa, and other countries.

In the framework of the Conference, leading scientists gave lectures on the recent theoretical, experimental, and applied investigations carried out at JINR with emphasis on the major results obtained at JINR during its history.Modern aspects of elementary particle physics were reviewed in reports of I.P. Ivanov (Portugal) and I.D. Kazakov. Problems of high energy physics were touched upon by D. Blaschke (Poland). Corresponding Member of RAS G.V. Trubnikov spoke about the JINR key facilities and infrastructure. The LIT Director V.V. Korenkov delivered a lecture on the problem of high-precision calculations and methods of data transfer. Properties of neutrino and the history of its discovery, its interaction with matter and advantages of neutron spectroscopy, as well as ultracold neutrons were presented in the reports by D.V. Naumov, S.A. Kulikov, and E.V. Lychagin. Noteworthy was also the report of A.G. Popeko on the key problems related to synthesis of superheavy nuclei. The use of powerful laser facilities in applied research and particle physics, brought about in European ELI-NP project (Romania, Hungary, the Czech Republic), was discussed in the lecture of F.Negoita. The main research issues of radiation biology were presented by Director of the Laboratory of Radiation Biology E.A. Krasavin.

During the Conference, young scientists took part in poster session and presented 190 oral reports on the following topics:
- Theoretical Physics;
- Mathematical Modeling and Computational Physics;
- High Energy Physics;
- Particle Accelerators and Nuclear Reactors;
- Experimental Nuclear Physics;
- Applied Research;
- Information Technology;
- Condensed Matter Physics;
- Life Science.

In the follow-up of the Conference a traditional competition for the JINR Prize for young scientists and specialists was organized. The Competition Committee selected twelve winners in four categories: Theoretical Research, Experimental Research, Research and Development, and Applied Research.

We are grateful to the JINR Directorate and the Russian Foundation for Basic Research for financial support, the members of Program Committee and all participants for their interest and fruitful cooperation.

We look forward to seeing you at future conferences!

<div align="right">

Yours sincerely,

A.V. Friesen

V. Chudoba

</div>

Contents

Particle Accelerators and Nuclear Reactors   97

Mathematical Modelling, Computational Physics and Information Technology   117

Applied Research   239

Life Science   271

Theoretical Physics

THE SCALAR FIELD POTENTIAL DISTRIBUTION FOR A CLOSED RADIALLY EXPANDING NULL STRING WITH AXIAL SYMMETRY

A. P. Lealykov* R. D.-A. Babadzhan†
V. I. Vernadsky CFU, Simferopol, Republic of Crimea, RF

Introduction

Cosmic strings are one-dimensional domains of energy concentration, which can naturally occur as a result of spontaneous symmetry breaking in phase transitions in the evolution of the Universe [1, 2]. The components of the energy-momentum tensor for a null string have the following form [3]:

$$T^{mn}\sqrt{-g} = \gamma \int d\tau d\sigma x^m_{,\tau} x^n_{,\tau} \delta^4(x^l - x^l(\tau, \sigma)) \tag{1}$$

Where subscripts m,n,l take on values 0, 1, 2, 3; the functions $x^m = x^m(\tau, \sigma)$ describe the null string trajectory of motion; τ and σ are the parameters on the world surface of a null string ; $x^m_{,\tau} = \partial x^m / \partial \tau$; g_{mn} is the metric tensor; $g = |g_{mn}|$; $\gamma = const$. In the cylindrical coorinate system $(x^0 = t, x^1 = \rho, x^2 = \theta, x^3 = z)$ the functions $x^\alpha(\tau, \sigma)$ for the trajectories of closed null string that are considered in this work are as follows:

$$t = \tau, \quad \rho = \tau, \quad \theta = \sigma, \quad z = Z(\theta), \quad \tau \in [0, +\infty), \quad \sigma \in [0, 2\pi] \tag{2}$$

where the function $Z(\theta)$ satisfies the closure conditions of the null string

$$Z(\theta)|_{\theta=0} = Z(\theta)|_{\theta=2\pi} \tag{3}$$

and invariance under inversion θ to $-\theta$.

$$Z(\theta) = Z(-\theta) \tag{4}$$

Hence, the quadratic form for the problem concerned can be expressed in the form

$$dS^2 = e^{2\nu} \left((dt)^2 - (d\rho)^2\right) - B(d\theta)^2 - e^{2\mu}(dz)^2 \tag{5}$$

where ν, μ, B are functions of the variables η, θ, z and $\eta = t - \rho$ Substituting (2) into (1) we obtain

$$T^{mn}\sqrt{-g} = \gamma \begin{pmatrix} 1 & 1 & 0 & 0 \\ 1 & 1 & 0 & 0 \\ 0 & 0 & 0 & 0 \\ 0 & 0 & 0 & 0 \end{pmatrix} \delta(z - Z(\theta))\delta(\rho - t) \tag{6}$$

*lelyakov@crimea.edu
†kararaja@mail.ru

System of Einstein Equations for a "Smeared" Problem

The components of the energy-momentum tensor for a real massles scalar field look like

$$T_{\alpha,\beta} = \varphi_{,\alpha}\varphi_{,\beta} - \frac{1}{2}g_{\alpha,\beta}L \tag{7}$$

where $L = g^{\alpha,\beta}\varphi_{,\alpha}\varphi_{,\beta}$, $\varphi_{,\alpha} = \partial\varphi/\partial x^{\alpha}$, φ -is the scalar field potential, and the subscripts α, β vary from 0 to 3. In order to ensure he self-consistency of the Einstein equations for (1), we require that

$$T_{\alpha,\beta} = T_{\alpha,\beta}(\eta, \theta, z) \rightarrow \varphi = \varphi(\eta, \theta, z) \tag{8}$$

The system of Einstein equations can be presented in the form

$$-\mu_{,\eta\eta} - \frac{B_{,\eta\eta}}{2B} - (\mu_{,\eta})^2 + \left(\frac{B_{,\eta}}{2B}\right)^2 + 2\nu_{,\eta}\left(\mu_{,\eta} + \frac{B_{,\eta}}{2B}\right) = \chi(\varphi_{,\eta})^2 \tag{9}$$

$$\frac{B_{,\eta z}}{2B} + \nu_{,\eta z} - \frac{1}{4}\frac{B_{,\eta}}{B}\frac{B_{,z}}{B} - \frac{B_{,\eta}}{2B}\nu, z - \frac{B_{,z}}{2B}\mu_{,\eta} - \mu_{,\eta}\nu, z = -\chi\varphi_{,\eta}\varphi_{,z} \tag{10}$$

$$e^{2(\nu-\mu)}\left\{\nu_{,zz} + \frac{B_{,zz}}{2B} + (\nu_{,z})^2 - \left(\frac{B_{,z}}{2B}\right)^2 - \mu_{,z}\nu_{,z} - \frac{B_{,z}}{2B}\left(\mu_{,z} - \nu_{,z} + \frac{B_{,z}}{2B}\right)\right\} +$$

$$+\frac{e^{2\nu}}{2B}\left\langle(\nu_{,\theta\theta}) + (\mu_{,\theta\theta})^2 + \nu_{,\theta})^2 + (\mu_{,\theta})^2 - \frac{B_{,\theta}}{2B}(\mu_{,\theta} + \nu_{,\theta}) + \mu_{,\theta}\nu_{,\theta}\right\rangle =$$

$$= -\chi\frac{e^{2\nu}}{2}\left(\frac{(\varphi_{,z})^2}{e^{2\mu}} + \frac{(\varphi_{,\theta})^2}{B}\right) \tag{11}$$

$$\frac{B}{e^{2\mu}}\left(2\nu_{,zz} + 3(\nu_{,z})^2 - 2\nu_{,z}\mu_{,z}\right) - 2\nu_{,\theta}\mu_{,\theta} - (\nu_{,\theta})^2 = \frac{\chi}{2}\left((\varphi_{,\theta})^2 - \frac{B(\varphi_{,z})^2}{e^{2\mu}}\right) \tag{12}$$

$$(\nu_{,z})^2 + \nu_{,z}\frac{B_{,z}}{B} - \frac{e^{2\mu}}{B}\left(2\nu_{,\theta\theta} + 3(\nu_{,\theta})^2 + \nu_{,\theta}\frac{B_{,\theta}}{B}\right) = \frac{\chi}{2}\left((\varphi_{,z})^2 - \frac{e^{2\mu}}{B}(\varphi_{,\theta})^2\right) \tag{13}$$

$$\nu_{,\eta\theta} + \mu_{,\eta\theta} - \frac{B_{,\eta}}{2B}(\nu_{,\theta} + \mu_{,\theta}) - \mu_{,\eta}(\nu_{,\theta} + \mu_{,\theta}) = \chi\varphi_{,\eta}\varphi_{,\theta} \tag{14}$$

$$\nu_{,\theta z} + \nu_{,z}(\nu_{,z} - \mu_{,\theta}) - \nu_{,\theta}\frac{B_{,z}}{B} = \chi\varphi_{,\theta}\varphi_{,z} \tag{15}$$

Let the scalar field distribution be initially concentrated in the "thin" ring, for which the variables η and z (10)-(15) vary in the intervals

$$\eta \in [-\Delta\eta; \Delta\eta], z \in [Z(\theta) - \Delta z; Z(\theta) + \Delta z] \tag{16}$$

where $\Delta\eta$ and Δz are small positive constants that determine the ring "thickness" i.e.

$$\Delta\eta << 1, \quad \Delta z << 1, \tag{17}$$

Then the ring is contracted into one-dimensional object (a null string),

$$\Delta\eta \rightarrow 0, \quad \Delta z \rightarrow 0, \tag{18}$$

12

The space, in which this "smeared" null string is located and where the variables η and z vary in the intervals

$$\eta \in (-\infty; +\infty), z \in (-\infty; +\infty), \theta \in [0; 2\pi] \qquad (19)$$

Can be conditionally divided into three regions:
region I

$$\eta \in (-\infty; -\Delta\eta) \cup (\Delta\eta; +\infty), z \in (-\infty; +\infty), \theta \in [0; 2\pi], \qquad (20)$$

region II

$$\eta \in [-\Delta\eta; \Delta\eta], z \in (-\infty; Z(\theta) - \Delta z) \cup (Z(\theta) + \Delta z; +\infty), \theta \in [0; 2\pi], \qquad (21)$$

region III

$$\eta \in [-\Delta\eta; \Delta\eta], z \in [Z(\theta) - \Delta z; Z(\theta) + \Delta z], \theta \in [0; 2\pi]. \qquad (22)$$

While contracting the scalar field into a string, the system of equations (10)-(15), for the scalar field should asymptotically coincide with the system of equations for the closed null string. Therefore, in regions I and II (15), (15)

$$\varphi \to 0, \quad \varphi_{,z} \to 0, \quad \varphi_{,\eta} \to 0, \quad \varphi_{,\theta} \to 0 \qquad (23)$$

And in region III

$$\frac{\varphi_{I,II}}{\varphi_{III}} \le 1, \quad \frac{(\varphi_{,z})_{I,II}}{(\varphi_{,z})_{III}} \le 1, \quad \frac{(\varphi_{,\eta})_{I,II}}{(\varphi_{,\eta})_{III}} \le 1, \quad \frac{(\varphi_{,\theta})_{I,II}}{(\varphi_{,\theta})_{III}} \le 1, \qquad (24)$$

where $\varphi_{I,II}$ are the scalar field potentials in regions I and II , φ_{III} is the scalar field potential in regions III (inside the "thin" ring), and the equalities take place at the region boundaries. According to Eq.(24), in region I , the scalar field potential at any fixed $\eta = \eta_0 \in (-infty; -\Delta\eta) \cup (\Delta\eta; +\infty)$ and for all $z \in (-\infty; +\infty)$

$$\varphi(\eta_0, \theta, z) \to 0. \qquad (25)$$

However, if we consider the distribution of scalar field potential at any fixed $\eta = \eta_0 \in [-\Delta\eta; \Delta\eta]$, (regions II and III), then in the case $z \in (-\infty; -\Delta z)$ (region II), it must be as Eq.(25). And, in the case $z \in [-\Delta z; \Delta z]$ (region III)

$$\frac{\varphi(\eta_0, \theta, z)_{III}}{\varphi(\eta_0, \theta, z)_{II}} > 1. \qquad (26)$$

Distribution of the Scalar Field Potential for a "Smeared" Null String

Under conditions (23)-(26), it is convenient to express the distribution of a scalar field potential in the form

$$\varphi(\eta, \theta, z) = \ln\left(\frac{1}{(\alpha(\eta) + \lambda(\eta)\mathrm{f}(\vartheta))^\gamma}\right) \qquad (27)$$

where $\vartheta = \vartheta(z, \theta) = z - Z(\theta)$,γ - is some positive constant. The functions $\alpha(\eta)$ and $\lambda(\eta)$ are symmetric with respect to the inversion η to $-\eta$:

$$\alpha(\eta) = \alpha(-\eta), \quad \lambda(\eta) = \lambda(-eta). \qquad (28)$$

13

The function $\alpha(\eta) + \lambda(\eta)f(\vartheta)$ is confined

$$0 < \alpha(\eta) + \lambda(\eta)f(\vartheta) \leq 1 \tag{29}$$

Hence, in expression (27) for the scalar field potential, the functions $\alpha(\eta)$ and $f(\vartheta)$ are bounded for all $\eta \in (-\infty; +\infty)$ and $z \in (-\infty; +\infty)$

$$0 \leq \alpha(\eta) \leq 1, \quad 0 \leq f(\vartheta) \leq f_0. \tag{30}$$

As an example, the functions

$$\alpha(\eta) = \exp\left\{-\frac{1}{\varepsilon + (\xi\eta)^2}\right\}, \quad f(\vartheta) = f_0\exp\left\{-\mu\left(1 - \exp\left\{-\frac{1}{(\zeta\vartheta)^2}\right\}\right)\right\}, \tag{31}$$

where the constants ξ and ζ describe the size (the "thickness") of the ring (fig.1), in which the scalar field is concentrated, satisfy the found conditions.
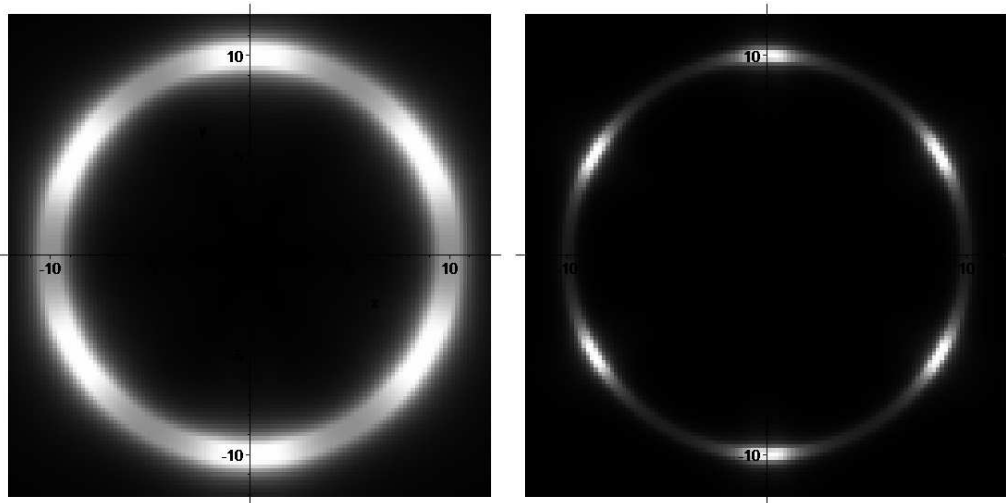
Figure 1: **Distribution of the scalar field potential given by Eqs.(31) and determined by the function $Z(\theta) = \cos(3\theta)$ on the surface $z = const$, $x \in [-12, 12]$, $y \in [-12, 12]$ t = 10. Left page: $\xi = \zeta = 1.1$, right page: $\xi = \zeta = 3$.**

Conclusions

In the work, the general form of the scalar field potential distribution for a closed "smeared" null string with axial symmetry are compared. The conditions imposed on the scalar field potential are obtained, under which the components of the energy-momentum tensors for a scalar field that contracts into a one-dimensional object and a closed null string asymptotically coincide. An example is given for the scalar potential distribution that satisfies those conditions.

References

[1] Vilenkin A., Shellard E.P.S. Cosmic strings and other topological defects , Cambridge Univ. Press, (1994) 534.

[2] Peebles P.S.E. Principles of physical cosmology , Prinston University Press, (1994).

[3] S.N. Roshchupkin, A.A. Zheltukhin, Class. Quantum. Grav, 12, (1995).

[4] O.P. Lelyakov, A.S. Karpenko, R.-D.O. Babadzhan, Ukr. J. Phys.V. 59, 5, (2014) 547.

DIFFUSION COEFFICIENT IN THE SOFT-WALL MODEL OF HOLOGRAPHIC QCD WITH HIGHER ORDER GRAVITY CORRECTIONS

N. Bhatnagar*, S. Siwach [†]
Department of Physics, Banaras Hindu University, Varanasi, India

Annotation

We have studied the effect of higher order gravity corrections(Gauss-Bonnet) on the conductivity and diffusion coefficient using soft wall model of holographic QCD. We have calculated the flow of conductivity, and then diffusion constant is calculated using the sliding membrane paradigm. Finally, the numerical results of conductivity and the diffusion coefficient for different values of the chemical potential is obtained.

Introduction

The study of transport properties of a strongly coupled system has always been a challenge as traditional perturbative approaches are not applicable. Introduction of AdS/CFT(anti-de Sitter/Conformal field theory) duality by Maldacena [1], makes the situation more conducive to study the low energy dynamics of strongly coupled theories. As suggested, the dynamics of strongly coupled theory in d-dimensions can be studied using its weakly coupled gravity dual in d+1 dimensions bulk, alternatively known as holography [2–4].

Diffusion coefficient or diffusivity in general can be calculated using Fick's law and found to be dependent on temperature,viscosity of the fluid and pressure. Many successful attempts of studying the diffusion coefficient and other transport coefficients for a strongly coupled system, which are of great practical importance, has been made using the AdS/CFT duality [5–7]. There are two models to study the strongly coupled system using holographic QCD; namely, Hard wall [8] and Soft wall [9] models. Soft wall model is the modified form with a dilaton field which act like a IR cut-off in order to introduce the confinement. Many of the features of QCD like hadron spectra and linear Regge trajectories have been successfully captured by the soft wall model.

We have studied the dependence of renormalization group(RG)flow of conductivity on gravity corrections in our previous work [10]. Here, we have investigated the dependence of the diffusion constant $D(u_c)$ on Gauss-Bonnet terms and chemical potential in the soft wall model.

Einstein-Maxwell system with Gauss-Bonnet corrections in the Soft Wall model

Our interest is to introduce the higher order gravity corrections(Gauss-Bonnet) in the soft wall model and calculate the transport properties of the system. The action with the

---

*bhtngr.neha@gmail.com
†sksiwach@hotmail.com

Gauss-Bonnet coupling term in the soft wall model is given by

$$S = \int d^5x \sqrt{-g}e^{-\phi} \left\{ \frac{1}{2\kappa^2}(R - 2\Lambda + \alpha R_{GB}) - \frac{1}{4g^2}F^2 \right\}, \tag{1}$$

where $R_{GB} = R^2 - 4R_{MN}R^{MN} + R^{MNPQ}R_{MNPQ}$ is Gauss-Bonnet term and α is the Gauss Bonnet Coupling constant. F^2 is the gauge field strength squared, $\kappa^2 = 8\pi G_5$ and $\Lambda = -6/l^2$ is the cosmological constant. The charged black hole solution of the above system is given as [11, 12]

$$ds^2 = \frac{r_+^2}{l^2 u}(-f(u)N^2 dt^2 + \sum_{i=1}^{3} dx^i dx^i) + \frac{l^2 du^2}{4u^2 f} \tag{2}$$

where $N^2 = \frac{1}{2}\left(\sqrt{1-4\alpha} + 1\right)$, $f(u) = \frac{1}{2\alpha}(1 - \sqrt{1 - 4\alpha(1-u)(1+u-au^2)})$, $a = \frac{l^2\kappa^2 Q^2}{6g^2}$, $Q = \frac{2\mu}{r_+}$ (Q is the charge of the black hole , μ is chemical potential and l is the AdS radius).

The linear dilaton profile $\phi = cu$ is taken as in [9], with $c = 0.388 GeV^2$. Taking the metric and gauge field perturbations as $g_{mn} = g_{mn}^0 + e^{\phi}h_{mn}$ and $A_m = A_m^0 + A_m$ and then introducing the Fourier transform of the fields as,

$$h_{mn}(t, z, u) = \int \frac{d^4k}{(2\pi)^4}e^{-i\omega t + ikz}h_{\mu\nu}(k, u)$$

$$A_m(t, z, u) = \int \frac{d^4k}{(2\pi)^4}e^{-i\omega t + ikz}A_{\mu}(k, u),$$

one gets the linearised equations of motion for vector modes of metric perturbations h_z^x, h_t^x and gauge field; (using the gauge condition $h_{u\nu} = 0$ and $A_u = 0$).

$$0 = \omega h_t'^x - \frac{u\mathcal{M}'}{\mathcal{M}}fN^2 k h_z'^x - \frac{3aN^2 A_x\omega}{\mathcal{M}} \tag{3}$$

$$0 = h_t''^x + \frac{\mathcal{M}'}{\mathcal{M}}h_t'^x + \frac{l^8}{4fr_+^2}\frac{\mathcal{M}'}{\mathcal{M}}(\omega k h_z^x + k^2 h_t^x) - \frac{3aN^2 A_x'}{\mathcal{M}} \tag{4}$$

$$0 = A_x'' + (\frac{f'}{f} - c)A_x' + \frac{l^4}{4N^2 f^2 r_+^2 u}(\omega^2 - k^2 f)A_x - e^{\phi}\frac{1}{N^2 f}h_t'^x \tag{5}$$

where, $\mathcal{M} = \frac{1 - 2\alpha f(u)}{u}$ [12].

Conductivity

In this section, we evaluate the AC(σ_A) and DC conductivity(σ_{DC}) flow in the soft wall model as defined in [13–15] using sliding membrane paradigm.

$$\sigma_A(\omega, u) = \frac{J^x}{i\omega A_x}, \tag{6}$$

where the current density J^x is obtained from the equation of the gauge field and is given by,

$$J^x = \frac{-1}{g^2}\sqrt{-g}e^{-\phi}F^{ux} + \frac{g_{xx}}{2\kappa^2}\sqrt{-g}A_t'h_t^x. \tag{7}$$

Then,the flow for AC conductivity at the cut-off surface u_c can be written as,

$$\frac{\partial_{u_c}\sigma_A}{i\omega} - \frac{g^2\sigma_A^2}{\sqrt{-g}e^{-\phi}g^{uu}g^{xx}} - \frac{2\kappa^2 g^{xx}\sqrt{-g}}{g^4\omega^2}(A_t')^2\frac{4u^2}{\mathcal{M}r_+^2} + \frac{\sqrt{-g}e^{-\phi}g^{xx}g^{tt}}{g^2} = 0 \tag{8}$$

DC conductivity flow can be evaluated at $\omega = 0$.

$$\sigma_{DC} = \frac{r_+}{g^2 l}e^{-c}\frac{(a-2c)^2\left(-3ae^{cu_c}+3au_c+a-2c\right)^2}{\left(a\left(3e^c-4\right)+2c\right)^2(a(2-3u_c)+2c)^2} \tag{9}$$

The frequency dependent AC conductivity flow for various values of the chemical potential is shown in Fig.1.
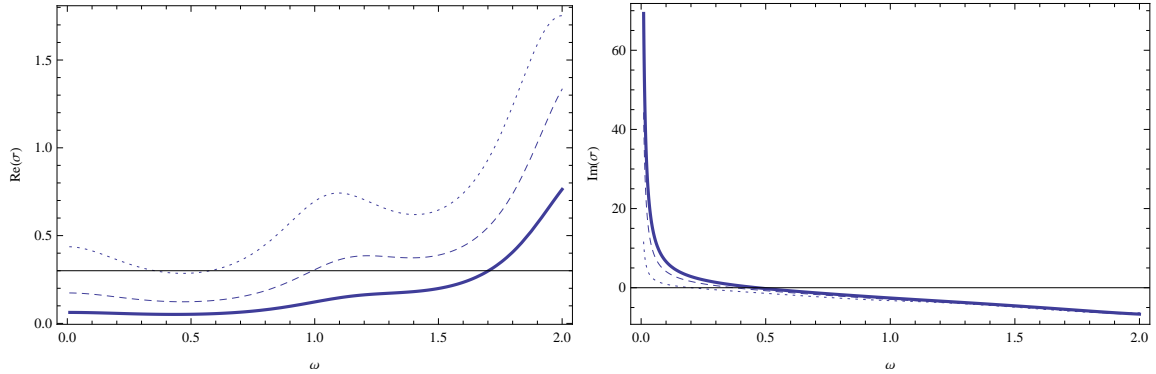
Figure 1: Frequency dependence of AC conductivity flow in the soft wall model for varying μ =0.01(dotted),0.05(dashed)and 0.1(thick) at α=0.01

Diffusion constant $D(u_c)$

In this section we evaluate the diffusion coefficient in the soft wall model with Gauss-bonnet corrections.Diffusion coefficient can be evaluated using the definition of conductivity at the cut-off surface following [14]

$$\frac{1}{\sigma_h(u_c)} = \frac{1}{\sigma_h(1)} - \frac{k^2}{i\omega}\frac{D(u_c)}{\sigma_h(1)} \tag{10}$$

The conductivity (which is identified with shear viscosity [12]) can be evaluated using the expression of Ohm's law and is given as,

$$\sigma_h := \frac{j^z}{f_{zt}} = (-u^2 M')\frac{j^z}{\tilde{f}_{zt}}. \tag{11}$$

The diffusion constant can be calculated in the scaling limit [16] for non-zero momentum limit, $\partial_t \sim \epsilon^2$ and $\partial_z \sim \epsilon$. The lowest order current density in the scaling limit is given by $\partial_u \tilde{j}^{t(0)} = 0,\ \partial_u j^z = 0$ where, $\tilde{j}^{t(0)} = j^{t(0)} - \frac{1}{g^2}\sqrt{-g}\frac{4u^3}{r_+^2}A_t'A_x^{(0)} = C_0$. Also,

$$f_{zt}(u) = -\frac{\tilde{f}^{(0)}(1)}{1-2(2-a)\alpha} + 2\kappa^2\int_u^1 du\frac{\partial_z j^{t(0)}}{\sqrt{-g}g^{uu}g^{tt}g_{xx}} \tag{12}$$

18

and the scaled matter equation can be written as, $\partial_u(\sqrt{-g}e^{-\phi}g^{uu}g^{xx}\partial_u A_x^{(0)}) = \sqrt{-g}\dfrac{4u^3}{r_+^2}A_t'h_t'^{x(0)}$. The solution for A_x^0 is given by,

$$A_x^{(0)}(u) = \frac{3ag^2l^3(e^{cu} - e^{cu_c})}{NQr_+^3\left[3a(e^{cu} - e^{cu_c}) + c(a(2 - 3u_c) + 2)\right]}. \tag{13}$$

Using (10), the diffusion constant at the cut-off (u_c) surface is given as

$$D(u_c) = \frac{\dfrac{l^2}{2r_+}Nf(u_c)}{(2(1 + a) - 3au_c)}[1 - 2\alpha(2 - a)] \tag{14}$$

Thus, from the above expression we notice the explicit dependence of diffusion constant on Gauss-Bonnet corrections term, shown in Fig 2. The dependence of shear viscosity $\sigma_h(u = 1)$ on Gauss-Bonnet term and chemical potential is also shown.
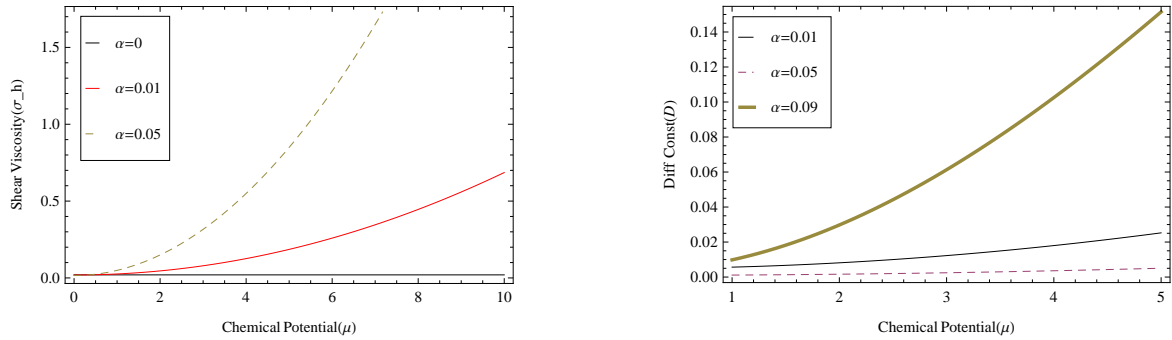
Figure 2: **Shear viscosity(Left)and Diffusion constant(Right) as a function of chemical potential for different Gauss-Bonnet corrections**

Conclusions

We have summarized the important results of transport properties like conductivity and diffusion constant in the soft wall model of low energy dynamics of QCD. We have found that the flow of AC and DC conductivity is independent of gravity corrections (Gauss-Bonnet terms). On the other hand an explicit dependence of diffusion constant and shear viscosity on the Gauss-Bonnet coupling and chemical potential has been shown in the soft wall model.

Acknowledgment

References

[1] J. M. Maldacena, Adv. Theor. Math. Phys. **2**, 231 (1998).

[2] S. S. Gubser, I. R. Klebanov and A. M. Polyakov, Phys. Lett. B 428 (1998) 105.

[3] E. Witten, Adv. Theor. Math. Phys. 2 (1998) 253.

[4] L. Susskind and E. Witten,

[5] D. T. Son and A. O. Starinets, JHEP 0209 (2002) 042; [hep-th/0205051].

[6] S. Takeuchi and Y. L. Wu, Phys. Rev. D 88 (2013) 026004 .

[7] R. C. Myers, A. O. Starinets and R. M. Thomson, JHEP 0711 (2007) 091.

[8] T. Sakai and S. Sugimoto, Prog. Theor. Phys. 113 (2005) 843.

[9] A. Karch, E. Katz, D. T. Son and M. A. Stephanov, Phys. Rev. D 74 (2006) 015005 .

[10] N. Bhatnagar and S. Siwach, Int. J. Mod. Phys. A 31 (2016) 1650030.

[11] R. G. Cai, Phys. Rev. D 65 (2002) 084014.

[12] X. -H. Ge, Y. Ling, Y. Tian and X. -N. Wu, JHEP 1201 (2012) 117.

[13] N. Iqbal and H. Liu, Phys. Rev. D 79 (2009) 025023.

[14] X. H. Ge, et.al. Prog. Theor. Phys. 120 (2008) 833.

[15] Y. Matsuo, S. -J. Sin and Y. Zhou, JHEP 1201 (2012) 130.

[16] I. Bredberg, C. Keeler, V. Lysov and A. Strominger, JHEP 1103 (2011) 141.

THE TWO-SPECIES ANNIHILATION REACTION: EFFECT OF FINITE CORRELATION TIME AND COMPRESSIBILITY

Š. Birnšteinová[1], T. Lučivjanský[1,2]

[1]*Pavol Jozef Šafárik University in Košice, Košice, Slovak Republic*

[2] *Fakultät für Physik, Universität Duisburg-Essen, Duisburg, Germany*

Annotation

The two-species annihilation reaction $A + B \to \emptyset$ with equal diffusion constants $D_A = D_B$ is studied in the presence of a velocity fluctuation. The velocity fluctuations are generated by a self-similar Gaussian ensemble. The special emphasize is put on the effect of finite correlation time and compressibility of the environment. Using the perturbative renormalization group the long-time behaviour of the model near its critical dimension is analyzed using a three-parameter expansion in ϵ, Δ and η, where ϵ is the deviation from the Kolmogorov scaling, Δ is the deviation from the (critical) space dimension $d_c = 2$, and η is the deviation from the parabolic dispersion law. We summarize possible asymptotic regimes corresponding to infrared (IR) fixed points of the renormalization group equations calculated up to the leading order in the perturbation theory.

Introduction

A diffusion-limited annihilation reaction $A + B \to \emptyset$ is sufficiently described by the mean field type rate equation in dimension $d > 4$ [1]. The classical rate equation for particle densities n_A and n_B with a homogeneous initial condition $n_A(0) = n_B(0) \equiv n_0$ is given by

$$\frac{\mathrm{d}n_A}{\mathrm{d}t} = \frac{\mathrm{d}n_B}{\mathrm{d}t} = -K_0 n_A n_B, \tag{1}$$

where K_0 is the rate constant [2]. Asymptotic decay ($t \to \infty$) for both densities goes as $n_A = n_B = (K_0 t)^{-1}$. In lower dimensions ($d \leq 2$) fluctuations become relevant and in comparison to the single spieces reaction we need to introduce the second critical dimenson $d = 4$, because of particle segregation into A and B domains in $d < 4$ [3, 4]. Densities for A and B spieces follow asymptotic decay $n_A = n_B = (K_0 t)^{-d/4}$ in $d < 4$ [5].

Dynamic action for the annihilation reaction

A stochastic problem can be mapped to a field theory using Doi approach [6] and coherent state representation [7]. The diffusion and reaction part of action with initial condition can be written as

$$\mathcal{S}_{dif} = -\int_0^\infty \mathrm{d}t \int \mathrm{d}^d x \left\{ \psi_A^\dagger \partial_t \psi_A - D_0 \psi_A^\dagger \nabla^2 \psi_A + \psi_B^\dagger \partial_t \psi_B - D_0 \psi_B^\dagger \nabla^2 \psi_B \right\},$$

$$\mathcal{S}_{reak} = -\int_0^\infty \mathrm{d}t \int \mathrm{d}^d x \left\{ K_0 \left[\psi_A^\dagger + \psi_B^\dagger + \psi_A^\dagger \psi_B^\dagger \right] \psi_A \psi_B \right\}, \tag{2}$$

$$\mathcal{S}_{init} = \int \mathrm{d}^d x \left\{ n_0 \psi_A^\dagger + n_0 \psi_B^\dagger - r_0 n_0 \psi_A^\dagger \psi_B^\dagger \right\}.$$

21

where D_0 is the diffusion constant [2].

To generate fluctuations of the advection velocity field we use the Kraichnan-Antonov model [8], with a correlation function

$$\langle \boldsymbol{v}_i(t, \boldsymbol{x})\boldsymbol{v}_j(t', \boldsymbol{x}')\rangle = \int \frac{\mathrm{d}\omega}{2\pi} \int \frac{\mathrm{d}^d\boldsymbol{k}}{(2\pi)^d}[P_{ij}(\boldsymbol{k}) + \alpha Q_{ij}(\boldsymbol{k})]D_{\boldsymbol{v}}(\omega, \boldsymbol{k})e^{-i(t-t')+i\boldsymbol{k}\cdot(\boldsymbol{x}-\boldsymbol{x}')}, \quad (3)$$

where $P_{ij}(\boldsymbol{k}) = \delta_{ij} - k_i k_j/k^2$ is the transverse projector and $Q_{ij} = k_i k_j/k^2$ is the longitudinal projector. The choice of the nonnegative parameter $\alpha = 0$ gives the incompressible model. The kernel function is of the form

$$D_{\boldsymbol{v}}(\omega, \boldsymbol{k}) = \frac{g_0 w_0 D_0^3 k^{2-2\Delta-2\epsilon-\eta}}{\omega^2 + (w_0 D_0 k^{2-\eta})^2}, \quad (4)$$

where g_0 is the coupling constant. Then advection part of the action has form

$$\begin{aligned}
\mathcal{S}_{adv} = &-\int_0^\infty \mathrm{d}t \int \mathrm{d}^d x \Big\{\psi_A^\dagger \boldsymbol{\nabla} \cdot (\boldsymbol{v}\psi_A) + \psi_B^\dagger \boldsymbol{\nabla} \cdot (\boldsymbol{v}\psi_B)\Big\} \\
&-\frac{1}{2}\int \mathrm{d}t \int \mathrm{d}^d x \int \mathrm{d}t' \int \mathrm{d}^d x' \, \boldsymbol{v}(t, \boldsymbol{x})D_{\boldsymbol{v}}^{-1}(t - t', \boldsymbol{x} - \boldsymbol{x}')\boldsymbol{v}(t', \boldsymbol{x}').
\end{aligned} \quad (5)$$

The Kraichnan-Antonov model contains two special cases [8]:
- the rapid-change model in the limit $w_0 \to \infty$ with the kernel function $D_v(\omega, k) \to g_0' D_0 k^{-d-2\epsilon+\eta}$
- the model with frozen velocity field corresponds to the case when $w_0 \to 0$ and the kernel function $D_v(\omega, k) \to g_0 D_0^2 k^{2-d-2\epsilon}$

The total action of the model can be rewritten as

$$\mathcal{S}(\psi_A^\dagger, \psi_A, \psi_B^\dagger, \psi_B, \boldsymbol{v}) = \mathcal{S}_{dif} + \mathcal{S}_{reak} + \mathcal{S}_{adv} + \mathcal{S}_{init}. \quad (6)$$

Statistical averages of random quantities can be obtaind using the generating functional

$$\mathcal{W}(\psi_A^\dagger, \psi_A, \psi_B^\dagger, \psi_B, \boldsymbol{v}) = e^{\mathcal{S}(\psi_A^\dagger, \psi_A, \psi_B^\dagger, \psi_B, \boldsymbol{v})}. \quad (7)$$

UV renormalization

The analysis of UV divergences ($\boldsymbol{x} \to 0$ and $t \to 0$) is based on the analysis of the canonical dimensions. Dynamical models have two scales, a space and a time scale. The total canonical dimension of some quantity F is given as $d_F = d_F^k + 2d_F^\omega$ and serve then for identification of possible ultraviolet (UV) divergencies. We rescale field and parameters of the model

$$\phi \to Z_\phi \phi, \quad \phi = \{\psi_A, \psi_A^\dagger, \psi_B, \psi_B^\dagger, \boldsymbol{v}\}, \quad e_0 = e\mu^{d_e}Z_e, \quad e \in \{D_0, \lambda_0, g_0, w_0\}, \quad (8)$$

where μ is the renormalization mass in the minimal substraction scheme and Z_e are renormalization constants which could be obtained from the requirement that they absorb UV divergences which seems like poles in small parameters of the model [8,9].

Stable IR regimes

The beta and gamma functions can be obtained from relations [9]

$$\gamma_e \equiv \mu\partial_\mu \ln Z_e, \quad \beta_e \equiv \mu\partial_\mu e. \tag{9}$$

We are interested in behavior at the low dimensions $(d < d_c)$, where the IR singularities $(\boldsymbol{x} \to \infty$ and $t \to \infty$) appear. This is governed by the IR stable fixed points, which are identified as zeros of the all beta functions

$$\beta_g(e^*) = \beta_\lambda(e^*) = \beta_w(e^*) = 0 \tag{10}$$

and positive eigenvalues of matrix

$$\Omega_{ij} = \partial\beta_i/\partial e_j|_{e=e^*}. \tag{11}$$

In order to find fixed points for the rapid-change model, it is convenient to introduce new variables [8]

$$u_0 = 1/w_0, \quad g_0' = g_0/w_0. \tag{12}$$

The limit $u_0 \to 0$ and $g_0' = const.$ corresponds to the rapid-change model, whereas the model with a frozen velocity field corresponds to the limit $w_0 \to 0$ and $g_0 = const.$

Table 1: Coordinates of the stable fixed points for the rapid-change model.

FP	g^*	u^*	λ^*
FP_1^I	0	0	0
FP_2^I	0	0	-4Δ
FP_3^I	$\frac{4(2\epsilon-\eta)}{1+\alpha}$	0	0
FP_4^I	$\frac{4(2\epsilon-\eta)}{1+\alpha}$	0	$-4\Delta + 2\frac{1-\alpha}{1+\alpha}(-2\epsilon+\eta)$

Table 2: Coordinates of the stable fixed points for a frozen velocity field.

FP	g^*	w^*	λ^*
FP_1^{II}	0	0	0
FP_2^{II}	0	0	-4Δ
FP_3^{II}	4ϵ	0	0
FP_4^{II}	4ϵ	0	$-4\Delta - (1-3\alpha)2\epsilon$
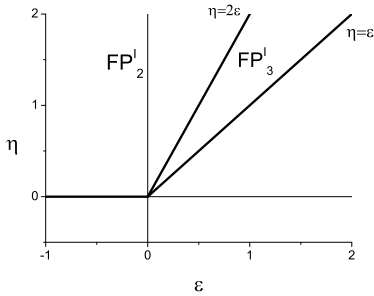
(a) $d = 2, \alpha < 1$
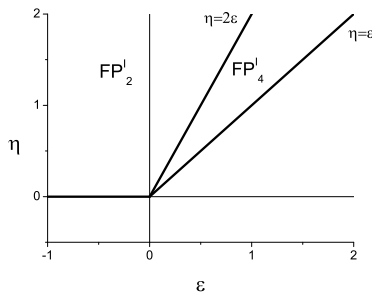
(b) $d = 2, \alpha > 1$
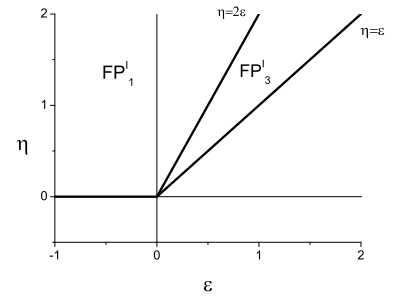
(c) $d > 2, \alpha < 1$

Figure 1: Regions of stability for the fixed points of the rapid change model.

For both the rapid change model and the model with frozen velocity field the first stable fixed points FP_1^I and FP_1^{II} are trivial without velocity and density fluctuations. For the

(a) $d = 2, \alpha < 1/3$ **(b)** $d = 2, \alpha > 1/3$ **(c)** $d > 2, \alpha < 1/3$
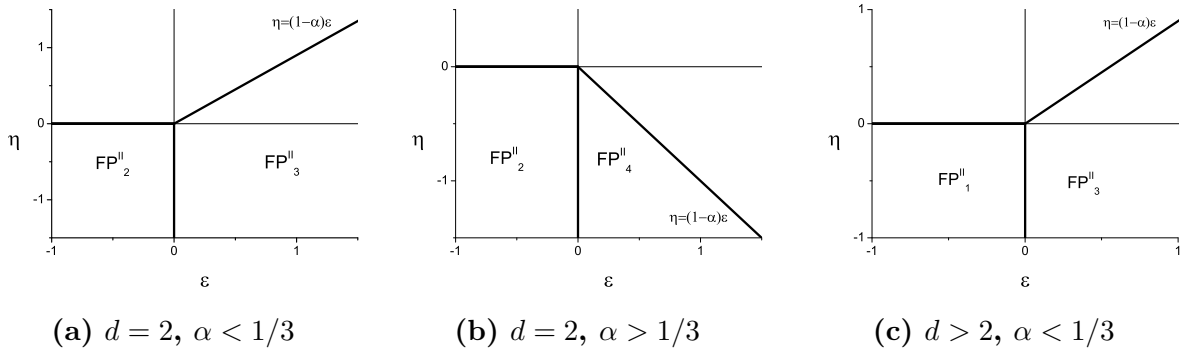
Figure 2: Regions of stability for the fixed points of frozen velocity field.

regime corresponding to the fixed points FP_2^I and FP_2^{II} the effect of velocity fluctuations is still irrelevant but reaction process is not.

The rest of fixed points correspond to regimes with relevant velocity fluctuations. In Figs. (1a) and (2a) we can see that for a small value of the parameter α for both considered limits reaction process is irrelevant even below critical dimension $d_c = 2$. Fluctuations of velocity field affect speed of reaction in low dimension, where correlation functions strongly depend on density fluctuations. For case $d > 2$ and a small value of the parameter α only regimes with relevant velocity fluctuation are stable which correspond to fixed points FP_3^I in the rapid-change model and FP_3^{II} in the model with a frozen velocity field.

Conclusions

The annihilation reaction is studied in the presence of random velocity field generated by the compressible Kraichnan-Antonov model. We analyzed possible asymptotic regimes in the limit of the rapid change model and a frozen velocity field up to the first order in the perturbation theory within three-(ϵ, η, Δ) parameter expansion. However, the model for velocity field is allowed only for small values of parameter alpha ($\alpha \ll 1$) [10] and thus careful interpretation is needed.

References

[1] B. P. Lee and J. Cardy, J. Stat. Phys. 80 (1995) 971.

[2] J. Honkonen, Acta Physica Slovaca 52 (2002) 533.

[3] U. C. Täuber, Critical Dynamics: A Field Theory Approach to Equilibrium and Non-Equilibrium Scaling Behavior, Cambridge University Press, Cambridge, 2014.

[4] U. C. Tuber, M. Howard and B. P. Vollmayr-Lee, J. Phys. A: Math. Gen. 38 (2005) R79-R131.

[5] D. Toussaint and F. Wilczek, J. Chem. Phys. 78 (1983) 2642.

[6] M. Doi, J. Phys. A 9 (1976) 1465.

[7] L. Peliti, J. Phys. (Paris) 46 (1985) 1469.

[8] N. V. Antonov, Physica D 144 (2000) 370.

[9] A. N. Vasil'ev, "The Field Theoretic Renormalization Group in Critical Behaviour Theory and Stochastic Dynamics", Chapman Hall/CRC Press, Florida, 2004.

[10] Krzysztof Gawędzki and Massimo Vergassola, Physica D 138 (2000) 63.

INFLUENCE OF VELOCITY FLUCTUATIONS IN THE MODEL-F OF CRITICAL DYNAMICS*

M. Dančo[1,2†], M. Hnatič[1,2,3], M .V. Komarova[4], T. Lučivjanský[3,5], M. Yu. Nalimov[4]

[1]*Institute of Experimental Physics, SAS, Košice, Slovakia*

[2]*Joint Institute for Nuclear Research, Dubna, Russia*

[3]*Faculty of Sciences, P.J. Šafarik University, Košice, Slovakia*

[4]*Department of Theoretical Physics, St. Petersburg University, St. Petersburg, Petrodvorets, Russia*

[5]*Fakultät für Physik, Universität Duisburg-Essen, Duisburg, Germany*

Annotation

It is shown how model F of critical dynamics can be generalized in the presence of velocity fluctuations within the means of field-theoretic formulation. Using the Dominicis-Janssen approach, we obtain a field theory model that allows for a perturbative renormalization group analysis.

Introduction

Traditional dynamic models [1] of the superfluid are based on the proper identification of slow modes, followed by either Zwanzig projection method or generalized Poisson brackets method [2]. The latter one is especially suitable for hydrodynamic systems. All these models neglect the turbulent phenomena of the superfluids as the corresponding contributions of the Navier-Stokes equation turn out to be irrelevant in the critical region. However, the viscosity vanishes in this region and the Reynolds number becomes effectively large. This means that the system may exhibit a turbulent behavior. A main goal of this study is to show how the influence of velocity fluctuations can be incorporated into model F of critical dynamics

The Model

Using the terminology proposed in [1] model F of critical dynamics is described by the order parameter of conjugated fields $\psi(\boldsymbol{x}, t), \psi^\dagger(\boldsymbol{x}, t)$ that are averages of the Bose-particle field operators, an external magnetic field $h_0(\boldsymbol{x}, t)$ and a field $m(\boldsymbol{x}, t)$ connected with temperature fluctuations in the system. Dynamics of all these fields is given by the Langevin equations

$$\partial_t \psi = f_\psi + \lambda_0(1 + ib_0)\frac{\delta S_F}{\delta \psi^\dagger} + i\lambda_0 g_{03}\psi\frac{\delta S_F}{\partial m}, \tag{1}$$

$$\partial_t \psi^\dagger = f_{\psi^\dagger} + \lambda_0(1 - ib_0)\frac{\delta S_F}{\delta \psi} - i\lambda_0 g_{03}\psi^\dagger\frac{\delta S_F}{\partial m}, \tag{2}$$

$$\partial_t m = f_m - \lambda_0 u_0\partial^2\left(\frac{\delta S_F}{\delta m}\right) + i\lambda_0 g_{03}\left(\psi^\dagger\frac{\delta S_F}{\delta \psi^\dagger} - \psi\frac{\delta S_F}{\delta \psi}\right). \tag{3}$$

The static action S_F is defined as

$$S_F = \int \mathrm{d}^d\boldsymbol{x} \int \mathrm{d}t \left(\psi^\dagger \partial^2 \psi - \frac{1}{2}m^2 + mh_0 - \frac{1}{6}g_{01}(\psi^\dagger\psi)^2 + g_{02}m\psi^\dagger\psi \right). \tag{4}$$

The random forces f_ψ, f_m are assumed to be Gaussian random variables with zero means and correlators D_ψ, D_m with the white-noise correlations in time. Time-momentum representation reads

$$D_\psi(p,t,t') = \lambda_0\delta(t-t'), \quad D_m(p,t,t') = \lambda_0 u_0 p^2 \delta(t-t'). \tag{5}$$

At the transition to the superfluid hydrodynamics, realized when the viscosity tends to zero, the Reynolds number $\mathrm{Re} \equiv LV/\nu_0$ increases (here ν_0 denotes a coefficient of molecular viscosity, L is an outer length of turbulence, and V is a characteristic (mean) velocity). This situation corresponds to the appearance of developed turbulence in the system. A stochastic equation for the critical dynamics of a Bose system in the presence of a random velocity field was proposed in [3]. The equations were derived in accordance with the equilibrium static limit and Galilean invariance and can be written in the compact notation

$$\nabla_t\varphi_a = \eta_a + (\alpha_{ab} + \beta_{ab})\frac{\delta S^{st}}{\varphi_b}, \qquad \nabla_t \equiv \partial_t + \boldsymbol{v}\cdot\boldsymbol{\partial}, \quad S^{st} = S_F - \frac{1}{2}\int \mathrm{d}^d\boldsymbol{x}\int \mathrm{d}t\,\boldsymbol{v}^2 \tag{6}$$

with the set of fields $\varphi_a \in \{\psi, \psi^\dagger, m, \boldsymbol{v}\}$ and the set of random forces $\eta_a \in \{f_\psi, f_{\psi^\dagger}, f_m, f_v\}$. The tensor α is a symmetric matrix of Onsager coefficients, and tensor β represents an antisymmetric matrix of streaming coefficients. The noise correlator of the force f_v can be expressed in the form

$$D_v(p,t,t') = g_{04}\nu_0^3 p^{\varepsilon-\delta}\delta(t-t') \tag{7}$$

in the space with dimension $d = 4 - \varepsilon$. The additional exponent δ allows for a deviation from the Kolmogorov turbulent regime. In fact, there are two physically possible and interested regimes. The first one is the regime with hydrodynamic fluctuations near the thermodynamic equilibrium that corresponds to the values $\varepsilon = 1$, $\delta = -1$. The second one is the Kolmogorov turbulent regime with $\varepsilon = 1$, $\delta = 4$.

Dynamical action for model F

The stochastic problem described by the set of Eqs. (6) with η force noise (5) and (7) can be transformed into the field theoretic model by the means of the Martin-Siggia-Rose (MSR) mechanism with the Dominicis-Janssen action [4,5]

$$S = \varphi'_a D_{ab}\varphi'_b + \varphi'_a\left[-\nabla_t\varphi_a + (\alpha_{ab} + \beta_{ab})\frac{\delta S^{st}}{\delta\varphi_b}\right]. \tag{8}$$

Using this procedure the field-theoretic action for model F with activated hydrodynamic modes then reads

$$\begin{aligned}
S = {} & 2\lambda_0\psi^{+\prime}\psi' - \lambda_0 u_0 m'\partial^2 m' + \boldsymbol{v}'D_v\boldsymbol{v}' + \psi^{+\prime}\Big\{-\partial_t\psi - \partial_i(v_i\psi) + \lambda_0(1+ib_0)[\partial^2\psi \\
& - g_{01}(\psi^+\psi)\psi/3 + g_{02}m\psi] + i\lambda_0\psi[g_{07}\psi^+\psi - g_{03}m + g_{03}h_0]\Big\} + \mathrm{H.c} + m'\Big\{-\partial_t - \partial_i(v_i m) \\
& - \lambda_0 u_0\partial^2[-m + g_{06}\psi^+\psi + h_0] + i\lambda_0 g_{05}[\psi^+\partial^2\psi - \psi\partial^2\psi^+]\Big\} + \boldsymbol{v}'\{-\partial_t\boldsymbol{v} + \nu_0\Delta\boldsymbol{v} - v_i\partial_i\boldsymbol{v}\},
\end{aligned} \tag{9}$$

where H.c. stands for a hermitian conjugate of the preceding expression and the following relations between charges are fulfilled

$$g_{05} = g_{03}, \quad g_{06} = g_{02}, \quad g_{07} = g_{02}g_{03}. \tag{10}$$

In the framework of the double (ε, δ) expansion the logarithmic theory does not have a static limit, which profoundly changes the renormalization procedure. We stress that the introduction of the new coupling constants g_{05}, g_{06}, g_{07} restores the multiplicative renormalizability of the model. The field-theoretic formulation has an advantage to be amenable to the full machinery of field theory [6]. Near criticality large fluctuations on all scales dominate the behavior of the system, which results into the divergences in Feynman graphs. The RG technique allows us to deal with them and as a result it allows for perturbative computation of critical exponent in a formal expansion around upper critical dimension. Thus, it provides us with information about the scaling behavior of Green functions. The relations between bare and renormalized constants then read

$$\lambda_0 = \lambda Z_\lambda, \qquad \nu_0 = \nu Z_\nu, \qquad u_0 = u Z_u, \qquad b_0 = b Z_b$$
$$g_{01} = g_1 \mu^\varepsilon Z_{g_1}, \qquad g_{02} = g_2 \mu^{\varepsilon/2} Z_{g_2}, \qquad g_{03} = g_3 \mu^{\varepsilon/2} Z_{g_3}, \qquad g_{04} = g_4 \mu^\delta Z_{g_4} \tag{11}$$

and renormalization of the fields is done by the replacement

$$\psi = \psi_R Z_\psi, \qquad \psi^+ = \psi_R^+ Z_{\psi^+}, \qquad \psi' = \psi_R' Z_{\psi'}, \qquad \psi^{+'} = \psi_R^{+'} Z_{\psi^{+'}}$$
$$m = m_R Z_m, \qquad m' = m_R' Z_{m'}, \qquad \boldsymbol{v} = \boldsymbol{v}_R Z_v, \qquad \boldsymbol{v}' = \boldsymbol{v}_R' Z_{v'}. \tag{12}$$

Directly from the knowledge of renormalization constants we thus can obtain RG functions called anomalous dimensions. Unfortunately, the one-loop approximation for renormalization constants as well as for RG functions yields expressions that are too large and their explicit form can be found elsewhere [7].

Conclusions

In this brief contribution we have summarized main points of how to extend critical model F in the presence of velocity fluctuations. A detailed analysis of the whole fixed points' structure can be found in [7].

References

[1] P. Hohenberg and B. Halperin, Rev. Mod. Phys. 49 (1977) 435 .

[2] R. Folk and G. Moser, J. Phys. A: Math. Gen 39 (2006) R207

[3] M. V. Komarova, D. M. Krasnov, and M. Y. Nalimov, Theor. Math. Phys. 169 (2011) 1441 .

[4] H. K. Janssen, Z. Phys. B 23 (1976) 377 .

[5] C. D. Dominicis, J. Phys. (Paris), Suppl. C1 37 (1976) 247 .

[6] A. N. Vasiliev, *The Field Theoretic Renormalization Group in Critical Behavior Theory and Stochastic Dynamics* (Chapman & Hall/CRC Press, New York, 2004).

[7] M. Dančo, M. Hnatič, M. V. Komarova, T. Lučivjanský, and M Yu. Nalimov, Phys. Rev. E 93 (2016) 012109.

ELECTROMAGNETIC EFFECTS ON STRONGLY INTERACTING QCD-MATTER

A. M. Diab[1,2] , A. N. Tawfik[1,2], M. T. Hussein[3] [1] *Egyptian Center for Theoretical Physics (ECTP), Modern University for Technology and Information (MTI), 11571 Cairo, Egypt*
[2] *World Laboratory for Cosmology And Particle Physics (WLCAPP), Cairo, Egypt*
[3] *Physics Department, Faculty of Science, Cairo University, Giza, Egypt*

Annotation

In order to study the temperature dependence of the quark-hadron phase structure and the QCD equation of state in vanishing and finite magnetic field, the SU(3) Polyakov linear-sigma model is utilized. In mean field approximation, the dependence of various magnetic properties such as magnetization, magnetic susceptibility and magnetic catalysis is analyzed in finite magnetic field. Furthermore, the influences of finite magnetic field on the temperature dependence of some transport properties (viscosity and conductivity) from Green-Kubo correlation are characterized.

Introduction

Due to oppositely directed off-central relativistic collision of two heavy ions, a huge magnetic field (eB) can be created in heavy-ion collision (HIC) experiments. At SPS, RHIC and LHC energies, the strength of this field ranges from 0.1 to 1 and 15 m_π^2, respectively [1, 2]. In fact, such field is much localized and short lived and thus it is assumed to have almost no effect on the detectors and their external magnet but remarkable influences on the strongly interacting quantum chromodynamics (QCD) matter. In the present work, we utilize the Polyakov linear-sigma model (PLSM) in analyzing the temperature dependence of the quark-hadron phase structure and the QCD equation of state (EoS) in vanishing and finite magnetic field. We also present estimation for the magnetization ($\mathcal{M}$), the magnetic susceptibility (χ_B) and the magnetic catalysis of as functions of temperature and compare them to recent lattice QCD calculations. Last but not least, we introduce a direct estimation for various transport properties such as bulk (ξ) and shear (η) viscosities and electric (σ_e) and thermal (κ) conductivities from the Green-Kubo (GK) correlations in finite magnetic field. The present paper is organized as follows. A short reminder to SU(3) PLSM in mean field approximation shall be presented in section II. Section III summarizes our calculations at finite temperature and finite magnetic field. Section IV is devoted to the conclusions.

The approach

PLSM is a successful approach for the quark-hadron phase transition(s), the QCD thermodynamic quantities, and the transport properties. Details about the model can be found in Ref. [3]. In the mean field approximation, the exchange of energy between particle and antiparticle at temperature (T) and baryon chemical potential (μ) is described by the grand canonical partition function (Z). The free energy in finite volume (V) is given as

$F = -T log[Z]/V$ or

$$F = U(\sigma_l, \sigma_s) + U(\phi, \phi^*, T) + \Omega_{\bar{q}q}(T, \mu, B) + \delta_{0,eB}\Omega_{\bar{q}q}(T, \mu), \tag{1}$$

where $U(\sigma_l, \sigma_s)$ is the pure mesonic potential [3] and the second term represents the Polyakov loop potential. In the present work, we use polynomial expansion for $U(\phi, \phi^*, T)$ in ϕ and ϕ^* [4]. The quarks and anti-quark contributions to the medium potential $\Omega_{\bar{q}q}$ can be divided into two regimes:

- In vanishing magnetic field ($eB=0$),

$$\Omega_{\bar{q}q}(T, \mu) = -2T \sum_{f=l,s} \int \frac{d^3p}{(2\pi)^3} \left\{ \ln g_f^+ \ln g_f^- \right\}, \tag{2}$$

where $g_f^\pm$ is the quark and antiquark contribution, respectively.
- In finite magnetic field ($eB \neq 0$), the concepts of Landau quantization and magnetic catalysis can be implemented. The magnetic field is assumed to be oriented along z-direction. Firstly, the finite magnetic field modifies the quarks dispersion relation,

$$E_{B,f} = [p_z^2 + m_f^2 + |q_f|(2n+1-\sigma)B]^{1/2}, \tag{3}$$

where q_f is the electric charge of fth quark-flavor, n is the quantized landau number and σ is related to the spin quantum number S; $\sigma = \pm S/2$. Secondly, at $eB \neq 0$ the potential becomes

$$\Omega_{\bar{q}q}(T, \mu, B) = -2 \sum_{f=l,s} \frac{|q_f|BT}{(2\pi)^2} \sum_{\nu=0}^{\infty}(2-\delta_0\nu) \int dp_z \left\{ \ln g_f^+ + \ln g_f^- \right\}, \tag{4}$$

where the $(2 - \delta_0\nu)$ term stands for degenerate Landau levels and the $(2n+1-\sigma)$ term is replaced by the number of Landau levels ν.

Results

At $eB \neq 0$, we introduce various properties of the QCD matter such as the magnetization ($\mathcal{M}$), the magnetic susceptibility χ_B, the magnetic catalysis and the EoS as functions of temperature and confront them to recent lattice QCD calculations. We also present numerical estimations for bulk and shear viscosity normalized to the thermal entropy (s) and the dimensionless electric and thermal conductivities, ξ/s, η/s, σ_e/T and κ/T^2, respectively. As assumed, the influence of the magnetic field is limited to z-direction, thus $B = B\hat{e}_z$, and the free energy density $f = F/V$ gets modifications as follows [5],

$$f = \epsilon^{\text{tot}} - \epsilon^{\text{field}} - Ts = \epsilon^{\text{tot}} - Ts - eB\mathcal{M}, \tag{5}$$

where $\epsilon^{\text{tot}} = \epsilon + \epsilon^{\text{field}}$ is the total energy density including the energy density (ϵ) of the system and $\epsilon^{\text{field}} = eB\mathcal{M}$ stemming from the influence of the magnetic field. The magnetization ($\mathcal{M}$) and magnetic susceptibility (χ_B) can be derived as,

$$\mathcal{M} = -\frac{1}{V}\frac{\partial F}{\partial(eB)}, \tag{6}$$

30
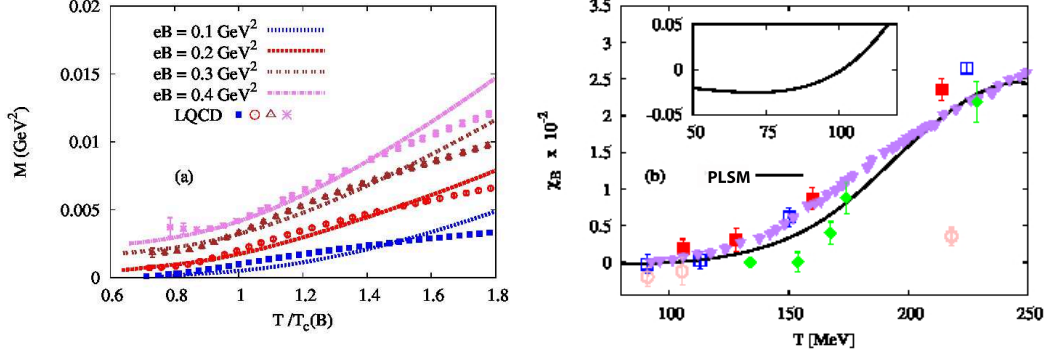
Figure 1: Left-hand panel presents the temperature dependence of the magnetization ($\mathcal{M}$) at $eB \neq 0$. Right-hand panel shows the magnetic susceptibility (χ_B) as a function of temperature at $eB = 0$. The PLSM results are compared with recent lattice QCD simulations (symbols) [5]

$$\chi_B = -1/V \frac{\partial^2 F}{\partial (eB)^2}|_{eB=0}. \tag{7}$$

Fig. 1 depicts the temperature dependence of the magnetization [left-hand panel (a)] in GeV2 at $eB \neq 0$ and the magnetic susceptibility (χ_B) [right-hand panel (b)] at $eB = 0$. The PLSM magnetization is confronted to recent lattice QCD calculation [5]. It is obvious that the magnetization (M¿0) increases with the temperature. This dependence reflects that the thermal QCD-medium is paramagnetic around and above the critical temperature. We also observe an evidence for weak diamagnetism at low temperatures; the magnetization decreases with the temperature, inside box.
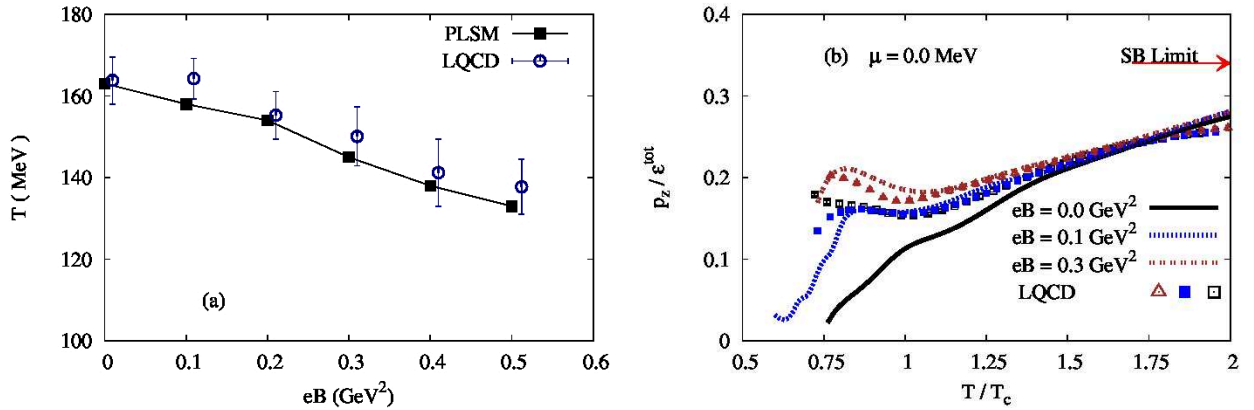
Figure 2: Left-hand panel (a) depicts the dependence of the critical temperature on B. The ratio $p_z/\epsilon^{\rm tot}$ is given as function of T/T_c at $eB \neq 0$. The PLSM results are compared with recent lattice QCD simulations (symbols) [5]

Left-hand panel of Fig.2 (a) shows the variation of the critical temperature with increasing magnetic field. The PLSM critical temperature is estimated from the intersection point (temperature) between the subtracted chiral condensate and the deconfinement phase transition. It is apparent that the critical temperature decreases with raising magnetic field. This phenomenon is known as inverse magnetic catalysis. The speed of sound squared c_s^2 plays an essential role in the estimation of EoS p_z ($\epsilon^{\rm tot}$). Right-hand panel of Fig.2 (b)

31

presents the PLSM calculations for $p_z/\epsilon^{\text{tot}}$ at $eB = 0$ (solid curve), $eB = 0.1$ (dotted curve) and $eB = 0.3$ GeV^2 (double-dotted curve). These results are compared with recent lattice QCD [5] (open square), (close square), and (open triangle), respectively. A good agreement is achieved in comparing the PLSM results with the lattice QCD. It seems that the agreement can be improved with increasing the magnetic field strength. For further PLSM results in presence of the magnetic field the readers are advised to consult Ref. [6].
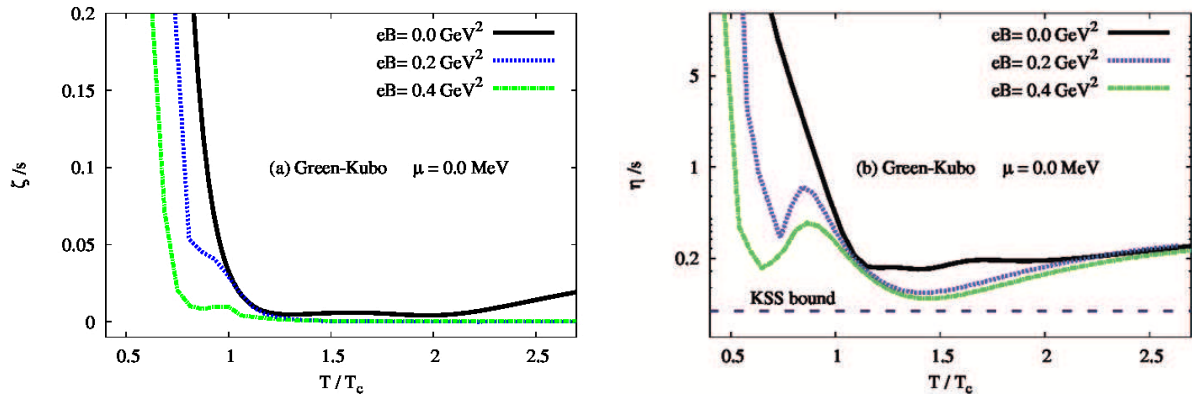
Figure 3: Left-hand panel (a) depicts ξ/s as a function of temperature in finite magnetic field $eB = 0.0$ (solid curve), $eB = 0.2$ and $eB = 0.4$ GeV^2 (dotted dash curve). Right-hand panel (b) shows the same as left-hand panel (a) but for η/s.

The response of QCD matter to the presence of finite magnetic field can be described by the transport coefficients, as well. From the Green-Kubo (GK) correlations, the bulk and shear viscosities (ξ and η) are related to the correlation functions of the trace of the energy-momentum tensor [7].

Fig. 3 depicts the ratios ξ/s and η/s as functions of temperature in finite magnetic field. The solid curve represents the results at $eB = 0.0$, while $eB = 0.2$ and $eB = 0.4$ GeV^2 are given as dotted, dot-dashed curves, receptively. The Kovtun, Son and Starinets (KSS) limit is represented by the dashed line. At low temperatures, ξ/s and η/s becomes very large. A peak positioned at T_c starts to appear. At extremely high temperatures, the coupling seems to become weak and the hadrons liberate into quarks and gluons. Therefore, the temperature dependent of both quantities becomes very weak. The response of QGP-matter for finite electric field can be determined by the electric conductivity σ_e, which is related to the flow of the charges. Left-hand panel of Fig. 4 (a) shows σ_e/T as a function of temperature and compares this with recent lattice QCD simulations [9–11] and different QCD-like models such as NJL and DQPM [8].

The heat conductivity κ is related to the heat flow in such relativistic fluid. From relativistic Navier-Stokes ansatz, the heat flow is proportional to the gradient of thermal potential. Right-hand panel (b) shows κ/T^2 as a function of temperature. The results are compared with NJL and DQPM models [8]. There are no lattice QCD calculations to compare with it.
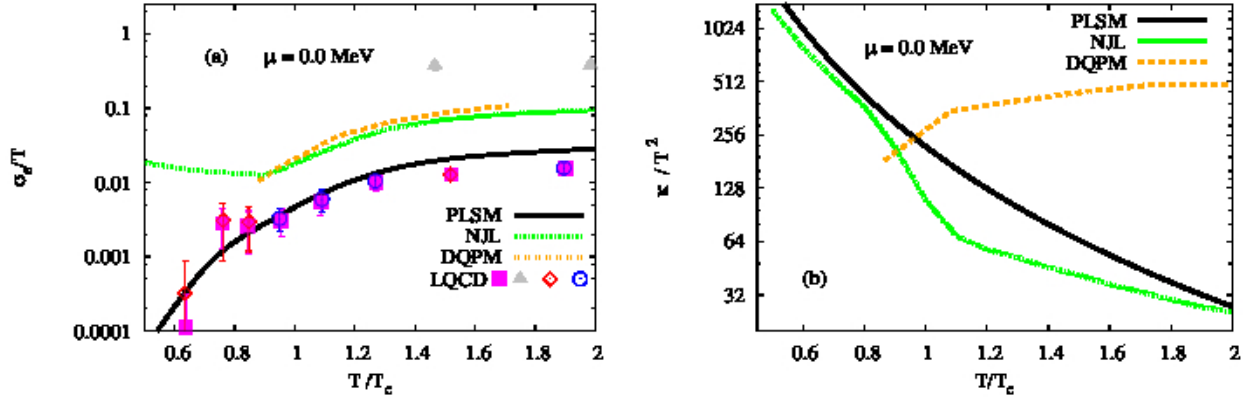
Figure 4: Left-hand panel (a) shows σ_e/T as a function of temperature. PLSM calculations (solid curve) are confronted to recent lattice QCD simulations [9–11] and also compared with NJL and DQPM models [8]. Right-hand panel (b) presents κ/T^2 as a function of temperature. PLSM calculation (solid curve) is compared with NJL and DQPM models [8].

Conclusions

The PLSM seems to be able to reproduce recent lattice QCD calculations for the magnetization, the magnetic susceptibility, the magnetic catalysis and the transport properties (viscosity and conductivity) in vanishing and finite magnetic field. We conclude that the QCD matter possesses paramagnetic property above the critical temperature but diamagnetic one at low temperatures. The PLSM confirms that inverse magnetic catalysis.

References

[1] V. Skokov, A. Y. Illarionov, and V. Toneev, Int. J. Mod. Phys. A 24 (2009) 5925.

[2] A. Bzdak and V. Skokov, Phys. Lett. B 710 (2012) 174 .

[3] A. Tawfik and A. Diab, Phys. Rev. C 91 (2015) 015204.

[4] C. Ratti, M. A. Thaler, and W. Weise, Phys. Rev. D 73 (2005) 014019.

[5] G.S. Bali, F. Bruckmann, G. Endrdi, S.D. Katz, and A. Schaefer, JHEP 1408 (2014) 177.

[6] A. Tawfik and A. Diab, and M.T. Hussein, arXiv:1604.08174 [hep-lat].

[7] D. Fernandez-Fraile and A. Gomez Nicola, Eur. Phys. J. C 62 (2009) 37.

[8] R. Marty, et. al., Phys. Rev. C 88 (2013) 045204.

[9] A. Amato, et. al., Phys. Rev. Lett. 111 (2013) 172001.

[10] H.-T. Ding, et. al., Phys. Rev. D 83 (2011) 034504.

[11] B. B. Brandt, et. al., JHEP 1303 (2013) 100.

FREEZEOUT PARAMETERS AND DYNAMICAL NET-CHARGE FLUCTUATIONS AT NICA ENERGIES

M. Hanafy[1,2*], A. N. Tawfik[2,3], L. I. Abou-Salem[1], A. G. Shalaby[1], A. Sorin[4], O. Rogachevsky[4], W. Scheinast[4]

[1] *Physics Department, Faculty of Science, Benha University, Benha, Egypt*

[2] *World Laboratory for Cosmology and Particle Physics (WLCAPP), Cairo, Egypt*

[3] *Egyptian Center for Theoretical Physics (ECTP), Modern University for Technology and Information (MTI), 11571 Cairo, Egypt*

[4] *Joint Institute for Nuclear Research, Dubna, Moscow region, Russia*

Annotation

The dependencies of different particle ratios on the nucleus-nucleus center-of-mass energy, which can be related to the chemical potential, are calculated by using hadron resonance gas (HRG) and Ultra-relativistic Quantum Molecular Dynamic (UrQMD) models. For UrQMD two different types of phase transitions are taken into consideration, namely crossover and first order, while the HRG model implements fully statistical aspects in describing the particle production and their correlations, especially in the hadron phase. The freezeout parameters, temperature (T) and baryon chemical potential (μ), are deduced by fitting various particle ratios estimated from UrQMD with HRG calculations at 7.7, 11.5, 19.6, 62.4 GeV. The results agree with the parameters which are independently determined from statistical fit of the measured particle ratios and the thermal-statistical approaches. Furthermore, the net-charge fluctuations for K/π, p/π and K/p determined UrQMD, and HRG are compared with the available STAR and NA49 measurements. The future NICA facility covers a wide range of low beam energies. The excellent agreement justifies the conclusion that both UrQMD and HRG are suitable approaches to explain both freezeout parameters and the dynamical net-charge fluctuations.

Introduction

The possible quark-hadron phase transition plays a central role in verifying the quantum chromodynamics (QCD), theory for strong interactions, which predicts that the confined hadrons is conjectured to undergo phase transition(s) to partonic matter called quark-gluon plasma (QGP) [1]. Characterizing QCD matter under extreme conditions of high temperature and density belongs to the main goal of the heavy-ion collisions experiments [2].

Various experimental signatures have been suggested for the detection of the quark-hadron phase transition [3–10] such as the net-charge fluctuations of various produced particles [8,10–12], which can be measured [11–16] and calculated [7–9] in terms of different quantities such as variance of the charge $[V(Q)]$, variance of the charge ratios $[V(R)]$, fluctuations of charged-particle ratios (D) and dynamical net-charge fluctuations (ν_{dyn}). The first three quantities are affected by detector acceptance, global charge conservation, charge asymmetry, background contributions and random efficiency loss [8,17], while ν_{dyn}

---

*mahmoud.nasar@fsc.bu.edu.eg

does not depend on the detector acceptance [8]. It is very suitable for antisymmetric charge distributions and the conservation of global charges [17].

The PHENIX experiment found that ν_{dyn} is consistent with that calculated within the HRG approach, especially if the latter is extrapolated to match with the detector acceptance [15]. This was confirmed by the STAR experiment [5], which also measured the dependence of ν_{dyn} of K/π, K/p, and p/π on the beam energy scan (BES) energies, $\sqrt{s_{NN}} = 7.7 - 200$ GeV [5]. Both CERES [15] and NA49 experiments [18] reported on consistency with pion gas predictions. Their variance was estimated as a function of multiplicities, azimuthal coverages of the detectors, collision centralities [15], collision participants and the pseudo-rapidity bins [11].

The produced particle yields and their volume-independent ratios are well described by statistical-thermal approaches [19–26], such as the hadron resonance gas (HRG) model [3]. At chemical equilibrium, these quantities are well reproduced (statistical fits) by - at least - two parameters, tbaryon chemical potential (μ_b) and freezeout temperature (T_{ch}). Accordingly, the chemical freezeout defines a later stage in the evolution of a heavy-ion collision in which the inelastic collisions no longer take place and consequently the number of produced particle is likely fixed [3].

In the present work, we utilize HRG [27] and the Ultra-relativistic Quantum Molecular Dynamic (UrQMD) v.3.4 models [28] in determining ν_{dyn} at a wide range of beam energies and both chemical freezeout parameters at energies ranging from 7 to ~ 20 GeV. T_{ch} and μ_b will be estimated from the statistical fit of various particle ratios generated from UrQMD at 7, 7.7, 9, 11, 11.5, 13, 19 and 19.6 GeV and from the statistical fit of HRG with measurements at 7.7, 11.5 and 19.6 GeV.

The horn in K^+/π^+ [29] and the minimum of the higher-order moments $\kappa\sigma^2$ of net-proton multiplicity [30] are two examples of interesting physics taking place within the range of energies covered by NICA. As mentioned, having the possibility to implement two types of the phase transition; first order and crossover, allows us the study of the possible effects of the hadronization processes on the final-state particle production.

The present paper is organized as follows. Section gives short reviews on HRG and UrQMD approaches. In Section , the deduced freezeout parameters (section) and the dynamical net-charge fluctuations (section) are presented. In Section , the conclusions are outlined.

Approaches

Hadron resonance gas (HRG) model

In grand-canonical ensemble, the partition function can be expressed as [3]

$$Z(T, V, \mu) = \mathrm{Tr}\left[\exp\left(\frac{\mu N - H}{T}\right)\right], \tag{1}$$

where H is the Hamiltonian, μ is the chemical potential, and T is the temperature of the system of interest. In the HRG approach, we assume that Eq. (1) sums up contributions from a large number of hadrons and resonances [3] combining light and strange quark

flavors listed out in the most recent particle data group compilation [31]

$$\ln Z(T,V,\mu) \;=\; \sum_i \frac{V g_i}{2\pi^2} \int_0^\infty \pm p^2 dp \, \ln\left[1 \pm \lambda_i \exp\left(\frac{-\varepsilon_i(p)}{T}\right)\right], \tag{2}$$

where $\pm$ represent fermions and bosons, respectively, $\varepsilon_i = \sqrt{p^2 + m_i^2}$ is the dispersion relation of the i-th particle and $\lambda_i = \exp(\mu_i/T)$ is its fugacity factor [3], with $\mu_i = b_i\mu_{\rm b} + S_i\mu_{\rm S} + Q_i\mu_{\rm Q}$ and $b_i(\mu_{\rm b})$, $S_i(\mu_{\rm S})$ and $Q_i(\mu_{\rm Q})$ are baryon, strange and charge quantum numbers (corresponding chemical potentials), respectively. The number density can be derived from the derivative with respect to the chemical potential of the corresponding quantum number

$$n_i(T,\mu) = \sum_i \frac{g_i}{2\pi^2} \int_0^\infty \frac{p^2 dp}{\exp\left[\frac{\mu_i - \varepsilon_i(p)}{T}\right] \pm 1}. \tag{3}$$

The decay branching ratios are taken into account [32].

The standard deviation charactering the fluctuations in p/π ratio, for instance, is given as [33–35]

$$\sigma_{p/\pi}^2 \;=\; \frac{\langle N_p^2 \rangle - \langle N_p \rangle^2}{\langle N_p \rangle^2} + \frac{\langle N_\pi^2 \rangle - \langle N_\pi \rangle^2}{\langle N_\pi \rangle^2} - 2\frac{\langle N_p N_\pi \rangle - \langle N_p \rangle \langle N_\pi \rangle}{\langle N_p \rangle \langle N_\pi \rangle}, \tag{4}$$

where N_p and N_π represent the number of charged protons and pions, respectively. The variance is a special case of covariance, which measures how much two *random* variables change with each other, of identical variables. The quantity $\langle N_p N_\pi \rangle$ gives the statistical average of the integrals or multiplicities of the simultaneous correlation of the production of both p and π

$$\sigma_{p/\pi}^2 \;=\; \frac{\langle N_p(N_p - 1) \rangle}{\langle N_p \rangle^2} + \frac{\langle N_\pi(N_\pi - 1) \rangle}{\langle N_\pi \rangle^2} - 2\frac{\langle N_p N_\pi \rangle}{\langle N_p \rangle \langle N_\pi \rangle} + \frac{1}{\langle N_p \rangle} + \frac{1}{\langle N_\pi \rangle}. \tag{5}$$

The last two terms in Eq. (5) represent *static* net-charge fluctuations in Piosson's limit, i.e., uncorrelated particle production and the charge dependence of the dynamical net-charge fluctuations for charge ratio is given in terms of second-order factorial moments, $\langle N_p(N_p - 1) \rangle$ and/or $\langle N_\pi(N_\pi - 1) \rangle$ and the covariance $\langle N_p N_\pi \rangle$. In other words, the dynamical fluctuations are depending on single- and two-particle multiplicities. Similar expressions for K/π and K/p ratios can be derived, straightforwardly.

Ultrarelativistic Quantum Molecular Dynamic (UrQMD) model

The hybrid UrQMD event-generator [37] is a well-known approach for high-energy collisions. The phase space of such collisions is simulated through implementing a large set of Monte Carlo solutions for a large number of paired partial-differential equations characterizing the time evolution of the phase-space densities. This covers very early stage (depending on the chosen configuration) up to the final state of the particle production. In case of crossover phase-transition, an equation of state for a dynamical fluid mixing a chiral hadronic state with a state of interacting constituent quarks shall be utilized, while for first-order phase-transition, both MIT bag model and HRG approaches are used. The

36

earlier assumed SU(3), while the latter SU(2) symmetry. Additional two differences should be emphasized; the latent heat and the degrees of freedom. In first-order phase-transition, they are larger than that in crossover.

There are some influences of a mere technical aspect of UrQMD to its physical outcome. This is a crucial limitation defining the range of applicability of this approach. When switching from the hydrodynamical treatment of the high-density stage of the hadronic medium back to the *"normal"* particle-based transport code, there might occur some bias to the resulting particle statistics [38]. Because we have selected the same particlization procedure in both cases, the differences of particle ratios between first order and crossover phase transitions might appear smaller than implied by the physical model.

Results and discussion

Chemical freezeout

In an ensemble of $10,000$ events generated by the hybrid UrQMD model at various energies and taking into account two types of the quark-hadron phase transition (crossover and first order), we present a systematic study for the ratios of various particle species. From the statistical fit with the HRG model and with STAR experiments, μ and T parameters are estimated.

We start with STAR BES at 7.7, 11.5 and 19.6 GeV. We find that the particle ratios are fairly compatible with the UrQMD simulations in which crossover phase-transition is assumed. The results from the HRG statistical fit of the particle ratios K^+/π^+, K^-/π^-, π^-/π^+, K^-/K^+, Λ/π^-, $\bar{p}/p$, $\bar{\Lambda}/\Lambda$, $\bar{\Sigma}/\Sigma$, $\bar{p}/\pi^-$ and Ω/π^- with the STAR BES measurements [39–42] can be summarized as:

- at 7.7 GeV, $T_{\rm ch} = 141$ MeV and $\mu_{\rm b} = 412$ MeV with $\chi^2/\text{dof} = 11.7/9$,
- at 11.5 GeV, $T_{\rm ch} = 150$ MeV and $\mu_{\rm b} = 312$ MeV with $\chi^2/\text{dof} = 6.9/9$, and
- at 19.6 GeV, $T_{\rm ch} = 153$ MeV and $\mu_{\rm b} = 149$ MeV with $\chi^2/\text{dof} = 7.6/9$.

The dependence of the freezeout temperature on the baryon chemical potential, which is inversely related to $\sqrt{s_{NN}}$, is illustrated in Fig. 1. It is obvious that the UrQMD results agree well with HRG calculations which are based on the higher-order moments of the net-proton multiplicity [43]. Also, the calculations from the SU(3) PLSM are slightly lower that both UrQMD variants [44]. There is a very small difference between UrQMD with crossover and first-order phase transition. The fits with measured particle ratios leads to relatively higher freezeout parameters than the ones with UrQMD. This might be due to the assumptions that the constituents of the HRG model are point-like, i.e., no excluded-volume corrections were taken into account, and the quark occupation factors are unity, i.e., light and strange quarks equilibrium, i.e., $\gamma_f = 1$, where f runs over the quark flavors.

Dynamical net-charge fluctuations

The charge dependence of ν_{dyn} is conjectured to give essential details about the correlations of various produced charges (particles) and on how they are correlated with each others. ν_{dyn} calculated as functions of beam energy (here, not restricted to NICA energies) for various charge-ratios K/π (a), K/p (b) and p/π (c) are depicted in Fig. 2. The HRG calculations are compared with STAR measurement in central $0 - 5\%$ Au+Au collisions
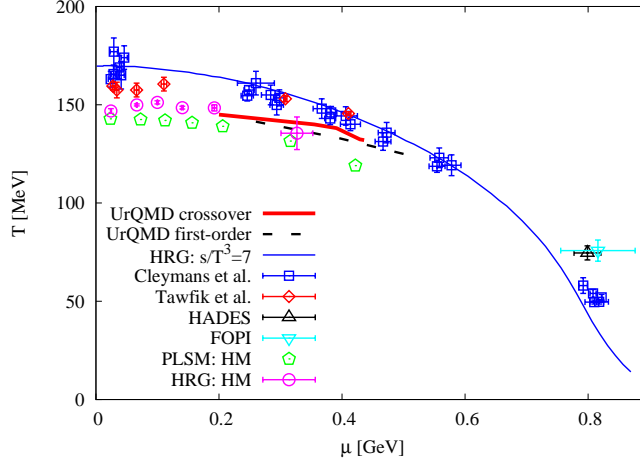
Figure 1: The resulting freezeout parameters (T vs. μ) from the hybrid UrQMD simulations with crossover (solid curve) and first-order phase-transition (dashed curve) compared with other phenomenological estimations.
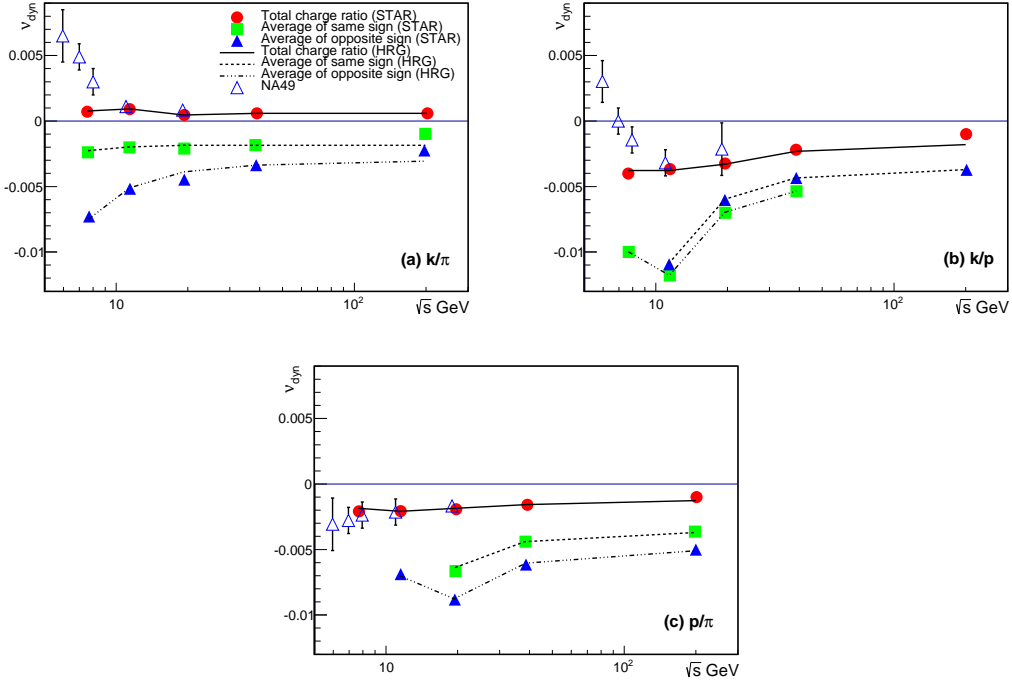
Figure 2: The energy dependence of ν_{dyn} calculated from the HRG model is compared with STAR [36] (solid symbols) and NA49 [33] (open triangles) measurements for the charge-ratios K/π (a), K/p (b) and p/π (c). The fluctuations of the charge ratios are determined as total and average of same and average of opposite charge-signs.

at $\sqrt{s_{NN}} = 7.7 - 200$ GeV [36] (solid symbols) and NA49 in central $0 - 3.5\%$ Pb+Pb collisions at $\sqrt{s_{NN}} = 6.3 - 17.3$ GeV [33] (open triangles) measurements. For each charge-ratio, three different cases are considered, namely the total and average of same and of opposite charge-signs are taken into consideration. They are characterized by solid, dashed, triple-dot-dashed curves, respectively.

The left-hand panel of Fig. 2 (a) shows ν_{dyn} for K/π charge-ratio. ν_{dyn} for total charges $(K^+ + K^-)/(\pi^+ + \pi^-)$ and average of same $(K^+/\pi^+ + K^-/\pi^-)$ and of opposite signs $(K^+/\pi^- + K^-/\pi^+)$ are compared with each others. Only $(K^+ + K^-)/(\pi^+ + \pi^-)$ have positive ν_{dyn}, which remain constant with increasing the beam energy. Nearly, same energy-dependence is also observed in average of same charges but with negative ν_{dyn}, while the average of opposite charges has relatively stronger energy-dependence. ν_{dyn} of opposite charges have larger negative values, which decrease with increasing energy.

The middle panel of Fig. 2 (b) presents the same as in left-hand panel but for K/p charge-ratio. The dynamical fluctuations for total charges increase and then saturate with increasing $\sqrt{s_{NN}}$. ν_{dyn} of average of same charges obviously increase with the energy. For oppositely charged particles-ratios, ν_{dyn} firstly decrease and then increase with the energy.

The right-hand panel of Fig. 2 (c) depicts the same as in previous panels but for p/π. ν_{dyn} of total charges slightly increase with the energy. Opposite charges firstly decrease and then increase with increasing the energy, while same-signed p/π increase. As in K/p, here the dynamical fluctuations are always negative.

Conclusions

Ten particle ratios are generated from the hybrid UrQMD v.3.4 at different center-of-mass energies. Two orders of quark-hadron phase-transition, namely crossover and first-order, are taken into consideration. We observe that almost all particle ratios from both orders are nearly similar, especially at lower energies (larger baryon chemical potentials). This might be understood due to the chemical freezeout, which takes place long after the hadronization process. Accordingly, the particle production at this stage seems not differ with respect to the stage of creation. In other words, we conclude that the resulting freezeout parameters are not influenced by the order of the phase transition – or that the aforementioned particlization bias hid a possible small influence. We also found that the resulting freezeout parameters from hybrid UrQMD agree well with the HRG calculations, in which higher-order moments of the net-proton multiplicity are utilized. Furthermore, we notice that the freezeout temperatures from SU(3) PLSM are lower that the ones from UrQMD.

The dynamical net-charge fluctuations (ν_{dyn}) are calculated within the HRG approach. ν_{dyn} for K/π, K/p and p/π charge-ratios are compared with STAR and NA49 measurements. An excellent agreement with the STAR BES results at $\sqrt{s_{NN}} = 7.7 - 200$ GeV is obtained. On the other hand, HRG agrees well with NA49 results at top SPS energies. But at lower SPS energies, HRG is not capable in reproducing NA49 ν_{dyn} for strange particles, particularly. We found that only $(K^+ + K^-)/(\pi^+ + \pi^-)$ has positive ν_{dyn}. All other charge ratios and combinations of various charges result in negative ν_{dyn}. The latter indicates that the cross term is dominant against single *uncorrelated* particle. We conclude that the correlations between charge-ratios are larger than the dynamical fluctuations in the noncorrelated charges.

References

[1] B. Muller, Rep. Prog. Phys. 58 (1995) 611.

[2] C. P. Singh, Phys. Rep. 236 (1993) 147.

[3] T. J. Tarnowsky (STAR Collaboration), Acta Phys. Polon. Supp. 5 (2012) 515 .

[4] B. I. Abelev *et al.*, (STAR Collaboration), Phys. Rev. Lett. 103 (2009) 092301.

[5] J. Adams *et al.*, (STAR Collaboration), Phys. Rev. C 68 (2003) 044905.

[6] S. Jeon and V. Koch, Phys. Rev. Lett. 83 (1999) 5435.

[7] S. Jeon and V. Koch, Phys. Rev. Lett. 85 (2000) 2076.

[8] C. Pruneau, S. Gavin and S. Voloshin, Phys. Rev. C 66 (2002) 044904.

[9] D. Bower and S. Gavin, Phys. Rev. C 64 (2001) 051902.

[10] C. A. Pruneau *et al.*, (STAR Collaboration), Heavy Ion Phys. 21 (2004) 261.

[11] S. Jena *et al.*, (ALICE Collaboration), PoS. WPCF 2011 (2011) 046.

[12] M. Weber (ALICE Collaboration), Nucl. Phys. A 904 (2013) 467.

[13] M. Weber *et al.*, (ALICE Collaboration), J. Phys. Conf. Ser. 389 (2012) 012036.

[14] You Zhou, Ke-Jun Wu and Feng Liu, Chin. Phys. C 34 (2010) 1436.

[15] K. Adcox *et al.*,Phys. Rev. Lett. 89 (2002) 082301.

[16] B. I. Abelev *et al.*, (STAR Collaboration), Phys. Rev. C 79 (2009) 024906.

[17] P. Christiansen, E. Haslum and E. Stenlund, Phys. Rev. C 80 (2009) 034903 .

[18] C. Blume *et al.*, Nucl.Phys. A 715 (2003) 55 .

[19] Abdel Nasser Tawfik, Int. J. Mod. Phys. A 29 (2014) 1430021.

[20] P. Braun-Munzinger, J. Stachel, J. P. Wessels, and N. Xu, Phys. Lett. B 344 (1995) 43.

[21] P. Braun-Munzinger, J. Stachel, J. P. Wessels, and N. Xu, Phys. Lett. B 365 (1996) 1.

[22] P. Braun-Munzinger, I. Heppe, and J. Stachel, Phys. Lett. B 465 (1999) 15.

[23] J. Cleymans and H. Satz, Z. Phys. C 57 (1993) 135.

[24] S. K. Tiwari and C. P. Singh, Adv. High Energy Phys 2013 (2013) 805413.

[25] J. Rafelski and J. Letessier, Phys. Rev. Lett. 85 (2000) 4695.

[26] F. Becattini, J. Cleymans, A. Keranen, E. Suhonen, and K. Redlich, Phys. Rev. C 64 (2001) 024901.

[27] A. Tawfik, *et al.*, Int. J. Mod. Phys. E 25 (2016) 1650018.

[28] H. Petersen *et al*, Phys.Rev. C 78 (2008) 044901.

[29] A. Andronic, P. Braun-Munzinger, and J. Stachel, Nucl. Phys. A 772 (2006) 167.

[30] A. Tawfik, Adv. High Energy Phys. 2013 (2013) 574871.

[31] K. A. Olive, *et al.*, Chinese Phys. C 38 (2014) 1.

[32] P. Braun-Munzinger and J. Stachel, J. Phys. G 28 (2002) 1971.

[33] C. Alt *et al.*, (NA49 Collaboration), Phys. Rev. C 79 (2009) 044910.

[34] T. Anticic *et al.*, (NA49 Collaboration), Phys. Rev. C 83 (2011) 061902.

[35] S. Jeon and V. Koch, *"Quark Gluon Plasma 3"*, Eds. R. C. Hwa and Xin-Nian Wang, (World Scientific Publishing, Singapore, 2004).

[36] T. J. Tarnowsky (STAR Collaboration), Acta Phys. Polon. Supp. 5 (2012) 515.

[37] S. A. Bass, *et al.*, Prog. Part. Nucl. Phys. 41 (1998) 255.

[38] P. Huovinen and H. Petersen, Eur. Phys. J. A 48 (2012) 171.

[39] L. Kumar (STAR Collaboration), Nucl. Part. Phys. 38 (2011) 124145 .

[40] S. Das (STAR Collaboration), Nucl. Phys. A. 904 (2013) 891.

[41] X. Zhu (STAR Collaboration), Acta Phys. Polon. B. Proc. Suppl. 5 (2012) 213.

[42] B. I. Abelev *et al.* (STAR Collaboration), Phys. Rev. C 79 (2009) 034909.

[43] P. Alba, W. Alberico, R. Bellwied, M. Bluhm, V. M. Sarti, M. Nahrgang, and C. Ratti, Phys. Lett. B 738 (2014) 305.

[44] Abdel Nasser Tawfik, Hesham Mansour, and Niseem Magdy, *"Fluctuations and Correlations of Various Conserved Charges from SU(3) Polyakov Linear-σ Model"*, submitted to IJMPA.

ANGULAR OBSERVABLES AND DIFFERENTIAL BRANCHING FRACTION OF THE DECAY $B_S \to \phi\mu^+\mu^-$ IN THE COVARIANT QUARK MODEL

A. N. Issadykov[1*], M. A.Ivanov[1†]

[1]*Joint Institute for Nuclear Research, Dubna, Russia*

Annotation

This paper is devoted to the study of the rare $B_s \to \phi\ell^+\ell^-$ decay where $\ell = \mu, \tau$. We compute the relevant form factors in the framework of the covariant quark model with infrared confinement in the full kinematical momentum transfer region. The calculated form factors are used to evaluate branching fractions and polarization observables in the cascade decay $B \to \phi(\to K^+K^-)\ell^+\ell^-$. We compare the obtained results with available experimental data and the results from other theoretical approaches.

Introduction

The transition $b \to s\ell^+\ell^-$ mediated by Flavor-Changing Neutral Current (FCNC) is one of the key point in the Standard Model (SM) which allows one to look for the possible manifestation of New Physics (NP). The physical processes induced by this transition are currently studied in great details at the LHC. The most popular and well–analyzed among them are the rare B-meson decays $B \to K^*(\to K\pi)\mu^+\mu^-$ and $B_s \to \phi(\to K^+K^-)\mu^+\mu^-$. The decay $\Lambda_b \to \Lambda(\to p\pi)\,\ell^+\ell^-$ can be considered to be a welcome complement to the above decay channels.

The LHCb Collaboration [1] reported a measurement of form-factor independent angular observables in the decay $B \to K^*\mu^+\mu^-$. One observable was found to be in disagreement with the SM on the level of 3.7 σ.

An angular analysis and a measurement of the differential branching fraction of the decay $B_s^0 \to \phi\mu^+\mu^-$ were presented in [2]. The results of the angular analysis are consistent with the SM. However, the differential branching fraction in one bin was found to be more than 3 σ below the SM predictions.

The observed discrepancies (sometimes called "$b \to s\ell\ell$ anomalies") have generated a plenty of theoretical studies [3]- [14] involving the various scenarios of NP and analysis of the uncertainties from hadronic contributions.

Covariant quark model

The covariant confined quark model [15]- [18] is an effective quantum field approach to hadronic interactions based on an interaction Lagrangian of hadrons interacting with their constituent quarks. The value of the coupling constant follows form the compositeness

---

*isadykov@theor.jinr.ru

†ivanovm@theor.jinr.ru

condition $Z_H = 0$, where Z_H is the wave function renormalization constant of the hadron. Matrix elements of the physical processes are generated by a set of quark loop diagrams according to the $1/N_c$ expansion. The ultraviolet divergences of the quark loops are regularized by including vertex functions for the hadron-quark vertices. These function also describe finite size effects related to the non-pointlike hadrons. The quark confinement [18] is built-in through an infrared cutoff on the upper limit of the scale integration to avoid the appearance of singularities in matrix elements. The infrared cutoff parameter λ is universal for all processes. The covariant confined quark model has limited number of parameters: t he light and heavy constituent quark masses, the size parameters which describe the size of the distribution of the constituent quarks inside the hadron and the infrared cutoff parameter λ. They are determined by a fit to available experimental data.

Form factors $B_s \to \phi$ transition

The matrix element is expressed through dimensionless form factors [19, 20]:

$$\langle \phi(p_2, \epsilon_2) \,|\, \bar{s}\, O^\mu \, b \,|\, B_s(p_1) \rangle = \tag{1}$$

$$= N_c \, g_{B_s} \, g_\phi \int \frac{d^4 k}{(2\pi)^4 i} \, \widetilde{\Phi}_{B_s}\left(-(k + w_{13}p_1)^2 \right) \widetilde{\Phi}_\phi\left(-(k + w_{23}p_2)^2 \right)$$

$$\times \quad \mathrm{tr}\left[O^\mu \, S_b(k + p_1) \, \gamma^5 \, S_s(k) \, \not{\epsilon}_2^\dagger \, S_s(k + p_2) \right]$$

$$= \frac{\epsilon_\nu^\dagger}{m_1 + m_2}\left(-g^{\mu\nu} P \cdot q \, A_0(q^2) + P^\mu P^\nu A_+(q^2) + q^\mu P^\nu A_-(q^2) \right.$$

$$\left. + i\, \varepsilon^{\mu\nu\alpha\beta} P_\alpha \, q_\beta \, V(q^2) \right),$$

$$\langle \phi(p_2, \epsilon_2) \,|\, \bar{s}\, (\sigma^{\mu\nu} q_\nu (1 + \gamma^5)) \, b \,|\, B_s(p_1) \rangle = \tag{2}$$

$$= N_c \, g_{B_s} \, g_\phi \int \frac{d^4 k}{(2\pi)^4 i} \, \widetilde{\Phi}_{B_s}\left(-(k + w_{13}p_1)^2 \right) \widetilde{\Phi}_\phi\left(-(k + w_{23}p_2)^2 \right)$$

$$\times \quad \mathrm{tr}\left[(\sigma^{\mu\nu} q_\nu (1 + \gamma^5)) \, S_b(k + p_1) \, \gamma^5 \, S_s(k) \, \not{\epsilon}_2^\dagger \, S_s(k + p_2) \right]$$

$$= \epsilon_\nu^\dagger \left(-(g^{\mu\nu} - q^\mu q^\nu / q^2) P \cdot q \, a_0(q^2) + (P^\mu P^\nu - q^\mu P^\nu P \cdot q / q^2) a_+(q^2) \right.$$

$$\left. + i\, \varepsilon^{\mu\nu\alpha\beta} P_\alpha \, q_\beta \, g(q^2) \right).$$

Here, $P = p_1 + p_2$, $q = p_1 - p_2$, $\epsilon_2^\dagger \cdot p_2 = 0$, $p_1^2 = m_1^2 \equiv m_{B_s}^2$, $p_2^2 = m_2^2 \equiv m_\phi^2$ and the weak matrix $O^\mu = \gamma^\mu(1 - \gamma^5)$. Since there are three quarks involved in these processes, we introduce the notation with two subscripts $w_{ij} = m_{q_j}/(m_{q_i} + m_{q_j})$ $(i, j = 1, 2, 3)$ so that $w_{ij} + w_{ji} = 1$. The form factors defined in Eq. (3) satisfy the physical requirement $a_0(0) = a_+(0)$, which ensures that no kinematic singularity appears in the matrix element at $q^2 = 0$ GeV.

Performing the loop integration in Eqs. (2) and (3) in a manner described in the previous section, one can obtain the form factors in the form of three-fold integrals which are calculated numerically by using the FORTRAN code with NAG library. The form factors
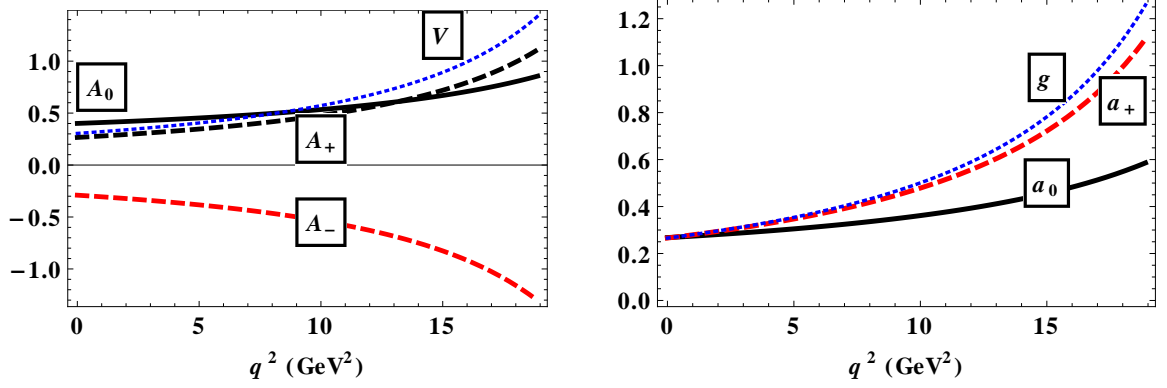
Figure 1: The q^2-dependence of the vector and axial form factors (upper plot) and tensor form factors (lower plot).

are calculated in the full kinematical region of momentum transfer squared. The curves are depicted in Fig. 1.

The results of our numerical calculations are with high accuracy approximated by the parametrization

$$F(q^2) = \frac{F(0)}{1 - as + bs^2}, \qquad s = \frac{q^2}{m_1^2}, \tag{3}$$

the relative error is less than 1%. The values of $F(0)$, a, and b are listed in Table 1. Since

Table 1: Parameters for the approximated form factors in Eq. (3).

	A_0	A_+	A_-	V	a_0	a_+	g
$F(0)$	0.40	0.27	−0.29	0.31	0.27	0.27	0.27
a	0.62	1.41	1.48	1.51	0.66	1.41	1.52
b	−0.30	0.38	0.45	0.47	−0.26	0.39	0.49

$a_0(0) = a_+(0) = g(0)$ we display in Table 2 the form factors $A_0^c(0) = (m_1 - m_2)[A_0(0) - A_+(0)]/(2m_2)$, $A_1^c(0) = A_0(0)(m_1 - m_2)/(m_1 + m_2)$, $A_2^c(0) = A_+(0)$ and $T_1^c(0) = g(0)$ obtained in our model and compare them with those from other approaches.

Table 2: The form factors at maximum recoil $q^2 = 0$.

	$V^c(0)$	$A_0^c(0)$	$A_1^c(0)$	$A_2^c(0)$	$T_1^c(0)$
This work	0.31 ± 0.03	0.28 ± 0.03	0.27 ± 0.03	0.27 ± 0.03	0.27 ± 0.03
Ref. [20]	0.32		0.29	0.28	0.28
Ref. [21]	0.434 ± 0.035	0.474 ± 0.037	0.311 ± 0.029	0.234 ± 0.028	0.349 ± 0.033
Ref. [22]	0.406 ± 0.020	0.322 ± 0.016	0.320 ± 0.016	0.318 ± 0.016	0.275 ± 0.014
Ref. [23]	0.43	0.38	0.30	0.26	0.35
Ref. [24]	0.25 ± 0.05	0.30 ± 0.05	0.19 ± 0.04		
Ref. [25]	0.339 ± 0.017		0.271 ± 0.014	0.212 ± 0.011	0.299 ± 0.016

Numerical results

In Table 3 the calculated values of branching fractions $B_s \to \phi\mu^+\mu^-$, $B_s \to \phi\tau^+\tau^-$, $B_s \to \phi\gamma$, $B_s \to \phi\nu\bar{\nu}$ and $B_s \to \phi J/\psi$ are given. The experimental errors shown in Table 3 result from combining the partial uncertainties in quadrature. The model uncertainties are estimated to be within 20%. We compare our results with those obtained in other approaches.

Table 3: Total branching fractions.

	This work	Ref. [22]	Ref. [25]	Ref. [26]	Ref. [1,2]
$10^7 \mathcal{B}(B_s \to \phi\mu^+\mu^-)$	9.11 ± 1.82	11.1 ± 1.1	11.8 ± 1.1	16.4	7.97 ± 0.77
$10^7 \mathcal{B}(B_s \to \phi\tau^+\tau^-)$	1.03 ± 0.20	1.5 ± 0.2	1.23 ± 0.11	1.51	
$10^5 \mathcal{B}(B_s \to \phi\gamma)$	2.39 ± 0.48	3.8 ± 0.4			3.52 ± 0.34
$10^5 \mathcal{B}(B_s \to \phi\nu\bar{\nu})$	0.84 ± 0.16	0.796 ± 0.080		1.165	< 540
$10^2 \mathcal{B}(B_s \to \phi J/\psi)$	0.16 ± 0.03	0.113 ± 0.016			0.108 ± 0.009

References

[1] R. Aaij *et al.* [LHCb Collaboration], Phys. Rev. Lett. 111 (2013) 191801; [arXiv:1308.1707 [hep-ex]].

[2] R. Aaij *et al.* [LHCb Collaboration], JHEP 1509 (2015) 179; [arXiv:1506.08777 [hep-ex]].

[3] S. Descotes-Genon, L. Hofer, J. Matias and J. Virto, arXiv:1510.04239 [hep-ph].

[4] S. Descotes-Genon, J. Matias, M. Ramon and J. Virto, JHEP 1301 (2013) 048; [arXiv:1207.2753 [hep-ph]].

[5] S. Descotes-Genon, T. Hurth, J. Matias and J. Virto, JHEP 1305 (2013) 137; [arXiv:1303.5794 [hep-ph]].

[6] S. Descotes-Genon, J. Matias and J. Virto, Phys. Rev. D 88 (2013) 074002; [arXiv:1307.5683 [hep-ph]].

[7] W. Altmannshofer and D. M. Straub, Eur. Phys. J. C 73 (2013) 2646; [arXiv:1308.1501 [hep-ph]].

[8] U. Egede, T. Hurth, J. Matias, M. Ramon and W. Reece, JHEP 1010 (2010) 056; [arXiv:1005.0571 [hep-ph]].

[9] M. Beneke, T. Feldmann and D. Seidel, Nucl. Phys. B 612 (2001) 25; [hep-ph/0106067].

[10] M. Beylich, G. Buchalla and T. Feldmann, Eur. Phys. J. C 71 (2011) 1635; [arXiv:1101.5118 [hep-ph]].

[11] J. Lyon and R. Zwicky, arXiv:1406.0566 [hep-ph].

[12] A. Bharucha, D. M. Straub and R. Zwicky, arXiv:1503.05534 [hep-ph].

[13] A. Khodjamirian, T. Mannel, A. A. Pivovarov and Y.-M. Wang, JHEP 1009 (2010) 089; [arXiv:1006.4945 [hep-ph]].

[14] X. W. Kang, B. Kubis, C. Hanhart and U. G. Meiner, Phys. Rev. D 89 (2014) 053015; [arXiv:1312.1193 [hep-ph]].

[15] G. V. Efimov and M. A. Ivanov, Int. J. Mod. Phys. A 4 (1989) 2031.

[16] G. V. Efimov and M. A. Ivanov, *The Quark Confinement Model of Hadrons*, (CRC Press, Boca Raton, 1993).

[17] A. Faessler, T. Gutsche, M. A. Ivanov, J. G. Körner and V. E. Lyubovitskij, Eur. Phys. J. direct C 4 (2002) 18. [hep-ph/0205287].

[18] T. Branz, A. Faessler, T. Gutsche, M. A. Ivanov, J. G. Körner, V. E. Lyubovitskij, Phys. Rev. D 81 (2010) 034010. [arXiv:0912.3710 [hep-ph]].

[19] S. Dubnička, A. Z. Dubničková, N. Habyl, M. A. Ivanov, A. Liptaj and G. S. Nurbakova, Few Body Syst. 57 (2016) 121; [arXiv:1511.04887 [hep-ph]].

[20] M. A. Ivanov, J. G. Körner, S. G. Kovalenko, P. Santorelli and G. G. Saidullaeva, Phys. Rev. D 85 (2012) 034004; [arXiv:1112.3536 [hep-ph]].

[21] P. Ball and R. Zwicky, Phys. Rev. D 71 (2005) 014029; [hep-ph/0412079].

[22] R. N. Faustov and V. O. Galkin, Eur. Phys. J. C 73 (2013) 2593; [arXiv:1309.2160 [hep-ph]].

[23] U. O. Yilmaz, Eur. Phys. J. C 58 (2008) 555 [arXiv:0806.0269 [hep-ph]].

[24] A. Ali, G. Kramer, Y. Li, C. D. Lu, Y. L. Shen, W. Wang and Y. M. Wang, Phys. Rev. D 76 (2007) 074018 [hep-ph/0703162 [HEP-PH]].

[25] Y. L. Wu, M. Zhong and Y. B. Zuo, Int. J. Mod. Phys. A 21 (2006) 6125 [hep-ph/0604007].

[26] C. Q. Geng and C. C. Liu, J. Phys. G 29 (2003) 1103 [hep-ph/0303246].

[27] K. A. Olive *et al.* [Particle Data Group Collaboration], Chin. Phys. C 38, 090001 (2014).

HIGH-ORDER WKB CORRECTIONS TO THE QUANTUM MECHANICAL TWO-COULOMB-CENTRE PROBLEM

M. Hnatič[1*], V. M. Khmara[1†], V. Yu. Lazur[2‡], O. K. Reity[2§]

[1]*Faculty of Science, P. J. Šafárik University, Šrobárová, Košice, Slovakia*
[2]*Department of Theoretical Physics, Uzhhorod National University, Uzhhorod, Ukraine*

Annotation

The asymptotic formulae for the two-Coulomb-centre quasiradial and quasiangular wave functions are obtained for large internuclear distances R by means of the modified perturbation theory. It is shown that in each order of $1/R$ the corrections to the wave functions can be expressed by a finite number of Coulomb wave functions with the modified charge. Simple analytical expressions for the first, second, and third corrections to quasiradial and quasiangular functions are derived. The consistent scheme for obtaining WKB expansions for solutions of the quasiangular equation in quantum mechanical two-Coulomb-centre problem $Z_1 e Z_2$ is developed. In the framework of this scheme quasiclassical two-Coulomb-centre wave functions for large distances between the fixed positive charges (nuclei) are constructed for the entire space of the negative particle (electron).

Introduction

The study of an electron motion in the field of two Coulomb centres (so-called $Z_1 e Z_2$ problem) began with the paper of the Pauli [1]. Since then this problem has attracted a lot of research mostly in connection with the problems of atomic and molecular physics (status of the problem and references on the subject up to 1976 can be found in [2]). The intensive studies of the problem of two Coulomb centres $Z_1 e Z_2$ during the last thirty years were stimulated not only by the availability of powerful computers and the successes achieved with asymptotic methods in solving ordinary differential equations, but also by the requirements of mesomolecular physics [3,4] and the theory of ion-atom collisions [5]. New forms of asymptotic solutions were obtained both for the problem of the hydrogen molecular ion H_2^+ [6] and for the problem of two centres with strongly differing charges [7–9].

As a suitable method for calculating the wave functions and all other quantities required in the problem of the interaction of two atoms or ions, we propose to employ the quasiclassical approach. This approach allows us to obtain analytic solutions, but it is limited by asymptotically large internuclear distances R. These distances should be so large that the quantum penetrability of the potential barrier separating atomic particles is much smaller than unity.

---

*hnatic@saske.sk

†viktor.khmara@student.upjs.sk

‡volodymyr.lazur@uzhnu.edu.ua

§okreity@gmail.com

Basic equations and perturbation theory

The motion of the electron in the field of two fixed nuclei with charges Z_1 and Z_2 is described by the following Schrödinger equation:

$$\left(-\frac{1}{2}\Delta - \frac{Z_1}{r_1} - \frac{Z_2}{r_2}\right)\Phi(\vec{r}, R) = E(R)\Phi(\vec{r}, R) \tag{1}$$

where r_1 and r_2 are the distances from the electron to nuclei 1 and 2, $E(R)$ is the electron energy and R is the distance between the nuclei. If we replace the wave function $\Phi(\vec{r}, R)$ by the product function

$$\Phi(\vec{r}, R) = R^2 \frac{U(\mu, R)}{\sqrt{(r_1 + r_2)^2 - R^2}} \frac{V(\nu, R)}{\sqrt{R^2 - (r_1 - r_2)^2}} \frac{e^{\pm im\phi}}{\sqrt{2\pi}} \tag{2}$$

and use new variables

$$\mu = (r_1 + r_2 - R)/2, \quad \mu \in [0, \infty); \quad \nu = (r_1 - r_2 + R)/2, \quad \nu \in [0, R],$$

we obtain the quasiradial and quasiangular equations for functions $U(\xi, R)$ and $V(\eta, R)$

$$U''(\mu) - \left[\gamma^2 - \frac{Z_1 + Z_2 + \lambda_\xi/R}{\mu} - \frac{Z_1 + Z_2 - \lambda_\xi/R}{R + \mu} + \frac{R^2(m^2 - 1)}{4\mu^2(R + \mu)^2}\right]U(\mu) = 0, \tag{3}$$

$$V''(\nu) - \left[\gamma^2 - \frac{Z_1 - Z_2 - \lambda_\eta/R}{\nu} + \frac{Z_1 - Z_2 + \lambda_\eta/R}{R - \nu} + \frac{R^2(m^2 - 1)}{4\nu^2(R - \nu)^2}\right]V(\nu) = 0 \tag{4}$$

where $\gamma = (-2E)^{1/2}$.

These new functions satisfy the following boundary conditions:

$$U(1) = 0 \quad U(\xi) \xrightarrow[\xi \to 0]{} 0, \quad V(\pm 1) = 0.$$

Here λ_ξ and λ_η are the separation constants depending on R, and m is the modulus of the magnetic quantum number. The two one-dimensional equations (3) and (4) are equivalent to the original Schrödinger equation provided the separation constants are equal:

$$\lambda_\xi = \lambda_\eta. \tag{5}$$

When R is much larger than the size of electron shells centred on the left-hand nucleus, the ratios μ/R and ν/R are small quantities in intra-atomic space. This fact allow us to use the perturbation theory to equations (3) and (4) in intra-atomic space to find the separation constants $\lambda_\xi, \lambda_\eta$. This was done in [10, 11] where using a slightly modified perturbation theory the asymptotic (for large R) solutions of the equations (3) and (4) was found. Normalizing the total wave function $\psi(\mu, \nu, \varphi)$ to unity we obtain the wave function of the electron moving near the first nucleus and perturbed by the second one up to R^{-3}:

$$\Psi^{pert} = C\left[f_{n_1}^{(0)}(\mu) + \sum_{p=1}^{3}\sum_{k=-p}^{p}c_{n_1+k}^{(p)}f_{n_1+k}^{(0)}(\mu)\right]\left[f_{n_2}^{(0)}(\nu) + \sum_{p=1}^{3}\sum_{k=-p}^{p}c_{n_2+k}^{(p)}f_{n_2+k}^{(0)}(\nu)\right] \tag{6}$$

where

$$f_l^{(0)}(x) = \left(\frac{(l+m)!}{l!(m!)^2(2l+m+1)} \right)^{1/2} (2\gamma x)^{(m+1)/2} e^{-\gamma x} F(-l,\, m+1,\, 2\gamma x), \qquad (7)$$

and C is the normalization constant, expression of which is not given here due to its cumbersomeness. Here $n = n_1 + n_2 + m + 1$ and for $p = 1, 2, 3$ all of the $c_{n_{1,2}+k}^{(p)}$ coefficients have been found using the method considered in [10, 11].

WKB solutions of the quasiangular equation in inter-centre region

Let us rewrite the quasiangular equation (4) in the form of one-dimensional Schrödinger equation:

$$V'' - \frac{q^2}{\hbar^2} V = 0 \qquad (8)$$

where $q = \sqrt{2(U_{eff} - E)}$ and the function

$$U_{eff} = -\frac{\tilde{Z}_1}{\nu} - \frac{\tilde{Z}_2}{R-\nu} + \frac{\hbar^2(m^2-1)}{8\nu^2(1-\nu/R)^2}, \qquad \tilde{Z}_{1,2} = \left[\pm(Z_1 - Z_2) - \lambda/R\right]/2$$

plays a role of the effective potential energy.

Representing the solution of (8) in the form of the expansion in powers of $\hbar$:

$$V^{quas} = e^{S/\hbar}, \quad S = \sum_{k=-1}^{\infty} \hbar^k S_k, \qquad (9)$$

and substituting (9) into (8) and equating to zero the coefficients of each power of $\hbar$, we arrive at the system of differential equations of the 1st order for the $S_k(\nu)$

$$\left(S'_{-1}\right)^2 = q^2; \qquad 2S'_{-1}S'_0 + S''_{-1} = 0; \qquad (10)$$

$$2S'_{-1}S'_k + S''_{k-1} + \sum_{j=0}^{k-1} S'_j S'_{k-j-1} = 0, \quad k = 1, 2, \ldots. \qquad (11)$$

As a solution of (10) we choose the function $S_{-1}(\nu) = -\int_{\nu_2}^{\nu} q(\nu')d\nu'$ corresponding to exponential damping of V^{quas} in the under-barrier region. The equation for S_0 is solved in the closed species and has the form $S_0 = \log(C_0/\sqrt{q})$. Finally, solutions of all the next equations of the recurrent system (11) are expressed by means of quadratures

$$S_k = \int \frac{1}{2q} \left(S''_{k-1} + \sum_{j=0}^{k-1} S'_j S'_{k-j-1} \right) d\nu + C_k, \quad C_k = \text{const}, \quad k = 1, 2, \ldots. \qquad (12)$$

For further consideration it is convenient to introduce two ranges of ν variation: $0 \leqslant \nu \ll \nu_m$ (ν_m is the maximum point of $U_{eff}(\nu)$ function) and $\nu_2 \ll \nu \ll \nu_3$. In the first range the perturbed function (6) is valid, and for the second range we employed the quasiclassical approach to find the quasiangular function $V(\nu)$. We note that where these ranges overlap,

the results obtained by the perturbation theory and by the quasiclassical approximation coincide. This allows us to find the integration constants C_k by means of matching the quasiclassical solution V^{quas} with asymptotic expansion of V^{pert} (6) in powers of $1/\nu$:

$$V^{quas}(\nu) \xrightarrow[\nu_2 \ll \nu \ll \nu_m]{} V^{as}(\nu) \tag{13}$$

Therefore, the solution of the quasiangular equation (8) in the quasiclassical approximation, which satisfies the boundary condition (13), is of the form (hereinafter $\hbar = 1$)

$$V^{quas} = \frac{C_0}{\sqrt{q}} \exp\left[-\int_{\nu_2}^{\nu} q d\nu' + S_1 + S_2 \right] \tag{14}$$

where the quasiclassical corrections S_1 and S_2 are determined by the formulae

$$
\begin{aligned}
S_1 = & -\frac{\tilde{Z}_1}{4\gamma^3\nu^2}\left(1 + \frac{17\tilde{Z}_1}{6\gamma^2\nu}\right) + \frac{\tilde{Z}_2}{4\gamma^3(R-\nu)^2}\left(1 + \frac{17\tilde{Z}_2}{6\gamma^2(R-\nu)}\right) \\
& + \frac{m^2-1}{16\gamma^3}\left(\frac{1}{\nu^3} + \frac{1}{\nu^2 R} - \frac{1}{R(R-\nu)^2} - \frac{1}{(R-\nu)^3}\right) + \frac{\tilde{Z}_1\tilde{Z}_2}{2\gamma^5 R^3}\log\frac{\nu}{R-\nu} \\
& + \frac{\tilde{Z}_1\tilde{Z}_2}{4\gamma^5 R}\left(\frac{3}{(R-\nu)^2} - \frac{3}{\nu^2} + \frac{1}{R}\left[\frac{1}{R-\nu} - \frac{1}{\nu}\right]\right) + C_1,
\end{aligned} \tag{15}
$$

$$S_2 = \frac{\tilde{Z}_1}{4\gamma^4\nu^3} + \frac{\tilde{Z}_2}{4\gamma^4(R-\nu)^3} + C_2, \tag{16}$$

and expressions for the integration constants C_0, C_1, and C_2 are not given here due to their cumbersomeness.

The final expression for two-Coulomb-centre wave function Ψ of $Z_1 e Z_2$ system has the form (2) where

$$U(\mu, R) V(\nu, R) = C(R) U^{pert}(\mu) V^{quas}(\nu). \tag{17}$$

Acknowledgement

References

[1] W. Pauli, Ann. Phys. (Leipzig), 68 (1922) 177.

[2] I.V. Komarov, L.I. Ponomarev and S.Yu. Slavyanov, *Spheroidal and Coulomb Spheroidal Functions* (Moscow: Nauka 1976).

[3] L.I. Men'shikov and L.N. Somov, Sov. Phys. Usp., 33 (8) (1990) 616.

[4] S.S. Gershtein, Yu.V. Petrov and L.I. Ponomarev, Sov. Phys. Usp., 33 (8) (1991) 591-615.

[5] R.K. Janev, L.P. Presnyakov and V.P. Shevelko, *Physics of Highly Charged Ions* (Springer, 1985).

[6] E.A. Solov'ev, Sov. Phys. Usp, 32 (3) (1989) 228.

[7] I.V. Komarov and E.A. Solov'ev, Theor. Math. Phys., 40 (1979) 645.

[8] T.P. Grozdanov, R.K. Janev and V.Yu. Lazur, Phys. Rev. A, 32 (1985) 3425.

[9] V. Yu. Lazur *et al*, Theor. Math. Phys. 87 (1991) 401.

[10] T.M. Kereselidze, Z.S. Machavariani and I.L. Noselidze, J. Phys. B., 29 (1996) 257-273.

[11] M.Hnatič, V.M. Khmara, V.Yu. Lazur and O.K.Reity, EPJ Web of Conferences, 108 (2016) 02028.

NEON TRIMER IN THE FRAMEWORK OF FADDEEV DIFFERENTIAL EQUATIONS

A. A. Korobitsin[1] , E. A. Kolganova[1,2]
[1]*Joint Institute for Nuclear Research, Dubna, Moscow region, Russia*
[2] *Dubna State University, Dubna, Moscow region, Russia*

Annotation

The properties of two- and three-atomic clusters of neon are studied. Differential Faddeev equations in the total angular momentum representation are used for the binding energies calculations of neon trimer system.

Introduction

Small clusters of rare gas atoms are of a great interest in the recent years. They belong to a large class of molecules interacting via potentials of van-der-Waals type and have unique quantum properties. One of these properties is the Efimov effect [1]. This unexpected and unnatural effect was predicted by the Russian physicist Vitaly Efimov in 1970. This effect reflects the difference in the properties of the two-body and the three-body systems.When there are at least two subsystems of zero binding energy, the three-body system has an infinite number of weakly bound states - this is the essence of the Efimov effect. This effect was experimentally confirmed only in 2006 [2] in ultracold gas of ^{133}Cs atoms. One of the best theoretically predicted example for this phenomenon is the helium trimer wherean excited state is of Efimov nature [3]. The first experimental measurements of the exited state in helium trimer were done recently in [4]. Calculations of ultracold three-body clusters require methods suitable for solving three-body bound state and scattering problems in configuration space. The aim of this paper is to develop the numerical algorithm for solving differential Faddeev equations in the total angular momentum representation [5,6] and to apply it to neon triatomic system.

Two-particles clusters

First experimental measurements of the spectrum of neon dimer ^{20}Ne$_2$ were given in [7]. Discrete spectrum of neon dimer in the s-state contains three levels, two of which are experimentally measured in [8] and have the energy value 24.22 ± 0.02 K and 4.405 ± 0.02 K, respectively. For the energy of the second excited state only an upper bound, namely 0.14 K, was determined. In this paper the binding energy, the average radius and the root mean square radius of Ne dimers calculated with the potentials TT [9] and HFD-B [10] are shown in Table 1.

Neon dimer has three bound states for zero orbital angular momentum. Calculated binding energies and average distances are in a good agreement with the reported in [3,11, 12]. Radial wave functions φ of all state of neon dimers are shown in Fig.1.

Table 1: Energy levels of the bound states $E_n(K)$, the average radius $\langle r \rangle$ (Å) and the root mean square radius $\sqrt{\langle r^2 \rangle}$ (Å) of Ne dimers, calculated with potentials T [9] and HFD-B [10]. The energies are given in units of K and are relative to the three-body dissociation threshold.

Level	0			1			2		
Potential	E_0	$\langle r \rangle$	$\sqrt{\langle r^2 \rangle}$	E_1	$\langle r \rangle$	$\sqrt{\langle r^2 \rangle}$	E_2	$\langle r \rangle$	$\sqrt{\langle r^2 \rangle}$
TT	24.0598	3.3329	3.3471	4.2049	4.2849	4.3438	0.0181	12.4793	13.8709
HFD-B	24.3715	3.3309	3.3452	4.4527	4.2527	4.3109	0.0276	11.2127	12.2721
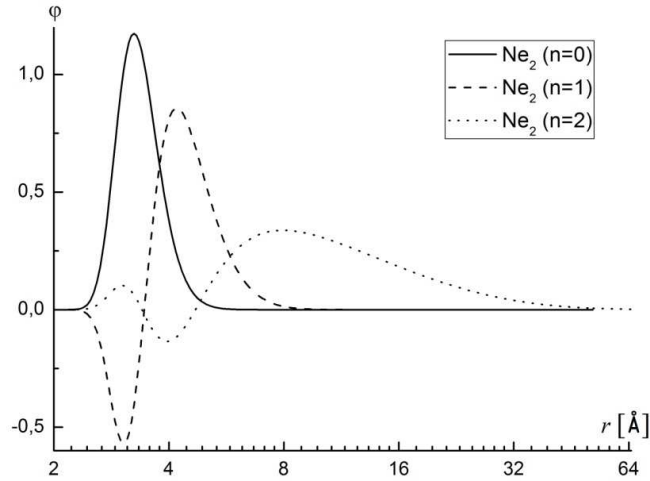
Figure 1: The radial wave functions φ of the ground and excited states of neon dimer, calculated with the TT potential [9].

Three-particle clusters

One of the effective methods for studying three-particle systems is based on using the differential Faddeev equations in the total angular momentum representation [5,6,13]. We consider the states with zero total angular momentum. The angular degrees of freedom corresponding to collective rotation of the three-body system can be separated and the kinetic energy operator reduces to

$$H_0 = -\rho^{-5}\partial_\rho\rho^5\partial_\rho - \frac{4}{\rho^2}\sin^{-2}\chi_\alpha \left(\partial_{\chi_\alpha}\sin^2\chi_\alpha\partial_{\chi_\alpha} + \sin^{-1}\theta_\alpha\partial_{\theta_\alpha}\sin\theta_\alpha\partial_{\theta_\alpha} \right), \qquad (1)$$

where ρ, χ_α, and θ_α are the hyperspherical coordinates expressed through standard Jacobi variables $\overrightarrow{x_\alpha}$, $\overrightarrow{y_\alpha}$, $\alpha = 1, 2, 3$:

$$\rho = \sqrt{x_\alpha^2 + y_\alpha^2}, \quad \tan(\frac{\chi_\alpha}{2}) = \frac{x_\alpha}{y_\alpha}, \quad \cos\theta_\alpha = \frac{(\overrightarrow{x_\alpha}, \overrightarrow{y_\alpha})}{\overrightarrow{x_\alpha}\,\overrightarrow{y_\alpha}},$$

$$x_\alpha = |\overrightarrow{x_\alpha}|, \quad y_\alpha = |\overrightarrow{y_\alpha}|, \quad \rho \in [0; \infty], \quad \{\chi_\alpha, \theta_\alpha\} \in [0; \pi] \otimes [0; \pi]. \qquad (2)$$

The total wavefunction Ψ of a three-body system can be written as the sum of Faddeev components Ψ_α:

$$\Psi(\rho, \chi_\alpha, \theta_\alpha) = \sum_\alpha \Psi_\alpha(\rho, \chi_\alpha, \theta_\alpha) \qquad (3)$$

satisfying Faddeev equations

$$(H_0 + V_\alpha - E)\Psi_\alpha(\rho, \chi_\alpha, \theta_\alpha) = -V_\alpha \sum_{\beta \neq \alpha} \Psi_\beta(\rho, \chi_\beta, \theta_\beta), \tag{4}$$

where V_α is the potential of interaction in the pair α and E is the total energy of the system.

For numerical solution it is suitable to substitute

$$\Phi_\alpha = \rho^{5/2} \sin\chi_\alpha \sin\theta_\alpha \Psi_\alpha. \tag{5}$$

The scaled components $\Phi_a lpha$ satisfy the boundary condition:

$$\Phi_\alpha(\rho = 0) = \Phi_\alpha(\chi_\alpha = 0, \pi) = \Phi_\alpha(\theta_\alpha = 0, \pi) = 0. \tag{6}$$

Then Eqs. (4) are rewritten in terms of Φ_α as follows:

$$(\tilde{H}_0 + V_\alpha(x) - E)\Psi_\alpha(\rho, \chi, \theta) = -V_\alpha(x) \sum_{\beta \neq \alpha} \Psi_\beta(\rho, \chi_\beta, \theta_\beta), \tag{7}$$

where $\chi \equiv \chi_\alpha$, $\theta \equiv \theta_\alpha$, $x = \rho \in cos(\chi_\alpha/2)$. The differential operator $\tilde{H}_0$ is given by

$$\tilde{H}_0 = -\partial_\rho^2 - \frac{4}{\rho^2}\left[\partial_\chi^2 + \sin^{-2}\chi\left(\partial_\theta^2 - \cot\theta\partial_\theta + \sin^{-2}\theta + \frac{1}{16}\right)\right]. \tag{8}$$

In this paper for the calculations of the spectrum of neon trimer we use finite-difference approximation and cubic polynomial splines for solving the differential equations (7) with the zero asymptotic boundary conditions. To increase the speed of calculation the template library Eigen [14] for linear algebra is used. We have applied developed numerical algorithm for solving the abovementioned equations for the ^{20}Ne three-atomic system. Atomic masses for neon isotope were taken from [15].To describe the interatomic interaction V the potential model HFD-B [10] were used. Table 2 contains the calculation results of binding energies of ground and first excited states for neon trimer, which are in a good agreement with the results obtained using different methods by other authors.

Table 2: The ground and first excited state energies (in K) for ^{20}Ne$_3$ calculated with HFD-B potential [10]. NB: * - using Morse potential model from Ref. [17].

E (K)	HFD-B	[11]	[12]	[16]	[17]
E_0	74.13	74.10	74.11	72.07*	72.07*
E_1	52.44	52.41	52.43	-	-

Investigation of the ground state energy convergence with respect to the number of grid points demonstrates that $N_\rho = 250$ is sufficient to get up to four accurate figures for the energy of the ground state (see Fig. 2).
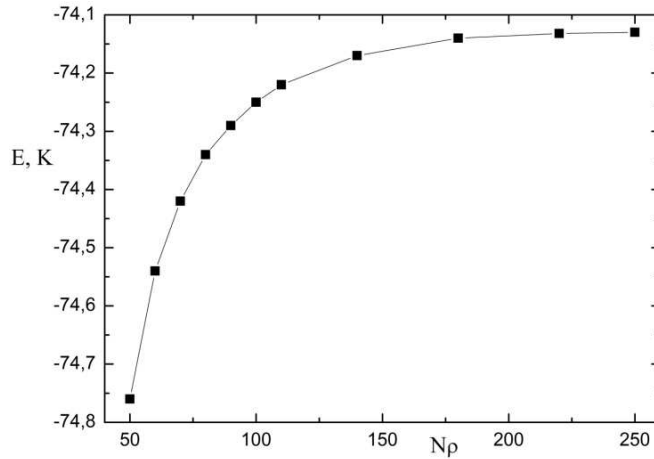
Figure 2: Convergence of the neon trimer ground state energy on the grids of N_ρ points for fixed value of $N_\theta = 100$ and $N_\chi = 10$.

Conclusions

In the course of this work we investigated the properties of neon clusters. Namely, we have calculated binding energy, the average radius and the root mean square radius for neon dimers and binding energies of ground and first excited states for neon trimer, using realistic potentials TT [9] and HFD-B [10].In order to perform the calculations we developed numerical algorithm for solving the differential Faddeev equations in the total angular momentum representation. This algorithm has been realized in the programming language C++. Our results are in a good agreement with the results obtained by other methods. The developed numerically effective computational scheme, especially in combination with an option of using multiple processors, makes it possible to calculate wide range of three-body problems. The calculation of scattering process is the next step of our work.

References

[1] V. N. Efimov, Sov. J. Nucl. Phys. 12 (1970) 1080; ibid, Phys. Lett. B 33 (1970) 563.

[2] T. Kraemer *et al.*, Nature (London) 440 (2006) 315.

[3] E. A. Kolganova, A.K. Motovilov, and W. Sandhas, Few-Body Syst. 51 (2011) 249.

[4] M. Kunitski *et al.*, Science 348 (2015) 551.

[5] V. V. Kostrykin, A. A. Kvinstinsky and S.P. Merkuriev, Few-Body Syst. 6 (1989) 97.

[6] A. A. Kvinstinsky and C.-Y. Hu, Few-Body Syst. 12 (1992) 7.

[7] Y. Tanaka and K. Yoshino, J. Chem. Phys. 57 (1972) 2964.

[8] A. Westand and F. Merkt, J. Chem. Phys. 118 (2003) 8807.

[9] K. T. Tang and J. P. Toennies, J. Chem. Phys. 118 (2003) 4976.

[10] R.A. Aziz and M.J. Slaman, J. Chem. Phys. 130 (1989) 187.

[11] M. Salci, S. B. Levin, N. Elander, and E. Yarevsky, J. Chem. Phys. 129 (2008) 134304.

[12] H. Suno, J. Chem. Phys. 135 (2011) 134312; ibid, J. Phys. B 49 (2016) 014003.

[13] V. A. Roudnev, S. L. Yakovlev, and S. A. Sofianos, Few-Body Syst. 37 (2005) 179.

[14] http://eigen.tuxfamily.org/

[15] I. Mills *et al.*, *"Quantities, Units and Symbols in Physical Chemistry"*,(Blackwell Scientific Publications, Oxford, 1993).

[16] M. Marquez *et al.*, J. Chem. Phys. 130 (2009) 154301.

[17] I. Baccarelli *et al.*, J. Chem. Phys. 122 (2005) 084313.

EVOLUTION OF QUARK-GLUON PLASMA AND QUARK-HADRON PHASE TRANSITION

Y. Kumar[1*], P. K. Sethy[2]

[1]*Department of Physics, Deshbandhu College, University of Delhi, New Delhi, India*
[2]*Department of Physics and Astrophysics, University of Delhi, Delhi, India*

Annotation

Using a simple phenomenological model, we calculate free energy of droplets of a quark-gluon plasma (QGP) with the consideration of chemical potential in quark mass. The dependence of quark mass on temperature and chemical potential including the curvature term enhances the evolution of quark-gluon plasma and produced to form a large stable QGP droplet. The results agree nicely with direct Lattice calculation in order to predict the order of phase transition. Thus our results are relevant in connection with free energy evolution of QGP and quark-hadron phase transition.

Introduction

The Lattice Quantum Chromo Dynamics (QCD) predicts a phase transition from Hadron Gas (HG) to Quark Gluon Plasma (QGP) at critical temperature, $T \sim 170$ MeV [1]. At high temperature and/or baryonic chemical potential, it is believed that when two heavy ions collide in central nuclear collision, a plasma of quarks and gluons is produced [2] and explore the phase structure of QCD matter [3, 4].

Since long many promising signatures in high energy heavy-ion collisions have been observed for the formation and evolution of QGP. The theoretical models and calculations based on Lattice QCD predict the order of phase transition. The recent results of Lattice QCD calculations show that at small baryon chemical potential and high temperature, the transition from the hadronic phase to the QGP phase is a smooth crossover [5], whereas a first order phase transition is expected at high baryon chemical region [6, 7]. But the fact is that it is not yet settled whether it exhibits a true phase transition or a crossover between these two phases. Unfortunately, it is completely unknown.

To fully understand the details of transition from the confined phase to the plasma phase, theorists need to review and re-examine the nature of phase transition that take place in heavy-ion collisions. In this, phenomenological studies are appropriate and significant. A phase transition is classified as a first order or crossover depending on the behaviour of free energy evolution.

Previous calculations were all performed in the limit of zero chemical potential. Now we compute the free energy with the consideration of chemical potential in quark mass including the curvature term. These results are thus relevant for investigations of quark-hadron phase transition and evolution of QGP in the ultra-relativistic heavy-ion collision at RHIC and LHC.

---

*yogesh.du81@gmail.com

Model outline

The droplet formation of QGP and quark-hadron phase transition has become a useful probe in the field of high energy heavy-ion collision [8,9]. Earlier many physicist suggested that the transition into QGP phase has a nature of either a first order or a weakly first order one [8,9]. But the current Lattice QCD results indicate that there is a crossover rather than a first order phase transition at zero or small chemical potential and high temperature. In the previous work [10], we have calculated the free energy using finite quark mass with the effect of curvature term considering zero chemical potential.

In order to new findings about this state, we now extend the previous work using chemcial potential. The quark mass is computed by replacing the factor T^2 to a good accuracy of temperature as $T^2 + \mu^2/\pi^2$ [11]. Now the quark mass has dependence on temperature as well as on chemical potential. Thus a dynamical quark mass uses as a finite value which is suitably modified by Kumar et al. [10]:

$$m_q^2(T,\mu) = \gamma_q \frac{N}{\ln(1 + \frac{k^2}{\Lambda^2})} \left(T^2 + \frac{\mu^2}{\pi^2} \right) \tag{1}$$

where, $k = [\frac{\gamma N^{\frac{1}{3}} T^2 \Lambda^2}{2}]^{\frac{1}{4}}$ is known as momentum with $N = \frac{16\pi}{[33-2N_f]}$ and number of flavor $N_f = 3$. The parametrization factor $\gamma^2 = 2[\frac{1}{\gamma_q^2} + \frac{1}{\gamma_g^2}]$ with $\gamma_q = 1/6$ and $\gamma_g = 6\gamma_q$ [10] and Λ is QCD parameter. We choose these parametrization factor because they nicely fit into our calculations and also help to enhance free energy evolution.

Evolution of quark gluon plasma

The work on free energy evolution of QGP has been done by Ramanathan et al. [9] using a simple statistical model. Further authors [12] have studied free energy of a quark gluon plasma with the inclusion of curvature term using dynamical quark mass considering zero chemical potential. In the present work, we modify earlier calculation of Ref. [10] with the effect of chemical potential.

We calculate the free energy for quarks, F_q by modifying the density of states using finite quark mass at fix value of chemical potential. These modification are taken care with the inclusion of curvature term in the density of states. Thus free energy of the constituent particles which set up the fireball is suitably modified using Ref. [10] and it is defined as:

$$F_q = \mp T g_q \int dk \rho(k) \ln(1 \pm e^{-(\sqrt{m_q^2+k^2}-\mu)/T}) \ , \tag{2}$$

Similarly, free energy for gluons, F_g is taken as Ref. [10]. Where $\rho(k)$ is the density of states of the particular particle (quarks, gluons, pions etc.), and g_q is the degeneracy factor. The interfacial free energy is defined as:

$$F_{interface} = \frac{1}{4} R^2 T^3 \gamma \ , \tag{3}$$

where, R is the radius of the droplet. In a similar manner, the free energy for the pionic enviornment is given as Ref. [9,10],

$$F_\pi = (3T/2\pi^2)\nu \int_0^\infty k^2 dk \ln(1 - e^{-\sqrt{m_\pi^2+k^2}/T}) \ . \tag{4}$$

Thus the total free energy F_{total} is calculated using all above energies and it is given as,

$$F_{total} = F_{q=u,d,s} + F_{gluon} + F_{\pi} + F_{interface} \,. \tag{5}$$

Also thermodynamic variables entropy and specific heat computed with the help of total free energy which shows a nature of phase transition. However using modified quark mass dependent on finite temperature and chemical potential including curvature term, the total free energy is calculated that explain the evolution of quark-gluon plasma and quark-hadron phase transition. Our results are significantly improved and help to enhance the size of QGP droplet.
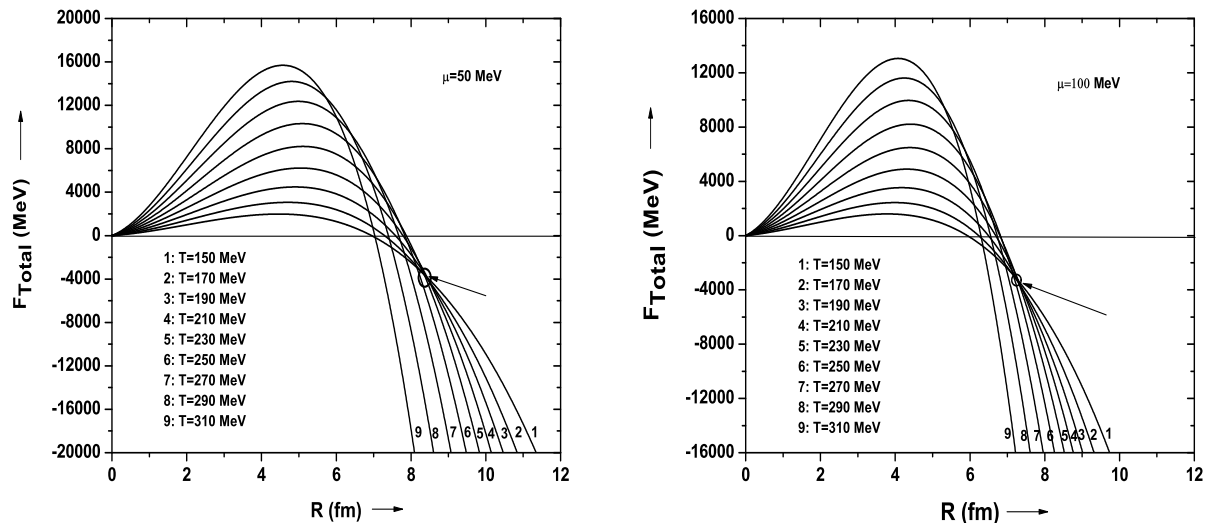
Figure 1: **Modified free energy F_{Total} with radius for various temperature T are shown at fix chemical potential μ=50 MeV (left) and μ=100 MeV (right).**

Results and discussion

In order to discuss the free energy evolution of QGP and quark -hadron phase transition, we present the modified results at various temperature and at fix value of chemical potential incorporating curvature term in total free energy. The figures describe the physical picture of QGP droplet formation and predict the order of phase transition. The calculations are performed in a similar way by modifying the Ref. [10], considering the chemical potential with a major difference that in present paper, is properly taken into account.

In figure 1, it is found that there is large barrier height in the free energy evolution that in turn to produce a large stable QGP droplet at $\mu = 50$ MeV in comparison to $\mu = 100$ MeV. The bunching of curves provide more realistic picture for the stabilty of QGP droplet as shown by arrowhead. In the left hand side of figure 1, the size of QGP droplet is large, around 8.5 fm at $\mu = 50$ MeV as compared to right hand side figure which is around 7.5 fm at $\mu = 100$ MeV. This critical observation shows that the size of QGP droplets goes on decreasing as the chemical potential increases. The results are also compared with earlier work of Ref. [10, 12].
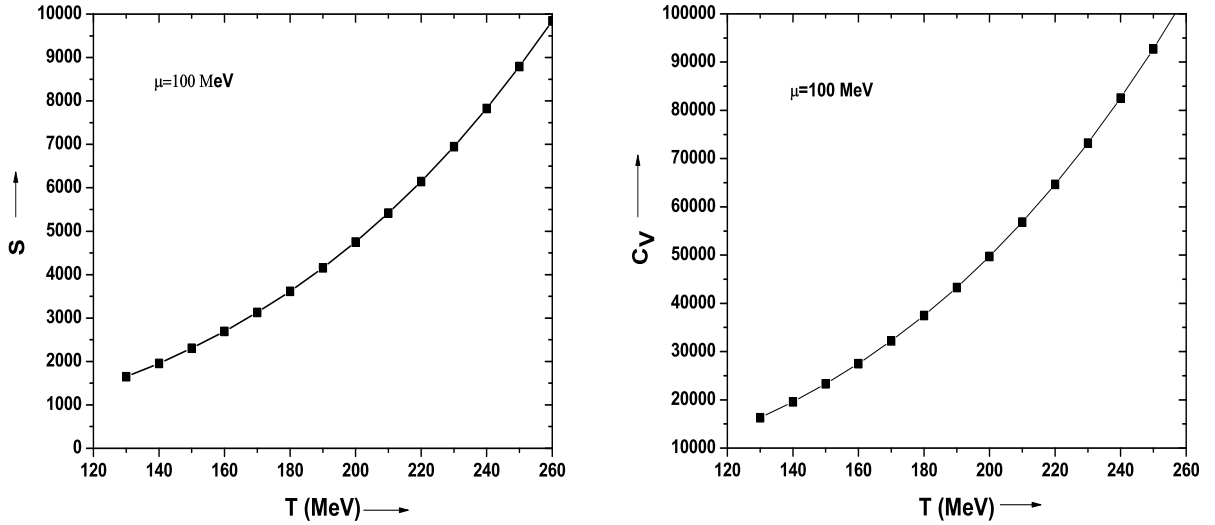
Figure 2: Variation of entropy S (left) and specific heat C_v (right) are shown with temperature T at fix chemical potential μ=100 MeV.

In figure 2, we found no discontinuity in both the entropy term and specific heat which shows phase transition is a smooth crossover rather than a first order phase transition. Our current results agree nicely with the recent results of lattice QCD simulation [5].

Thus the use of finite quark mass with finite temperature and chemical potential including the curvature term enhances the droplet size of QGP with large positive barrier height that in turn to make more stability in the plasma evolution. The results are in good agreement with Lattice QCD simulation in order to predict the order of phase transition. Finally our results should be of relevance in connection with free energy evolution of QGP and quark-hadron phase transition.

References

[1] S. Borsanyi *et al.*, JHEP 1009 (2010) 073.

[2] J. P. Blaizot, Nucl. Phys. A 661 (1999) 3.

[3] S. Hamieh, J. Letessier and J. Rafelski, Phys. Rev. A 67 (2003) 014301.

[4] S. Hamieh, K. Redlich and A. Tounsi, J. Phys. G 30 (2004) 481.

[5] Y. Aoki, G. Endrodi, Z. Fodor, S.D. Katz and K.K. Szabo, Nature 443 (2006) 675.

[6] S. Ejiri, Phys. Rev. D 78 (2008) 074507.

[7] E.S. Bowman and J. I. Kapusta, Phys. Rev. C 79 (2009) 015202.

[8] G. Neergaad and J. Madsen, Phys. Rev. D 60 (1999) 054011.

[9] R. Ramanathan *et al.*, Pram. J. Phys. 68 (2007) 757.

[10] Y. Kumar, JOP : Conf. Series 668 (2016) 012110.

[11] V.M. Bannur, Eur. Phys. J. C 50 (2007) 629634.

[12] S.S. Singh *et al.*, Pram. J. Phys. 74 (2010) 27.

NON-LEADING LIGHT-CONE DISTRIBUTION AMPLITUDE OF *B*-MESON

A. L. Kuznetsova*

P. G. Demidov Yaroslavl State University, Yaroslavl, Russia

Annotation

There are two functions only, called leading and non-leading Light-Cone Distribution Amplitudes (LCDAs), which are entering the transition matrix element from the B-meson state to the vacuum one. Three different models are suggested for the leading LCDA (the exponential model, light-meson-like model, and two-parametric Braun-Ivanov-Korchemsky model) as well as the modified exponential model by Lee and Neubert is known which are widely used in applications. The non-leading LCDA can be related with the leading one by virtue of the Wandzura-Wilczek relation. Both leading and non-leading LCDAs are calculated within the two simplest models but two other, more complicated models are presented by the leading LCDA only. We have calculated the non-leading LCDA following from the leading models by Braun, Ivanov and Korchemsky and by Lee and Neubert in the Wandzura-Wilczek approximation. Using both leading and non-leading LCDAs, the momentum-transverse-dependent first inverse moments in all these models are calculated. These moments are of importance, for example, in the analysis of exclusive radiative, semileptonic and hadronic decays of B-mesons.

Introduction

B-meson is also known as the open-beauty heavy meson which consists of the light u- or d-quark and heavy b-antiquark. In the Heavy Quark Effective Theory (HQET) framework [1, 2], the heavy antiquark is considered as the stationary source and the meson dynamics is completely determined by the motion of the light quark. Despite another type of interaction, this system is very similar to the hydrogen atom. The heavy antiquark in the heavy meson behaves like a proton in the hydrogen atom and the light quark looks like an electron. Let us remember that the proton spin in the hydrogen atom is decouple in the non-relativistic approximation, its effects on the energy levels are absent completely and this is also true for the heavy meson in the infinitely-heavy-mass limit of the b-antiquark. As a consequence, the pseudoscalar B- and vector B^*-meson are equivalent up to $1/m_b$ corrections. From the theoretical point of view, decays of B-mesons are described by transition matrix elements from the B-meson state into the vacuum or hadronic one. If we restrict ourselves the transition matrix element from the B-meson state to the vacuum, there are two functions only which are called the leading and non-leading Light-Cone Distribution Amplitudes (LCDAs). Three models for the leading LCDA [3–5] are suggested to simplify calculations of the decays amplitude, which are widely used in physical applications. Lee and Neubert [6] presented the modified form of the model [3] which matches the asymptotic form following from the perturbative QCD with the non-perturbative exponential behavior. The non-leading LCDA can be related with the leading one by virtue of the

---

*elf-torgovez@yandex.ru

Wandzura-Wilczek relation [3]. Both leading and non-leading LCDAs are calculated within the simplest models [3, 4] but two other, more complicated models [5, 6] are presented by the leading LCDA only. Using these LCDAs, the momentum-transverse-dependent first inverse moments of these models can be calculated which are of importance, for example, in the analysis of exclusive radiative, semileptonic and hadronic decays of B-mesons.

Within the HQET framework, it is convenient to introduce the effective mass $\bar{\Lambda} = m_M - m_Q$ of the meson which is equal to the difference between the masses of the heavy meson m_M and heavy quark m_Q. Note that numerically $\bar{\Lambda} = 0.5$ GeV for B- and D-mesons with the lowest masses. At the language of Quantum Field Theory (QFT), to describe the heavy meson as a bound state of quark and antiquark one needs to introduce a bilocal operator with quantum numbers of the meson which is called the meson interpolating current. Such a current is constructed from the field $q(z)$ of a light quark and field $\bar{h}_v(x)$ of the heavy antiquark (the leading Fock decomposition):

$$\widetilde{O}(z) = \bar{h}_v(0)\, \Gamma_A\, E(0, z)\, q(z), \tag{1}$$

where Γ_A is a suitable structure from Dirac matrices. The requirement of the bilocal-operator gauge invariance results in the introduction of a gauge link $E(0, z)$ between the quark fields which is called the Wilson line. The gluon fields $A_\mu^a(z)$, which are relevant for the quark interaction, are path-ordered along the Wilson line [3]. One projection of the gluonic field only gives contribution to the Wilson line. The choice of the Fock-Schwinger gauge makes trivial the Wilson line, $E(0, z) = 1$, In the Fock-Schwinger gauge for gluons, and the presentation of meson interpolating currents becomes quite simple.

Since the light-quark mass can be neglected in the Heavy-Quark Symmetry limit, then this quark propagates with the speed of light and is situated on the light cone. To describe such a quark, it is convenient to introduce two light-like vectors n_+^μ and n_-^μ which determine the light-cone plane. The origin of the plane is identified with the position of the heavy quark. These two vectors can be related with the physical ones: the quark four-momentum $p^\mu = p_+ n_-^\mu$ and its position $z^\mu = z_- n_+^\mu$ on the light cone.

The general decomposition of the transition matrix element from the meson state $|(v)(v)\rangle$ (the B-meson is considered as the heavy meson further) to the vacuum one $|0\rangle$ [7]:

$$\langle 0|q_j(z)\, \bar{h}_{vi}(0)|\bar{B}(v)\rangle = -\frac{if_B M_B}{4} \left[(1 + \hat{v}) \left\{ \tilde{\varphi}_+^B(t) + \left[\tilde{\varphi}_-^B(t) - \tilde{\varphi}_+^B(t) \right] \frac{\hat{z}}{2t} \right\} \gamma_5 \right]_{ij}, \tag{2}$$

where $v^\mu = (n_+^\mu + n_-^\mu)/2$ is the heavy-meson four-velocity, $t = (vz)$ and M_B and f_B are the B-meson mass and leptonic decay constant, respectively. This matrix element is parametrized in terms of two distribution amplitudes $\varphi_+^B(t)$ and $\varphi_-^B(t)$ which describe the light-quark motion inside the meson. It is convenient to work with the Fourier transforms of the distribution amplitudes:

$$\tilde{\varphi}_\pm^B(t) = \int_0^\infty d\omega\, \mathrm{e}^{-i\omega t} \phi_B^\pm(\omega). \tag{3}$$

Two distribution amplitudes $\varphi_B^+(\omega)$ and $\varphi_B^-(\omega)$ considered are related to each other by the Wandzura-Wilczek relation [3, 4]:

$$\phi_B^-(\omega) = \int_\omega^\infty \frac{\phi_B^+(\omega')}{\omega'}\, d\omega' \tag{4}$$
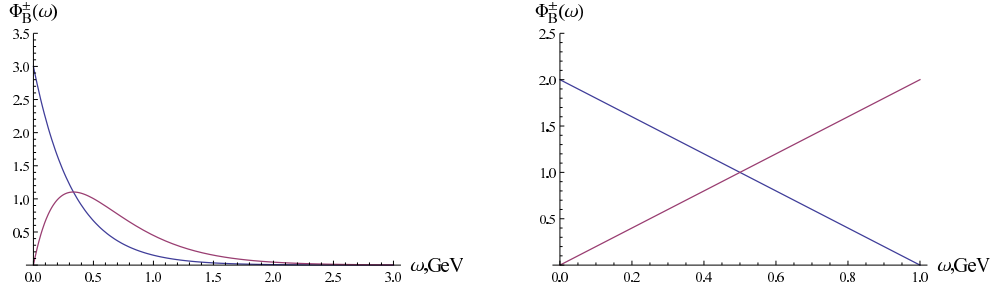
Figure 1: The exponential model (left panel) and light-meson-like model (right panel).
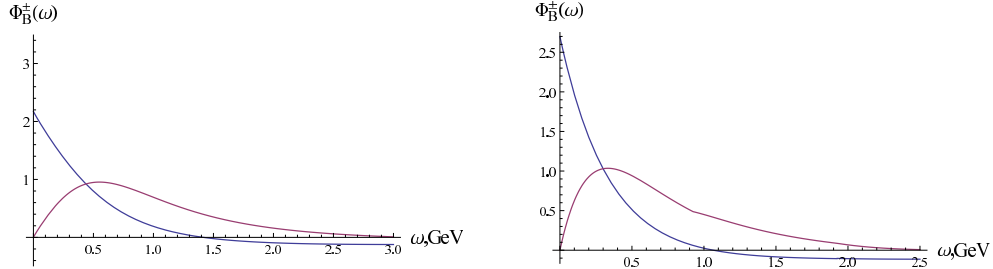
Figure 2: BIK model (left panel) and Improved exponential model (right panel).

In calculations of B-meson decays, one requires not the distribution amplitudes themselves but some integrals of these amplitudes. As a special case, let us calculate the following first inverse moments of the distribution amplitudes:

$$\lambda_B^{-1} = \int_0^\infty \frac{d\omega}{\omega}\, \phi_B^+(\omega), \qquad \lambda_{B,\pm}^{-1}(q^2) = \int_0^\infty \frac{\phi_B^\pm(\omega)\, d\omega}{\omega - q^2/M_B - i\epsilon}, \tag{5}$$

where q^2 is the four-momentum squared. Note that the moment $\lambda_{B,-}^{-1}(q^2)$ is logarithmically divergent in the limit $q^2 \to 0$.

Models for the Distribution Amplitudes

The distribution amplitudes are non-perturbative quantities and usual perturbative methods of QFT [6] are inapplicable. The commonly used method of their calculation is the QCD Sum Rules [3, 5]. To combine these distribution amplitudes with hard kernels in amplitudes of physical processes, one needs to model them by some analytical expressions called the distribution amplitude models. At present, several models for the distribution amplitudes have been suggested. Two simplest ones are the exponential model [3] which appeared to be the most popular and light-meson-like model [4]. The energy dependence of these distribution amplitudes is presented in Fig. 1.

More involved models are the two-parametric model by Braun, Ivanov, and Korchemsky (BIK) [5] and improved exponential model by Lee and Neubert [6]. The later one matches the exponential behavior at low momenta of light quark and QCD-based behavior (the radiative tail) at large momenta. For these models the leading distribution amplitude only was studied while the non-leading amplitude was skipped. We have calculated these non-leading amplitudes and their explicit analytical expressions will be presented elsewhere [9]. The energy dependence of both leading and non-leading distribution amplitudes is presented in Fig. 2.

64
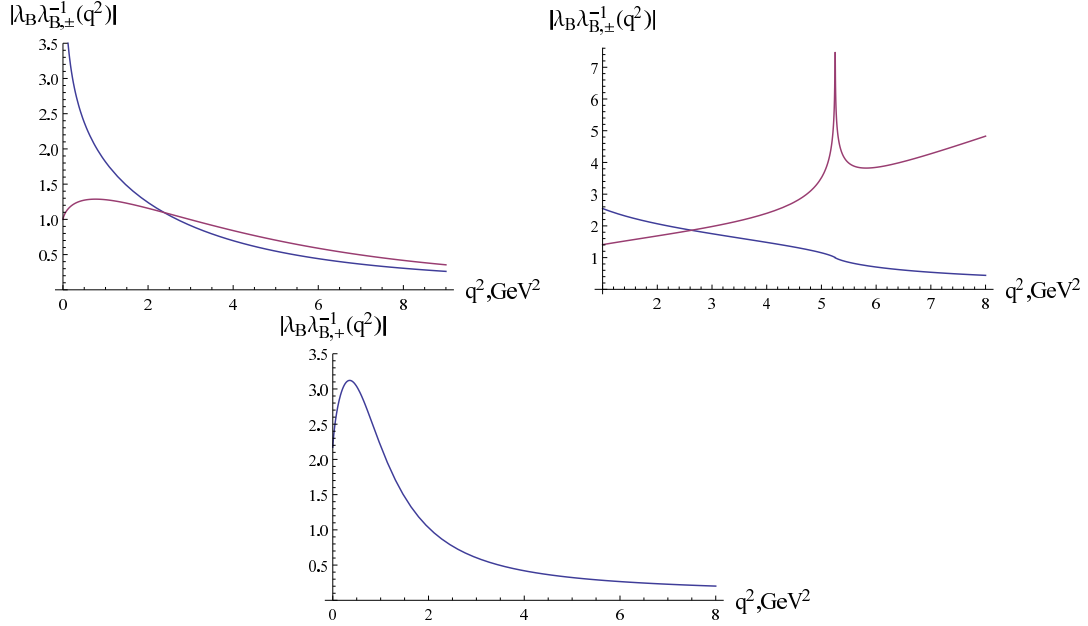
Figure 3: First inverse moments for LCDAs models. The exponential (left panel), light-meson-like (center panel), and BIK (left panel) models.

As mentioned above, one needs moments of these amplitudes in getting decay widths of heavy mesons. Among moments, first inverse ones (5) are of special interest. The momentum-dependent first inverse moments of the leading and non-leading distribution amplitudes in the exponential, light-meson-like and BIK models are presented in Fig. 3. Explicit analytic expressions are also obtained and will be presented elsewhere [9].

The uncertainty induced by a choice of the distribution amplitude model of the heavy meson on the semileptonic decay rates of B-mesons is also interesting to study which is not yet been worked out.

Conclusions

The transition matrix element from the B-meson state to the vacuum one is determined by two functions only which are called the leading and non-leading Light-Cone Distribution Amplitudes (LCDAs). Several models for the leading LCDA are known at present which are widely used in applications. The non-leading LCDA can be related with the leading one by virtue of the Wandzura-Wilczek relation. Both leading and non-leading LCDAs are calculated within the simplest models [3, 4] but two other, more complicated models [5, 6] are presented by the leading LCDA only. We have calculated the non-leading LCDA related with the models [5,6] in the Wandzura-Wilczek approximation. Using these LCDAs the momentum-transverse-dependent first inverse moments in all these models have been calculated. These moments are of importance in the analysis of exclusive decays of B-mesons.

65

References

[1] T. Mannel, *Effective Field Theories in Flavor Physics*. New York: Springer, 2004. 175 p.

[2] A. G. Grozin, *Heavy quark effective theory*. New York: Springer, 2004. 213.

[3] A. G. Grozin and M. Neubert, Phys. Rev. D 55 (1997) 272.

[4] H. Kawamura, J. Kodaira, C.-F. Qiao, and K. Tanaka, Phys. Lett. B 523 (2001) 111.

[5] V. M. Braun, D. Y. Ivanov, and G. P. Korchemsky, Phys. Rev. D 69 (2004) 034014.

[6] S. J. Lee and M. Neubert, Phys. Rev. D 72 (2005) 094028.

[7] M. Beneke and T. Feldmann, Nucl. Phys. B592 (2001) 3.

[8] M. E. Peskin and D. V. Schroeder, *An Introduction to Quantum Field Theory*, New York: Addison-Wesley, 1995. 865 p.

[9] A. L. Kuznetsova and A. Ya. Parkhomenko, in preparation.

EFFECTS OF FINITE CORRELATION TIME AND COMPRESSIBILITY ON THE ACTIVE-TO-ABSORBING-STATE PHASE TRANSITION: RENORMALIZATION GROUP APPROACH

N. V. Antonov[1], M. Hnatič[2,3], A. S. Kapustin[1], T. Lučivjanský[2,4*], L. Mižišin[2,3]

[1] *Department of Theoretical Physics, St. Petersburg University, St. Petersburg, Petrodvorets, Russia*
[2] *Faculty of Sciences, Šafárik University, Košice, Slovakia*
[3] *Joint Institute for Nuclear Research, Dubna, Russia*
[4] *Fakultät für Physik, Universität Duisburg-Essen, Duisburg, Germany*

Annotation

The direct bond percolation process is studied in the presence of compressible velocity fluctuations. The velocity field is modeled by the stochastic Gaussian field with finite correlation time and compressibility taken into account. It is shown how the field-theoretic action can be constructed, which is convenient for the renormalization group analysis.

Introduction

The directed bond percolation (DP) process [1] is one of the most important model, that describes formation of the fractal structures. The distinctive property of DP is the exhibition of non-equilibrium second order phase transition [2] between an absorbing (inactive) and an active state. Similar to the equilibrium critical behavior, emerging scale invariant behavior, can be analyzed with the help of renormalization group (RG) technique. The deviations from the ideal models are known to have a profound effect on the critical behavior. The main aim of this article is to show how the model for the DP process in the presence of compressible velocity fluctuations can be constructed and later on analyzed using the perturbative renormalization group technique.

The model

The continuum description [2,3] of DP in terms of a density field $\psi = \psi(t, \boldsymbol{x})$ arises from a coarse-graining procedure in which a large number of microscopic degrees of freedom have been averaged out. The coarse grained stochastic equation then reads

$$\partial_t \psi = D_0(\boldsymbol{\nabla}^2 - \tau_0)\psi - \frac{\lambda_0 D_0}{2}\psi^2 + \eta, \tag{1}$$

where η denotes the random noise, $\partial_t = \partial/\partial t$ is the time derivative, $\boldsymbol{\nabla}^2$ is the Laplace operator, D_0 is the diffusion constant, λ_0 is the coupling constant and τ_0 measures deviation from the criticality. The Gaussian noise term η with zero mean stands for the neglected fast microscopic degrees of freedom. The mathematical model has to respect the absorbing state condition, that is $\psi = 0$ is always a stationary state. From this condition follows [3] that the correlation function of the noise is proportional to the field ψ

$$\langle \eta(t_1, \boldsymbol{x}_1)\eta(t_2, \boldsymbol{x}_2) \rangle = \lambda_0 D_0 \psi(t_1, \boldsymbol{x}_1)\delta(t_1 - t_2)\delta^{(d)}(\boldsymbol{x}_1 - \boldsymbol{x}_2). \tag{2}$$

*tomas.lucivjansky@uni-due.de

In realistic situations underlying properties of the environment, which are not usually taken into account, may lead to a change in the universal properties of the system. In this paper, we focus on the effect of advective velocity fluctuations, which are considered to be both finite correlated in time and compressible. Following the work [4] the velocity field is considered to be a random Gaussian variable with zero mean and correlator of the form

$$\langle v_i(t, \boldsymbol{x}) v_j(0, \boldsymbol{0})\rangle = \int \frac{\mathrm{d}\omega}{2\pi} \int \frac{\mathrm{d}^d \boldsymbol{k}}{(2\pi)^d} D_v(\omega, \boldsymbol{k}) \mathrm{e}^{-i\omega t + \boldsymbol{k} \cdot \boldsymbol{x}}, \tag{3}$$

where d is the space dimension and the kernel function $D_v(\omega, \boldsymbol{k})$ is chosen in the form

$$D_v(\omega, \boldsymbol{k}) = [P_{ij}^k + \alpha Q_{ij}^k] \frac{g_{10} u_{10} D_0^3 k^{4-d-y-\eta}}{\omega^2 + u_{10}^2 D_0^2 (k^{2-\eta})^2}. \tag{4}$$

Here $P_{ij}^k = \delta_{ij} - k_i k_j / k^2$ is a transverse and Q_{ij}^k is a longitudinal projection operator, $k = |\boldsymbol{k}|$, a positive parameter $\alpha > 0$ can be interpreted as a simplest possible deviation from the incompressibility condition $\boldsymbol{\nabla} \cdot \boldsymbol{v} = 0$. The coupling constant g_{10} and exponent y describe the equal-time velocity correlator or equivalently, the energy spectrum of the velocity fluctuations. On the other hand parameter $u_{10} > 0$ and exponent η describe dispersion behavior of the mode k. The exponents y and η are analogous to the standard expansion parameter $\varepsilon = 4 - d$ in the static critical phenomena [8]. According to the general rules of the RG approach we formally assume that the exponents ε, y and η are of the same order of magnitude and constitute small expansion parameters in a perturbation sense.

The advection is usually incorporated into the model by the replacement ∂_t by the Lagrangian derivative $\partial_t + (\boldsymbol{v} \cdot \boldsymbol{\nabla})$. However, due to the assumed compressibility this is not sufficient [6] and also the term $(\boldsymbol{\nabla} \cdot \boldsymbol{v})$ has to be added

$$\partial_t \rightarrow \partial_t + (\boldsymbol{v} \cdot \boldsymbol{\nabla}) + a_0 (\boldsymbol{\nabla} \cdot \boldsymbol{v}), \tag{5}$$

with the additional parameter a_0.

For the effective use of RG method it is advantageous to reformulate the stochastic problem (1-4) into the field-theoretic language. This can be achieved in the standard fashion [7, 8] and the resulting dynamic functional can be written as a sum

$$\mathcal{J}[\varphi] = \mathcal{J}_{\mathrm{diff}}[\varphi] + \mathcal{J}_{\mathrm{vel}}[\varphi] + \mathcal{J}_{\mathrm{int}}[\varphi], \tag{6}$$

where $\varphi = \{\tilde{\psi}, \psi, \boldsymbol{v}\}$ stands for the complete set of fields and $\tilde{\psi}$ is the response field. The corresponding terms have the following form

$$\mathcal{J}_{\mathrm{diff}}[\varphi] = \int \mathrm{d}t \int \mathrm{d}^d \boldsymbol{x} \left\{ \tilde{\psi} [\partial_t - D_0 \boldsymbol{\nabla}^2 + D_0 \tau_0] \psi \right\}, \tag{7}$$

$$\mathcal{J}_{\mathrm{vel}}[\boldsymbol{v}] = -\frac{1}{2} \int \mathrm{d}t_1 \int \mathrm{d}t_2 \int \mathrm{d}^d \boldsymbol{x}_1 \int \mathrm{d}^d \boldsymbol{x}_2 \ v_i(t_1, x_1) D_{ij}^{-1}(t_1 - t_2, \boldsymbol{x}_1 - \boldsymbol{x}_2) v_j(t_2, \boldsymbol{x}_2), \tag{8}$$

$$\mathcal{J}_{\mathrm{int}}[\varphi] = \int \mathrm{d}t \int \mathrm{d}^d \boldsymbol{x} \ \tilde{\psi} \left\{ \frac{D_0 \lambda_0}{2} [\psi - \tilde{\psi}] - \frac{u_{20}}{2D_0} \boldsymbol{v}^2 + (\boldsymbol{v} \cdot \boldsymbol{\nabla}) + a_0 (\boldsymbol{\nabla} \cdot \boldsymbol{v}) \right\} \psi. \tag{9}$$

Using this action one can construct the perturbation theory in the form of Feynman diagrams. Basic elements are propagators and interaction vertices, which are graphically
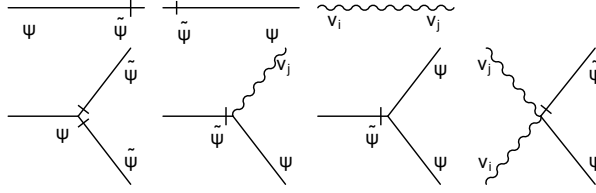
Figure 1: Elements of the perturbation theory in the graphical representation.

represented in the Fig. 1. All but the third term in (9) stems directly stems from the nonlinear terms in (1) and (5). The third term proportional to $\propto \tilde{\psi}\psi\boldsymbol{v}^2$ deserves a special attention. Presence of such term is prohibited in the original Kraichnan model due to the underlying Galilean invariance. However, in our case the finite time correlations of the velocity fluctuations does not impose such restriction. In the language of Feynman graphs, one can then show that such term will indeed be generated. It can be readily seen considering first three graphs in the following expansion

$$\Gamma_{\tilde{\psi}\psi\boldsymbol{vv}} = \frac{u_2}{D}\delta_{ij}Z_8 + \quad \text{[diagram]} \quad + \quad \text{[diagram]} \quad + \frac{1}{2} \quad \text{[diagram]} \quad + \quad \text{[diagram]}$$

$$+ \quad \text{[diagram]} \quad + \quad \text{[diagram]} \quad + \quad \text{[diagram]} \quad + \quad \text{[diagram]} \quad . \tag{10}$$

At this stage, we would like to briefly discuss parameter a_0. In the case of passive scalar advection [4] the choice $a_0 = 1$ corresponds to the conserved quantity ψ (density), whereas for the choice $a_0 = 0$ it is the auxiliary field field $\tilde{\psi}$. However, due to the percolation interactions both fields ψ and $\tilde{\psi}$ are now fluctuating quantities. In RG procedure then both counterterms $\tilde{\psi}(\boldsymbol{v}\cdot\boldsymbol{\nabla})\psi$ and $\tilde{\psi}(\boldsymbol{\nabla}\cdot\boldsymbol{v})\psi$ will be generated. In order to illustrate this point let us consider Feynman diagrams for the 1PI function $\tilde{\psi}\psi\boldsymbol{v}$ to the 1-loop approximation. This can be formally written as

$$\Gamma_{\tilde{\psi}\psi\boldsymbol{v}} = -ip_j Z_4 - iaq_j Z_5 + \quad \text{[diagram]} \quad + \quad \text{[diagram]} \quad , \tag{11}$$

where p is a momentum of the field ψ and q of the field $\boldsymbol{v}$, respectively. A straightforward calculation of the first graph using the dimensional regularization [8] gives us

$$\text{[diagram]} \quad = \frac{i\lambda_0^2}{4d(2\pi)^d\varepsilon}[2p_j - q_j]. \tag{12}$$

Let us imagine the graph (12) as a part of some high-order diagram for an incompressible velocity field. In such case all velocity propagators are proportional to the transverse projector P_{ij} and after contraction with (12) the compressible part evidently drops out. However, in our model the velocity propagator (4) contains also a longitudinal part. Moreover in contrast to the Kraichnan model, now also the second graph in (11) is divergent

(due to the finite correlations in time the graph does not contain a closed loop of retarted propagators [8]).

We conclude that compressibility and non-Galilean nature of the velocity correlator lead to the quite involved extension of the model, which requires careful analysis. Note, that the incompressible case in presence of a term $\tilde{\psi}\psi\boldsymbol{v}^2$ has been analyzed in [9].

Renormalization group analysis

The field-theoretic formulation summarized in (7)-(9) has an advantage to be amenable to the machinery of field theory [8]. Near criticality $\tau = 0$ large fluctuations on all scales dominate the behavior of the system, which results into the divergences in Feynman graphs. The RG technique allows us to deal with them and as a result it allows for a pertubative computation of critical exponent in a formal expansion around the upper critical dimension. Thus provides us with information about the scaling behavior of the Green functions. The renormalization of the model can be achieved through the relations

$$D_0 = D Z_D, \qquad \tau_0 = \tau Z_\tau + \tau_C, \qquad a_0 = a Z_a, \qquad g_{10} = g_1 \mu^{y+\eta} Z_{g_1},$$
$$u_{10} = u_1 \mu^\eta Z_{u_1}, \qquad \lambda_0 = \lambda \mu^\varepsilon Z_\lambda, \qquad u_{20} = u_2 Z_{u_2},$$
$$\tilde{\psi} = Z_{\tilde{\psi}} \tilde{\psi}_R, \qquad \psi = Z_\psi \psi_R, \qquad \boldsymbol{v} = Z_v \boldsymbol{v}_R. \tag{13}$$

where μ is the reference mass scale in the MS scheme [8].

We have found [10] that depending on the values of a spatial dimension ε, scaling exponents y and η, describing statistics of velocity fluctuations and a degree of compressibility α, the model exhibits 8 distinct universality classes. Some of them are already well-known: the Gaussian (free) fixed point, a directed percolation without advection and a passive scalar advection. The remaining points correspond to new universality classes, for which an interplay between advection and percolation is relevant. It has to be kept in mind that only relatively small values of α are allowed ($\alpha \ll 1$). In order to properly describe effects of strong compressibility and to better understand non-universal effects for turbulent advection one should proceed one step further and employ a more sophisticated model for velocity fluctuations, e.g. one introduced in the work [11].

Conclusions

In this brief article we have summarized main points of the field-theoretic study of directed percolation process in the presence of compressible velocity field. The detailed results for the renormalization constants and analysis of the scaling behavior can be found elsewhere [10].

References

[1] D. Stauffer, A. Aharony, *Introduction to Percolation Theory*, Taylor & Francis, London, 1992.

[2] H. Hinrichsen, Adv. Phys. 49 (2001) 815.

[3] H.-K. Janssen, U. C. Täuber, Ann. Phys. 315 (2004) 147.

[4] N. V. Antonov, Physica D 144 (2000) 370.

[5] A. N. Vasil'ev, *The Field Theoretic Renormalization Group in Critical Behavior Theory and Stochastic Dynamics*, Boca Raton: Chapman Hall/CRC, 2004.

[6] N. V. Antonov, A. S. Kapusin, J. Phys. A:Math. Theor. 43 (2010) 405001.

[7] C. de Dominicis, J. Phys. Colloq. France 37 (1976) 1-247.

[8] H.-K. Janssen, Z. Phys. B 23 (1976) 377.

[9] M. Dančo, M. Hnatič, T. Lučivjanský, L. Mižišin, Theor. Math. Phys. 176 (2013) 898.

[10] N. V. Antonov, M. Hnatič, A. S. Kapustin, T. Lučivjanský, L. Mižišin, Phys. Rev. E 93 (2016) 012151.

[11] N. V. Antonov, M. Yu. Nalimov, A. A. Udalov, Theor. Math. Phys. 110 (1997) 385.

THE EFFECTS DUE TO CONTINUATION OF PERTURBATIVE QCD RESULTS INTO THE TIMELIKE DOMAIN

S. A. Popov*

Joint Institute for Nuclear Research, Dubna, Russia

Annotation

The effects due to continuation of spacelike perturbative QCD results into the timelike domain are studied. The perturbative contribution to the spectral function is explicitly calculated. The R–ratio of electron–positron annihilation into hadrons is studied and the higher-order π^2-terms are calculated.

Introduction

Quantum chromodynamics (QCD) has two features: confinement and asymptotic freedom. Confinement is the phenomenon that free quarks cannot be observed. Asymptotic freedom means that quarks interact weaker as process energy increases [1–3].

Asymptotic freedom allows perturbation theory to be applied at high energies. But the perturbation theory can only be directly employed in the theoretical description of physical observables depending on the spacelike kinematic variable $Q^2 = -q^2 > 0$. By making use of dispersion relations one can overcome this difficulty and calculate the theoretical expressions for physical observables depending on the timelike kinematic variable $s = q^2 > 0$. The well-known observable depending on the timelike kinematic variable is so-called R–ratio of e^+e^- annihilation into hadrons:

$$R(s) = \frac{\sigma(e^+e^- \to \text{hadrons}; s)}{\sigma(e^+e^- \to \mu^+\mu^-; s)}.$$

The hadronic vacuum polarization function

The hadronic vacuum polarization function $\Pi(q^2)$ is defined through the hadronic vacuum polarization tensor $\Pi_{\mu\nu}$:

$$\Pi_{\mu\nu}(q^2) = i \int d^4x \exp(iqx) \langle 0|T\{J_\mu(x)J_\nu(0)\}|0\rangle = \frac{i}{12\pi^2}(q_\mu q_\nu - g_{\mu\nu}q^2)\Pi(q^2),$$

where $J_\mu(x) = \sum_f Q_f : \bar{\psi}\gamma_\mu\psi :$ is the quark electromagnetic current. $\Pi(\xi)$ has the only cut along the positive semi-axis of real ξ. The subtracted Cauchy integral formula gives:

$$\Delta\Pi(q^2, q_0^2) = \Pi(q^2) - \Pi(q_0^2) = \frac{1}{2\pi i} \oint_C \frac{(q^2 - q_0^2)\Pi(\xi)}{(\xi - q^2)(\xi - q_0^2)}d\xi.$$

$R(s)$ stands for the discontinuity of the $\Pi(q^2)$ across the physical cut:

$$R(s) = \frac{1}{2\pi i} \lim_{\varepsilon \to 0_+} \left(\Pi(s + i\varepsilon) - \Pi(s - i\varepsilon)\right), \qquad s = q^2 > 0,$$

---

*serzero2007@gmail.com
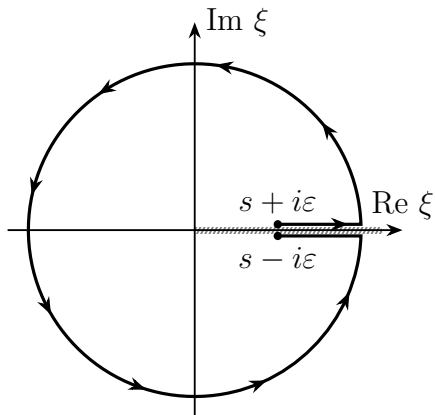
Figure 1: Possible choice for the integration contour in the dispersion relation for $R(s)$.

so one can derive the dispersion relation for the hadronic vacuum polarization function:

$$\Delta\Pi(q^2, q_0^2) = \frac{q^2 - q_0^2}{2\pi i} \lim_{\varepsilon \to 0_+} \int\limits_0^{+\infty} \frac{\Pi(\xi + i\varepsilon) - \Pi(\xi - i\varepsilon)}{(\xi - q^2)(\xi - q_0^2)} \mathrm{d}\xi = (q^2 - q_0^2) \int\limits_0^{+\infty} \frac{R(\xi)\mathrm{d}\xi}{(\xi - q^2)(\xi - q_0^2)}.$$

Adler function $D(Q^2)$

It is convenient to deal with the so-called Adler function [4]:

$$D(Q^2) = -\frac{\mathrm{d}\Pi(-Q^2)}{\mathrm{d}\ln(Q^2)}, \qquad Q^2 = -q^2 > 0.$$

The dispersion relations between $D(Q^2)$ and $R(s)$ read [4–6]:

$$D(Q^2) = Q^2 \int\limits_0^{+\infty} \frac{R(\xi)}{(\xi + Q^2)^2} \mathrm{d}\xi, \qquad R(s) = \frac{1}{2\pi i} \lim_{\varepsilon \to 0_+} \int\limits_{s+i\varepsilon}^{s-i\varepsilon} D(-\xi) \frac{\mathrm{d}\xi}{\xi}.$$

The derivation of before-mentioned relations does not require any phenomenological or model assumptions to be made and relies on the basic properties of $\Pi(q^2)$: the location of the cut in the complex plane and the asymptotic ultraviolet behavior.

In the framework of the perturbative approach the Adler function at the ℓ loop level is approximated as follows:

$$D_{pert}^{(\ell)}(Q^2) = 1 + d_{pert}^{(\ell)}(Q^2), \qquad d_{pert}^{(\ell)}(Q^2) = \sum_{j=1}^{\ell} d_j \left[a_s^{(\ell)}(Q^2) \right]^j,$$

where $a_s^{(\ell)}(Q^2) = \alpha_s^{(\ell)}(Q^2)\beta_0/(4\pi)$ — the ℓ–loop couplant, $\beta_0 = 11 - 2n_f/3$, n_f is the number of active flavors. At the moment only first four perturbative expansion coefficients d_j of the Adler function have been calculated [7–9]. By making use of integral relations, $R(s)$ in the ultraviolet domain $s \to \infty$ can be approximated by power series:

$$R_{pert}^{(\ell)}(s) = 1 + r_{pert}^{(\ell)}(s), \qquad r_{pert}^{(\ell)}(s) = \sum_{j=1}^{\ell} r_j \left[a_s^{(\ell)}(|s|) \right]^j, \qquad r_j = d_j - \delta_j.$$

73

This represents continuation of the "spacelike" theoretical predictions into the timelike domain. In the course of analytic continuation arise so-called π^2–terms [10, 11].

$$\delta_1 = \delta_2 = 0, \qquad \delta_3 = \frac{\pi^2}{3}d_1, \qquad \delta_4 = \frac{\pi^2}{3}\left(3d_2 + \frac{5}{2}\frac{\beta_1}{\beta_0^2}d_1\right).$$

Strictly speaking, all terms in expression $R_{pert}^{(\ell)}(s) - D_{pert}^{(\ell)}(|s|)$ are considered π^2-terms.

Spectral function

The strong corrections $d(Q^2)$ and $r(s)$ must satisfy resembling relations:

$$d(Q^2) = Q^2 \int\limits_0^{+\infty} \frac{r(\xi)}{(\xi + Q^2)^2}\mathrm{d}\xi, \qquad r(s) = \frac{1}{2\pi i}\lim_{\varepsilon \to 0_+}\int\limits_{s+i\varepsilon}^{s-i\varepsilon} d(-\xi)\frac{\mathrm{d}\xi}{\xi}.$$

For sake of simplicity, the common factor $N_c \sum_{f=1}^{n_f} Q_f^2$ is omitted. It's convenient to define the spectral density $\rho(\sigma)$ [12, 13] and the partial spectral density $\rho_j(\sigma)$ given by:

$$r(s) = \int\limits_s^{+\infty} \rho(\sigma)\frac{\mathrm{d}\sigma}{\sigma}, \quad \rho(\sigma) = \sum_{j=1}^{\infty} d_j\rho_j(\sigma), \quad \rho_j(\sigma) = \frac{1}{2\pi i}\lim_{\varepsilon \to 0_+}\left[(a_s(-\sigma - i\varepsilon))^j - (a_s(-\sigma + i\varepsilon))^j\right].$$

In the framework of the perturbative approach β-function in RG equation for the strong running coupling is approximated by power series:

$$\frac{\mathrm{d}\ln a(\mu^2)}{\mathrm{d}\ln \mu^2} = \beta(a(\mu^2)) \approx -a(\mu^2) - B_1 a^2(\mu^2) - B_2 a^3(\mu^2) - ...,$$

where $a(\mu^2) = \alpha(\mu^2)\beta_0/(4\pi)$, $\alpha(\mu^2) = g^2(\mu^2)/(4\pi)$ — running coupling, $B_j = \beta_j/\beta_0^{j+1}$.

From RG equation one can derive the following expression ($\xi = \ln \mu^2$):

$$\frac{\mathrm{d}^n a^m}{\mathrm{d}\xi^n} = (-1)^n \sum_{j_1,...,j_n} \prod_{k=1}^{n}\left(B_{j_k}(m + (j_1 + ... + j_{k-1}) + (k-1))\right) \cdot a^{m+(j_1+...+j_n)+n}.$$

The coefficients $B_{\{j;n;m\}}$ can be obtain through a recursive formula:

$$B_{\{j;n+1;m\}} = \sum_{l=0}^{j} B_{j-l}(m + n + l) \cdot B_{\{l;n;m\}}.$$

In particular $B_{\{j,1,m\}} = mB_j$, so one can easily calculate $B_{\{l;n;m\}}$ step by step.

The function $f(\xi) = a^m(\xi)$ is analytic at every point in $\{\xi \in \mathbb{C} : -\pi < \mathrm{Re}\, \xi < \pi\}$, so:

$$f(\xi_0 + \Delta\xi) - f(\xi_0 - \Delta\xi) \simeq 2\sum_{k=0}^{\infty} \frac{f^{(2k+1)}(\xi_0)}{(2k+1)!} \cdot (\Delta\xi)^{2k+1}, \qquad \xi = \ln \mu^2.$$

Hence the expression for partial spectral density reads:

$$\rho_m(s) \simeq \frac{1}{2\pi i}\left[f(\ln s - i\pi) - f(\ln s + i\pi)\right] = \sum_{k=0}^{\infty}\sum_{j=0}^{\infty} \frac{(-1)^k\pi^{2k}}{(2k+1)!}B_{\{j;2k+1;m\}}a^{j+(2k+1)+m}(|s|).$$

74

Calculation of δ_k coefficients

One can integrate the expression for $\mathrm{d}a^m/\mathrm{d}\xi$ and in any order obtain:

$$\int\limits_{\xi}^{+\infty} a^n(t)dt = \sum_{k=0}^{\infty} T_{nk} a^{n+k-1}(\xi) + \mathcal{O}\left(a^\ell\right), \qquad n \geq 2,$$

where T_{nk} is the coefficient of the $(n+k-1)$-th term. The strong correction to R-ratio:

$$r(s) = \sum_{m=1}^{\infty} d_m \int\limits_{s}^{+\infty} \rho_m(\sigma)\frac{d\sigma}{\sigma} = \sum_{m=1}^{\infty} d_m \sum_{k,j=0}^{\infty} \frac{(-1)^k \pi^{2k}}{(2k+1)!} B_{\{j;2k+1;m\}} \sum_{t=0}^{\infty} T_{j+(2k+1)+m,t} a^{j+2k+m+t}(|s|).$$

That enables one to explicitly calculate δ_k:

$$\delta_3 = \frac{\pi^2}{3}d_1, \quad \delta_4 = d_1\frac{5\pi^2}{6}B_1 + d_2\pi^2, \quad \delta_5 = d_1\pi^2\left(\frac{B_1^2}{2} + B_2 - \frac{\pi^2}{5}\right) + d_2\frac{7\pi^2}{3}B_1 + 2d_3\pi^2,$$

$$\delta_6 = d_1\frac{7\pi^2}{6}\left(B_1B_2 - \frac{11}{10}\pi^2 B_1 + B_3\right) + d_2\frac{\pi^2}{3}\left(4B_1^2 + 8B_2 - 3\pi^2\right) + d_3\frac{9}{2}\pi^2 B_1 + d_4\frac{10}{3}\pi^2.$$

Results

In this work the perturbative contribution to the spectral function $\rho_j(\sigma)$ is explicitly calculated, the R–ratio of electron–positron annihilation into hadrons is studied and the higher-order π^2–terms are calculated.

References

[1] G. t Hooft, (1972)

[2] D. J. Gross, F. Wilczek, Phys. Rev. Lett. 30 (1973) 1343.

[3] H. D. Politzer, Phys. Rev. Lett. 30 (1973) 1346.

[4] S. L. Adler, Phys. Rev. D10 (1974) 3714.

[5] A. V. Radyushkin, report JINR E2-82-159 (1982)

[6] N. V. Krasnikov, A. A. Pivovarov, Phys. Lett. B 116 (1982) 91001.

[7] P. A. Baikov, K. G. Chetyrkin, J. H. Kuhn, Phys. Rev. Lett. 101 (2008) 012002.

[8] P. A. Baikov, K. G. Chetyrkin, J. H. Kuhn, Phys. Rev. Lett. 104 (2010) 132004.

[9] P. A. Baikov, K. G. Chetyrkin, J. H. Kuhn, J. Rittinger, Phys. Lett. B714 (2012) 052.

[10] J. D. Bjorken, report SLAC-PUB-5103 (1989).

[11] A. L. Kataev, V. V. Starshenko, Mod. Phys. Lett. A 10 (1995) 10.1142/S0217732395000272.

[12] K. A. Milton, I. L. Solovtsov, Phys. Rev. D55 (1997) 5295.

[13] K. A. Milton, I. L. Solovtsov, Phys. Rev. D59 (1999) 107701.

PHENOMENOLOGICAL THEORY OF MESON GAS IN THE NON-PERTURBATIVE QUARK-GLUON CONDENSATE

G. M. Vereshkov[1,2*], G. U. Prokhorov[2†], R. S. Pasechnik[3‡]

[1] *Research Institute of Physics, Southern Federal University, Rostov-on-Don, Russian Federation*

[2] *Institute for Nuclear Research of Russian Academy of Sciences, Moscow, Russian Federation*

[3] *Theoretical High Energy Physics, Department of Astronomy and Theoretical Physics, Lund University, Lund, Sweden*

Annotation

Thermodynamic properties of strongly interacting matter were investigated in a wide temperature range within the framework of phenomenological quantum-field model of meson gas on the non-linear background, corresponding to quark-gluon condensate. The coincidence of microscopic quantum-field approach and thermodynamic analysis of extremes of generating functional was proves the inner coincidence of the model. Laws of change of particle masses, condensate amplitude, heat capacity and other thermodynamic quantities with temperature growth were revealed and then used to show and discuss the existence of phase transition in meson gas in high temperature area.

Model

Properties of hadrons significantly depend on the condition of quark-gluon condensate [1]. Energy density of quark-gluon condensate in vacuum case can be evaluated

$$
\begin{aligned}
\varepsilon_{g(vac)} &= -\frac{9}{32}\langle 0|\frac{\alpha_s}{\pi}G^a_{\mu\nu}G^{\mu\nu}_a|0\rangle + \frac{1}{4}\langle 0|m_u\bar{u}u + m_d\bar{d}d + m_s\bar{s}s|0\rangle \\
&\equiv -v_0^4 = -(265 \pm 15 MeV)^4 .
\end{aligned}
\tag{1}
$$

Quark-gluon condensate has two main subsystems. The first and the most important on is gluon condensate, which is induced as the fluctuations during tunnelling processes between different classical vacuum Yang-Mills solutions

$$
\langle 0|\frac{\alpha_s}{\pi}G^a_{\mu\nu}G^{\mu\nu}_a|0\rangle = (360 \pm 20 MeV)^4 .
\tag{2}
$$

Gluon condensate induces quark condensate, which is connected with gluon condensate amplitude through correlation length l_g

$$
\langle 0|\bar{s}s|0\rangle \simeq \langle 0|\bar{u}u|0\rangle \simeq \langle 0|\bar{d}d|0\rangle \simeq -l_g\langle 0|\frac{\alpha_s}{\pi}G^a_{\mu\nu}G^{\mu\nu}_a|0\rangle \simeq -(235 \pm 15 MeV)^3 ,
$$

$$
l_g = (\Lambda_g)^{-1} \simeq (1100 MeV)^{-1} .
\tag{3}
$$

*gveresh@gmail.com

†prokhorov@theor.jinr.ru

‡Roman.Pasechnik@thep.lu.se

Vacuum masses of the mesons are induced by the vacuum condensates of the corresponding quarks. In particular for π-meson (similar expressions appear for other mesons, except η', which mass has a contribution induced by gluon anomaly)

$$m^2_{\pi(vac)} = -\frac{(m_u + m_d)\langle 0|\bar{u}u + \bar{d}d|0\rangle}{f_\pi^2} \, . \tag{4}$$

Decay constants of different mesons $f_\pi, f_K, f_\eta, f_{\eta'}$ are approximately equal and also there is a relation between f_π and v_0, which is significant for the next model

$$f_\pi \simeq f_K \simeq f_\eta \simeq f_{\eta'} \simeq 130 MeV \, , \, f_\pi = \frac{v_0}{k_\pi} \, , \, k_\pi \simeq 2 \, . \tag{5}$$

A simple phenomenological model of meson gas, reproducing the main properties of mesons in vacuum, in particular (2)-(5), has the next Lagrangian

$$\mathcal{L} = \frac{1}{2}\partial_\mu\sigma\partial^\mu\sigma + 2g^2v_0^2\sigma^2 - g^4\sigma^4 + \frac{1}{2}(\partial_\mu\pi_\alpha\partial^\mu\pi_\alpha + \partial_\mu\eta\partial^\mu\eta + \partial_\mu\eta'\partial^\mu\eta') -$$

$$\frac{1}{2}\Big[2\kappa g^2(m_u + m_d)\sigma^2\pi_\alpha\pi_\alpha + \frac{2}{3}\kappa g^2(m_u + m_d + 4m_s)\sigma^2\eta^2 + \frac{4}{3}\kappa g^2(m_u + m_d + m_s + \Lambda_{an})\sigma^2\eta'^2\Big] +$$

$$\partial_\mu\bar{K}\partial^\mu K - \kappa g^2(m_u + m_d + 2m_s)\sigma^2\bar{K}K \, , \, \kappa = 4k_\pi^2\Big(\frac{9}{8}\Lambda_g + m_u + m_d + m_s\Big)^{-1} \, . \tag{6}$$

The Lagrangian (6) includes the fields of the lightest mesons and sigma field. An only field, forming non-zero vacuum condensate v is sigma field $\sigma = \frac{v}{g} + \tilde{\sigma}$, $\frac{v}{g} = \langle\sigma\rangle$ (here $\langle\rangle$ means expectation value over quantum vector of state) is a condensate part and $\tilde{\sigma}$ describes sigma meson particles after quantisation.

Quantum-field approach

One could easily construct quantum equations of motion for the model, describing evolution of meson fields and condensate amplitude. In particular, for sigma field one obtains

$$\partial_\mu\partial^\mu\sigma - 4g^2v_0^2 + 4g^4\sigma^3 + \Big[2\kappa g^2(m_u + m_d)\pi_\alpha\pi_\alpha + \frac{2}{3}\kappa g^2(m_u + m_d + 4m_s)\eta^2 +$$

$$\frac{4}{3}\kappa g^2(m_u + m_d + m_s + \Lambda_{an})\eta'^2 + 2\kappa g^2(m_u + m_d + 2m_s)\bar{K}K\Big]\sigma = 0 \, . \tag{7}$$

Equation for the condensate can be constructed after averaging of (7) over quantum state vector

$$gv\Big(-4v_0^2 + 4v^2 + 12g^2\langle\tilde{\sigma}^2\rangle + 2\kappa(m_u + m_d)\langle\pi_\alpha\pi_\alpha\rangle + \frac{2}{3}\kappa g^2(m_u + m_d + 4m_s)\langle\eta^2\rangle +$$

$$\frac{4}{3}\kappa(m_u + m_d + m_s + \Lambda_{an})\langle\eta'^2\rangle + 2\kappa(m_u + m_d + 2m_s)\langle\bar{K}K\rangle\Big) = 0 \, . \tag{8}$$

Now it is necessary to multiply (7) to $\tilde{\sigma}$ and factorize operator products. After that one obtains equation for $\tilde{\sigma}$

$$\partial_\mu\partial^\mu\tilde{\sigma} + m_\sigma^2\tilde{\sigma} = 0 \, , \, m_\sigma^2 = 8g^2v^2 \, . \tag{9}$$

The same operations for other fields allow to find masses of other mesons. In particular, for π-meson

$$\partial_\mu \partial^\mu \pi_\alpha + m_\pi^2 \pi_\alpha = 0 \,, \ m_\pi^2 = 2\kappa(m_u + m_d)(v^2 + g^2 \langle \tilde{v} \rangle) \,. \tag{10}$$

As one can see in vacuum (all the expectation values equal zero) the masses of the mesons are the same as (4) and condensate has amplitude v_0 in vacuum case. So model (6) reproduces basic properties of meson gas and QCD vacuum. Using Bose statistics in (9) and (10) and dimensional regularisation one could obtain temperature dependence of the condensate and meson masses. For the condensate amplitude we have

$$v^2 = v_0^2 - 3g^2 \Big(J_1(T, m_\sigma) + \frac{1}{16\pi^2} m_\sigma^2 ln \frac{m_\sigma^2}{m_{\sigma(vac)}^2} \Big) - \frac{3}{2} \kappa(m_u + m_d) \Big(J_1(T, m_\pi) +$$

$$\frac{1}{16\pi^2} m_\pi^2 ln \frac{m_\pi^2}{m_{\pi(vac)}^2} \Big) - \frac{1}{6} \kappa(m_u + m_d + 4m_s) \Big(J_1(T, m_\eta) + \frac{1}{16\pi^2} m_\eta^2 ln \frac{m_\eta^2}{m_{\eta(vac)}^2} \Big) -$$

$$\kappa(m_u + m_d + 2m_s) \Big(J_1(T, m_K) + \frac{1}{16\pi^2} m_K^2 ln \frac{m_K^2}{m_{K(vac)}^2} \Big) -$$

$$\frac{1}{3} \kappa(m_u + m_d + m_s + \Lambda_{an}) \Big(J_1(T, m_{\eta'}) + \frac{1}{16\pi^2} m_{\eta'}^2 ln \frac{m_{\eta'}^2}{m_{\eta'(vac)}^2} \Big) \,. \tag{11}$$

Here J_1 is defined from the general formula

$$J_n(T, m_\phi) = \frac{1}{2\pi^2} \int_0^\infty \frac{p^{2n} dp}{w_{p(\phi)}} \frac{1}{e^{\frac{w_{p(\phi)}}{T}} - 1} \,, \ n = 0, 1, 2 \,. \tag{12}$$

Thermodynamic approach

The results of the previous subsection can be reproduced from the condition of minimum of generating functional $\mathcal{F}(T, v, m_\sigma, \mathcal{M})$

$$\mathcal{F}(T, v, m_\sigma, \mathcal{M}) = \frac{1}{3} \langle T_i^i \rangle =$$

$$-\frac{1}{3} \Big(J_2(T, m_\sigma) + 3J_2(T, m_\pi) + J_2(T, m_\eta) + 4J_2(T, m_K) + J_2(T, m_{\eta'}) \Big) +$$

$$\frac{1}{64\pi^2} m_\sigma^4 ln \frac{m_\sigma^2}{\sqrt{e} m_{\sigma(vac)}^2} + \frac{3}{64\pi^2} m_\pi^4 ln \frac{m_\pi^2}{\sqrt{e} m_{\pi(vac)}^2} + \frac{1}{64\pi^2} m_\eta^4 ln \frac{m_\eta^2}{\sqrt{e} m_{\eta(vac)}^2} +$$

$$\frac{4}{64\pi^2} m_K^4 ln \frac{m_K^2}{\sqrt{e} m_{K(vac)}^2} + \frac{1}{64\pi^2} m_{\eta'}^4 ln \frac{m_{\eta'}^2}{\sqrt{e} m_{\eta'(vac)}^2} -$$

$$\frac{m_\sigma^2}{2g^2} (\mathcal{M}^2 - v^2) - 2v_0^2 \mathcal{M}^2 + v^4 + 6v^2(\mathcal{M}^2 - v^2) + 3(\mathcal{M}^2 - v^2)^2 \,, \tag{13}$$

which depends on the order parameter and meson masses.

Minimisation over $v, m_\sigma, \mathcal{M}$ leads to the equations for masses (9), (10) (and other mesons) and condensate (11), obtained previously from microscopic quantum-field approach, which means the coincidence of the model.

Analysis of the model predictions

Phase transition and condensate dynamics

Analysis of the form of free energy $\mathcal{F}(T, v) \equiv \mathcal{F}\Big(T, v, m_\sigma(T, v), \mathcal{M}(T, v)\Big)$ as a function of order parameter v, for different temperatures provides information about phase structure of meson gas. One can see first-order phase transition near the temperature $T_c \sim 400 MeV$.

Also temperature dependence of the condensate can be investigated from the analysis of the minima of free energy. The results of calculations are shown on the Fig.1 a). An interesting effect is incomplete melting of QCD condensate for $T > T_c$.
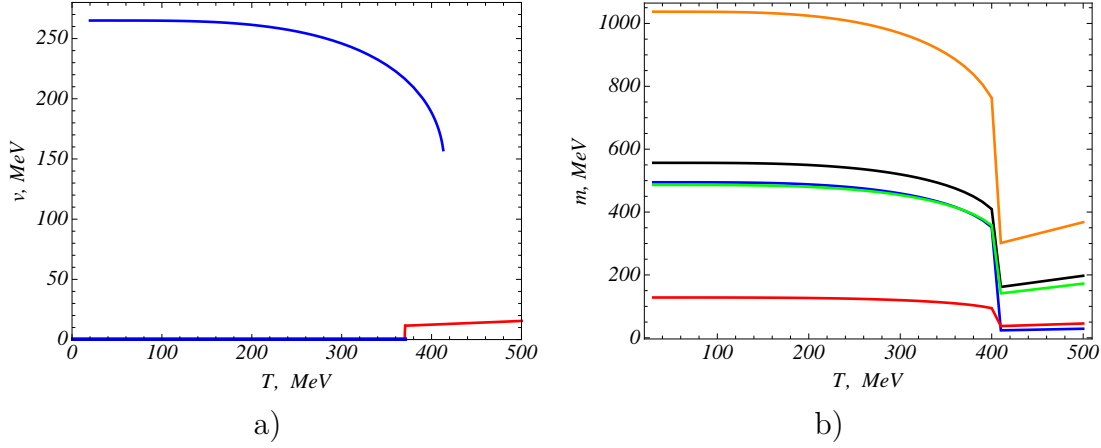
Figure 1: a) - Temperature dependence of condensate amplitude $v(T)$, b) - temperature evolution of the masses (from the top) of η', η, σ, K, π.

Meson masses

From (11) and (9), (10) the dependence of meson masses of temperature can be defined - this temperature dependence is the result of the change of the properties of QCD vacuum. On the Fig.1 b) temperature evolution of the masses is shown. Masses decrease and above T_c $m_\sigma < 2m_\pi$. It means the stabilisation of sigma meson (channels $\sigma \to \pi^0 \pi^0$ and $\sigma \to \pi^+ \pi^-$ are closed) in high temperature region, which is a rather interesting effect.

Other thermodynamic quantities

Temperature dependence of other thermodynamic quantities also can be investigated. In particular, in low energy phase entropy density is described by the next expression

$$\mathcal{S}_{low}(T) = -\frac{\partial \mathcal{F}(T, v(T))}{\partial T} = \frac{1}{T}\Big(m_\sigma^2 J_1(T, m_\sigma) + 3m_\pi^2 J_1(T, m_\pi) + m_\eta^2 J_1(T, m_\eta) +$$

$$4m_K^2 J_1(T, m_K) + m_{\eta'}^2 J_1(T, m_{\eta'}) + \frac{4}{3}\Big(J_2(T, m_\sigma) + 3J_2(T, m_\pi) +$$

$$J_2(T, m_\eta) + 4J_2(T, m_K) + J_2(T, m_{\eta'})\Big)\Big). \tag{14}$$

Also speed of sound, energy density, pressure and capacity were calculated.

We have constructed a model of meson gas with non-linear sigma field, giving contribution to gluon condensate. It allows to reconstruct vacuum properties of mesons as well as their properties for non-zero temperature. The existence of first order phase transition is shown. It is shown that QCD condensate doesn't melt in high temperature region and also the stabilisation of sigma-meson was obtained.

References

[1] E. V. Shuryak, World Sci. Lect. Notes Phys. 71 (2004) 1 [World Sci. Lect. Notes Phys. 8 (1988) 1].

GLUONIC COMPONENT OF ULTRARELATIVISTIC PSEUDOSCALAR FLAVOR-SINGLET MESON

A. V. Rusov [*]

P. G. Demidov Yaroslavl State University, Yaroslavl, Russia

Annotation

There are the pseudoscalar η- and η'-mesons which contain the flavor-singlet on the $SU(3)_F$-group component in addition to the octet one. Both quark and gluonic content contribute to the flavor-singlet part. Non-local interpolating currents are introduced for the gluonic component of these mesons. In the assumption that the mesons are energetic particles, the internal quark or gluon fields entering interpolating currents are situated near the light cone determined by the meson four-momentum and the fields' separation. The existing conformal symmetry of the currents allows to make a twist decomposition of the interpolating currents. The asymptotic forms of selected quark and gluonic LCDAs parameterizing the matrix elements of definite-twist currents are presented.

Introduction

Hadrons are bound states of quarks, antiquarks and gluons. Hadrons are divided into two large groups: mesons — particles with the integer total angular momentum J and baryons which have the half-integer J. Ordinary mesons consist of quarks and antiquarks which are fermions with the spin $s = 1/2$. Each meson is characterized by its spin-parity J^P, where $\vec{J} = \vec{L} + \vec{S}$ is the total angular momentum and $P = (-1)^{L+1}$ is the meson parity which depends on the angular momentum only. So, the ordinary meson with the lowest angular momentum $L = 0$ can be either a pseudoscalar $J^P = 0^-$ or vector $J^P = 1^-$ particle while the similar meson in the state with the first angular excitation $L = 1$ has the positive parity and can be scalar $J^P = 0^+$, axial-vector $J^P = 1^+$, or tensor $J^P = 2^+$ particle after the quantum angular-momentum summation rule is taken into account. For true neutral mesons one can also introduce the additional quantum number called the charged parity $C = (-1)^{L+S}$ which contains an information about the total spin of the bound state. According to this classification the experimentally observed η- and η'-mesons are particles with $J^{PC} = 1^{-+}$ (the true neutral pseudoscalar mesons) which are discussed in this paper.

Let us concentrate on the light quarks u, d, and s. They are satisfying the approximate global flavor $SU(3)_F$ symmetry which is broken due to the difference in quark masses [1]. As the result, mesons constructed from these quarks differs also by their masses and, as a consequence, by their properties. Nevertheless, such a symmetry allows to combine mesons with the same spin-parity into symmetry multiplets. Low-lying pseudoscalar mesons belong either the octet or singlet representation of the $SU(3)_F$ group. As the symmetry is approximate, mesons from different representations can mix, in particular, the η_8- and η_0-states are unobservable but their superpositions

$$\eta = \eta_8 \cos\theta_p - \eta_0 \sin\theta_p, \qquad \eta' = \eta_8 \sin\theta_p + \eta_0 \cos\theta_p, \tag{1}$$

[*]alex.rusov@bk.ru

are the physical mesons. Here, θ_p is the octet-singlet mixing angle and the phenomenological analysis results the interval $\theta_p \in [-20°, -10°]$ [1]. It is also possible to construct a true neutral pseudoscalar ($J^{PC} = 0^{-+}$) state η_G from two gluons which can mix with the flavor-octet η_8 and flavor-singlet η_0. So, one can expect an admixture of the two-gluon state in the physical η- and η'-mesons. Experimentally, the gluonic component in the η-meson seems to be strongly suppressed [1] and can be neglected in further analysis. In a difference, the gluonic component in the η'-meson is not so small which confirms, for example, by the enlarge of its mass in comparison with the η-meson mass [1]. In this approach, the 3-state mixing matrix is characterized by two mixing angles θ_p and ϕ_G [2]. Phenomenological analysis based on radiative decays of light pseudoscalar $P \to V\gamma$ and vector $V \to P\gamma$ mesons results the interval $\phi_G = (12 \pm 13)°$ [3]. According this analysis, unmixing of gluonic and quark states is still possible but the admixure of gluonic component in the η'-meson more preferable and should be considered systematically.

Interpolating Currents

To describe a meson in quantum field theory, one needs to determine a set of interpolating currents with quantum numbers of the meson considered. Their matrix elements between the meson and vacuum states are non-vanishing. For the pseudoscalar meson, there are two local interpolating currents [4]:

$$J_{5\mu}(x) = \bar{q}_2(x)\gamma_\mu\gamma_5 q_1(x), \quad J_5(x) = \bar{q}_2(x)\gamma_5 q_1(x), \tag{2}$$

where $q_{1,2}(x)$ are light quark fields. There is the operator relation between the axial-vector current $J_{5\mu}(x)$ and the pseudoscalar meson field $\varphi(x)$

$$\bar{q}_2(x)\gamma_\mu\gamma_5 q_1(x) = -f_M \partial_\mu \varphi(x) \tag{3}$$

where f_M is the leptonic decay constant of the meson M with the four-momentum p_M^μ. The corresponding matrix element at the origin ($x^\mu = 0$) is as follows [4]:

$$< 0 \mid \bar{q}_2(0)\gamma^\mu\gamma_5 q_1(0) \mid M(p_M) >= i f_M p_M^\mu. \tag{4}$$

An internal dynamics of the meson shows itself in study of non-local interpolating currents, in particular, the non-local axial-vector current can be written in the form [4]:

$$J_{5\mu}(x_2, x_1) = \bar{q}_2(x_2)\gamma_\mu\gamma_5 [x_2, x_1] q_1(x_1), \tag{5}$$

where $[x_2, x_1]$ is the path-ordered exponential which ensures the gauge invariance of the operator. In the Fock-Schwinger gauge of gluonic fields, which is assumed further in this paper, this exponential becomes trivial ($[x_2, x_1] = 1$) and disappears from the currents.

Before the analysis of the $\eta^{(\prime)}$-meson can be done, it is convenient to work out the procedure on a more simple particle, say, on the π^--meson which consists of the u-antiquark and d-quark. The matrix element of the non-local axial-vector interpolating current $J_{5\mu}(x_2, x_1)$ between the states of the fast-moving π^--meson and vacuum can be written as follows [4]:

$$< 0 \mid \bar{u}(z)\gamma_\mu\gamma_5 d(-z) \mid \pi^-(p_\pi) >= i f_\pi p_\mu \int_0^1 du \, e^{i\xi(pz)}\phi_\pi(u) + i f_\pi \frac{m_\pi^2 z_\mu}{2(pz)} \int_0^1 du \, e^{i\xi(pz)}g_\pi(u), \tag{6}$$

where u is the quark energy measured in units of the π^--meson energy and $\xi = 2u - 1$. In the frame where the meson is an ultrarelativistic particle, the quarks can be assumed to be massless particles which are situated on the light cone. So, their positions are determined in terms of the light-like vector z_μ ($z^2 = 0$) and the origin of the frame is chosen to be the center-of-mass point of the quark system. To specify the light-cone plane, it is necessary to introduce another vector p^μ which can be also determined as a light-like vector ($p^2 = 0$):

$$p^\mu = p_\pi^\mu - \frac{m_\pi^2 z^\mu}{2(p_\pi z)}, \tag{7}$$

where p_π^μ and m_π are the four-momentum and mass of the π-meson. Note the relations among the vectors: $(pz) = (p_\pi z)$ and $(p_\pi p) = m_\pi^2/2$. The functions $\phi_\pi(u)$ and $g_\pi(u)$ entering (5) are the Fourier transforms of the form factors $\Phi_\pi(pz)$ and $G_\pi(pz)$ and known as the Light-Cone Distribution Amplitudes (LCDAs). Two other LCDAs $\phi_\pi^p(u)$ and $\phi_\pi^\sigma(u)$ can be introduced to parametrize the matrix elements of pseudoscalar and pseudotensor currents, respectively [4].

The generalization on the η- and η'-mesons is rather easy and connected with the replacement of the decay constant f_π to the constants accompanying each term in the interpolation current as well as the $SU(3)_F$-corrections induced by the s-quark should be taken into account.

Consider gluonic interpolating currents of the flavor-singlet pseudoscalar meson. From the gluonic field-strength tensor $G_{\mu\nu}^a(x)$ and the dual one $\tilde{G}_{\mu\nu}^a(x)$ it is possible to produce the pseudoscalar and two pseudotensor of the 2nd and 4th rank gluonic currents from which the most complicated gluonic operator — the pseudotensor of the 4th rank — is not considered here. To avoid unnecessary complications originated due to the mixing of quark and gluonic components in the η'-meson which can be utilized further, we restrict ourselves on the pure gluonic state — the pseudoscalar glueball η_G. The transition matrix element of pseudoscalar gluonic current sandwiched between the fast-moving glueball state $|\eta_G(p_G) >$ and vacuum one $|0 >$ can be written in the form [5]:

$$< 0 \mid \frac{\alpha_{\text{st}}}{4\pi} G_{\mu\nu}^a(z)\tilde{G}^{a\mu\nu}(-z) \mid \eta_G(p_G) >= a_M \int_0^1 du\, e^{i\xi(pz)} \phi_{4M}^{(g)}(u), \tag{8}$$

where α_{st} is the strong coupling, p_G^μ is the glueball four-momentum, and z^μ and p^μ are light-like vectors. The constant a_M is determined in the local limit ($z^\mu \to 0$) through the QCD axial anomaly [6]:

$$a_M =< 0|\frac{\alpha_{\text{st}}}{4\pi} G_{\mu\nu}(0)\tilde{G}^{\mu\nu}(0)|\eta_G(p_G) >, \tag{9}$$

and the gluonic LCDA $\phi_{4M}^{(g)}(u)$ is the dimensionless function normalized to unity. As for the second rank pseudotensor gluonic current, one should subtracted first all the traces and the resulting transition matrix element can be decomposed into three independent Lorentz structures as follows:

$$< 0|G_{\mu\rho}(z)\tilde{G}_\nu^\rho(-z) - \frac{g_{\mu\nu}}{4} G_{\rho\sigma}(z)\tilde{G}^{\rho\sigma}(-z)|\eta_G(p_G) >= \tag{10}$$

$$= p_\mu p_\nu\, \Phi_2^{(g)}(pz) + \left(p_\mu z_\nu + p_\nu z_\mu - \frac{(pz)}{2}\, g_{\mu\nu}\right) \Phi_4^{(g)}(pz) + z_\mu z_\nu \Phi_6^{(g)}(pz).$$

Three form factors $\Phi_t^{(g)}(pz)$, where $t = 2, 4, 6$, can be Fourier-transformed into the gluonic LCDAs $\phi_t^{(g)}(u)$:

$$\Phi_t^{(g)}(pz) = F_t \int_0^1 du\, e^{i\xi(pz)} \phi_t^{(g)}(u), \tag{11}$$

where F_t are dimensional constants which can be expressed through the leptonic decay constant f_M of the meson. Vanishing of this operator in the local limit puts the condition $\Phi_t^{(g)}(0) = 0$ on the form factors and, as the consequence, makes the corresponding LCDAs to be antisymmetric functions: $\phi_t^{(g)}(-u) = -\phi_t^{(g)}(u)$.

Asymptotics of LCDAs

There is a symmetry based on the collinear conformal group [7] to which the quantum fields situated on the light cone are satisfied. So, it is possible to decompose each quantum field on components with the definite twist $t = \ell - s$, where ℓ and s are the canonical dimension (in units of a mass) of the field and its spin projection on the field momentum [7]. The expansion of these operators near the origin is an infinite series of conformal operators of increasing conformal spins (the conformal tower) starting from the lowest one $j_{\min} = (\ell + s)/2$ [7]. In particular, the quark field $q(z)$ with $\ell = 3/2$ is a sum of two components $q_+(z)$ and $q_-(z)$ with the spin projections $s = \pm 1/2$ and twists $t = 1$ and $t = 2$, respectively. The corresponding conformal towers are started from the operators with $j_{\min} = 1$ and $j_{\min} = 1/2$. For the composite operators constructed from such fields, the operator twist is the additive quantum number and the leading conformal operator is assumed to have a lowest twist. Note that conformal operators are mixing under the operator renormalization but their expansion in local operators is completely determined by the collinear conformal group [7]. As the examples, the twist expansion of the quark pseudoscalar and axial-vector interpolating currents are as follows:

$$J_5^{(q)}(z, -z) \equiv \bar{q}(z)\gamma_5 q(-z) = \bar{q}_+(z)\gamma_5 q_-(-z) + \bar{q}_-(z)\gamma_5 q_+(-z), \tag{12}$$

$$J_5^{(q)\mu}(z, -z) \equiv \bar{q}(z)\gamma^\mu \gamma_5 q(-z) = \bar{q}_+(z)\gamma_+ \gamma_5 q_+(-z) n_-^\mu + \tag{13}$$
$$+ \bar{q}_+(z)\gamma_\perp^\mu \gamma_5 q_-(-z) + \bar{q}_-(z)\gamma_\perp^\mu \gamma_5 q_+(-z) + \bar{q}_-(z)\gamma_- \gamma_5 q_-(-z) n_+^\mu.$$

In a similar way, one can perform the twist expansion of the pseudoscalar gluonic current:

$$J^{(g)} \equiv G_{\mu\nu}^a(z)\tilde{G}^{a\mu\nu}(-z) = -2\varepsilon_{\perp\rho\sigma} G_{+-} G_{\perp\perp}^{\rho\sigma} - 2\varepsilon_{\perp\rho\sigma} \left[G_{+\perp}^\rho G_{-\perp}^\sigma - G_{-\perp}^\sigma G_{+\perp}^\rho \right]. \tag{14}$$

It is possible to realize a similar twist expansion for the pseudotensor current:

$$J_{\mu\nu}^{(g)}(z) \equiv G_{\mu\rho}(z)\tilde{G}_\nu^\rho(-z) - \frac{g_{\mu\nu}}{4} G_{\rho\sigma}(z)\tilde{G}^{\rho\sigma}(-z), \tag{15}$$

and the result will be presented elsewhere [8].

Sandwiching the composite operator with the definite twist between the meson state and the vacuum one, one obtains the corresponding LCDA of the same twist. It can be written as an expansion in terms of characteristic polynomials produced by the corresponding representation of the collinear conformal group [7]. Coefficients of this expansion are scale-dependent quantities and vanishing in the asymptotic limit of large momenta $\mu \to \infty$.

As a result, the scale-independent term only is left in this limit and its explicit form is determined by lowest conformal spins j_k of internal fields in the composite operator. In particular, the asymptotics of two-particle distribution amplitudes have a simple form [4]. In the the case of the operator produced by two fields, the general form of the asymptotic distribution amplitude has the form:

$$\phi^{\mathrm{as}}(u_1, u_2) = \frac{\Gamma(2j_1 + 2j_2)}{\Gamma(2j_1)\Gamma(2j_2)}\, u^{2j_1-1}\,(1-u)^{2j_2-1}\,, \tag{16}$$

where u is the reduced energy of the field with conformal spin j_1. So, the asymptotic forms of the quark-antiquark light-cone distribution amplitudes of the pseudoscalar meson are as follows [4]:

$$\phi_\pi^{\mathrm{as}}(u) = \phi_\sigma^{\mathrm{as}}(u) = 6u(1-u), \quad \phi_p^{\mathrm{as}}(u) = g_\pi^{\mathrm{as}}(u) = 1, \tag{17}$$

where u is the reduced energy of the quark in the meson, while similar asymptotics of LCDAs corresponding to the pseudoscalar gluonic current have the forms:

$$\phi_{1,1}^{(g),\mathrm{as}}(u) = 6u\,(1-u)\,, \qquad \phi_{3/2,1/2}^{(g),\mathrm{as}}(u) = 3u^2, \qquad \phi_{1/2,3/2}^{(g),\mathrm{as}}(u) = 3\,(1-u)^2\,, \tag{18}$$

where u is the reduced energy of the gluon. The asymptotic form of other gluonic operators is also obtain and will be presented elsewhere [8].

It is desirable to know the scale dependence of LCDAs but, at present, it is under consideration. This analysis is not simple as the operators are mixing under renormalization. For the leading twist-2 quark and gluonic operators, the mixing problem appeared to be an analytically solvable but twist-3 mixing for the flavor-singlet mesons still remains to be analyzed.

Conclusions

In this paper the flavor-singlet pseudoscalar mesons are considered, of which the η- and η'-mesons are the representatives. Both quark and gluonic components are taken into account and the corresponding non-local interpolating currents are presented. In the assumption that the mesons are energetic particles, the internal quark or gluon fields entering interpolating currents are situated near the light cone determined by the meson four-momentum and the fields' separation. The existing conformal symmetry of the currents allows to realize the twist decomposition of the interpolating currents. Matrix element of each current of the definite twist sandwiched between the meson state and the vacuum one can be parametrized by the LCDA. The asymptotic forms of selected quark and gluonic LCDAs are presented.

References

[1] K. Olive *et al.* Chin. Phys. C 38 (2014) 090001.

[2] H.-Y. Cheng, H.-n. Li, and K.-F. Liu, Phys. Rev. D 79 (2009) 014024.

[3] R. Escribano and J. Nadal, JHEP 05 (2007) 006.

[4] P. Ball, JHEP 01 (1999) 010.

[5] S. S. Agaev *et al.*, Phys. Rev. D 90 (2014) 074019.

[6] M. E. Peskin and D. V. Schroeder, *An Introduction to Quantum Field Theory*, New York: Addison-Wesley, 1995. 865 p.

[7] V. M. Braun, G. P. Korchemsky, and D. Mueller, Prog. Part. Nucl. Phys. 51 (2003) 311.

[8] A. Ya. Parkhomenko and A. A. Rusov, in preparation.

CRITICAL BEHAVIOR OF DIRECT PERCOLATION PROCESS IN THE PRESENCE OF COMPRESSIBLE VELOCITY FIELD

J. Honkonen[1], T. Lučivjanský[2,3], V. Škultéty [4,5]

[1]*Department of Military Technology, National Defence University, Helsinki, Finland*

[2] *Fakultät für Physik, Universität Duisburg-Essen, Duisburg, Germany*

[3] *Faculty of Sciences, P.J. Šafárik University, Košice, Slovakia*

[4] *Department of Physics, Stockholm University, AlbaNova University Centre, Stockholm, Sweden*

[5] *Department of Physics, University of Helsinki, University of Helsinki, Finland*

Annotation

The renormalization group analysis is a useful tool for studying critical behavior of stochastic systems. In this work, the field theoretic renormalization group has been applied to a scalar model representing directed bond percolation, known as the Gribov process, in the presence of the random velocity field. Turbulent mixing has been modeled by a compressible form of the stochastic Navier-Stokes equation. A new universality class and corresponding critical exponents have been found.

Introduction

Various systems exhibit universal behavior at the critical point. A typical example of the non-equilibrium critical behavior is the direct bond percolation (DP) that exhibits an active-to-absorbing state phase transition in the vicinity of critical percolation probability p_c [1,2]. An interesting question is how the turbulent mixing influences its critical behavior. In this work we assume that the turbulent mixing is generated by the compressible Navier-Stokes (cNS) equation where the compressibility is described by an additional field related to the density.

Classical formulation of the problem

The classical stochastic description of DP is given by the Langevin equation [1]

$$\partial_t \psi = D_0 \left[\left(-\tau_0 + \partial^2 \right) \psi + \lambda_0 \psi^2 / 2 \right] + \zeta, \tag{1}$$

where $\partial_t = \partial/\partial t$, ∂^2 is the Laplace operator, D_0 is the diffusion constant, λ_0 is the coupling constant, $\psi = \psi(t, \boldsymbol{x})$ represents the coarse grained field, $\tau_0 = (p - p_c)$ is the (unrenormalized) deviation from the criticality and ζ is the Gaussian random noise with the correlator

$$\langle \zeta(t, \boldsymbol{x}) \zeta(t', \boldsymbol{x}') \rangle = D_0 \lambda_0 \psi(t, \boldsymbol{x}) \delta(t - t') \delta^d(\boldsymbol{x} - \boldsymbol{x}'). \tag{2}$$

The factor ψ in the correlator guarantees that the fluctuations cease to exist in the absorbing state. The subscript "0" here and henceforth denotes the bare (unrenormalized) parameters. Scaling exponents that describe dynamic observables are customarily defined through the relations [1]

$$P(t) \propto t^\delta, \quad N(t) \propto t^\Theta, \quad R^2(t) \propto t^z, \tag{3}$$

where $\propto$ stands for the asymptotic equality [2]. Turbulent fluctuations are governed by cNS equation augmented by the continuity equation [3]

$$\rho \nabla_t v_i = \nu_0 [\delta_{ij} - \partial_i \partial_j] v_k + \mu_0 \partial_i \partial_k v_k - \partial_i p + \eta_i, \quad \partial_t \rho + \partial_i (\rho v_i) = 0, \tag{4}$$

where v_i, p and ρ are the velocity, pressure, and density fields, μ_0 and ν_0 are two independent viscosities and $\nabla_t = \partial_t + v_i \partial_i$ is the Lagrangian derivative. The noise η obeys the Gaussian distribution law with following properties

$$\langle \eta_i(t, \boldsymbol{x}) \rangle = 0, \quad \langle \eta_i(t, \boldsymbol{x}) \eta_j(t', \boldsymbol{x}') \rangle = \delta(t - t') \int_{k > m} \frac{\mathrm{d}^d \boldsymbol{k}}{(2\pi)^d} \mathcal{D}_{ij}^f(\boldsymbol{k}) \mathrm{e}^{i(\boldsymbol{x} - \boldsymbol{x}') \cdot \boldsymbol{k}}, \tag{5}$$

where $m = L^{-1}$ is the reciprocal of the integral turbulence scale L which provides infrared (IR) regularization, with the correlator $\mathcal{D}_{ij}^f(\boldsymbol{k})$, which will be specified later. In order to get a closed system of equations one can proceed as follows [4]. Using the equation of state $(p - \overline{p}) = c_0^2 (\rho - \overline{\rho})$ linearized near mean values $\overline{p}$ and $\overline{\rho}$, where c_0 is the speed of sound, and introducing a new field $\phi = c_0^2 \ln(\rho/\overline{\rho})$ we can rewrite equations (4) into

$$\nabla_t v_i = \nu_0 [\delta_{ij} - \partial_i \partial_j] v_k + \mu_0 \partial_i \partial_k v_k - \partial_i \phi + \eta, \quad \nabla_t \phi = -c_0^2 \partial_i v_i, \tag{6}$$

where we have divided cNS equation by the density ρ and rescaled viscosities by the mean value $\overline{\rho}$.

Field theoretical formulation of the problem

The s tochastic model (1) is completely equivalent to field theoretic model [5] with double number of fields $\varphi = \{\psi, \psi'\}$ described by the Dominicis-Janssen action

$$\mathcal{J}_{\mathrm{per}} = -\psi'[\partial_t - D_0 \partial^2 + D_0 \tau_0]\psi + D_0 \lambda_0 [\psi' - \psi]\psi' \psi / 2, \tag{7}$$

where the integration over all variables has been implied and prime field ψ' stands for the Martin-Siggia-Rose response field [6]. The field theoretical formulation implies that the statistical averages and random quantities can be computed as a functional integral over the full set of fields with weight $\exp \mathcal{J}_{\mathrm{per}}$, i.e. $\langle \ldots \rangle = \int \mathcal{D}[\psi', \psi] \ldots \exp(\mathcal{J}_{\mathrm{per}})$. In order to include velocity fluctuations, we replace the temporal derivative with the covariant derivative for the compressible fluid [7]

$$\partial_t \psi \rightarrow \partial_t \psi + a_0 \partial_i (v_i \psi) + (1 - a_0)(v_i \partial_i)\psi = \nabla_t \psi + a_0 (\partial_i v_i)\psi. \tag{8}$$

For the linear advection diffusion system without interactions, the physical values of a_0 equal either 1 (conservation of ψ - density of an impurity) or 0 (conservation of ψ' - concentration of the impurity). Due to the nonlinearities in the DP, none of the fields ψ and ψ' can be regarded as conserved. A field theoretic formulation of the model (6) is

$$\mathcal{J}_{\mathrm{NS}} = \frac{1}{2} v_i' D_{ik}^f v_k' + v_i' \{ -\nabla_t v_i + \nu_0 [\delta_{ik} \partial^2 - \partial_i \partial_k] v_k + u_0 \nu_0 \partial_i \partial_k v_k - \partial_i \phi \} + \tag{9}$$

$$+ \phi'[-\nabla_t \phi + v_0 \nu_0 \partial^2 \phi - c_0^2 (\partial_i v_i)], \tag{10}$$

88

where we have introduced $u_0 = \mu_0/\nu_0$ for dimensional reasons and added a new term $v_0\nu_0\partial^2\phi$ to ensure multiplicative renormalizability [4]. The correlator $D_{ij}^f(\boldsymbol{k})$ is defined as follows [8]

$$\mathcal{D}_{ij}^f(\boldsymbol{k}) = g_{10}\nu_0^3 k^{4-d-y}\big\{P_{ij}(k) + \alpha Q_{ij}(k)\big\} + g_{20}\nu_0^3\delta_{ij}, \tag{11}$$

where $P_{ij} = \delta_{ij} - \partial_i\partial_j/\partial^2$ and $Q_{ij} = \partial_i\partial_j/\partial^2$ are projection operators, $\alpha > 0$ is an arbitrary parameter determining the structure of the random force and $0 < y \leq 4$ plays the role of the RG expansion parameter, analogous to that played by $\varepsilon = 4 - d$ in the theory of the critical phenomena. Its physical value is 4 when $\mathcal{D}^f(\boldsymbol{k}) \propto \delta(\boldsymbol{k})$. It corresponds to the energy injection from largest eddies [5]. Parameters g_{10}, g_{20} are coupling constants, where the appearance of the latter one will be explained later.

The influence of compressible turbulent mixing on percolation is thus described by the total action functional $\mathcal{J} = \mathcal{J}_{\mathrm{NS}} + \mathcal{J}_{\mathrm{per}} + \mathcal{J}_{\mathrm{adv}}$, where $\mathcal{J}_{\mathrm{adv}} = -\psi'\left[v_i\partial_i + a_0(\partial_iv_i)\right]\psi$ is a new term that arises from (8).

Renormalization, Infrared stability, Critical exponents

The analysis of UV divergences is based on the analysis of canonical dimensions [9]. For power counting in dynamical models such as (7) and (9) it is convenient to introduce the total canonical dimension $d_F = d_F^k + 2d_F^\omega$ with the normalization conditions

$$d_k^k = -d_{\boldsymbol{x}}^k = 1, \quad d_k^\omega = d_{\boldsymbol{x}}^\omega = 0, \quad d_\omega^k = d_t^k = 0, \quad d_\omega^\omega = -d_t^\omega = 1. \tag{12}$$

Canonical dimensions for models (7) and (9) are given in tables 1 and 2. It is seen that our models becomes logarithmic (all the coupling constants are simultaneously dimensionless) at $\varepsilon = 4 - d = 0$ and $y = 0$. The total canonical dimension of an arbitrary 1-irreducubile Green function $\Gamma = \langle\Phi\ldots\Phi\rangle_{1\text{-ir}}$ is given by relation [5] $d_\Gamma = d + 2 - \sum_\Phi N_\Phi d_\Phi$ where Φ stands for the set of all fields. The total dimension d_Γ in logarithmic theory is the formal index of the UV divergence $\delta_\Gamma = d_\Gamma|_{\varepsilon=y=0}$. Renormalization of model (7) has been carried out in [7] near $d = 4$ and (9) in [4] near $d = 3$. In order to have a consistent theory, we have to renormalize both models near dimension four. At $d = 4$ however, an additional divergence in $\langle v'v'\rangle$ with $\delta_\Gamma = 0$ arises. This can be eliminated by the counterterm $v'v'$ (see (11)) [8]. We then conclude that the renormalized action can be written in the form

$$\mathcal{J}_R = \mathcal{J}_{\mathrm{velR}}(\varphi) + \mathcal{J}_{\mathrm{perR}} + \mathcal{J}_{\mathrm{advR}}, \tag{13}$$

$$\mathcal{J}_{\mathrm{velR}}(\varphi) = \frac{1}{2}v_i'D_{ik}^f v_k' + v_i'\big[-\nabla_t v_i + Z_1(\delta_{ik}\partial^2 - \partial_i\partial_k)v_k + Z_2 u\nu\partial_i\partial_k v_k - Z_4\partial_i\phi\big]$$
$$+ \phi'[-\nabla_t\phi + Z_3 v\nu\partial^2\phi - Z_5 c^2(\partial_i v_i)], \tag{14}$$

$$\mathcal{J}_{\mathrm{perR}} = -\psi'[Z_7\partial_t - Z_8 D\partial^2 + Z_9 D\tau]\psi + \frac{D\lambda}{2}[Z_{10}\psi' - Z_{11}\psi]\psi'\psi, \tag{15}$$

$$\mathcal{J}_{\mathrm{advR}} = -\psi'\left[Z_7 v_i\partial_i + Z_{12}a(\partial_i v_i)\right]\psi, \tag{16}$$

where the original models can be obtained by the multiplicative renormalization of the fields and parameters

$$e_0 = e\mu^{d_e}Z_e, \quad e_0 = \{g_{10}, g_{20}, g_{30}, u_0, \nu_0, v_0, c_0, D_0, \tau_0, w_0, a_0\}, \tag{17}$$

$$\varphi \to \varphi Z_\varphi, \quad \varphi = \{\boldsymbol{v}, \boldsymbol{v}', \phi, \phi', \psi, \psi'\}. \tag{18}$$

Table 1: Canonical dimensions of the bare fields and bare parameters for the model of velocity fluctuations

Q	$\boldsymbol{v}'$	$\boldsymbol{v}$	ϕ'	ϕ	m,μ,Λ	ν_0,ν	c_0,c	g_{10}	g_{20}	$u_0,v_0,u,v,g_1,g_2,\alpha,\beta$
d_Q^k	$d+1$	-1	$d+2$	-2	1	-2	-1	y	ε	0
d_Q^ω	-1	1	-2	2	0	1	1	0	0	0
d_Q	$d-1$	1	$d-2$	2	1	0	1	y	ε	0

Table 2: Canonical dimensions of the bare fields and bare parameters for the model of directed percolation process

Q	ψ'	ψ	λ_0	D_0	$g_{30}=\lambda_0^2$	$w_0=D_0/\nu_0$	a_0
d_Q^k	$d/2$	$d/2$	$\varepsilon/2$	-2	ε	0	0
d_Q^ω	0	0	0	1	0	0	0
d_Q	$d/2$	$d/2$	$\varepsilon/2$	0	ε	0	0

Asymptotic regimes [5] are determined by the asymptotic behavior of the flow equations $\beta_e = \mu\partial_\mu e$. The long time and large scale behavior is governed by IR stable points, which are defined as $\beta(g^*) = 0$, $g = \{g_1, g_2, g_3, u, v, a\}$ with positive real parts of eigenvalues of the matrix $\Omega_{ij} = \partial\beta_i/\partial g_j|_{g=g^*}$. This leads to the existence of the scaling behavior of green functions and the critical dimensions of quantity F is given by the relations [5]

$$\Delta_F = d_F^k + \Delta_\omega d_F^\omega + \gamma_F^*, \quad \Delta_\omega = 2 - \gamma_D^*, \tag{19}$$

where $\gamma_x \equiv \mu\partial_\mu Z_x$ is so-called anomalous dimension of a quantity x. Critical exponents can be then obtained via relations [1]

$$\delta = (d + \gamma_\psi + \gamma_{\psi'})/2\Delta_\omega, \quad \Theta = -(\gamma_\psi + \gamma_{\psi'})/\Delta_\omega, \quad z = 2/\Delta_\omega, \tag{20}$$

Conclusions

In this work we have construct model of DP process advected by turbulent flow governed by compressible Navier-Stokes equation. Dimensional analysis as well as multiplicative renormalizability has been discussed. Appearance of new universality class is expected. In contrast to [10] stability of new regime where the percolation is relevant for physical values of parameters ε, y is also expected.

References

[1] H. K. Janssen, U. C. Täuber, Ann. Phys. 315 (2004) 147.

[2] M. Henkel, H. Hinrichsen, S. Lübeck, *Non-Equilibrium Phase Transitions: Volume 1- Absorbing Phase Transition* (Springer, Dordrecht, 2008).

[3] L. D. Landau, E. M. Lifshitz, *Fluid mechanics* (Pergamon, 1980).

[4] N. V. Antonov, M. Yu. Nalimov, A. A. Udalov, Theor. Math. Phys. 110 (1997) 305.

[5] A. N. Vasil'ev, *The Field Theoretic Renormalization Group in Critical Behavior Theory and Stochastic Dynamics* (Chapman Hall/CRC, Boca Raton, FL, 2004).

[6] P.C. Martin, E.D. Siggia, H.A. Rose, Phys. Rev. A 8 (1973) 423.

[7] N. V. Antonov, A. S. Kapustin, J. Phys. A: Math. Theor. 43 (2010) 405001.

[8] J. Honkonen, M. Yu. Nalimov, Z. Phys. B 99 (1996) 297.

[9] J. Zinn-Justin, *Quantum Field Theory and Critical Phenomena* (Oxford University Press, Oxford, 1996).

[10] N. V. Antonov, A. S. Kapustin, A. V. Malyshev, Theor. Math. Phys. 169 (2011) 1470.

RELATIVISTIC $^3D_1$ PARTIAL-WAVE CONTRIBUTION TO THE THREE-NUCLEON SYSTEM

S. A. Yurev^{1,2*}, S. G. Bondarenko^1, V. V. Burov^1

^{1}*Joint Institute for Nuclear Research, Dubna, Russia*
^{2} *Far Eastern Federal University, Vladivostok, Russia*

Annotation

The three-nucleon system is investigated using the Faddeev equations within the Bethe-Salpeter approach. The relativistic nucleon-nucleon interaction is chosen in a separable form. Three partial-wave states - $^1S_0$,$^3S_1$ and $^3D_1$ - are taken into account. The Gauss quadrature method is used to calculate the integrals and find the triton binding energy by iterations.

Introduction

Three-body calculations in nuclear physics are of great interest used describing three-nucleon bound states (^3He, T), processes of elastic, inelastic and deep inelastic scattering the leptons off light nuclei and also the hadron-deuteron reactions (for example, $pd \rightarrow pd$, $pd \rightarrow ppn$). Investigation of the nuclei ^3He and T is also interesting because it allows us to investigate further (in addition to the case of the deuteron) evolution of the bound nucleon thereby contributing to the explanation of so-called *EMC*-effect. In quantum mechanics the Faddeev equations are commonly used to describe the three-particle systems. The main feature of Faddeev equations is that all particles interact through a pair potential.

However at the high momentum transfer relativistic effects should be taken into account. The Bethe-Salpeter (BS) [1] equation is one of the most consistent approaches to describe the NN interaction. In this formalism, one has to deal with a system of nontrivial integral equations for both the NN scattered states and the bound state – the deuteron. To solve a system of integral equations, it is convenient to use a separable *Ansatz* [2] for the interaction kernel in the BS equation. In this case, one can transform integral equations into a system of algebraic linear ones which is easy to solve. Parameters of the interaction kernel are found from an analysis of the phase shifts and inelasticity, low-energy parameters and deuteron properties (binding energy, moments, etc.).

The relativistic three-particle systems are described by the Faddeev equations within the BS approach - so called Bethe-Salpeter-Faddeev equations. All nucleons have equal masses and the scalar propagators instead of spinor ones are used for simplicity. The spin-isospin structure of the nucleons is taken into account by using the so-called recoupling-coefficient matrix. The work mainly follows the ideas of the article [3]. In the paper [4] only S partial-states were considered for the one-rank kernel. In this paper the relativistic $^3D_1$ partial-wave is added into formalism using the three-rank Graz-II kernel [5].

---

*yurev@jinr.ru

Three-particle case

The relativistic three-particle system can be described by the Bethe-Salpeter-Faddeev equations

$$
\begin{bmatrix} T^{(1)} \\ T^{(2)} \\ T^{(3)} \end{bmatrix} = \begin{bmatrix} T_1 \\ T_2 \\ T_3 \end{bmatrix} - \begin{bmatrix} 0 & T_1 G_1 & T_1 G_1 \\ T_2 G_2 & 0 & T_2 G_2 \\ T_3 G_3 & T_3 G_3 & 0 \end{bmatrix} \begin{bmatrix} T^{(1)} \\ T^{(2)} \\ T^{(3)} \end{bmatrix} \tag{1}
$$

where full matrix $T = \sum_{i=1}^{3} T^{(i)}$, and G_i is the two-particle (j and n) Green function (ijn is cyclic permutation of (1,2,3)):

$$
G_i(k_j, k_n) = 1/(k_j^2 - m_N^2 + i\epsilon)/(k_n^2 - m_N^2 + i\epsilon). \tag{2}
$$

For the system of equal-mass particles the Jacobi momenta can be written in the following form:

$$
p_i = \frac{1}{2}(k_j - k_n), \quad q_i = \frac{1}{3}K - k_i, \quad K = k_1 + k_2 + k_3. \tag{3}
$$

It is suitable to introduce the amplitude $\Psi^{(i)}(p_i, q_i; s)$ for the bound state of the three particles in the following form:

$$
\Psi^{(i)}(p_i, q_i; s) = \langle p_i, q_i | T^{(i)} | M_B \rangle \equiv \Psi_{LM}(p, q; s), \tag{4}
$$

where $M_B = \sqrt{s} = 3m_N - E_B$ is the mass of the bound state (triton) and $s = K^2$ is the total momentum squared. For the equal-mass case all $\Psi^{(i)}$ functions are equal to each other.

The total orbital angular momenta of the triton can be presented as $\boldsymbol{L} = \boldsymbol{l} + \boldsymbol{\lambda}$, where $\boldsymbol{l}$ is the angular momentum corresponding to nucleon pair with relative impulse $\boldsymbol{p}$ and $\boldsymbol{\lambda}$ is the angular momentum corresponding to relative impulse $\boldsymbol{q}$.

To separate the angular dependence the amplitude can be written in the following form:

$$
\Psi_{LM}(p, q; s) = \sum_{a\lambda} \Psi_{\lambda L}^{(a)}(p_0, |\mathbf{p}|, q_0, |\mathbf{q}|; s) \mathcal{Y}_{\lambda LM}^{(a)}(\hat{\mathbf{p}}, \hat{\mathbf{q}}), \tag{5}
$$

with the angular part

$$
\mathcal{Y}_{\lambda LM}^{(a)}(\hat{\mathbf{p}}, \hat{\mathbf{q}}) = \sum_{m\mu} C_{lm\lambda\mu}^{LM} Y_{lm}(\hat{\mathbf{p}}) Y_{\lambda\mu}(\hat{\mathbf{q}}), \tag{6}
$$

where the two-nucleon state with spin s, angular moment l and total momentum j ($a \equiv {}^{2s+1}l_j$) is introduced, C is the Clebsch-Gordan coefficients and Y is spherical harmonics.

If one consider two-nucleon separable interaction the amplitude $\Psi_{\lambda L}^{(a)}$ can be written as

$$
\Psi_{\lambda Li}^{(a)}(p_0, p, q_0, q; s) = \sum_{ij} g_i^{(a)}(p_0, p) \tau_{ij}^{(a)}(s) \Phi_{\lambda Lj}^{(a)}(q_0, q; s), \tag{7}
$$

where function $\Phi_{\lambda L i}^{(a)}$ satisfies the following integral equation:

$$\Phi_{\lambda L i}^{(a)}(q_0, q; s) = \frac{i}{4\pi^3} \sum_{a'\lambda'} \sum_{kj} \int_{-\infty}^{\infty} dq_0' \int_0^{\infty} q'^2 dq' \, Z_{\lambda\lambda'ik}^{(aa')}(q_0, q; q_0', q'; s)$$

$$\frac{\tau_{kj}^{(a')}[(\frac{2}{3}\sqrt{s} + q_0')^2 - q'^2]}{(\frac{1}{3}\sqrt{s} - q_0')^2 - q'^2 - m^2 + i\epsilon} \Phi_{\lambda'j}^{(a')}(q_0', q'; s), \tag{8}$$

with

$$Z_{\lambda\lambda'ik}^{(aa')}(q_0, q; q_0', q'; s) = C_{(aa')} \int d\cos\vartheta_{qq'} K_{\lambda\lambda'L}^{(aa')}(q, q', \cos\vartheta_{qq'})$$

$$\frac{g_i^{(a)}(-\frac{1}{2}q_0 - q_0', |\mathbf{q}/2 + \mathbf{q}'|)g_k^{(a')}(q_0 + \frac{1}{2}q_0', |\mathbf{q} + \mathbf{q}'/2|)}{(\frac{1}{3}\sqrt{s} + q_0 + q_0')^2 - (\mathbf{q} + \mathbf{q}')^2 - m_N^2 + i\epsilon} \tag{9}$$

and

$$[\tau^{-1}(s)]_{ij} = [\lambda^{-1}]_{ij} - \frac{i}{4\pi^3} \sum_{L=0,2} \int_{-\infty}^{\infty} dk_0 \int_0^{\infty} k^2 \, dk \, g_i^{(L)}(k_0, k) g_j^{(L')}(k_0, k) \, G(k_0, k; s). \tag{10}$$

which appears here from solution of two body problem, and

$$K_{\lambda\lambda'L}^{(aa')}(q, q', \cos\vartheta_{qq'}) = (4\pi)^{3/2} \frac{\sqrt{2\lambda + 1}}{2L + 1}$$

$$\sum_{mm'} C_{lm\lambda 0}^{Lm} C_{l'm'\lambda'm-m'}^{Lm} Y_{lm}^*(\vartheta, 0) Y_{l'm'}(\vartheta', 0) Y_{\lambda'm-m'}(\vartheta_{qq'}, 0) \tag{11}$$

where

$$\cos\vartheta = (\frac{q}{2} + q'\cos\vartheta_{qq'})/|\frac{\mathbf{q}}{2} + \mathbf{q}'|, \qquad \cos\vartheta' = (q + \frac{q'}{2}\cos\vartheta_{qq'})/|\mathbf{q} + \frac{\mathbf{q}'}{2}|$$

and

$$C_{(aa')} = \begin{bmatrix} \frac{1}{4} & -\frac{3}{4} & -\frac{3}{4} \\ -\frac{3}{4} & \frac{1}{4} & \frac{1}{4} \\ -\frac{3}{4} & \frac{1}{4} & \frac{1}{4} \end{bmatrix} \tag{12}$$

is the spin-isospin recoupling-coefficient matrix with $(a) =^1 S_0, ^3 S_1, ^3 D_1$.

The system of integral equations (8-11) has the number of singularities, however in the case of the bound three-particle system ($\sqrt{s} < 3m_N$) all this singularities do not cross the path of integration on q_0 and thus do not affect to the Wick-rotation procedure $q_0 \to iq_4$.

The system of Eqs. (8-11) after the Wick-rotation procedure is well analytically defined and can be solved by different numerical methods. One of them is discussed in the next section.

Solution and results

In order to solve the system of integral equations the iterations method is used. The mappings for the variable of integration on q $[0, \infty)$ and q_4 $(-\infty, \infty)$ to $[-1, 1]$ interval are introduced.

The binding energy of the three-nucleon system is satisfied the following condition (see details in [6]):

$$\lim_{n \to \infty} \frac{\Phi_n(s)}{\Phi_{n-1}(s)}\bigg|_{s=M_B^2} = 1 \tag{13}$$

where n is number of iteration.

In the paper the Graz-II kernels of interaction [5] with three probability ($p_D = 4, 5, 6\%$) of the $^3D_1$-state are used for calculations. Results are given in Table 1 both for nonrelativistic and relativistic cases and for S-states and $S + D$-states. The experimental value is 8.48 MeV.

Table 1: Three-nucleon binding energy calculated with Graz-II NN kernel

$p_D, \%$	Nonrelativistic		Relativistic	
	$^1S_0, ^3S_1$	$^1S_0, ^3S_1, ^3D_1$	$^1S_0, ^3S_1$	$^1S_0, ^3S_1, ^3D_1$
4	8.372	8.334	8.628	8.617
5	7.964	7.934	8.223	8.217
6	7.569	7.548	7.832	7.831

As it seen from the Table 1 kernels with different p_D can give results for binding energy both bigger and smaller the experimental value. The relativistic results are systematically higher then nonrelativistic ones to about 3%. Also the $^3D_1$ partial-state gives rather small contribution to the three-nucleon binding energy - about -0.5%.

Conclusions

In the paper three-body system is investigated by using Bethe-Salpeter-Faddeev equations. In the calculations the three-rank Graz-II potential is used. The BSF integral equations are solved by using iterations method. The binding energy of the triton and amplitudes of the $^1S_0$, $^3S_1$ and $^3D_1$ partial-wave states of the triton are found.

Is was shown that kernels with different p_D can give results for binding energy both bigger and smaller the experimental value. The relativistic results are systematically higher then nonrelativistic ones to about 3% and the $^3D_1$ partial-state gives rather small contribution to the three-nucleon binding energy - about -0.5%.

References

[1] E.E. Salpeter, H.A. Bethe, Phys. Rev. 84 (1951) 1232.

[2] S.G. Bondarenko, V.V. Burov, A.V. Molochkov, G.I. Smirnov, H. Toki, Prog. Part. Nucl. Phys. 48 (2002) 449.

[3] G. Rupp and J. A. Tjon, Phys. Rev. C 37 (1988) 1729.

[4] S. Bondarenko, V. Burov, S. Yurev, EPJ Web of Conferences 108 (2016) 02015.

[5] L. Mathelitsch, W. Plessas, W. Schweiger, Phys. Rev. C **26**, 65 (1982); G. Rupp, J.A. Tjon, Phys. Rev. C. 45 (1992) 2133.

[6] R. A. Malfliet and J. A. Tjon, Nucl. Phys. A 127 (1969) 161-168.

Particle Accelerators and Nuclear Reactors

STOCHASTIC COOLING SYSTEM AT NUCLOTRON

I. Gorelyshev, N. Shurkhno, A. Sidorin, G. Trubnikov
Joint Institute for Nuclear Research, Dubna, Russia

Annotation

Stochastic cooling system is one of the crucial elements for NICA accelerator-collider facility. The preparatory experimental work on longitudinal stochastic cooling is carried out at accelerator Nuclotron. Filter and time-of-flight stochastic cooling methods are chosen to be operating at Nuclotron. In this work the structure of the system is described. Given algorithms allow to make remote adjustment of system components features (e.g. filter frequency, delay line time) and to switch all devices to operational regime.

Introduction

NICA accelerator-collider complex is under construction in JINR [1]. One of the challenging technologies of the collider project is the stochastic cooling. It is required for beam accumulation and luminosity preservation. Stochastic cooling is developed in Russia for the first time and operational regimes differ from those used before in the world. So before the run of NICA a test channel was put into operation at Nuclotron.

General scheme

Stochastic cooling is a microwave broadband system with feedback via the beam. The working principle is the following: pickup electrodes detect noise from the beam, signal propagates through the system and applies on the kicker. For effective operation signal has to be properly amplified and delayed. If delay and amplification are correctly adjusted one has the reduction of betatron amplitudes in case of transverse cooling or momentum spread in case of longitudinal cooling. General scheme of Nuclotron stochastic cooling system is presented at the Figure 1. This system has bandwidth 2-4 GHz and 60W maximum output power. It consists of pickup with preamplifiers, notch filter, block of switches, variable delay and attenuation anddiagnostic devices to maintain different modes of operation, main amplifier and kicker.
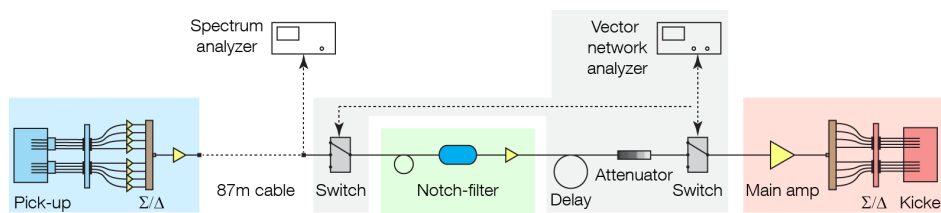
Figure 1: General scheme of Nuclotron.

Pickup and Kicker

Pickup and kicker are HESR type ring-slot couplers which were designed and constructed in FZ Jülich [2]. Pickup is installed in vacuum chamber and has 8 outputs from 8 azimuthal

positions around the beam (Fig. 2, left panel). Signals from outputs are amplified and can be combined into transverse horizontal, transverse vertical and longitudinal common signals (Fig. 2, right panel).
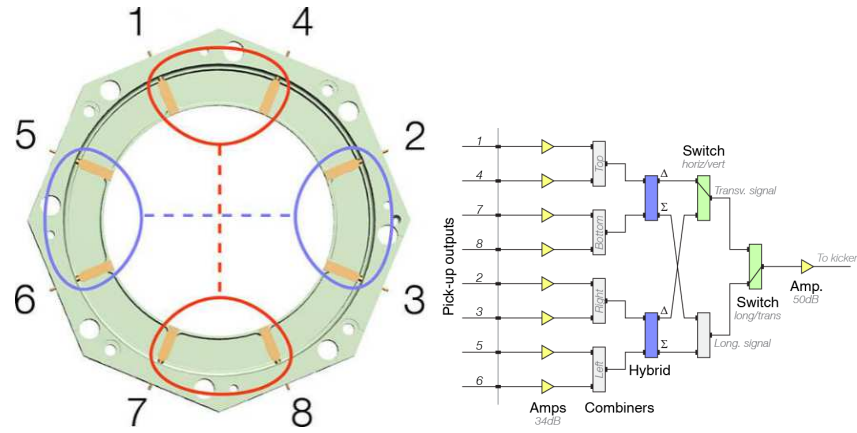
Figure 2: Left panel: Pickup transverse cross section. Right panel: commutation scheme.

Kicker is the same device as pickup. It has identical commutation scheme with no amplifiers. The difference is that common signal splits to 8 signals at kicker.

Notch Filter

Notch filter (Fig. 3) receives RF signal from pickup. The signal is modulated by infrared laser and is divided into two lines.
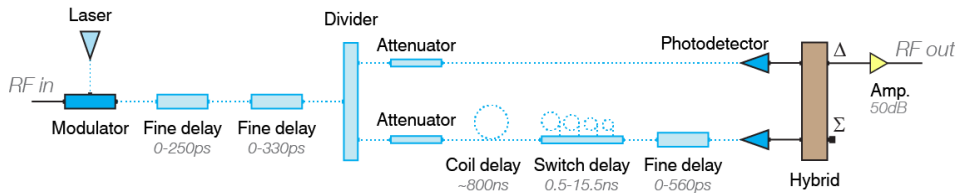
Figure 3: Scheme of optical notch filter.

Part of the signal from the short line passes directly to the output, another part from the long line passes through coil delay, switch delay and fine delay. Each line has photodetector demodulating optical signals to RF at its end. Signals from two lines are combined with 180° phase shift and outgoing signal is enlarged by 50 dB amplifier. To realize time-of-flight method the long line of the filter has to be switched off. Variable Delay and Attenuation These simple devices are manipulated by a set of switches. Each switch contacts either short line or modified (delay or attenuation) line (Fig. 4).
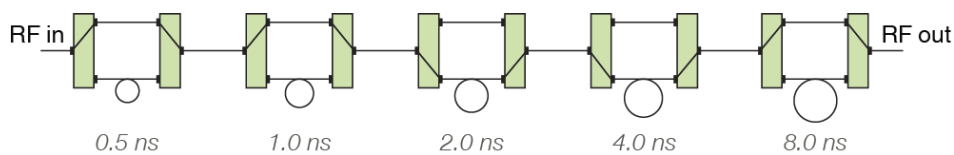
Figure 4: Scheme of variable delay.

Variable delay has 0.5, 1, 2, 4, 8 ns modified lines and range of manipulation 0-16 ns. Variable attenuation has 1, 2, 4, 8, 16, 24 dB lines and range of manipulation 0-55 dB.

Main Amplifier

For stochastic cooling system it is required to have approximately frequency independent amplitude and phase response. Amplitude and phase response of main 60W amplifier was measured andthe result is given on Fig.5. For bandwidth 2-4 GHz amplifier has excellent amplitude response, phase response is good enough, but has to be improved by phase equalizer.
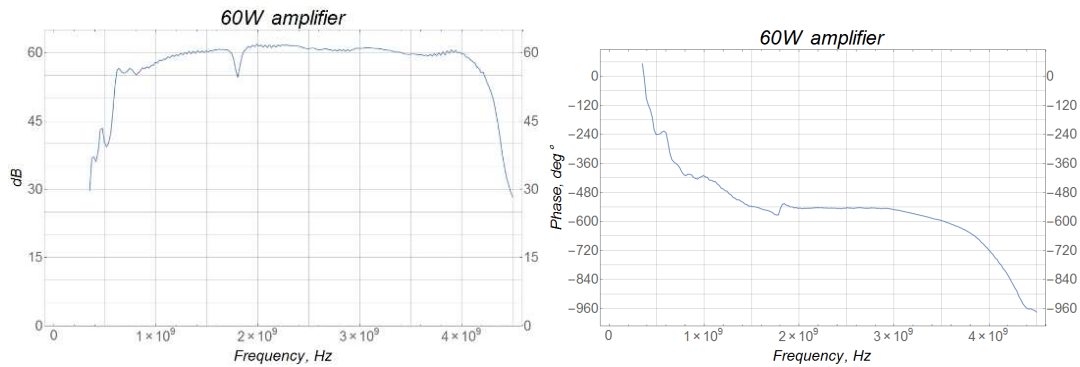
Figure 5: Left panel: amplitude. Right panel: phase response of main 60W amplifier.

Remote control and modes of operation

While system is in operation it needs to be quickly adjusted and remotely controlled. Thus application for remote control and automatic adjustment was developed (Fig. 6).
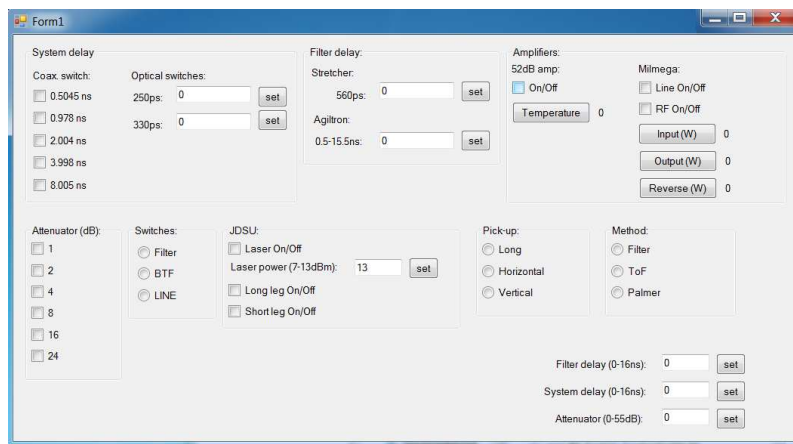
Figure 6: Interface window of the application for remote control and automatic adjustment.

Stochastic cooling system at Nuclotron has 3 modes of operation: filter adjustment, measurement of beam transfer function - BTF(system delay adjustment) and cooling. Commutation between these regimes is provided by block of switches (Fig. 7).
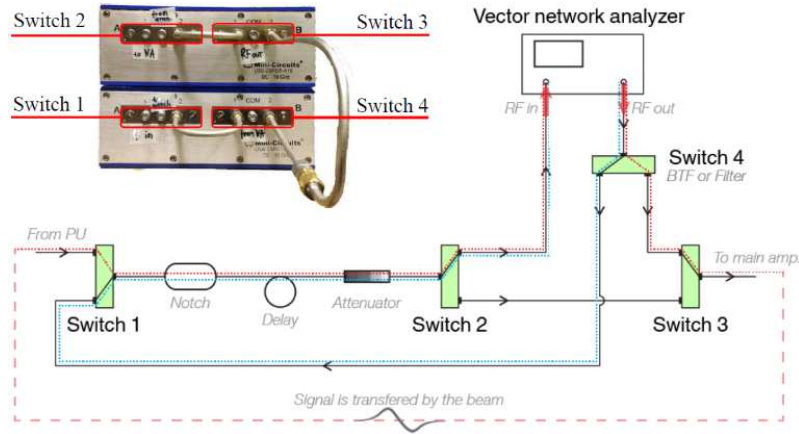
Figure 7: Operational regimes of stochastic cooling system at Nuclotron.

Adjustment in first two modes is supported by network analyzer measurements. In the first mode signal from network analyzer passes only through notch filter, variable delay and attenuation. In BTF mode the signal from the analyzer is transferred via the beam, and returns through the system. In the cooling regime the loop consisting of system components and the beam is closed.

Experimental results

Nuclotron stochastic cooling system was developed, assembled, adjusted and tested. The momentum cooling of bunched and coasting beam of D+ and C6+ was obtainedduring several runs at Nuclotron [3].As an example the momentum cooling of coasting deuteron beamis presented at the Fig. 8, left panel. The beam intensity was 2×10^9 and energy 3 GeV/u. The RMS momentum spread was reduced by approximately a factor of 2.2 within 480 s.This process of longitudinal cooling was also calculated by solving the Fokker-Planck equation [4].The simulation and experimental results are in reasonable agreement (Fig. 8, right panel).
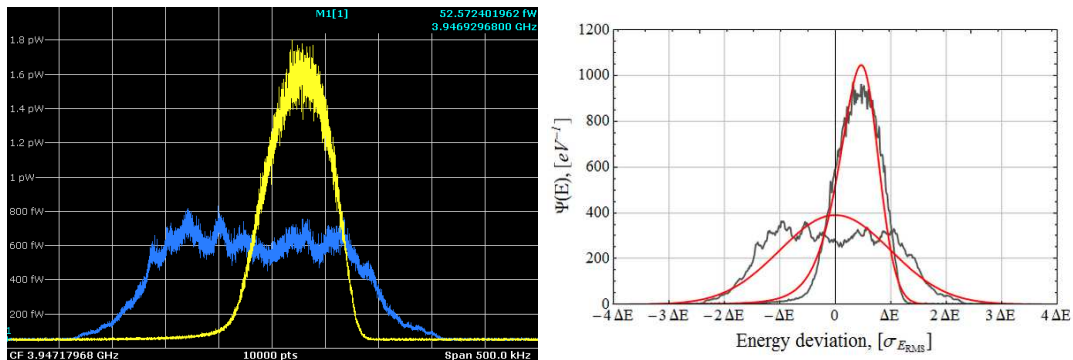
Figure 8: Reduction of beam energy spread: left panel: experimental result, right panel: comparison with simulation.

Conclusions

New developed scheme was set in operation. All system components proved to be reliable and effective. With the developed software for remote control and adjustments the system can be easily operated and adjusted. Nuclotron experiments provided the basis for developing a stochastic cooling system of NICA collider and showed appropriateness of HESR type kicker for NICA and FAIR.Based on experience with stochastic cooling at Nuclotron the CDR for the NICA stochastic cooling system had been worked out, development of the TDR is in progress.

References

[1] A. Sisakian *et al., XXIII Int. Symposium. on Lepton and Photon Interactions at High Energy, LP07, Daegu, Korea,* (2007).

[2] R. Stassen *et al., "The stochastic cooling system of HESR",* COOL'11, Alushta, Ukraine, September 2011, p.191.

[3] A. O. Sidorin, G. V. Trubnikov, N. A. Shurkhno, Phys. Usp. 59 (2016) 3.

[4] T. Katayama, N. Tokuda, Part. Accel. 21 (1987) 99.

DEVELOPMENT OF TOOLS FOR REAL-TIME BETATRON TUNE MEASUREMENTS AT THE NUCLOTRON

E. V. Gorbachev, A. E. Kirichenko, D. V. Monakhov*, S. V. Romanov, V. I. Volkov
Joint Institute for Nuclear Research, Dubna, Russia

Annotation

A betatron tune measurement system was developed and tested at the Nuclotron. A white noise and chirp signals were used for transverse beam motion excitation. A custom FlexRIO digitizer module was developed which provides excitation signal generation for kicker electrodes and real-time signal acquisition from pickup electrodes. A high resolution FFT algorithm was implemented inside a NI PXI FPGA module, connected to digitizer. The measurement system is integrated with the NICA control system based on the TANGO Controls. Results and tests performed with the Nuclotron beam are presented.

Introduction

One of the key parameters of the synchrotron accelerator is the betatron tune. It is defined by the arrangement and strength of the focusing and defocusing quadrupoles (FODO lattice) around the ring. The ideal particle will follow a particular trajectory, which closes on itself after one revolution - the closed orbit. The real particles perform oscillations around the ideal closed orbit. These transverse oscillations are called betatron oscillations, and they exist in both horizontal (X) and vertical (Z) planes. The number of such oscillations per one beam turn is called betatron tunes - Q_x and Q_z. If an integer part of the tune agrees with the accelerator model predictions, large optics errors can be ruled out, such as dipole errors, which lead to the integer resonances. The fractional part of the tune have a strong effect on a beam lifetime and emittance, since quadrupole errors lead to resonances at half-integer Q values, sextupole fields excite resonances at third-integer Q values and so on [1]. That is why an accelerator working point (Q_x, Q_z) has to be chosen in a reasonable distance from the resonance lines on the calculated diagram of resonances [2]. Measuring and controlling the betatron tunes can improve the beam lifetime and reduce the beam loss during acceleration. In the following, the fractional part of the tune will also be denoted by Q.

Measurement methods

Two approaches to measure the fractional part of the betatron tune was implemented and tested. The first method to measure the Q is to excite transverse beam motion and to detect the transverse beam position over a number N of successive turns [3]. The fractional part of the betatron tunes (Q_x, Q_z) can be calculated as the ratio of the betatron oscillation frequency (f_β) and the particle revolution frequency $(f_{\rm rev})$:

$$Q = \frac{f_\beta}{f_{\rm rev}}. \tag{1}$$

---

*monahov@sunse.jinr.ru

Thus, to calculate Q value we must know the exact values of the revolution frequency (f_{rev}) and the betatron oscillation frequency ((f_β) at the same time. The excitation signal can be selected from a white noise and a chirp - signal in which the frequency increases ("up-chirp") or decreases ("down-chirp") with time. The power density of the detected signal is computed via a Fast Fourier Transformation (FFT), and the betatron tune (f_β) is identified as the frequency with the highest amplitude peak. The frequency resolution of the FFT is the ratio of sampling rate to the size of the data frame. The maximum FFT error due to the discreteness of the frequency steps is equal to [4]:

$$\Delta f = \frac{f_s}{2N}, \tag{2}$$

where N is total number of samples in the data frame, f_s is ADC sampling frequency.

For example, with a constant sampling frequency of 10 MHz and a frame length of 8192 samples, the frequency resolution is approximately 1.2 kHz. The measurement system accuracy was improved by data windowing (Hamming window, which has a side-lobe level -42 dB) before the FFT calculation and parabolic interpolation of the signal in the vicinity of the resonance peak. When the magnitude of the frequency error is expressed in units of Δf, the largest error with the interpolation is 6.8% of Δf [4]. Thus, frequency resolution is increased 15 times after data windowing and interpolation, so to get the same frequency resolution of 1.2 kHz with $f_s = 10$ MHz only 1024 samples are used.

The second method to measure the Q is to provide the ADC sampling with a beam revolution frequency. In this case the resonance peak position obtained by the FFT is the fractional part of Q with no additional computations. The beam revolution frequency (f_{rev}) at the Nuclotron changes non-linearly from 125 kHz to 1.2 MHz during acceleration. The accelerating frequency harmonic number is 5. The results are shown on Fig. 1.

The measurement system implementation

A custom FlexRIO digitizer module was developed for a real-time signal acquisition and generation of an excitation signal. Vendor ID 0xAB66 was obtained from National Instruments for production of the FlexRIO modules at JINR. In the following, FlexRIO digitizer module will be denoted by "Digitizer". This module is an 8 layer PCB board with two AD9244 (14-bit, 65 MSPS ADC), one DAC904 (14-bit, 165 MSPS DAC), one analog input for the beam revolution frequency, which is taken from RF system, one analog input for synchronization with the start of injection. All inputs and outputs are galvanically isolated using the RF transformers (ADT1-6T). The ADCs are used to digitize an amplified signal, which are coming from pickup electrodes, mounted in X and Z planes. DAC is used to output an excitation signal. To excite transverse beam oscillations scanning frequency (chirp) and band-limited white noise were used. A chirp signal is generated by a direct digital synthesis (DDS) in a predetermined frequency range and scanning time. DDS is implemented in the FPGA (Virtex-5) and a generated signal is output from the FlexRIO "Digitizer" DAC. The DAC sampling frequency is filtered from the output signal by a 4th order elliptic low pass filter. Further, an excitation signal is amplified by the AR 800A3A RF amplifier and then applied to the kicker electrodes via impedance transformers. FlexRIO "Digitizer" module has a direct access to the I/O ports of the FPGA. The FlexRIO digitizer module inserted into 132-pin connector of the NI PXIe-7962R FPGA module for the PXI system
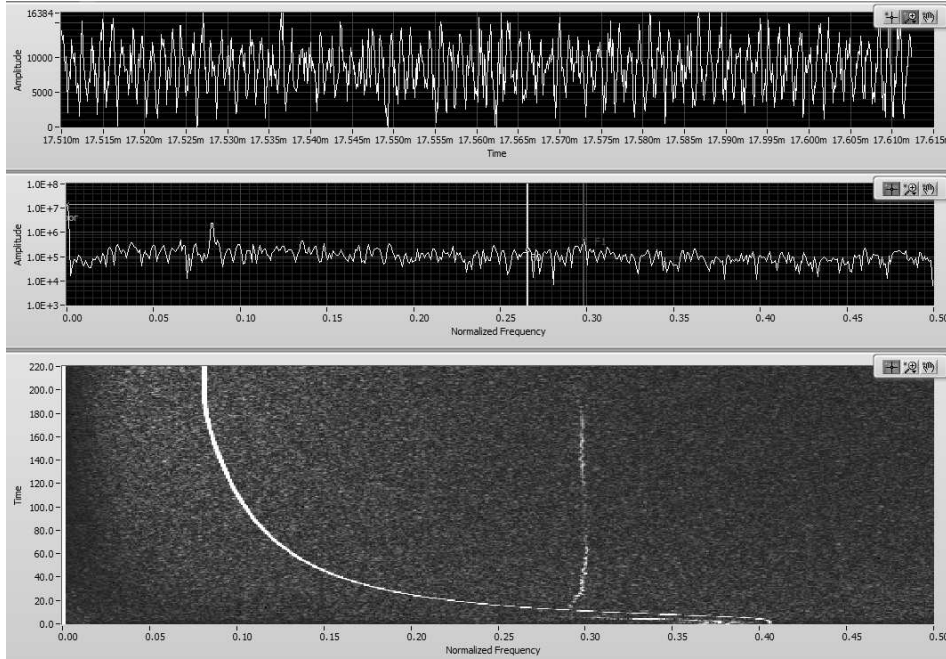
Figure 1: Q_x measurement during acceleration with mixed constant frequency 50 kHz from the signal generator (bright track on the left of the figure), the ADC sampling frequency is equal to the beam revolution frequency, excitation signal is white noise, frame size is 1024 samples, measured value of Q_x is 0.283.

crate NI PXIe-1082 which is 8-slot 3U PXI Express chassis with a 1 GB/s per-slot backplane data bus. The PXI system crate also contains necessary additional modules such as Tegam-4040A (two channel differential amplifier) and NI PXIe-8135 (high-performance Intel Core i7-3610QE processor-based system controller). Windowing of the input signals, interpolation and FFT algorithms are implemented in the FPGA. The signal processing (FFT calculation) starts simultaneously with the start of the input data accumulation and ends at the same time with the end of the data accumulation. The resources of the PXI system controller (PXIe-8135) are used for distributed control system based on TANGO Controls software toolkit [6] in which devices are controlled and monitored in a local distributed network. The signals from the two ADC channels and the FFT results are stored in the internal memory (512 MB DDR2) of the FPGA module. Built-in memory allows one to record the digitized data with the sampling frequency of 10 MHz from two 14-bit ADC channels for up to 4 seconds and the results of the FFT. After the end of the data accumulation results are transferred to the system controller PXIe-8135 via the DMA channel and displayed via remote TANGO Controls client application (Fig.1). The data transfer takes 0.9 sec.

Conclusions

The betatron tune measurement system was successfully tested during 51th run of the Nuclotron. The implementation of a high resolution FFT algorithm in an FPGA has allowed the real-time acquisition of the betatron tune. The implementation of a digital frequency synthesizer (DFS) inside the FPGA module allowed one to produce chirp and

white noise excitation signals. The further improvements are planned to increase the sensitivity of the measurement system and use diode detection technique which can improve the tune measurement resolution by one order of the magnitude [7].

References

[1] F. Zimmermann, *Measurement and Correction of Accelerator Optics*(Stanford University, Stanford, CA 94309, USA, SLAC-PUB-7844, June 1998).

[2] G. Trubnikov, I. Meshkov, A. Butenko, G. Khodzhibagiyan, A. Sidorin. *NICA collider complex: challenges and perspectives. Status of the Project.* (JINR-SAR Round Table, 05 July 2015).

[3] A. Boccardi, M. Gasior, R. Jones, K. Kasinski, R. J. Steinhagen. *The FPGA-based continuous FFT tune measurement system for the LHC and its test at the CERN SPS.* (European Organization for Nuclear Research, CERN AB Department, CERN-AB-2007-062, Geneva, Switzerland, August 2007).

[4] M. Gasior, J. L. Gonzalez. *Improving FFT frequency measurement resolution by parabolic and gaussian interpolation.* (European Organization for Nuclear Research, CERN, AB division, AB-Note-2004-021 BDI, Geneva, Switzerland, February 2004).

[5] NI LabVIEW FPGA Module: http://www.ni.com/labview/fpga

[6] TANGO Controls: http://www.tango-controls.org

[7] M. Gasior, R. Jones. *High Sensitivity Tune Measurement by Direct Diode Detection* (CTWA01, Proceedings of DIPAC 2005, Lyon, France).

NEUTRON SPECTRUM DETERMINATION OF THE P(37)+D$_2$O SOURCE REACTION BY THE DOSIMETRY FOILS METHOD

M. Stefanik[1,2*], P. Bem[1], M. Gotz[1], M. Honusek[1], M. Majerle[1], K. Katovsky[3], J. Novak[1], E. Simeckova[1]

[1] *Nuclear Physics Institute of the ASCR p.r.i., Řež, Czech Republic*
[2] *Czech Technical University, FNSPE, Prague, Czech Republic*
[3] *Brno University of Technology, FEEC, Prague, Czech Republic*

Annotation

The accelerator-driven fast neutron generator at the Nuclear Physics Institute of the ASCR in Řež near Prague uses the unique target with flowing heavy water. The thick target neutron field of the p + D$_2$O source reaction was investigated for a proton energy of 37 MeV. The spectral neutron flux close to the source target at 0° was determined by using the multi-foil activation method and validated against the MCNPX predictions. The produced broad neutron spectrum up to 34 MeV is relevant to the IFMIF (International Fusion Material Irradiation Facility) spectrum and suitable for the integral validation of activation cross-section data and radiation hardness tests of electronics against fast neutrons[†].

Introduction

Nuclear Physics Institute of the ASCR in Řež has developed and is operating the accelerator-driven fast neutron sources of white and quasi-monoenergetic spectra [1]. The source reactions of p + D$_2$O and p + Be employing the variable-energy proton beam of the U-120M isochronous cyclotron are used to produce the high intensity continuous spectra up to 34 MeV. These spectra represent a useful tool for integral benchmark and nuclear data validation. Similarly, the p + ^{7}Li(C) source reaction serves for the quasi-monoenergetic spectra production in the energy range of 16-35 MeV and it is used for microscopic cross-section measurements of (n, xn) reaction in corresponding energy region.

P(37) + D$_2$O fast neutron source

For integral benchmark experiments and validation activation cross-section data in the energy range relevant to the IFMIF (International Fusion Material Irradiation Facility) [2], the fast neutron source with the thick heavy water target was developed utilizing the NPI variable-energy cyclotron U-120M. To simulate the neutron spectrum in the energy range relevant to IFMIF (energy range up to 35 MeV and weak tail up to 55 MeV), the p + D$_2$O source reaction has been investigated for the proton-beam energy of 37 MeV, and the high-flux neutron source was developed. It was found that the deuteron break-up process induced by 37 MeV protons on heavy water produces the neutron white-(IFMIF-like)-spectrum with the high intensity, mean energy of 14 MeV (corresponding to the ITER) and spectrum extending up to 34 MeV.

---

*milan.stefanik@fjfi.cvut.cz
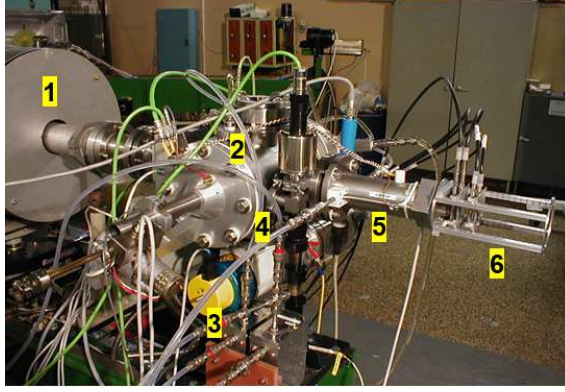
Figure 1: Heavy-water target station and aluminum holder with activation foils (1 - quadrupole triplet, 2 - beam - diagnostic, 3 - separated vacuum hardware, 4 - heavy - water flow tube, 5 - target chamber, 6 - sample holder).

Neutron activation technique and reaction rate

For the broad neutron spectrum measurement in the close vicinity from the source target where the dimensions of target and samples and the target-to-samples distances are comparable, the multi-foil activation technique is the most appropriate method. This technique makes it possible to reconstruct the neutron spectrum using the gamma-activities of radionuclides produced by the nuclear reactions in the activation foil. The result of activation measurements is the activation detector response to the neutron field, i.e. the reaction rate $R_R(s^{?1})$ which can be calculated by using the following equation:

$$R_R = \frac{S(E_\gamma)\lambda\frac{t_{\text{real}}}{t_{\text{live}}}}{N_0\varepsilon^\gamma_{\text{FEP}}(E_\gamma)I_\gamma(E_\gamma)(1-e^{-\lambda t_{\text{irr}}})e^{-\lambda t_{\text{cool}}}(1-e^{-\lambda t_{\text{real}}})\eta_B} \tag{1}$$

where λ is the decay constant of the produced radionuclide, S the number of counts in the full energy peak (FEP) for gamma-ray, N_0 the number of target nuclei in the activation detector, $\varepsilon^\gamma_{\text{FEP}}$ the absolute detection efficiency for the FEP, I_γ the intensity per decay, t_{irr} the irradiation time, t_{cool} the cooling time, treal or t_{live} the real time or live time of the spectroscopic measurement, and η_B is the proton-beam intensity fluctuation factor. From measured reaction rates, the neutron spectrum is reconstructed by using the appropriate unfolding code.

Neutron spectrum determination

For the neutron spectrum determination of the p(37)-D$_2$O source reaction at the sample position, the multi-foil activation method was utilized. The set of activation detectors in the form of spectroscopic thin foils consisted of 10 materials sensitive to the various parts of the neutron energy spectrum according to activation cross-sections. In particular, the Al, Au, In, Nb, Ti, Fe, Ni, Y, Lu, and Co with high purity and delivered by GoodFellow were used in the neutron activation experiment. In the irradiation experiment lasting several hours at a beam current of 11.6 μA, the stacks of the foils were located on the aluminum holder at a distance of 3 mm from the neutron source. The overview of the neutron generator and samples is shown in Fig. 1. After irradiation, the induced radioactivities of activation

109

foils were repeatedly measured by two HPGe semiconductor detectors with various cooling times. The reaction products observed in measured gamma-ray spectra were identified on the basis of energies, intensities, and half-life periods. From these data, the reaction rates were obtained and used for the neutron spectrum reconstruction. Reactions successfully observed in the experiment are summarized in Table 1.

Table 1: Reactions observed in experiment and used for neutron spectrum reconstruction

Reaction	Reaction threshold	Half-life period	C/E (%)	C/Eerr (%)
^{59}Co(n,α)^{56}Mn	0.00	2.58 h	1.06	8.42
^{93}Nb(n,α)^{90m}Y	0.00	3.19 h	0.93	7.68
^{197}Au(n,γ)^{198}Au	0.00	2.69 d	1.00	8.00
^{nat}Fe(n,x)^{51}Cr	0.00	27.7 d	1.04	8.00
^{nat}Ni(n,x)^{58}Co	0.00	70.86 d	0.98	7.68
^{115}In(n,n')^{115m}In	0.34	4.49 h	0.98	9.54
^{59}Co(n,p)^{59}Fe	1.57	44.5 d	1.06	8.00
^{nat}Ti(n,x)^{46}Sc	1.62	83.8 d	1.01	8.00
^{nat}Ni(n,x)^{60}Co	2.12	5.27 y	0.87	7.68
^{nat}Fe(n,x)^{56}Mn	2.97	2.58 h	1.00	8.00
^{27}Al(n,α)^{24}Na	3.25	14.9 h	1.03	8.42
^{nat}Ti(n,x)^{48}Sc	3.28	1.82 d	1.05	8.00
^{nat}Ti(n,x)^{47}Ca	3.68	4.54 d	0.89	10.20
^{nat}Ni(n,x)^{57}Co	6.05	271.8 d	0.98	7.68
^{197}Au(n,2n)^{196}Au	8.11	6.18 d	1.05	8.00
^{93}Nb(n,2n)^{92m}Nb	9.06	10.2 d	0.97	6.68
^{59}Co(n,2n)^{58}Co	10.63	70.9 d	1.07	8.00
^{89}Y(n,2n)^{88}Y	11.61	106.7 d	0.99	7.68
^{nat}Fe(n,x)^{54}Mn	12.14	312.3 d	1.05	8.00
^{nat}Ni(n,x)^{57}Ni	12.43	1.48 d	1.02	8.43
^{nat}Lu(n,x)^{173}Lu	14.51	1.37 y	1.05	7.68
^{197}Au(n,3n)^{195}Au	14.79	186.1 d	0.96	8.00
^{59}Co(n,3n)^{57}Co	19.35	271.8 d	0.93	8.00
^{197}Au(n,4n)^{194}Au	23.21	38.0 h	1.03	8.00

Results

For the neutron spectrum reconstruction from measured reaction rates and guess spectrum obtained from the MCNPX [3] calculations employing the LA-150h data library [3], a modified version of the SAND-II [4] unfolding code together with the cross-section data from the EAF-2010 library [5] was utilized. For the neutron spectrum deconvolution, the 24 activation and threshold reactions were successfully used, and the corresponding C/E (calculated over experimental reaction rate ratios) are summarized in Table 1. Both, the SAND-II unfolded and MCNPX calculated spectra are presented in Fig. 2.
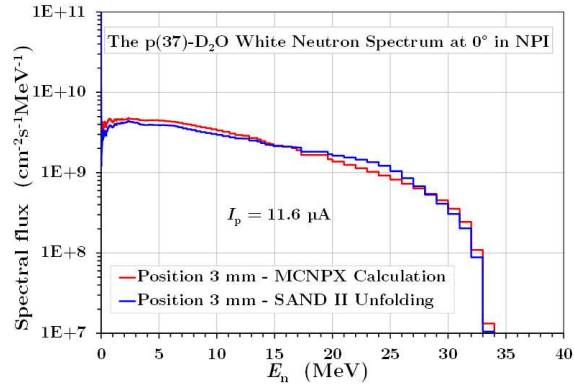
Figure 2: Neutron energy spectrum of the p(37)+D$_2$O neutron source at the NPI Řež.

Conclusions

The multi-foil activation technique was used for the broad neutron spectrum determination from the p(37)-D$_2$O neutron source at the cyclotron U-120M of the Nuclear Physics Institute ASCR in the energy range up to 34 MeV. The obtained neutron field of the NG-2 generator based on heavy water target is used for the integral benchmarks, cross-section data validation, testing the hardness of electronics against the fast neutrons, and other types of irradiation experiments.

References

[1] P. Bem *et al., The NPI cyclotron-based fast neutron facility*, (Proceedings of International Conference on Nuclear Data for Science and Technology ND2007, France, 2007).

[2] A. Möslang, *International Fusion Materials Irradiation Facility*, (Conceptional Design Evaluation Report, A Supplement to the CDA by the IFMIF TEAM, 1999).

[3] D. B. Pelowitz *et al., MCNPX User's Manual v. 2.6.0*, (Los Alamos National Laboratory, Los Alamos, 2008).

[4] SAND-II-SNL, PSR-345, UKAEA FUS, 1996.

[5] R. A. Forrest *et al.*, "EAF-2007", UKAEA FUS, 2007.

MECHANICAL ISSUES ARISING DURING THE DESIGN OF BUS-BARS FOR SUPERCONDUCTING PARTICLE ACCELERATORS

Ł. Tomkow

Wrocław University of Technology, Wrocław, Poland

Annotation

Modern particle accelerators require high magnetic fields to efficiently bend and shape particle beams. To obtain these fields large electric currents are needed to be passed through coils. This calls for the application of superconducting magnets, which allow lossless transport of electric current. The magnets are supplied with electricity by bus-bars. They are cables used to carry large currents. In the case of normal materials they often have the form of rails. In modern accelerators most often superconducting cables are applied. Bus-bars are also used to connect the sections of an accelerator. Similarly to magnets, the bus-bars are made of superconducting material, they require to be cooled below critical temperature [1]. The major concern of this work is SIS-100 accelerator, currently under construction in GSI, Darmstadt, Germany. Liquid helium is used as a cooling medium in the case if this accelerator [2]. Interestingly, in SIS-100 transfer lines the bus-bars are coupled with helium pipes forming a single transfer line carrying both coolant and current. Nuclotron-type cables are used in which a superconductor is cooled by an internal helium flow, while a superconductor is located externally. This paper addresses two examples of issues connected with the design of a bus-bar. The first one derives from high Lorentz forces appearing due to large currents. The may lead to stresses and deformation of spacers. The other described problem are flow-induced vibrations appearing in thin channels transporting cooling medium. Both problems were analyzed using COMSOL simulation software.

Stresses caused by Lorentz force

Large currents present in superconducting bus-bars lead to the appearance of significant Lorentz forces, which possibly may damage both the bus-bar and a spacer. Spacers are used to stabilize the assembly of a transfer line containing helium pipes and superconducting cables. The cross-section of the bus-bar part of the assembly is shown in Fig. 1. In the case of SIS-100, they are made of G-10. This is a fiberglass epoxy with favorable electric and thermal properties. It is important to remember that most of materials change they properties with the decrease of temperature. Fortunately, mechanical strength of G-10 increases at low temperatures. However, it is still lower than that of steel at the same temperature [3]. In the design phase the changes of thermal expansion coefficient should also be considered.

The damage to the structure of a superconducting may also occur. In this case critical current would decrease, leading to increased risk of quench. Quench is a sudden transition from superconducting to normal state accompanied by release of energy in the form of heat. Such release may cause the destruction of the section of a transfer line by destroying a bus-bar and evaporating cooling medium. Quenches should be avoided and any stress affecting the bus-bar should be recognized. In the case of this work the risk has been assessed by
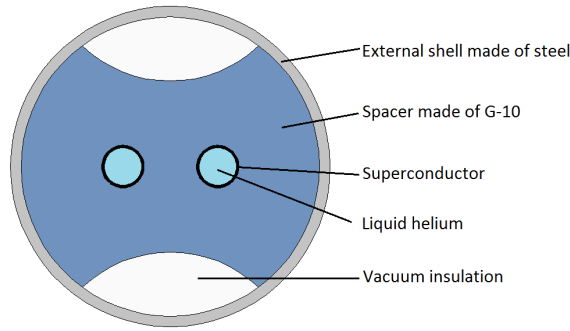
Figure 1: The assembly of a bus-bar.

the means of simulation. In the case of this work two simulations were performed. Initially an electrical model has been created to calculate Lorentz forces. Resultant forces were introduced to a mechanical model in order to find stresses and deformations.

Fig. 2. shows the total value of Lorentz force affecting a single line of the bus-bar per meter length in a horizontal direction. Applied current mimics the one which will be supplied to the actual bus-bar. The waveform is triangular, the frequency of current changes is 1 Hz. The maximum current is 14 kA. It can be seen Lorentz force is proportional to the square of an applied current. Also, the changes are periodical which may lead to the fatigue of material.
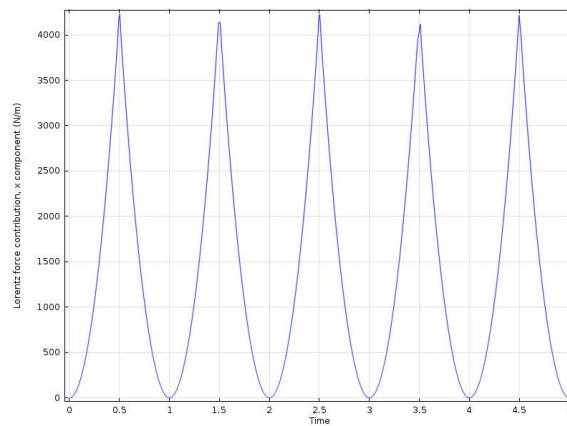
Figure 2: Lorentz force affecting a single line of the bus-bar in a horizontal direction

The result of the application of the calculated Lorentz force at the maximum current to the assembly is shown in Fig.3. It can be seen that the largest stress occurs at the central section of assembly, where the bus-bars and the spacer are compressed. The largest deformation can be observed at the further sides of the bus-bar lines. Calculated stresses are almost an order of magnitude lower than the strength of G-10. Actual value will be much higher. Under current assumptions the entire length of the bus-bar assembly is filled with a spacer material. The obtained results of simulation may help to assess the number and positioning of spacers needed to maintain the safe level of stresses to avoid damage.

113
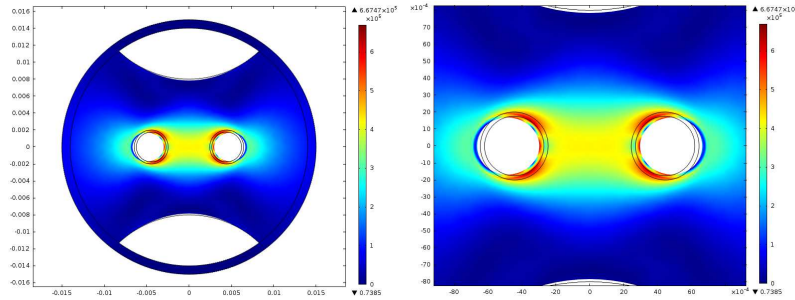
Figure 3: Stresses and deformations (exaggerated 10000 times for better visibility). Right - zoom of the central section of the assembly

Flow-induced vibrations

As mentioned, superconductors present in bus-bars have to be cooled with liquid helium. During the flow through the accelerator heat leaks cause its temperature to rise. Since helium has relatively low specific heat its temperature is prone to changes. It must not exceed critical temperature of the superconductor in order to avoid quench. In SIS-100 helium transfer pipes small heat exchangers (re-coolers) were applied. Small part of main helium flow is expanded and rerouted through a re-cooler. Therefore the temperature along entire accelerator is maintained below the critical temperature. However, this kind of heat exchanger placed inside a larger pipe may cause the formation of Kármán vortex street, which in turn leads to the vibrations of the re-cooler. Fig. 4. shows the example of a re-cooler and border conditions. Also the forces appearing during the operation of heat exchanger are shown.
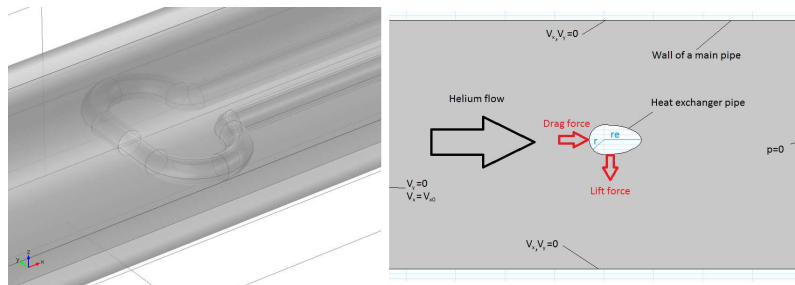
Figure 4: Left - isometric view of a re-cooler, right - border conditions and forces

The simulations were performed in 2D on the axis of a large pipe. The surface was perpendicular to the axis of a re-cooler. Fig. 5. shows the example of velocity pattern appearing during the flow and forces affecting the re-cooler. Kármán vortex street is clearly visible in the figure. The values of forces were calculated by integrating pressure and direction component over an entire surface of the re-cooler pipe. Considering small size of the re-cooler the values of forces are low. However, they exhibit a repetitive pattern, which may cause resonance.

By analyzing the changes of force affecting the re-cooler over time the vortex shedding frequency can be assessed. In order to avoid dangerous resonance it should be as far as possible from a natural frequency of the re-cooler. At resonance conditions even small forces may cause large deviations from normal position and in turn the damage to the heat
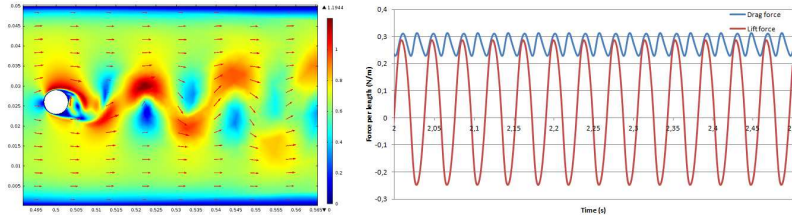
Figure 5: Left - the example of velocity distribution, right - forces affecting a re-cooler

exchanger. Natural frequency of the re-cooler can be changed by varying the location of supports. Vortex shedding frequency can be reduced by using pipes with different shapes and dimension. The first solution is generally simpler.

Conclusions

The requirements of modern particle accelerators considering the operational parameters of bus-bars are very high. They force trade-offs between mechanical strength and electrical, thermal properties of systems. With the increase of power and complexity of accelerators new problems and needs will certainly appear. For example, novel materials for spacers will be required, with higher mechanical strength and lower thermal conductivity. This works shows also that computer simulations can be a powerful in the recognition and assessment of risks appearing during the design of accelerators. They save time and money when compared to an experimental approach. However, the application of their results require certain degree of scientific and engineering intuition in order to recognize unreliable results.

References

[1] P. P. Granieri, M. Casali, D. Richter, *Heat Transfer in the LHC Main Superconducting Bus Bars*, (CERN-ATS-2011-023).

[2] A. Bleile, E. Fischer , W. Freisleben , A. Mierau , P. Schnizer , P. Szwangruber, Physics Procedia 67 (2015) 781.

[3] C. L. Goodzeit, *Superconducting Accelerator Magnets: An Introduction to Mechanical Design and Construction Methods*, USPAS January, 2001

Mathematical Modelling, Computational Physics and Information Technology

FEASIBILITY STUDIES OF TiO$_2$ POLYMORPHS: ANATASE, BROOKITE AND RUTILE USING (DFTB+)

M. Gandamipfa[1], P. E. Ngoepe[1]

[1] *Materials Modeling Centre, University of Limpopo, Sovenga, South Africa*

Annotation

Titanium dioxide nanoparticles, which are anticipated for use in a wide range of batteries industries, have been shown to exhibit enhanced properties compared to their bulk counterparts. This enhancement has mostly been attributed to their large surface-area and has attracted enormous research interest in recent years. In this work, structural and electronic calculations have been performed on anatase TiO$_2$ nanoparticles using DFTB+ code. It is found that the values of the lattice parameters and band gaps energy of TiO$_2$ polymorphs after introducing Lennard-Jones dispersion corrections are in good agreement with the experimental values. It is assumed that the accurate calculations could be due to the inclusion of dispersion correction within DFTB+.

Introduction

Titanium dioxide (TiO$_2$) is a safe, abundant and inexpensive photocatalytic material. TiO$_2$ is widely used material due to important technological applications [1, 2]. TiO$_2$ exist in many polymorphs. Amongst them anatase, brookite and rutile [3] are well-known minerals in nature abundantly available and show excellent electronic conductivity/performance as base materials in electronics and to fulfil the energy demand of the future [4]. The gap between valence and conduction bands and the structural property are very important to all of these applications. However, due to optical gaps slightly above 3 eV for the TiO$_2$ polymorphs: rutile 3.0 eV [5, 6], anatase 3.4 eV [7] and brookite 3.3 eV [6], hence natural TiO$_2$ is only photoactive in the UV region of the electromagnetic spectrum and also an inefficient active solar cell material. The material advantages of TiO$_2$ can be used indirectly in technically and economically viable dye-sensitized solar cells [8] where it acts as an electron-transporting substrate for a chemisorbed photoactive dye. In this paper, a new DFTB+ method to calculate properties of TiO$_2$ polymorphs structures is proposed. For the convenience of discussion, we classified TiO$_2$ polymorphs in three categories: phases that have been found in minerals: the anatase, brookite and rutile phase. The structure optimization and electronic band structure calculations are carried out for those three TiO$_2$ polymorphs. DFTB+ method is adopted to calculate the band energies at high-symmetry k-points in the first brillouin zone. The DFTB+ structural properties and band gap energies would be helpful for future research work on electrical properties of these TiO2 polymorphs.

Methodology

The Density Functional based Tight Binding (DFTB+) method [9] occupies an important place in the hierarchy of techniques available for the atomistic modeling of materials. Large scale simulations of technologically relevant problems are dominated by the use of

empirically derived forcefields. However, since they are adapted to a finite set of equilibrium situations (mostly experimental data and ab initio results for equilibrium configurations), they usually apply well to systems that are within the parameterization space. The tiorg [10] parameters set from the DFTB are used. It has been developed to handle bulk titanium oxide, titanium oxide surfaces, and the interactions of titanium oxide with organic molecules. This set extends the biological mio set and can handle O, N, C, S, H, and Ti. It has been tested on bulk Ti, bulk TiO_2 (rutile and anatase), various molecules containing Ti and C, N, H, S or O, and on TiO_2 surfaces interacting with water A simple and good approximation the local density approximation (LDA) is employed, which is based on the known exchange-correlation energy of the uniform electron gas [11]. The DFTB+ method is employed for structure optimization and ground state electronic structure calculations. The MonkhorstPack scheme [12] is used for the k-point sampling in the first Brillouin zone. A $6 \times 6 \times 3$ k-point grid is chosen for anatase. A $4 \times 4 \times 4$ k-point grid is chosen for TiO2 polymorphs with brookite. A $6 \times 6 \times 8$ k-point grid is chosen for rutile.

Results and discussion
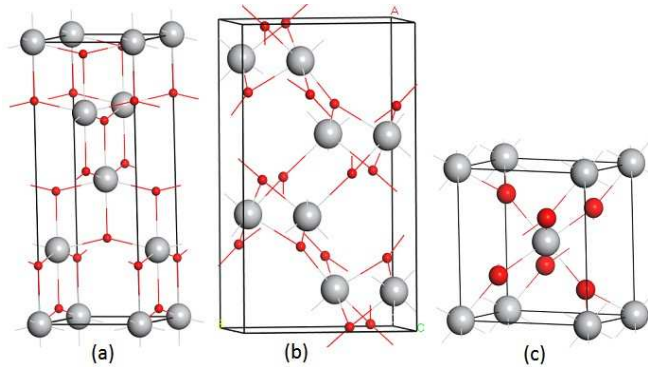
Figure 1: TiO_2: Anatase (a), brookite (b) and rutile (c), large spheres represent titanium and small spheres oxygen.

The polyhedral structures of TiO_2 polymorphs investigated in this work are given in Figure 1 with space groups I41/amd, Pbca and P42/mnm respectively. Anatase has a tetragonal body-centered structure and is comprised of TiO_6 octahedra sharing two adjacent edges with two other octahedral. Geometry optimized structures lattice parameters at zero pressure for the three TiO_2 polymorphs are listed in Table 1. The lattice parameters of the anatase, brookite and rutile are in agreement with the available experimental data [13, 14]. However, the value of c for anatase (9.403 Å) is about 1.14% smaller than the experimental one (9.511 Å) [15]. This relative discrepancy for the value of c is recently corrected by performing DFTB+ calculations with inclusion the dispersion correction. Our calculations after adding the dispersion correction term gives a lattice parameter (c=9.486 Å) agreeing well with experimental data (c = 9.51 Å). For consistency dispersion correction is also used in other TiO_2 polymorphs structures calculations in this paper.

Table 1: The calculated structural parameters for TiO$_2$ polymorphs compared with previous work. Notations: Without dispersion correction (No DC), With dispersion correction (DC), A [13], B [15], C [13], D [16], E [13] and F [14]

	Work	Method	Lattice parameters (Å)		
			a	b	C
Anatase	No DC	DFTB+	3.887	-	9.403
	DC	DFTB+	3.800	-	9.486
	A	PW-LDA	3.753	-	9.428
	B	Exp.	3.785	-	9.511
Brookite	No DC	DFTB+	9.256	5.471	5.179
	DC	DFTB+	9.257	5.475	5.192
	C	PW-LDA	9.540	5.390	5.533
	D	Exp.	9.184	5.447	5.145
Rutile	No DC	DFTB+	4.672	-	2.997
	DC	DFTB+	4.679	-	2.998
	E	PW-LDA	4.613	-	2.849
	F	Exp.	4.592	-	2.958

Conclusion

In this study, we have investigated the structural and electronic properties of the three naturally occurring TiO$_2$ polymorphs anatase, brookite and rutile. DFTB+ calculations cannot predict more accurate results for TiO$_2$ polymorphs without adding UFF-based Lennard-Jones dispersion corrections. The obtained structural parameters using DFTB+ approach were found to be in good agreement with previously reported computational and experimental work.

References

[1] M. Mohamad , B. Ul Haq, R.Ahmed, A. Shaari, N. Ali, R. Hussain, Mat. Scien. Semicond. Proc. 31 (2015) 405.

[2] T. Arlt, M. Bermejo, M. A. Blanco, L. Gerward, J. Z. Jiang, J. Staun Olsen, J. M. Recio, Phys. Rev. B, 61 (2000) 14414.

[3] V. W. H. Bauer, Acta Crystallogr., 14 (1961) 214-216.

[4] L. Gerward, J. S. Olsen, J. Appl. Cryst.,30 (1997) 259.

[5] Cab, R. d. Coss, G. Oskam, Nanotechnology,19 (2008) 145605.

[6] T. Zhu, S. -P. Gao, J. Phys. Chem. C,118 (2014) 11385.

[7] P. R. Bueno, E. Camargo, E. Longo, E. Leite, S. A. Pianaro, J. A. Varela, J. Mater. Sci. Lett., 15 (1996) 2048.

[8] R. Asahi, Y. Taga, W. Mannstadt, A. J. Freeman, Phys. Rev. B, 69 (2000) 7459.

[9] S.-D. Mo, W. Y. Ching, Phys. Rev. B, 51 (1995) 13023.

[10] H. Dixit, *First-Principles Electronic Structure Calculations of Transparent Conducting Oxide Materials*, (Departement Fysica, Universiteit Antwerpen, Antwerpen, Belgium, 2012).

[11] J. Pascual , J. Camassel , H. Mathieu, Phys. Rev. B, 18 (1978) 5606.

[12] A. Amtout, R. Leonelli, Phys. Rev. B, 51 (1995) 6842.

[13] H. Tang, F. Levy , H. Berger, P. E. Schmid, Phys. Rev. B, 52 (1995) 7771.

[14] A. Hagfeldt, G. Boschloo, L. Sun , L. Kloo, H. Pettersson, Chem. Rev., 110 (2010) 6595.

[15] T. Frauenheim, G. Seifert, M. Elstner, T. Niehaus, C. Kohler,M. Amkreutz, M. Sternberg, Z. Hajnal, A. Di Carlo, S. Suhai, J. Phys. Cond. Matter, 14 (2002) 3015.

[16] J. P. Perdew, Y Wang, Phys. Rev., B 45 (1992) 13244.

NUMERICAL CALCULATION OF SCALING EXPONENTS FOR THE DIRECT PERCOLATION IN THE SECOND ORDER PERTUBATION THEORY

M. Dančo[1*], M. Hnatič[1,2†], T. Lučivjanský[2,3‡], L. Mižišin[1,2§]

[1] *Joint Institute for Nuclear Research Dubna, Moscow Region, Russia*
[2] *Faculty of Science, P. J. Šafárik University, Košice, Slovakia*
[3] *Fakultät für Physik, Universität Duisburg-Essen, Duisburg, Germany*

Annotation

Direct percolation process near the second-order phase transition between an absorbing and an active state is investigated by means of the renormalization group approach. We have carried out a numerical calculation of the scaling exponents and the β functions in the higher order perturbation theory.

Introduction

Directed bond percolation (DP) is a prominent model that exhibits a non-equilibrium phase transition between an active and an absorbing state [1, 2]. In the absorbing state, the environment does not contain active particles, whereas in the active state, the number of active particles fluctuates around a mean value. The DP phase transition can be observed in different physical phenomena, e.g. the Reggeon field theory [3], the contact process [4] and certain cellular automata. The DP also serve for modeling many physical processes (various models of the spreading disease [5, 6], stochastic reaction diffusion processes on a lattice [6] and others).

In this work, the percolation problem is investigated near its second-order phase transition by means of the renormalization group (RG) approach. We present a numerical calculation of the renormalization group functions in the ε-expansion where ε is the deviation from the upper critical dimension $d_c = 4$. Within this procedure anomalous dimensions γ are expressed in terms of irreducible renormalized Feynman diagrams and thus the calculation of renormalization constants could be entirely skipped [7]. The renormalization procedure is applied in terms of the R operation [8].

Model and Method

A field theoretical formulation of the percolation process [6] is based on the following Dominicis-Janssen action

$$\mathcal{J} = \psi^\dagger(-\partial_t + D_0\partial^2 - D_0\tau_0)\psi + \frac{D_0\lambda_0}{2}[(\psi^\dagger)^2\psi - \psi^\dagger\psi^2], \tag{1}$$

*danco@saske.sk

†hnatic@saske.sk

‡tomas.lucivjansky@upjs.sk

§lukas.mizisin@student.upjs.sk

where ψ is a coarse-grain density of percolating particles, $\psi^\dagger$ is an auxiliary (Martin-Siggia-Rose) response field, D_0 is a diffusion constant, λ_0 is a positive coupling constant and τ_0 is a deviation from the threshold value of injected probability (an analog of critical temperature in static models). Integrals over spatial and time variables have been omitted in (1). The model is studied near its critical dimension $\varepsilon = 4 - d$ in the region where τ_0 acquires its critical value. The expansion parameter of the perturbation theory is rather λ_0^2 than λ_0 as it could be easily seen by a direct inspection of Feynman diagrams. Hence it is more convenient to introduce a new charge $u = \lambda^2$.

The renormalized action functional can be written in the following form

$$\mathcal{J}_R = \psi^\dagger(-Z_1\partial_t + Z_2 D\partial^2 - Z_3 D\tau)\psi + \frac{Z_4 D\lambda\mu^\varepsilon}{2}[(\psi^\dagger)^2\psi - \psi^\dagger\psi^2]. \tag{2}$$

It can be shown [6] that this kind of a model is multiplicatively renormalizable. Furthermore the action functional $\mathcal{J}_R$ can also be obtained from the action $\mathcal{J}$ by the standard procedure of multiplicative renormalization of all the fields and parameters

$$\psi_0 = \psi Z_\psi, \quad \psi_0^\dagger = \psi^\dagger Z_{\psi^\dagger}, \quad D_0 = D Z_D, \quad \lambda_0 = \lambda\mu^\varepsilon Z_\lambda, \quad \tau_0 = \tau Z_\tau. \tag{3}$$

The relations between renormalized constants $Z_i, i = 1, 2, 3, 4$ are obtained in a straight-forward fashion and read

$$\begin{aligned}
Z_1 &= Z_\psi Z_{\psi^\dagger}, & Z_2 &= Z_D Z_\psi Z_{\psi^\dagger}, \\
Z_3 &= Z_D Z_\tau Z_\psi Z_{\psi^\dagger}, & Z_4 &= Z_D Z_\lambda Z_{\psi^\dagger}^2 Z_\psi = Z_D Z_\lambda Z_{\psi^\dagger} Z_\psi^2.
\end{aligned} \tag{4}$$

Moreover, the relation $Z_\psi = Z_{\psi^\dagger}$ is satisfied.

In this work, at the normalization point (NP), $p = 0$, $\omega = 0$ and $\tau = \mu^2$ is considered. The counterterms are then specified at the normalization point, and for numerical calculation, it is advantageous to express the renormalization constants in terms of normalized Green functions

$$\begin{aligned}
\bar{\Gamma}_1 &= \partial_{i\omega}\Gamma_{\psi^\dagger\psi}\big|_{p=0,\omega=0}, & \bar{\Gamma}_3 &= -\frac{\Gamma_{\psi^\dagger\psi} - \Gamma_{\psi^\dagger\psi}\big|_{\tau=0}}{D\tau}\bigg|_{p=0,\omega=0}, \\
\bar{\Gamma}_2 &= -\frac{1}{2D}\partial_p^2\Gamma_{\psi^\dagger\psi}\big|_{p=0,\omega=0}, & \bar{\Gamma}_4 &= \frac{\Gamma_{\psi^\dagger\psi^\dagger\psi} - \Gamma_{\psi^\dagger\psi\psi}}{D\lambda\mu^\epsilon}\bigg|_{p=0,\omega=0}.
\end{aligned} \tag{5}$$

In contrast to the minimal subtraction (MS) scheme, the RG constants defined by conditions (5) do not depend on τ (see, e.g., Parts 3.3–3.5 in [8]). Accordingly, the RG equations are the same as in the MS scheme

$$(\mu\partial_\mu + \beta_u\partial_u - \tau\gamma_\tau\partial_\tau - D\gamma_D\partial_D)\Gamma_i^R = (n_\psi\gamma_\psi + n_{\psi^\dagger}\gamma_{\psi^\dagger})\Gamma_i^R, \tag{6}$$

where μ is a reference mass scale, n_ψ and $n_{\psi_\dagger}$ are the numbers of the corresponding fields entering the Green function under consideration, $\gamma_x = \mu\partial_\mu \log Z_x$ are anomalous dimensions and $\beta_u = u(-2\varepsilon - \gamma_u)$ is a beta function describing the flow of the charge u under the RG transformation [8]. Using these equations the relations for the normalized functions can be found

$$(\mu\partial_\mu + \beta_u\partial_u - \tau\gamma_\tau\partial_\tau - D\gamma_D\partial_D)\bar{\Gamma}_i^R = \gamma_i\bar{\Gamma}_i^R. \tag{7}$$

124

Here, anomalous dimensions γ_i are obtained from relations (4) between the renormalization constants

$$\gamma_1 = 2\gamma_\psi, \quad \gamma_3 = 2\gamma_\psi + \gamma_D + \gamma_\tau, \quad \gamma_2 = 2\gamma_\psi + \gamma_D, \quad \gamma_4 = 3\gamma_\psi + \gamma_D + \gamma_\lambda. \tag{8}$$

Taking into account the renormalization scheme we can express the anomalous dimension in terms of the renormalized derivatives of the one-particle irreducible Green function $\bar{\Gamma}_i$ at the normalization point [7, 9, 10]

$$f_i \equiv R[-\tilde{\tau}\partial_{\tilde{\tau}}\bar{\Gamma}_i(\tilde{\tau})]\big|_{\tilde{\tau}=1}. \tag{9}$$

Anomalous dimensions can be obtain in terms of the renormalized derivatives of the one-irreducible Green function $\bar{\Gamma}_i$ with respect to $\tilde{\tau}$ at the normalized point

$$\gamma_i = \frac{2f_i}{1 + f_2}, \quad i = 1, 2, 4. \tag{10}$$

The main benefit of this procedure considering (9) is that the operator R is taken at the normalization point and it can be expressed in terms of a subtracting operator $1 - K_i$ that eliminates all divergences from the Feynman graphs [8]

$$R\Gamma = \prod_i (1 - K_i)\Gamma, \tag{11}$$

where the product is taken over all relevant subgraphs of the given Feynman graph, including also the graph as a whole. In the null-momentum (NM) scheme we obtain the following representation for the R-operator [7, 10]

$$R\chi = \prod_i \frac{1}{n_i!} \int_0^1 da_i \, (1 - a_i)^{n_i} \partial_{a_i}^{n_i+1} \chi(\{a\}), \tag{12}$$

where the product is taken over all one-irreducible subgraphs χ_i (again including the graph χ as a whole) with the canonical dimension $n_i \geq 0$ and a_i is a parameter that stretches momenta flowing into the i-th subgraph inside this graph. The universal quantities, critical exponents in the form of the ε-expansion, is independent of the renormalization scheme.

Calculation

In the procedure, anomalous dimensions γ are expressed in terms of renormalized Feynman diagrams and thus combining (8) and (9) we can derive relations for anomalous dimensions γ for fields and parameters of the model

$$\gamma_\psi = \frac{f_1}{1 + f_2}, \qquad \gamma_D = \frac{2(f_2 - f_1)}{1 + f_2}, \qquad \gamma_u = 2\frac{2f_4 - f_1 - 2f_2}{1 + f_2}. \tag{13}$$

The scaling regime is associated with fixed points of the corresponding RG functions. The asymptotic behavior is governed by infrared fixed points and the coordinates fixed points

can be found from the requirement that β functions vanish. In our case, we have only one β function

$$\beta_u = u(-2\varepsilon - \gamma_u) \approx u\left(-2\varepsilon + \frac{3u}{4} - \frac{3u\varepsilon}{8} - \frac{3u^2\varepsilon}{128} - 0.389626u^2\right). \tag{14}$$

Results are the trivial (Gaussian) fixed points ($u = 0$) and the fixed point corresponds percolation process

$$u^* = 8\varepsilon/3 + 5.02756\varepsilon^2 + O(\varepsilon^3). \tag{15}$$

Moreover, γ_ψ^* and γ_D^* at the fixed point are given by

$$\gamma_\psi\big|_{u=u^*} = -\varepsilon/6 - 0.13614\varepsilon^2 \qquad \gamma_D\big|_{u=u^*} = \varepsilon/6 + 0.116824\varepsilon^2 \tag{16}$$

These results were obtained by a numerical calculation in which the actual form of integrals is determined by the R operator using the Feynman representation. Subsequently, the momentum integrals are calculated by Monte Carlo methods [11]. To the second order of perturbation theory, there are two diagrams for the function $\Gamma_{\psi^\dagger\psi}$ and 11 diagrams for the function $\Gamma_{\psi^\dagger\psi^2}$.

After determination of the coordinate for the fixed point it can be appropriated to examine exponents in the critical areas. First, the dynamical critical exponent η has the following value

$$\eta \equiv 2\gamma_\psi\big|_{u=u^*} = -\varepsilon/3 - 0.27228\varepsilon^2 + \mathcal{O}(\varepsilon^3) \tag{17}$$

The exponent z that is associated with the radius of gyration of the active particles takes the form

$$z \equiv 2 - \gamma_D\big|_{u=u^*} = 2 - \varepsilon/6 - 0.11682\varepsilon^2 + \mathcal{O}(\varepsilon^3) \tag{18}$$

These results have an excellent agreement with analytic calculation of critical exponents [2].

Our two-loop results are in agreement with analytic calculations and our numerical method is suitable for the calculation of the Feynman graphs to the three-loop order. To this end, it is necessary to take into account altogether 17 graphs for the one-irreducible Green function $\Gamma_{\psi^\dagger\psi}$ and 150 graphs for the function $\Gamma_{\psi^\dagger\psi^2}$. One just has to keep in mind that in order to achieve the required accuracy, computer time needed for calculation of each of the diagrams is much longer. The work in this direction is still in progress.

Acknowledgement

References

[1] H. K. Janssen, Z. Phys. B: Condens. Matter 42 (1981) 151.

[2] U. C. Täuber, *Adv. Solid State Phys.* 43 (2003) 659.

[3] P. Grassberg, K. Sundermeyer, Phys. Lett. B 77 (1978) 220.

[4] I. Jansen, R. Dickman, Physica A 203 (1994) 175.

[5] J. L. Cardy and R. L. Sugar, J. Phys. A 13 (1980) L423.

[6] H. K. Janssen and U. C. Täuber, Ann. Phys. 315 (2005) 147.

[7] L. Ts. Adzhemyan and M. V. Kompaniets, Theor. Math. Phys. 169 (2011) 1450.

[8] A. N. Vasil'ev, *The Field Theoretic Renormalization Group in Critical Behavior Theory and Stochastic Dynamics*, [in Russian], (PIYaF, St. Petersburg (1998); English trans., Chapman and Hall/CRC, Boca Raton, Fla (2004)).

[9] L. Ts. Adzhemyan, M. V. Kompaniets, S. V. Novikov, and V. K. Sazonov, Theor. Math. Phys. 175 (3) (2013) 719.

[10] L. Ts. Adzhemyan and M. V. Kompaniets, Journal of Physics Conference Series 523 (2014) 012049.

[11] R. Kreckel, comput. Phys. Commun. 106 (1997) 258 ; "Pvega." ftp://ftphep.physik.uni-mainz.de/pub/pvegas/; "Cuba – a library for multidimensional numerical integration," http://feynarts.de/cuba/

PARCS/TRACE COUPLED NEUTRONICS THERMAL-HYDRAULICS CALCULATION OF THE L335 BENCHMARK

F. Novotny[1*], K. Katovsky[1], J. Matejkova[1]
[1]*Department of Power Engineering, FEEC, BUT, Brno, Czech Republic*

Annotation

This study deals with Control Rod Ejection Benchmark – NEACRP-L335 and coupled neutronics thermal-hydraulic calculation. Coupled calculation is used to evaluate transients which occur during nuclear reactor operation. Control Rod Ejection is a transient problem, therefore utilization of the coupled calculation is appropriate. New thermal-hydraulic model was developed in TRACE. This model includes new 3D Cartesian Vessel Component which is utilized to represent reactor core. Cartesian Vessel component more closely represents real reactor core than Cylindrical Vessel Component, therefore this component was implemented in the TRACE. Correct function of the Cartesian Vessel Component as well as the correct function of the automapping procedure with Cartesian Vessel Component is under investigation within this study. Brief description of the used codes (PARCS and TRACE) is also given in this paper. Comparison of the coupled calculation results with PARCS standalone calculation and with original results of the benchmark shows an agreement.

Introduction

Testing of new capabilities of reactor core simulators and thermal hydraulic codes is a very important part of its use. With the increase of the calculation resources more detailed model, method and equations can be implemented in to the codes and this implementations has to be verified. Very convenient method of the verification is benchmark recalculation with new models and methods. The codes PARCS and TRACE are under ongoing evolution and the US NRC put a lot of resources to developing new features of these codes. The focus within this study is dedicated to the reactor vessel and reactor core. New 3D Cartesian Vessel Component together automaping procedure for coupled PARCS/TRACE calculation is verified on the L335 Control Rod Ejection Benchmark. [1,2]. Benchmark NEACRP-L335 is divided into six separate cases. The first one (A1) is studied within this study. During this scenario the peripheral control rod is ejected from the reactor core. The reactor is operation on hot zero power (HZP), mass flow though the core is 12893 kg/s and the inlet temperature is 286°C. Transient lasts 5 s and the control rod ejection occur at 0.1 s. [3,4] Model description The benchmark is focused on neutron physics calculation therefore only reactor core can be simulated within the benchmark specification. Model consists of inlet part, which is modeled by four components and these components represent lower plenum of reactor core, outlet part, which has the same structure as inlet part, and reactor core itself. Reactor core is built with new 3D Cartesian Vessel Component which captures more in detail the geometry of rector core according to the 3D Cylindrical Vessel. The disadvantage of 3D Cartesian Vessel is higher computer resources needs. Typical 3D Cylindrical Vessel

---

*Filip.Novotny@vutbr.cz

has 18 nodes in every axial level; new 3D Cartesian Vessel has 168 nodes in every axial level. The Cartesian Vessel together with all other components is shown in the Fig. 1. [2]
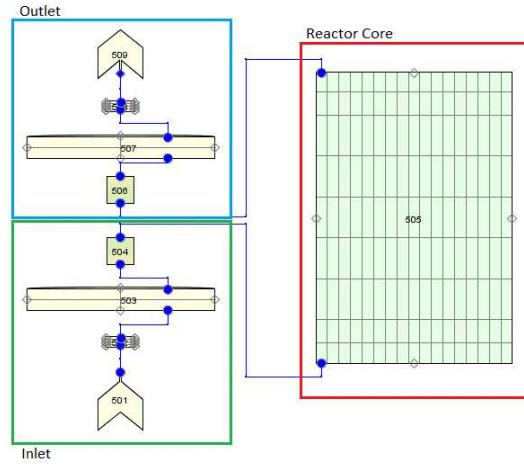
Figure 1: Developed TRACE model of NEACRP 3-D PWR Core Transient Benchmark. [5]

Results

There were performed stand-alone PARCS and coupled PARCS/TRACE steady state and transient calculation. Results of these calculations and reference calculation results [4] are given in the following tables. Significant parameters are compared in these tables such as boron density (Boron), radial peaking factor (Fxy), total peaking factor (Fq), Doppler temperature (Tdoppler) and centerline temperature of fuel pin (Tcenter). The results of steady state calculation with both models (PARCS, PARCS/TRACE) are given in the Table 1. According to this table the PARCS calculation slightly overestimates the reference

Table 1: Steady state results L335 part A1 [4]

	Boron (ppm)	Power	F_{xy}	F_q	$T_{doppler}$ (° C)	T_{center} (° C)
Reference	567.7	$1 \cdot 10^{-6}$	1.909	2.874	286.0	286.0
PARCS	561.26	$1 \cdot 10^{-6}$	1.9113	2.8987	286.04	-
PARCS/TRACE	565.68	$1 \cdot 10^{-6}$	1.8925	2.8508	285.86	285.86

results. Coupled calculation underestimates reference results. But both calculations are in very good agreement with reference calculation. Results of transient calculation are given in the Table 2 and 3. There are two significant time points, power maximum and end of transient, in the transient calculation. Significant parameters are compared in these two time points. Same behavior like in the steady-state calculation occurs, i.e. PARCS calculation overestimates and coupled calculation underestimates reference results. Main difference is in the time of power peak. There is almost 100 ms delay in the coupled calculation. This can be caused by different thermal-hydraulic solver in the both models. The parameters at the end of the transient are in good agreement for both calculations.

Table 2: Transient results (power maximum) - L335 part A1 [4]

	Time (c)	Power	F_{xy}	F_q	$T_{doppler}$ (° C)	T_{center} (° C)
Reference	0.560	1.179	-	-	294.5	343.6
PARCS	0.545	1.2508	-	-	295.06	-
PARCS/TRACE	0.621	1.0787	-	-	294.78	341.5

Table 3: Transient results (end of the transient; Time = 5 s) - L335 part A1 [4]

	Time (c)	Power	F_{xy}	F_q	$T_{doppler}$ (° C)	T_{center} (° C)
Reference	5	0.196	-	-	343.3	673.3
PARCS	5	0.1989	-	-	325.42	-
PARCS/TRACE	5	0.1896	-	-	322.52	641.7

Following figure shows the most important parameters of the core. Figure 2, left panel presents relative power during the transient. As it was stated in the Table 2 the power peak in the stand-alone calculation is higher but the trend of the both simulation is same and predict behavior correctly. Same statement can be done for second important parameter which is reactivity (Figure 2, left panel). The trend of both calculations is same and calculated reactivity is in good agreement therefore the neutron physics calculation with both models gives similar results and main differences are in the thermal-hydraulic solution.
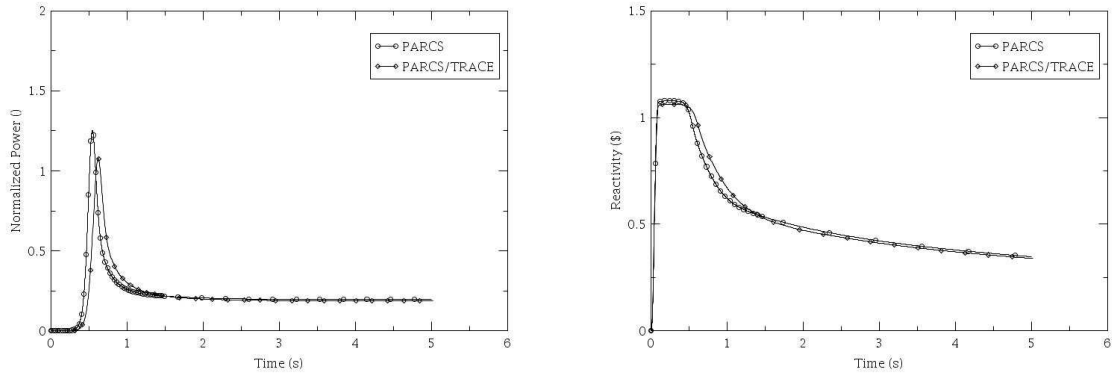
Figure 2: Comparison of core relative power (left panel) and total reactivity in the reactor core (right panel) for both PARCS and PARCS/TRACE calculation.

Conclusion

Main goal of this article was to verified new 3D Cartesian Vessel Component together with verifying of the automapping function within this component. This verification was performed by recalculation of the NEACRP-L335 Benchmark and results were compared

with stand-alone PARCS calculation and with reference results. This comparison shows very good agreement with reference results and coupled calculation adds more parameters, e.g. Tcenterline, which can be compared and are not included in the stand-alone PARCS calculation. Main disadvantage of this calculation is calculation time which is 10 times greater than stand-alone calculation. Nevertheless this disadvantage is compensated with more detailed solution and within the increasing of the computer resources this will not be disadvantage anymore. Models with this 3D Cartesian Vessel Component are very detailed and can be used as a reference models. This will be the huge benefit for the future calculations. During the verification several problems were found. The automapping function cannot be utilized in the graphical interface SNAP and coupled calculation cannot be run through this interface also. Both problem were sent to SNAP developers and are under their investigation.

Acbowleddgment

References

[1] *Applied Programming Technology, Inc., Symbolic Nuclear Analysis Package*, User's manual, (2012), p. 170.

[2] *Nuclear Regulatory Commision, TRACE V5.840*, Users Manual, Washington DC, (2014),p. 894.

[3] H. Finnemann, A. Galati, NEACRP 3-D LWR Core Transient Benchmark, Erlangen, (1991) 75.

[4] H. Finnemann, H. Bauer, A. Galati, R. Martinelli, Results of LWR Core Transient Benchmark, Erlargen, (1993) 83.

[5] F. Novotny, *Preparation of the stand-alone TRACE model for NEACRP-L335 Benchmark*, (Proceedings of the 21st Student Competition Conference), (2015), p. 631-635.

[6] T. Downar, Y. Xu, V. Seker, *PARCS - U.S. NRC Core Neutronics Simulator*, UM-NERS-09-0001 (2013) 165.

WEB-SERVICE FOR MONITORING OF THE HETEROGENEOUS CLUSTER HYBRILIT

M. Vala[1,2], A. Mayorov[1,3], Y. Butenko[1,3], G. Podolyan[1,3], A. Bulatov[1,3]

[1] *Laboratory of Information Technologies, Joint Institute for Nuclear Research*
[2] *Institute of Experimental Physics of SAS, Kosice, Slovakia*
[3] *State University "Dubna", Russia, Dubna*

Annotation

The heterogeneous cluster HybriLIT is designed for the development of parallel applications and for carrying out parallel computations asked by a wide range of tasks arising in the scientific and applied research conducted by JINR. The efficient work on the cluster needs the implementation of service of statistics provided to the users.

Introduction

Heterogeneous cluster HybriLIT is a part of Multifunctional information computing complex (MICC) of the Laboratory of Informational Technologies of JINR in Dubna [1]. As the number of users if growing, there arise a necessity of developing a service that would gather statistic data about usage of cluster resources. Service itself is a web-interface that contains real-time information about cluster load, running jobs, etc. All data is gathered by means of SLURM system and is uploaded to database where statistics is formed.

Technologies

In development of this service, multiple technologies and tools were used. First of all, for the building of web-service we used Node.js programming platform, which using JavaScript as its general programming language. With the help of Node.js, JavaScript is linking external libraries, which use multiple languages and provide their calls inside application. Node.js is based on event-oriented and asynchronous programming. One of this platforms advantages is simplicity of scaling of network servers. As JS-framework, AngularJS has been chosen. This framework contains impressive array of instruments, that allows create powerful, simple in maintenance, structured applications. AngularJS significantly simplifies development of dynamic applications due to bilateral data binding; that was the key feature which determined the choice of that framework. Bilateral data binding means that business-model and user-interface are linked and the change of one will cause changes of the others. For visualisation of statistics JavaScript libraries such as C3.js and Highcharts were used. C3.js is a JavaScript library based on D3.js which allows make sightly lightweight diagramms. Highcharts is a JavaScript library with powerful set of tools for flexible setting of diagramms forms. This library allows make dynamic graphics with good-looking animations, while processing few thousands of points real-time without serious resource using. For transferring data about the cluster state from sensors to a web-service, ZeroMQ is used. This library contains tools for creation of message queue system. It works on different architectures and supports more than 20 programming languages. In addition, it allows working with web-sockets on high level of abstraction. The library automatizes

data-buffering, queue-processing, creation and restoration of links and some other things which allow developer to concentrate on architecture and logic of the application.

Acquisition of data about cluster state

One of the service function is acquiring data about the cluster load in real-time. For getting the data, we have developed specialized sensors. They are written in C++ language with libgtop2 library. Sensors send all acquired data to broker, which puts data from all sensors to packages and redirecting them to web-server. Queue system is developed by means of ZeroMQ library in C++.
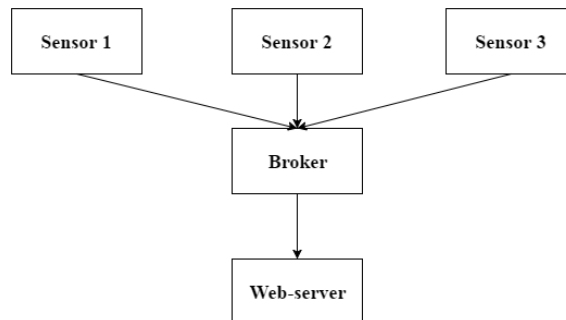
Figure 1: Scheme of transferring data from cluster to web-server

Already developed functions

At the moment web-service is in the alfa-testing state. Currently it includes the following developed functions:
- Information about general CPU, memory and network load of the cluster in form of pie diagrams at the main page.
- Information about users: name, login, password, home catalogue
- Information about completed jobs on cluster in the form of tables. It has "search" and "sort" functions for table columns
- Information about currently processing jobs on the cluster in the form of table. It has "search" and "sort" functions for table columns
- Information about the cluster resources usage for hour/day/month in the form of pointed diagram and pie diagram
- Information about the cluster load (CPU, memory and network) in real-time in the form of tables and diagrams
- Information about the cluster resources usage for hour/day/week/month by JINR laboratories and various universities.

Plans

Web-service is being constantly developed and we add new functions and possibilities. Next version will contain the following functions:
1. Authentication system for users with personal web-pages
2. Statistics of cluster usage by users/user-groups

3. History of cluster load
4. Several language support
5. New web-design

Conclusion

Web-service of monitoring of the heterogeneous cluster HybriLIT allows users organize their work more efficiently by providing all necessary information about it. This service is being actively developed.

References

[1] Project HybriLIT - http://hybrilit.jinr.ru

[2] Web-service for monitoring of heterogeneous cluster - http://stat-hlit.jinr.ru

[3] Node.js - https://nodejs.org/en

[4] AngularJS - https://angularjs.org

[5] C3.js - http://c3js.org/

[6] Highcharts - http://www.highcharts.com/

[7] ZeroMQ - http://zeromq.org/

STUDY OF DEEP INELASTIC REACTIONS WITHIN MULTIDIMENSIONAL DYNAMICAL MODEL OF NUCLEUS-NUCLEUS COLLISIONS

V.V. Saiko[1,2*], A.V. Karpov[1,2†]

[1] *Joint Institute for Nuclear Research, Dubna, Russia*
[2] *Dubna University, Dubna, Russia*

Introduction

The deep inelastic collisions (DIC) is the main reaction channel of nucleus-nucleus collisions of heavy ions at above-barrier energies. A strong dissipation of total kinetic energy of colliding nuclei and nucleon exchange between them are the key features of DIC. Interest to this kind of reactions is renewed at recent time in part due to predicted possibility of synthesis of unknown neutron-rich isotopes of heavy and superheavy elements with quite large cross sections [1, 2]. Application of multidimensional dynamical model of nucleus-nucleus collisions for describing deep inelastic ^{136}Xe + ^{209}Bi reaction was performed at present work. Calculations of energy, angular and charge distributions are performed for three collision energies $E_{\mathrm{cm}} = 526$, 684, and 861 MeV.

Model

In order to consider a nuclear dynamics one need to choose most important degrees of freedom of interacting system. One may split a collision of two nuclei onto three main stages: approaching stage, mono-nucleus formation and separation on final fragments. It is necessary to realistically describe the interacting system by involving many degrees of freedom. Their number should be large enough to reproduce the main features of the process. On the other hand, we are limited by the present computational possibilities. Developed model has eight degrees of freedom: distance between geometrical centers of two nuclei r, two ellipsoidal surface deformations β_i, mass and charge asymmetries η_A, η_Z, two angles of rotation of the nuclei φ_i, and angle between symmetry axis and beam direction Θ. They are schematically shown in Fig. 1. The values of multidimensional potential energy, inertia and friction tensors are the main quantities regulating the nuclear dynamics. We calculate them on a grid before starting the dynamical calculations. Potential energy is calculated within the macro-microscopic model [3]:

$$V(r, \beta_1, \beta_2, \eta_Z, \eta_A) = V_{\mathrm{mac}}(r, \beta_1, \beta_2, \eta_Z, \eta_A) + \delta E(r, \beta_1, \beta_2, \eta_Z, \eta_A)$$

where V_{mac} is the macroscopic part of the potential calculated within the finite range liquid drop model [3], δE is the shell correction calculated within two-center shell model [4, 5]. Example of multidimensional adiabatic potential energy for the ^{136}Xe + ^{209}Bi system is shown in Fig. 1. For more details on the potential energy calculations see [5,6]. The inertia tensors are calculated within the Werner-Wheeler approach for incompressible irrotational flow as function of the collective degrees of freedom: $m_{ij}(r, \beta_1, \beta_2, \eta_A) =$ where $\{i, j\} = \{r, \beta_1, \beta_2, \eta_A, \eta_z\}$. For the friction tensor we apply the one-body dissipation mechanism.

*saiko@jinr.ru

†karpov@jinr.ru
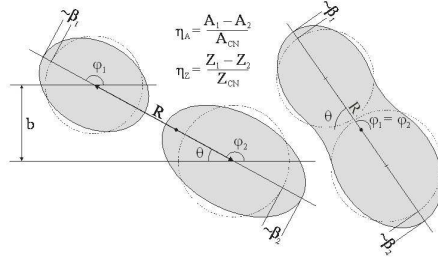
Figure 1: Schematic view of nuclear degrees of freedom.

The traditional approach based on the Langevin equations was used to consider the evolution of the nuclear system:

$$\frac{dq_i}{dt} = \mu_{ij}p_j,$$
$$\frac{dp_i}{dt} = F_i^{conservative} + F_i^{dissipation} + F_i^{random}$$

where q_i and p_i are, correspondingly, the collective degrees of freedom and their conjugate momenta, μ_{ij} is the inversed mass $\parallel \mu_{ij} \parallel = \parallel m_{ij} \parallel^{-1}$ tensor The conservative, dissipation, and random forces are calculated by the following expressions:

$$F_i^{conservative} = -\frac{\partial V}{\partial q_i} - \sum_{j,k} frac{p_jp_k}{2}\frac{\partial \mu_{jk}}{\partial q_i}, \tag{1}$$

$$F_i^{dissipation} = -\sum_{j,k} \gamma_{ij}\mu_{jk}p_k,$$

$$F_i^{random} = \sum_{j,k} \Theta_{ij}\xi_j(t).$$

Here $\xi_i(t)$ are the normalized random variables with Gaussian distribution $\langle \xi_i(t) \rangle = 0$, $\langle \xi_i(t), \xi_{j+1}(t') \rangle = 2\delta(t - t')$ and Θ_{ij} are the amplitudes of the random force defined from the Einsteins equation: $\Theta_{ik}\Theta_{kj} = \gamma_{ij}T$ and T is the nuclear temperature. Numerical solution of the Langevin equations (2) starts from approaching stage of collision (50 fm distance between nuclei) and finishes when two reaction products are formed and separated on approximately 50 fm distance. The solution of these equations is a trajectory in the space of collective coordinates. It provides full information about single collision, such as: charges and masses of reaction products, their total kinetic energy, scattering angles, etc.

In order to calculate the differential cross section in this approach one should test a large number of trajectories at different impact parameters $0 < b < b_{\max}$ and select them according to experimental energy, angle, charge and mass conditions. The differential cross section is then calculated in a standard way:

$$\frac{d^2\sigma}{dEd\Omega}(E, \Theta) = \int_0^{b_{max}} \frac{\Delta N(E, \Theta)}{N_{tot}(b)} \frac{bdb}{sin\Theta\Delta\Theta\Delta E}. \tag{2}$$

Results

The reaction ^{136}Xe + ^{209}Bi was chosen for testing the developed dynamical model of nucleus-nucleus collisions, because a rather complete set of experimental data for this
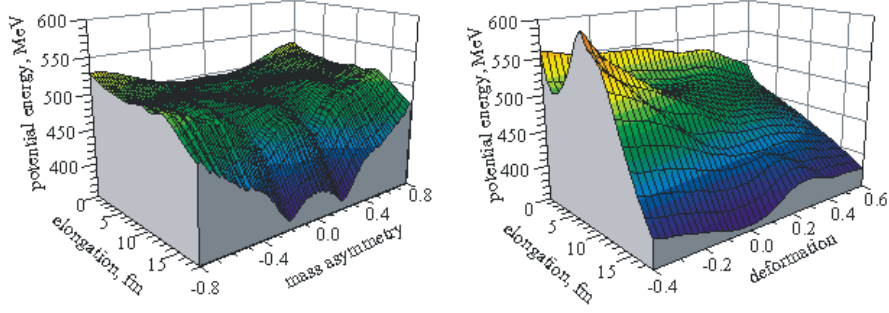
Figure 2: Multidimensional adiabatic potential energy surfaces for the ^{136}Xe + ^{209}Bi system in elongation - mass asymmetry coordinates (left) and elongation - deformation coordinates (right).
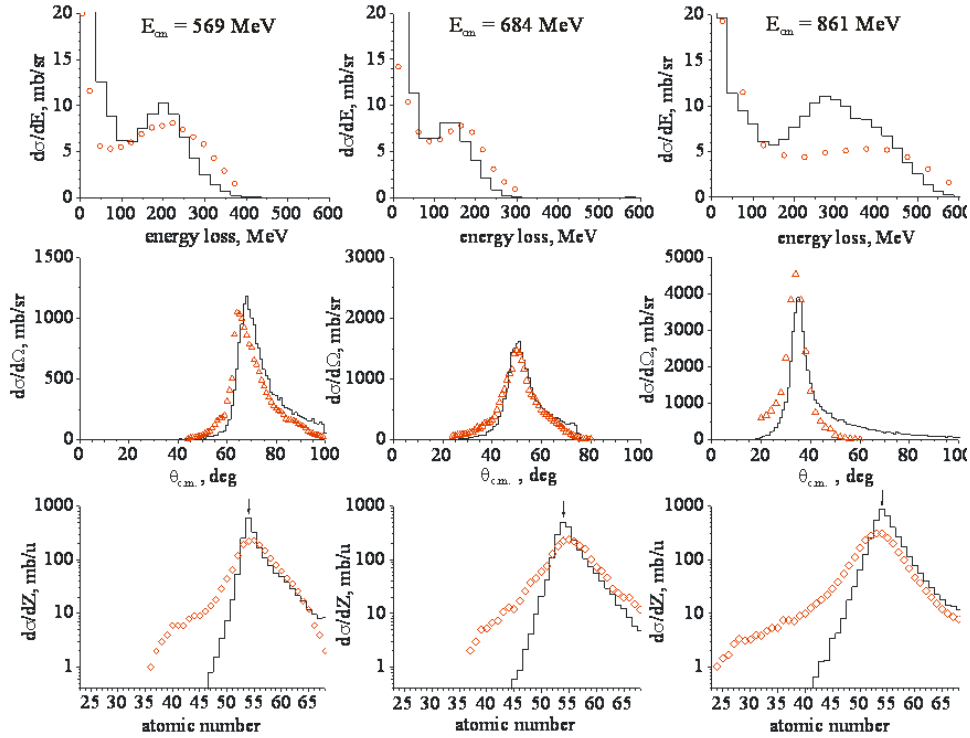
Figure 3: Comparison of experimental data (symbols) and theoretically calculated energy, angle and charge distributions (histograms) for the ^{136}Xe + ^{209}Bi reaction at energies $E_{cm} =$ 569, 684 and 861 MeV. Arrows illustrate the projectile's charge. The experimental data are taken from [7–9].

reaction was measured at different energies [7–9]. These experimental data include the energy distributions of reaction products as functions of total kinetic energy loss, the angular distributions of light fragments as functions of scattering angle at the center of mass system, and the charge distributions of light fragments as functions of atomic number. We calculate these distributions at three energies $E_{cm} =$ 569, 684, 861 MeV. All the theoretical distributions are in a good qualitative agreement with the corresponding experimental data (see Fig. 3). Some under-estimation of the outer shoulder of the charge distribution is visible for all reaction energies. It was mentioned in [7] that some contribution to these part of the charge distributions may be due to the sequential fission of Bi-like fragments.

137

The most important parameters of the model are friction and nucleon transfer coefficients μ_0 and λ_0. The performed analysis of the ^{136}Xe + ^{209}Bi reaction allowed us to fix these model parameters. The reasonable values $\mu_0 = 0.5 \cdot 10^{-22}$ Mev·s/fm3 and $\lambda_0 = 0.3 \cdot 10^{22}$ s^{-1} are determined.

Conclusion

The multidimensional dynamical model of nucleus-nucleus collisions was tested on the ^{136}Xe + ^{209}Bi reaction at three above-barrier energies. The model reproduces all basic features of heavy ion collisions. Such a good agreement between theoretically calculated and experimental data allows us to fix the model parameters.

References

[1] V. Zagrebaev and W. Greiner, J. Phys. G 34 (2007) 1.

[2] V. Zagrebaev and W. Greiner, J. Phys. G 35 (2008) 125103.

[3] P. Mller et al., At. Data and Nucl. Data Tables 59 (1995) 185 .

[4] J. Maruhn and W. Greiner, Z. Phys. A 251 (1972) 431.

[5] V. Zagrebaev et al., Phys. Part. Nucl. 38 (2007) 4.

[6] Nuclear Reaction Video project : http://nrv.jinr.ru/nrv/webnrv/driving/

[7] W.W. Wilcke et al., Phys. Rev. 22, 1 (1980) 128.

[8] W.U. Schrder et al., Phys. Rep. 45, 5 (1978) 301.

[9] H.J. Wollersheim et al., Phys. Rev. 24, 5 (1981) 2114.

THE MATHEMATICAL MODEL OF WAX DEPOSITION PROCESS IN THE PIPELINE

O. Strizhenko, D. Sergeev
St.Petersburg State University, St.Petersburg, Russia

Annotation

One of the most common problems in the heavy oil production involves the formation of paraffin wax deposits in pipelines. The inner surface of the pipeline becomes fouled with these paraffin deposits, which reduces the flow diameter, decreases overall through-out, and results in a higher pressure drop when oil is pumped through the pipeline. The deposits within the pipelines decrease the capacity of the duct and cause pipelines breaking. Wax deposition is a serious problem of oil production in the petroleum industry. Therefore, accurate prediction of this solid deposition problem can result in increasing the efficiency and safety of oil production.

The authors consider the problem of wax deposition in pipelines and the growth model of paraffin deposits in pipelines which is based on the model developed in the Michigan University. The model describes deposits growth time dependence based on molecular diffusion. This model also includes the aging of the deposits that is a process of increasing of the wax fraction in the deposit due to the internal diffusion.

This research is intended to be a part of the project dealing with the development of the flow simulator. The discussed model is to be integrated in the VSS (Ventilation System Simulator).

Introduction

Wax deposition is a very complex phenomenon that in recent years is one of the major challenges in oil industry. Wax deposited on the inner surface of crude oil pipelines can reduce or completely stop the oil flow and the oil industry bears large losses. The cost for preventing and removing paraffin deposits is substantial. The studies beginning from the early 1990s have shown that this cost amounts to as much as 0.25 of the global GPD Figure 1.

Predictive modeling of wax deposition has become an indispensable approach, not only to understand the fundamental physics of wax deposition during oil transportation in pipelines but also to design effective remediation strategies. Burger [3] investigated the main significant physical processes leading to wax deposition in pipelines and shown that particulate deposition such as shear dispersion, Brownian diffusion and gravity settling are not significant for the conventional flows in a pipeline [3], [4].

Our research is based on the model developed in the University of Michigan [5], [6], [7].The model describes deposits growth dependence on time based on molecular diffusion. This model also includes the ageing of the deposits that is a process of increasing of the wax fraction in the deposit due to the internal diffusion. A coupled system of differential equations is needed in order to describe the growth and the aging of the deposit (1) and
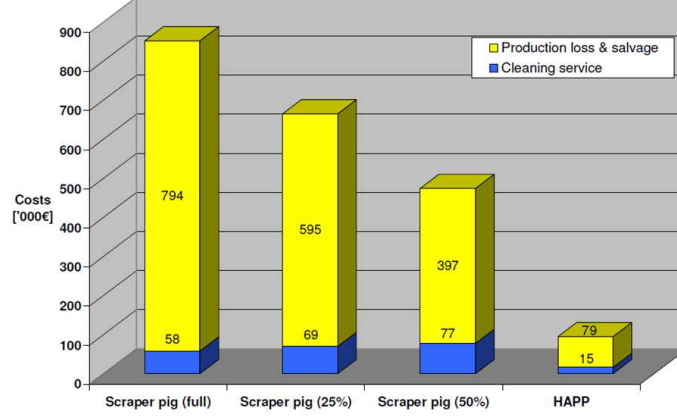
Figure 1: The costs required for cleaning procedures for 15 km length pipe with paraffin wax layer thickness 10 mm [1]

(2):

$$(-2\pi r_{eff})\rho_{wax}F_w\frac{dr_{eff}}{dt} = (2\pi r_{eff})K_M(C_b - C_{wo}(T_i)) - (2\pi r_{eff})\left[-D_e\left.\frac{dC}{dr}\right|_i\right] \qquad (1)$$

$$\pi\rho_{wax}(r_i^2 - r_{eff}^2)\frac{dF_w}{dt} = 2\pi r_{eff}\left[-D_e\left.\frac{dC}{dr}\right|_i\right] \qquad (2)$$

where $\rho_{wax}(kg/m^3)$ is the density of deposits, $r_i(m)$ is the radius of the clean pipe, $C_{wo}(kg/m^3)$ is the solubility of wax in oil, $F_w(-)$ is the wax content, $\frac{dC}{dr}|_i$ is the concentration gradient at the wall, $\frac{dF_w}{dt}(s^{-1})$ is the change of wax fraction in deposit with time (aging), $C_b(kg/m^3)$ is the concentration of the wax in the bulk, $T_i(K)$ is the pipe inlet temperature and $D_e(m^2/s)$ is the effective diffusivity in the deposit, $r_{eff}(m)$ is the effective flow radius at the time of interest, $K_M(m/s)$ - mass transfer coefficient.

Thus, the deposit thickness given by (3):

$$\delta(t) = r_i - r_{eff}(t) \qquad (3)$$

The continuity equations for heat and mass transfer, or the heat and mass balance equations, are used to obtain the temperature and concentration gradients in the fluid. Given in radial coordinates, the governing equation for heat transfer can be written as (4) and (5):

$$v_z\frac{\partial T}{\partial z} = \frac{1}{r}\frac{\partial}{\partial r}\left[r(\alpha_T + +\epsilon_H)\frac{\partial T}{\partial r}\right] - \beta(T - T_{wo}) \qquad (4)$$

$$v_z\frac{\partial C}{\partial z} = \frac{1}{r}\frac{\partial}{\partial r}\left[r(D_{wo} + \epsilon_m)\frac{\partial C}{\partial r}\right] - k_r(C - C_{ws}) \qquad (5)$$

Where $v_z(m/s)$ is the fluid velocity in lateral direction, $T(C)$ is the temperature, $C(kg/m^3)$ is the concentration of wax dissolved in oil, $z(m)$ is the axial distance, $r(m)$ is the radial position, ϵ_H and $\epsilon_m(m^2/s)$ are the turbulent heat and mass diffusivities, $\alpha_T(m^2/s)$ is the turbulent heat diffusivity, $D_{wo}(m^2/s)$ is the binary diffusion coefficient of wax in oil, $\beta(s^{-1})$ is a crystallization constant for heat of fusion and $k_r(s^{-1})$ is the precipitation rate constant.

Results and Discussion

During this research work the authors performed the simulation of the deposits growth in the pipe. The properties used in the modeling are presented in the Table 1:

Table 1: The parameters of the model used in the simulation

Pipe properties	length: $2.44m$; inner radius: $0.0072m$; wall temperature: $8.3°C$
Oil properties	density: $900kg/m^3$; thermal conductivity: $0.149W/(mK)$; specific heat: $1986J/(kgK)$; wax content: $0.67wt$
Paraffin properties	density: $970kg/m^3$
Oil flow properties	velocity: $0.2m/c$; temperature: $22.8°C$

Calculation results are presented in the corresponding figures below Figure 1 and Figure 2. The results were compared with the results obtained in the Michigan University and corresponded well to them.
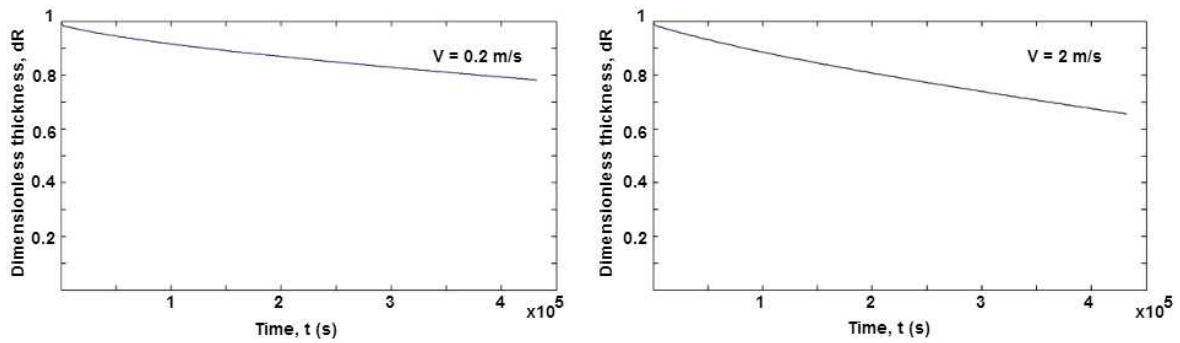
Figure 2: Dimensionless internal radius of the pipe in time depending on the velocity
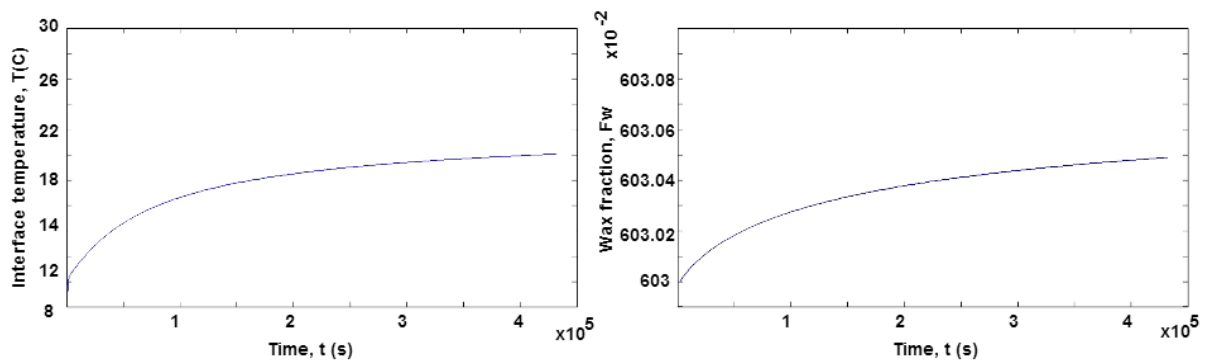
Figure 3: Interface temperature and wax content in time

Formation of paraffin wax deposition is a complex process, which is influenced by many factors: temperature differences, pressure changes, flow velocity, oil-water ratio,conduit

141

wall wettability and roughness, composition of the oil etc. The authors check the influence of velocity on the process of wax deposition. The results can be found at the Figure 1:

This research work is going to be a part of the project with regards to the development of the flow simulator and the discussed model is to be integrated in the SMTVSS. In the scope of this simulator complex network if pipeline is represented as graph. This representation enables to write mass and energy conservation laws in terms of the graph components by rules developed by Kirchhoff and are known as Kirchhoff's laws and simplify the flow distribution problem resolving [8].

An integration of WALTER into SMTVSS add a possibility to provide quick flow distribution calculation in the scope of complex network of pipelines and more detailed calculation of wax deposition growth in the certain pipelines in which f.e. this growth is the most likely.

References

[1] S. Mokhatab, B. Towler *Wax prevention and remediation in subsea pipelines and flowlines* [Internet].World Oil Online Magazine Article(IA) (2009);

[2] L. F. A. Azevedo, A. M. Teixeira, Petr. Scien. Tech. (2003) 393.

[3] E. D. Burger, T. K. Perkins, J. H. Striegler, JPT, 6 (1981) 1075.

[4] J.J.C. Hsu, M.M. Santamaria, *Wax Deposition of Waxy Live Crudes Under Turbulent Flow Conditions*, (69th Annual Technical Conference and Exhibition in New Orlean LA), (1994) 25.

[5] Zh. Huang, *Application of the fundamentals of heat and mass transfer to the investigation of wax deposition in subsea pipelines*, (University of Michigan, PhD, 2011).

[6] K. Rosvold, *Wax deposition models*, (Norwegian University of Science and Technology, Master Thesis), June 2008

[7] P. Singh, R. Venkatesan, H. S. Fogler, N. R. Nagarajan, AIChE J., (46) (2000) 1059.

[8] O.Strizhenko, Mod. Prob. Appl. Math. & Computer Science, (2012) 226.

PARALLEL REALIZATIONS OF LOCALLY ONE-DIMENSIONAL DIFFERENCE SCHEMES FOR SOLVING THE INITIAL-BOUNDARY VALUE PROBLEMS FOR THE MULTIDIMENSIONAL HEAT EQUATIONS

V. A. Tokareva* †, Streltsova O.I., Zuev M.I.
Joint Institute for Nuclear Research, Dubna, Russia

Annotation

Economic schemes are especially useful for solving initial-boundary problems for multidimensional heat equations using the finite difference method. Parallel realizations of locally one-dimensional schemes for solving initial-boundary problems for multidimensional quasilinear heat equation are considered in the work. They allow to perform calculations on multicore computing nodes (OpenMP realization), calculations using graphics processing units (CUDA realization) and Intel Xeon Phi coprocessors (OpenMP realization with coprocessor extensions). Comparative analysis of efficiency for developed parallel realizations has been performed.

Introduction

Actual problems of modern physics lead to the need for solving the equations of mathematical physics, described in [1–3]. One of the basic groups of such problems is related to the heat equation.

Therefore, it is actual to develop and implement a variety of parallel algorithms for solving initial-boundary value problems for heat equations using different approaches to the selection of schemes for the numerical solution.

Computational scheme

We seek a solution of the initial-boundary value problem for the two-dimensional heat equation:

$$\frac{\partial U}{\partial t} = \sum_{\alpha=1}^{2} \frac{\partial}{\partial x_\alpha} \left(k_\alpha(x,t) \frac{\partial U}{\partial x_\alpha} \right) + f(x,t), \ x \in D, \ t > 0, \tag{1}$$

where $U = U(x,t)$ is the temperature, which is the function of the spatial coordinates $x = (x_1, x_2)$ and time t, $k_\alpha(x,t)$ are the coefficients of temperature conductivity, $f(x,t)$ is the power density of the heat sources/sinks, D is the bounded rectangular area with edge Γ, defined with initial-boundary conditions

$$\begin{cases} U(x,0) = U_0(x) \\ U|_\Gamma = \mu(x,t) \end{cases} \tag{2}$$

using locally one-dimensional scheme

$$\frac{\partial v_\alpha}{\partial t} = L_\alpha v_\alpha + \varphi_\alpha, \quad t_j \le t \le t_{j+1} \tag{3}$$

where $L_\alpha v(\alpha) = \frac{\partial}{\partial x_\alpha}\left(k_\alpha(x,t)\frac{\partial v(\alpha)}{\partial x_\alpha}\right)$, $\sum_{\alpha=1}^{2}\varphi_\alpha = f$ (further we take $\varphi_1 = f$, $\varphi_2 = 0$) and the following coupling conditions are fulfilled: $v_\alpha^j = v_{\alpha-1}^{j+1}$ on the grid

$$\omega = \omega_\tau \times \omega_{h_x h_y}, \quad \omega_\tau = \{t_j = j\tau, j = 0, \ldots, N_t - 1\},$$

$$\omega_{h_x h_y} = \{(x_{i_1}, y_{i_2} : \ x_{i_1} = x_l + i_1 h_x, i_1 = 0, \ldots, N_{x-1}; \ \ y_{i_2} = y_l + i_2 h_y, i_2 = 0, \ldots, N_{y-1}\}.$$

An important advantage of this method is that it includes the best features of explicit schemes, demanding small amount of calculations, and implicit ones, being unconditionally stable [4].

We used the computational difference scheme with weights [1]:

$$\frac{v^{n+1} - v^n}{\tau} = \sigma\Lambda(v^{n+1}) + (1-\sigma)\Lambda(v^n) + f, \quad t = 0, ..., N_t - 1, \ \ \sigma \in [0,1],$$

leading to the system of linear algebraic equations (SLAE) of the following kind:

$$\frac{\sigma}{h^2}v_{i+1}^{n+1} - \left(\frac{2\sigma}{h^2} + \frac{1}{\tau}\right)v_{i+1}^{n+1} + \frac{\sigma}{h^2}v_{i-1}^{n+1} = -\left(f_i + (1-\sigma)\frac{v_{i+1}^n - 2v_i^n + v_{i-1}^n}{h^2} + \frac{v_i^n}{\tau}\right),$$

$$i = 1, ..., N - 1, \ \ t = 0, ..., N_t - 1, \ \ \sigma \in [0,1],$$

with grid steps h for x and τ for t, solved by the tridiagonal matrix algorithm [2].

Accuracy of calculations using the scheme was considered by the equation:

$$\varepsilon_n = \max_{0 \le i \le N} | v_i - U_i | .$$

Analysis of realizations

For considring numerical scheme the next parralel realisations of algorithm were developed: CPU realization using OpenMP [5] technology; OpenMP realization with coprocessor extensions for Intel Xeon Phi [6] coprocessors, GPU realization using CUDA [7] technology.
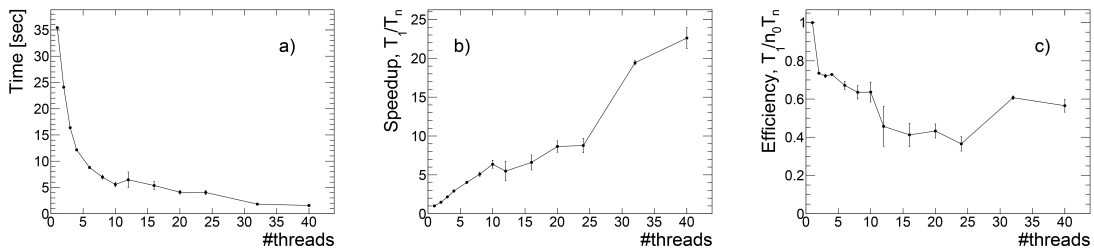
Figure 1: a) Computation time; b) speed-up; c) efficiency for the two-dimensional heat equation vs. the number of threads, OpenMP realization

All realizations were implemented on C++ language using parallel libraries for OpenMP and CUDA technologies. For solving SLAE MKL [8] library was used for CPU and cuS-PARSE [9] for GPU realisations.

For comparing CPU realisations (Fig. 1, 2) the following characteristics were used: computational time, speedup T_1/T_n, efficiency $T_1/n_0 T_n$, where T_1 is calculation time for one-thread run, T_n is calculation time for n-thread run and n_0 is number of threads.

For GPU realization calculation time was compared with ones for single CPU and 40-thread CPU OpenMP realizations (Fig. 3).
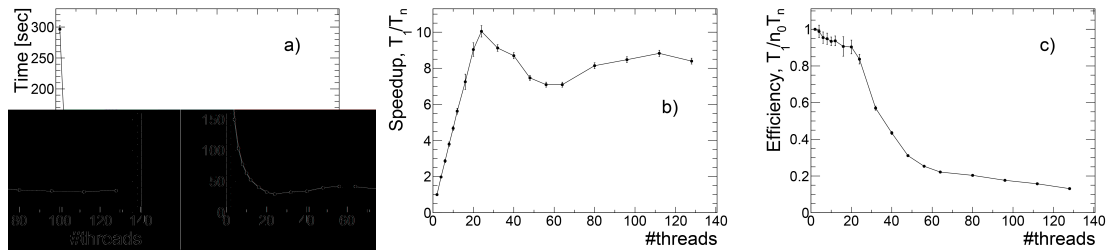
Figure 2: a) Computation time; b) speed-up; c) efficiency for the two-dimensional heat equation vs. the number of threads, OpenMP& coproc. Xeon Phi realization
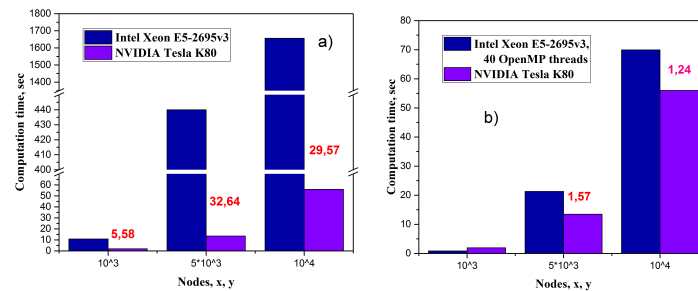
Figure 3: Comparison of computation time for a) single CPU and single GPU (CUDA) cores; b) 40-thread CPU realization (OpenMP) and single GPU core (CUDA).

The calculations were performed on heterogeneous computing cluster HybriLIT [10] (LIT JINR), and the parallelization details are presented in the Parallel features project [11] together with the program solutions for all computing architectures mentioned above.

Conclusions and outlook

Parallel implementations using OpenMP and CUDA technologies have been implemented and tested using resources provided by the cluster.

An acceleration has been studied for various numbers of grid nodes and threads on the CPU and GPU architectures.

Parallel algorithms allow reducing the time of calculations by the factor of 23 using the multicore component of the cluster (where OpenMP is the algorithm realization) and by the factor of up to 32,64 using the graphical accelerators (where CUDA is the algorithm realization). On the other hand, for tasks with small (about 10^3) grid sizes CPU realization shows better computing times (about 2,25 times faster).

Out further studies will be aimed on improving OpenMP for Xeon Phi realization.

References

[1] A. A. Samarskii, A. N. Tichonov *Equations of Mathematical Physics*, (Courier Corporation, 1963, p. 765).

[2] A. A. Samarskii *Introduction into theory of difference schemes*, (M.: Nauka, 1971, p. 552)

[3] A. A. Samarskii, A. V. Gulin *Numerical methods*, (M.: Nauka, 1989, p. 432)

[4] S. I. Serdjukova, Comput. Math. Math. Phys., 4 (1964) 212.

[5] Official OpenMP web source: – http://www.openmp.org/

[6] *Building a Native Application for Intel Xeon Phi Coprocessors, official Intel web source*: https://software.intel.com/en-us/articles/building-a-native-application-for-intel-xeon-phi-coprocessors

[7] *Cuda parallel computing, official Nvidia web source*: http://www.nvidia.ru/object/cuda-parallel-computing-ru.html

[8] *Intel Math Kernel Library*, web source: http://software.intel.com/en-us/intel-mkl

[9] *Cuda toolkit documentation: cuSPARSE*: http://docs.nvidia.com/cuda/cusparse/#abstract

[10] *Heterogeneous cluster HybriLIT*, Official site: http://hybrilit.jinr.ru/

[11] *Parallel features* project.: https://gitlab-hlit.jinr.ru/

ON THE ENTANGLEMENT SPACE REPRESENTATION FOR 2-QUBIT SYSTEM IN THE MIXED X-STATES

A. Khvedelidze[1,2,3*], A. Torosyan[1†]

[1] *Joint Institute for Nuclear Research, Dubna, Russia*

[2] *Institute of Quantum Physics and Engineering Technologies, Georgian Technical University, Tbilisi, Georgia*

[3] *National Research Nuclear University, MEPhI, Moscow, Russia*

Annotation

The problem of quantification of entanglement/separability is exemplified by 2-qubit system in the so-called mixed X-states. For this system the 5-dimensional representation of the entanglement space $\mathcal{E}_X$ is given and its subspace, corresponding to the separable X-states, is identified. It is shown, that among the X-states density matrices, with an arbitrary given spectrum, there exists the 4-parametric family of separable states.

Introduction

According to the axioms of quantum mechanics, an arbitrary quantum system in a mixed state is characterized by a Hermitian, semipositive density operator with the unit trace. For a composed bipartite system the density operator acts on the tensor product space, $\mathcal{H} = \mathcal{H}_1 \otimes \mathcal{H}_2$, where $\mathcal{H}_1$ and $\mathcal{H}_2$ are the Hilbert spaces of A and B subsystems respectively. If the corresponding mixed state admits a convex decomposition

$$\varrho = \sum_k \omega_k \varrho_1^k \otimes \varrho_2^k, \qquad \omega_k \geq 0, \quad \sum_k \omega_k = 1,$$

with subsystems density operators ϱ_1^k, ϱ_2^k and probability distribution ω_k, then it is called **separable**. States, that cannot be written in this form, are the **entangled** [1].

In the present note we consider a special class of bipartite 2×2 system, composed from a pair of 2-level subsystems, a 2-qubit systems. Namely, let two qubits be in the so-called X-state, the state whose density matrix has a shape, similar to the Latin letter "X"(see for details [2] and [3]):

$$\varrho_X = \begin{pmatrix} \varrho_{11} & 0 & 0 & \varrho_{14} \\ 0 & \varrho_{22} & \varrho_{23} & 0 \\ 0 & \varrho_{32} & \varrho_{33} & 0 \\ \varrho_{41} & 0 & 0 & \varrho_{44} \end{pmatrix}, \tag{1}$$

where the diagonal entries are real numbers, while the elements of the minor diagonal are pairwise complex conjugated. Taking into account the unit trace condition, we conclude, that the most generic X-state is 7-parametric.

Correlations in a composite system depend only on the relative characteristics of its parts. Such characteristics are known by the name of the **Local Unitary (LU)** invariants, the scalar functions of density matrices, invariant under the LU-group action. The latter is

---

the subgroup of the unitary group, that acts on each subsystem independently. These LU-invariants can be considered as functions, whose domain of definition is the so-called **entanglement space** $\mathcal{E}$, which is given by the following quotient:

$$\mathcal{E} := \frac{\text{State space}}{\text{Group of LU-transformations}}. \tag{2}$$

For a generic binary system, composed from two n_1, n_2-dimensional subsystems, the LU--transformations form the subgroup $\mathrm{U}(n_1) \times \mathrm{U}(n_2) \subset \mathrm{U}(n)$ and entanglement space is $\mathfrak{P}_+(\mathbb{R}^{n^2-1})/\mathrm{U}(n_1) \times \mathrm{U}(n_2)$. Here we are interested in the description of entanglement in specific 2-qubit system with mixed X-states. Therefore, identifying the space state in the equation (2) with the 7-dimensional space of X-states and the group of LU-transformations in its denominator with the corresponding LU-group, $G_X = SO(2) \times SO(2)$, we arrive at the entanglement space of the mixed X-states, $\mathcal{E}_X$. In the next sections the representation for the entanglement space $\mathcal{E}_X$ will be given and its subvariety of *separable states* will be described.

Eigenvalue decomposition for X-states

At first, let us note that every $X-$state (1) under the action of 2-parametric diagonal unitary matrices

$$K(u,v) = \mathrm{diag}\left[e^{iu}, e^{iv}, e^{-iv}, e^{-iu},\right], \qquad u, v \in [0, 2\pi], \tag{3}$$

transforms to the $X-$state, whose all entries are nonnegative. Indeed,

$$K(u,v)^{\dagger} \varrho_X K(u,v) = \begin{pmatrix} \varrho_{11} & 0 & 0 & e^{-2iu}\varrho_{14} \\ 0 & \varrho_{22} & e^{-2iv}\varrho_{23} & 0 \\ 0 & e^{2iv}\varrho_{32} & \varrho_{33} & 0 \\ e^{2iu}\varrho_{41} & 0 & 0 & \varrho_{44}. \end{pmatrix}. \tag{4}$$

Hence, for $2u = \mathrm{Arg}(\varrho_{14})$ and $2v = \mathrm{Arg}(\varrho_{23})$ the resulting $X-$state represents a real symmetric matrix with positive elements. Noting, that $K(u,v)$ can be written as the direct product of two copies of the Cartan subgroup of $SU(2)$

$$K(u,v) = \exp(\imath \frac{u+v}{2}\sigma_3) \times \exp(\imath \frac{u-v}{2}\sigma_3), \tag{5}$$

with the standard Pauli matrices $(\sigma_1, \sigma_2, \sigma_3)$ basis for $\mathfrak{su}(2)$ algebra, we conclude that any 7-dimensional $X-$state is $G_X = SO(2) \times SO(2)-$equivalent to a certain 5-dimensional representative state. Furthermore, using the principal axis transformation for the real symmetric 5-parametric density matrix, we arrive at the following parametrization:

$$\varrho_X = K(u,v)W(\phi_1, \phi_2)P\mathrm{diag}(\lambda_1, \lambda_2, \lambda_3, \lambda_4)PW^{\dagger}(\phi_1, \phi_2)K^{\dagger}(u,v), \tag{6}$$

where the spectrum $\{\lambda_1, \lambda_2, \lambda_3, \lambda_4\}$ forms a partially ordered simplex $\underline{\Delta}_3$:

$$\sum_{i=1}^{4} \lambda_i = 1, \quad 1 \geq \lambda_1 \geq \lambda_2 \geq 0, \quad 1 \geq \lambda_3 \geq \lambda_4 \geq 0. \tag{7}$$

and

$$W(\phi_1, \phi_2) = \left(\begin{array}{c|c} e^{i\frac{\phi_1}{2}\sigma_2} & 0 \\ \hline 0 & e^{i\frac{\phi_2}{2}\sigma_2} \end{array} \right), \qquad P = \left(\begin{array}{cccc} 1 & 0 & 0 & 0 \\ 0 & 0 & 0 & 1 \\ 0 & 0 & 1 & 0 \\ 0 & 1 & 0 & 0 \end{array} \right).$$

The equation (6) shows that the entanglement space $\mathcal{E}_X$ locally represents the 5-dimensional direct product space with three factors, $\mathcal{E}_X \sim \underline{\Delta}_3 \times S^1 \times S^1$.

The X-states separability

The representation (6) is well adapted to the analyse of the separability as a function of density matrices eigenvalues $\{\boldsymbol{\lambda}\}$. To formulate the separability criterion, one can use the concept of a partial transposition of a 2-qubit density matrix, which is defined as a transposition operation in one of two subsystems (say, in the second one): $\varrho^{T_2} = I \otimes T\varrho$. Under the transposition the Pauli matrices change as $T(\sigma_1, \sigma_2, \sigma_3) \to (\sigma_1, -\sigma_2, \sigma_3)$. According to the Peres-Horodecki criterion [4], which is a necessary and sufficient condition of separability for 2×2 and 2×3 dimensional systems, a state ϱ is separable iff its partial transposition is semi-positive as well. Applying the Peres-Horodecki criterion to the diagonal 5-dimensional X-state density matrix (6), we find that the X-state density matrix is separable iff:

$$\begin{cases} (\lambda_1 - \lambda_2)^2 \cos^2 \phi_1 + (\lambda_3 - \lambda_4)^2 \sin^2 \phi_2 \leq (\lambda_1 + \lambda_2)^2, \\ (\lambda_3 - \lambda_4)^2 \cos^2 \phi_2 + (\lambda_1 - \lambda_2)^2 \sin^2 \phi_1 \leq (\lambda_3 + \lambda_4)^2. \end{cases} \tag{8}$$

The separability conditions (8) can be rewritten in the form of two linear inequalities:

$$\begin{cases} x - y \leq a, & 0 \leq x \leq c, \\ y - x \leq b, & 0 \leq y \leq d. \end{cases} \tag{9}$$

in two variables:

$$x = (\lambda_1 - \lambda_2)^2 \cos^2 \phi_1, \qquad y = (\lambda_3 - \lambda_4)^2 \cos^2 \phi_2 \tag{10}$$

and four parameters:

$$a = (\lambda_1 + \lambda_2)^2 - (\lambda_3 - \lambda_4)^2, \quad c = (\lambda_1 - \lambda_2)^2, \quad b = -(\lambda_1 - \lambda_2)^2 + (\lambda_3 + \lambda_4)^2, \quad d = (\lambda_3 - \lambda_4)^2,$$

obeying the inequalities:

$$a + b \geq 0, \quad a + d \geq 0, \quad b + c \geq 0. \tag{11}$$

Now it is an easy to check that the inequalities (9) have solutions with respect to x and y for all possible values of parameters a, b, c and d, constrained by the equations (11). In other words, for all eigenvalues from the partially ordered simplex (7), the inequalities (8) determine non empty definition domain of angles ϕ_1 and ϕ_2 in the representation (6). Typical domains on the (x, y)−plane are depicted on the Fig. 1.
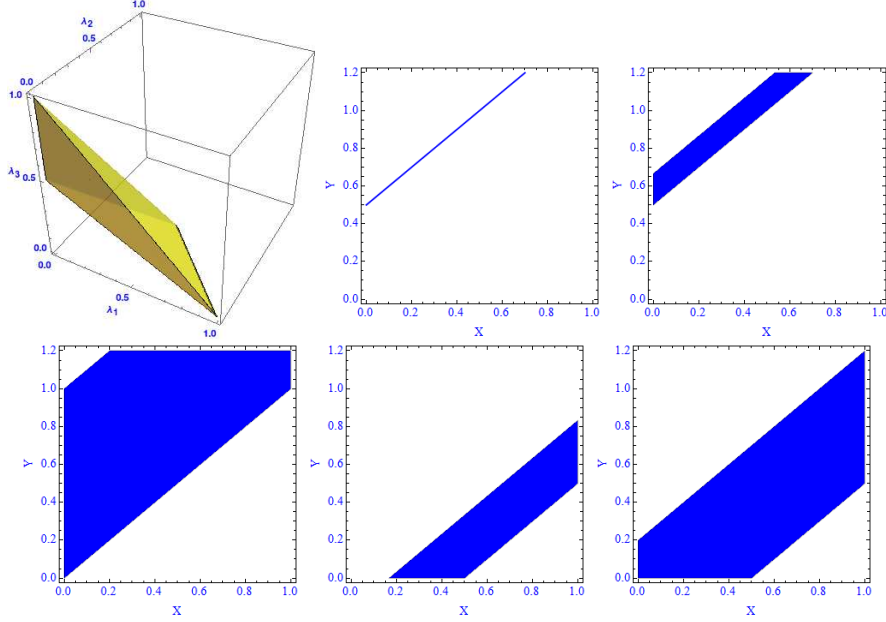
Figure 1: Plot (I) - the partially ordered simplex $\underline{\Delta}_3$. Plots (II-VI) - families of solutions to the Eqs. (9) corresponding to the following decomposition of $\underline{\Delta}_3$: Domain (II) : $a < 0$, $b = -a$, $c \geq 0$, $d \geq b$; Domain (III): $a < 0$, $b > -a$, $c \geq 0$, $d \geq -a$; Domain (IV): $a = 0$, $b \geq 0$, $c \geq 0$, $d \geq 0$; Domain (V): $a > 0$, $-a \leq b \leq 0$, $c \geq -b$, $d \geq 0$; Domain (VI): $a > 0$, $b > 0$, $c \geq 0$, $d \geq 0$.

Conclusions

As it was mentioned above, the entanglement properties of 2-qubit states remain unchanged under the LU-transformations and hence they admit description in terms of the corresponding polynomial invariants in elements of the density matrices. More precisely, the entanglement space $\mathcal{E}$ can be parametrized by these LU-invariants. Particularly, since the Peres-Horodecki separability criterion can be written in the form of polynomial inequalities in the $SU(2) \otimes SU(2)$- invariant polynomials [5], [6] the space of separable states can be characterized using the LU-invariants. It is worth to note, that the description for separable X-states of 2-qubit system, proposed in the present note, is an alternative to the usage of the polynomial invariants. The reveal of connections between two approaches we leave for the forthcoming publications.

References

[1] R.F. Werner, Phys. Rev. A 40 (1989) 4277.

[2] T. Yu and J.H. Eberly, Quant. Inform. Comp., 7 (2007) 459.

[3] P. Mendonca, M. Marchiolli and D. Galetti, Ann. Phys.. 351 (2014) 79.

[4] A. Peres, Phys. Rev. Lett. 77 (1996) 1413.

[5] V. Gerdt, A. Khvedelidze and Yu. Palii, Zapiski POMI 373 (2009) 104.

[6] V. Gerdt, A. Khvedelidze and Yu. Palii, Phys. of Atomic Nucleii, 74 (2011) 893.

High Energy Physics

NOνA TEST BENCH AT JINR

A. I. Antoshkin[1],[*], N. V. Anfimov[1], O. B. Samoylov[1], A. P. Sotnikov[1]

[1]*Joint Institute for Nuclear Research, Dubna, Russia*

Annotation

The main goal of the NOνA experiment is to study oscillation parameters in the neutrino and antineutrino beams: measurements of the mass hierarchy and CP-violation phase in the lepton sector. Two identical highly-segmented detectors based on PVC-tubes filled with a liquid scintillator to detect signals from muon and electron neutrinos were built. Masses of each are 300 and 14000 tons. Avalanche PhotoDiode is used to measure signal response. Total amount of these devices in the large Far Detector is 344064. The NOνA test bench was made at JINR for studying native electronic responses through Avalanche PhotoDiode and Front-End board chain. The bench was used to perform investigations for physical signals in the detectors also. In this work we are presenting the NOνA-JINR bench results which show signal shaping studies, simulation of the electronic response on hypothetical magnetic monopole signals and other required to do simulations and precise energy measurements.

Introduction

A NOνA cell is a tube filled with liquid scintillator. Light from the scintillator is captured by the fibers and is transmitted to the APD. Fibers from 32 cells are grouped on one APD board (See Fig. 1, left panel).
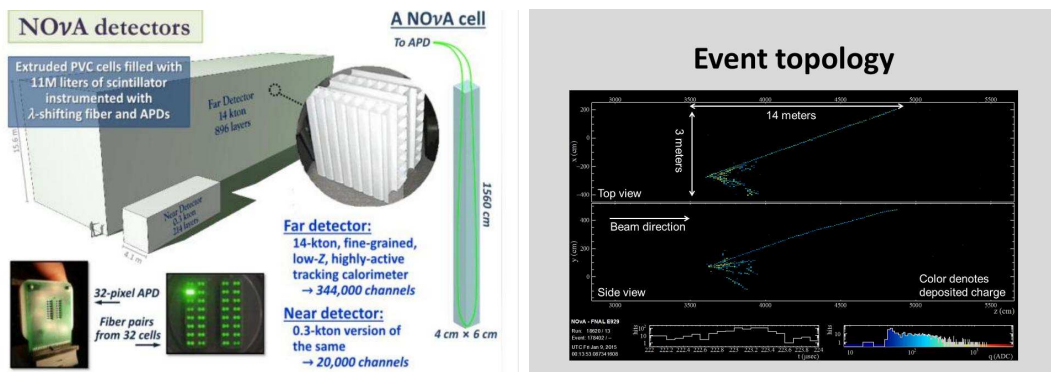
Figure 1: Left Panel: general design of NOνA detectors. Right panel: event display

Neutrino production

The NuMI beam at Fermilab creates a "spill" of neutrinos every 1.3 seconds. Each spill lasts for only 10 millionths of a second: and careful timing (with the aid of the GPS

system) is used so that the computers collecting the NOνA data know exactly in which 10 microseconds this happened. Looking only at the slice of time during which the beam fired now shows only two things: a cosmic ray muon on the left side of the detector, and the interesting spray to the right (See Fig. 1, right panel). That is the result of a neutrino from Fermilab hitting an atom in the NOνA detector, producing a spray of subatomic particles that cause the scintillator they pass to give off flashes of light. The scale on the bottom right is color-coded to show how much light each cell saw: from blue (not a lot) to red (a thousand times the minimum). For more details see [1].

This q is the number of the ADC counts. Signals that we are looking for the main NOνA scientific goals are not really huge ($q < 100$).

Flashes
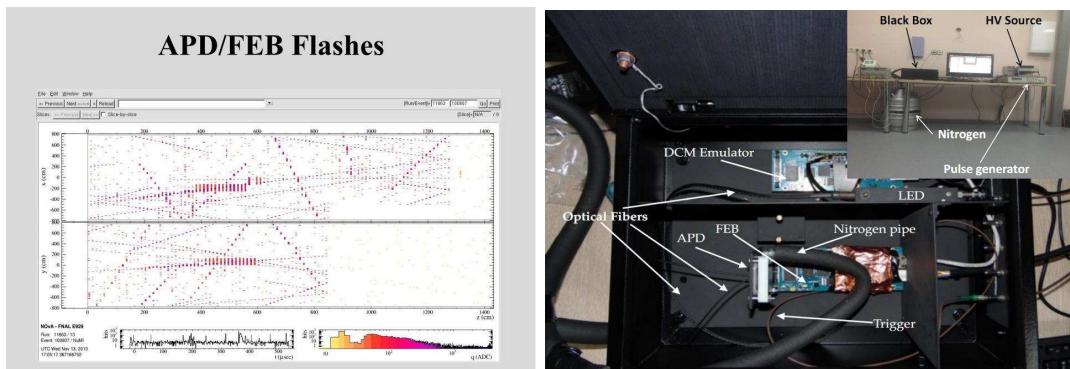
Figure 2: Left panel: event display for the Far detector. Right panel: design of the Bench

We can see the interesting hit structures on Fig. 2, left panel. They were called Flashes. The main feature of the flashes is that most of the FEB channels in the same FEB produce signals over thresholds simultaneously (See [2]) but these events take place only in high energy region. It makes them really important for high energy deposition and may take effect on background estimation (cosmic muons) or some Exotics (monopoles etc).

That's why one of the main reasons to have test bench was the investigation of hit structures but of course it is not only one. It is possible to measure the shaping parameters of the electronics and electronics' response to different initial light signals. It is very important for the MC simulation and right understanding of the electronics behaviour.

General technical information

NOνA test bench at JINR consists of a few parts (See Fig. 2, right panel). First is the native NOνA electronics – Avalanche PhotoDiode and Front-End Board. Second is the special hardware – download cable, DCM-emulator, LED, Low and High Voltage Sources, Pulse generator and cooling system. Third is a PC with necessary software.

All sensitive devices were put into a black metal box. The black box allows to perform all the measurements with photodetectors like APD and PMT and screens all external

electromagnetic noises. Since APD in NOνA operate at -15 degrees we employed the cooling system based on Nitrogen evaporation flow.

Pulse generator waits for the FEB trigger and sends the electric pulse to the LED. After that the light pulse from the LED comes through the fibers to the APD and FEB is reading at this moment.

Results

Cross-talk measurements and dynamic range extension

When test bench had been built we started with APD response on different light intensities measurements. It was very important for understanding the detectors performance for high energy dissipations. By sending very high intensity light into a single APD pixel which saturates ADC we found out that the same small inverted signals occur in most of channels. First we checked FEB by injecting a huge charge into a single FEB channel and we observed normal cross-talk in neighboring channels that drops exponentially. The next step was to check APD feeding chain. We performed measurement of APD gain with different temperatures to study APD operation voltage at different temperatures (See Fig. 3, left panel). In NOνA detectors all the APDs operate with the gain about 100. We employed different capacitors into FEB PCB and obtained different value of negative cross-talk pulse. The suggestion was that capacitance blocks a voltage drop which was named signal sag.

Sag is a value of the amplitude of the inverted signal in the neighboring channels in case of huge amplitude in the primary one. We put different amplitudes to APD and measured the value of the sag. The first result was that relative value of the sag doesn't depend on the amplitude. It is equal to 1.89% Sag doesn't depend on the temperature and only thing that can define it is bypass capacitor (See Fig. 3, right panel). If we replace original capacitor by 9.4 nF we could reduce the effect sevenfold. This effect could be very helpful for extending of the ADC dynamic range. Sag can be measured in many channels (up to 31) which gains precision. As the result we can increase the statistics and expand the dynamic range by 10 times. For more information about the results of the bench activity see [3].

Monopole simulation

The approximate scheme of the special analog simulation of the electronic's response on hypothetical magnetic monopole signals (See Fig. 4). "Ordinary" response is the standard behaviour of our electronics for the external signal. Underneath there is a theoretically predicted monopole signal. Since monopole leaves a huge energy and travels slowly through the detector the light pulse duration may reach level of a few μs. After the convolution with electronic shaping it was anticipated to obtain signal like it shown on Fig. 4. During the simulation we noticed that the tail of the signal was longer than it's expected and it depends on the amplitude. The behaviour of this effect is linear.

155
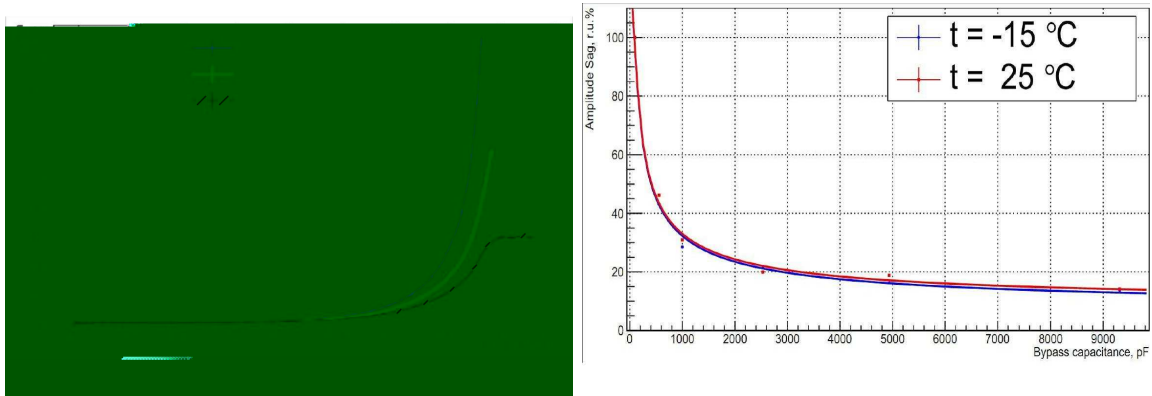
Figure 3: Left panel: APD gain dependence on voltage with different temperatures. Right panel: Sag reduction dependence vs capacitance on APD board
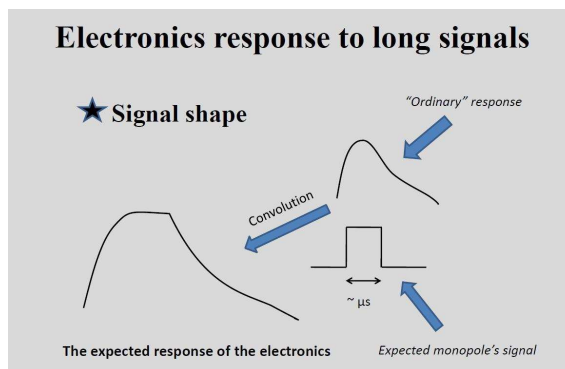
Figure 4: Monopole simulation

Response to long signals

Special kind of experimental setup was made for this purpose. In addition to the ordinary setup PMT and Digitizer were added (See Fig. 5). PMT was used to monitor the shape of
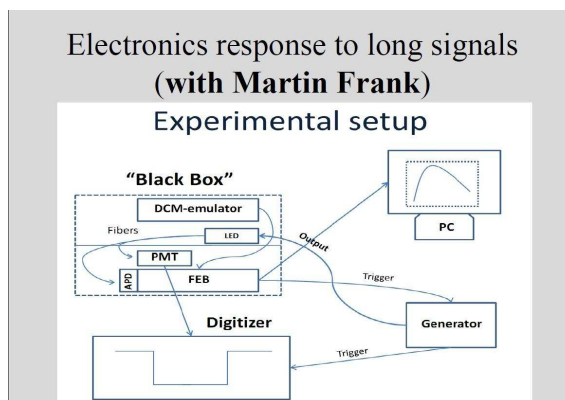
Figure 5: Experimental setup for monopole simulation

the initial light pulse and ADC with fast sampling to digitize PMT's signals. The main idea was to send light with the same integral intensity which corresponds to the constant charge.

156

We tried to generate rectangular-like light pulses. The ASIC shaper integrates the APD pulse width and converts into a Rise time and shaping parameters vary on pulse amplitude. We thank Dr. Martin Frank for useful discussions and help during this measurement.

Shaping parameters

For simulation of the detectors performance NOνA collaborators asked us to find all the shaping parameters for both detectors. It was necessary for computer modeling and simulations. The concept of the measurement was the same that aforementioned. The fall time isn't fit to the table value. It linearly depends on the amplitude. The Rise time doesn't fit to the table value either but it doesn't vary or the variation is negligible.

Conclusions

We develop the powerful tool for direct manipulation and measurements with NOνA electronics. A lot of issues have been solved and we hope that JINR NOνA bench will solve many problems or clarify some misunderstood features in the future.

References

[1] Site of the NOνA experiment. URL: https://www-nova.fnal.gov/

[2] N. Anfimov *et al.*, DocDB – 11405-v1 (unpublished).

[3] A. Antoshkin, DocDB – 14261-v1 (unpublished).

STUDYING OF ZONAL CHARACTERISTICS OF PMT

T. A. Antoshkina*

Joint Institute for Nuclear Research, Dubna, Russia

Annotation

The JUNO experiment requires a huge ammount of PMTs because required sensitivity may be achieved by maximazing collection efficiency. That's why the mass testing techniques have to be developped. The integral characteristics of PMT, which are made faster and easier, are less sensitive to variations in the zonal characteristics of the photocathode. The differential measurements may be used as a cross-check for the integral ones. The theoretical calculation of the number of photons absorbed in photocathode was made taking into account Fresnel coefficients between media with differing refractive indices.

Formulation of the problem

An unique experiment, named JUNO for Jiangmen Underground Neutrino Observatory is under construction in southern China by a wide international collaboration. One of the JUNO's main challenges is required energy resolution of 3% at 1 MeV of released energy in order to be sensitive to the neutrino mass ordering effects. We would like to understand, how the zonal characteristics eventually influence on the integral ones. This requires to know how the quantum efficiency at each PMT's point influence on overall quantum efficiency of the PMT.

Quantum Efficiency

There are 2 types of Quantum Efficiency. External Quantum Efficiency (EQE) is the ratio of the number of collected charge carriers to the number of photons of a given energy shining from outside (incident photons). Internal Quantum Efficiency (IQE) is the ratio of the number of collected charge carriers to the number of photons of a given energy that shine from outside and are absorbed inside.

$$EQE \quad = \quad \frac{electrons/sec}{photons/sec} \tag{1}$$

$$IQE \quad = \quad \frac{electrons/sec}{absorbed\,photons/sec} = \frac{EQE}{1 - Reflection - Transmission} \tag{2}$$

The IQE is always larger than the EQE. A low IQE indicates that the active layer is unable to make good use of the photons. The EQE therefore depends on both the absorption of light and the collection of charges. Once a photon has been absorbed and has generated an electron, this electron must be collected. Good work of PMT requires good IQE. We can measure EQE, becaucse we know the light source power and a signal collected from the PMT. Consequently, to calculate IQE it is necessary to know how much

---

*ta.antoshkina@gmail.com

light is absorbed in the PMT's photocathode.

General Formulas

The simpliest case

Let's consider first the simpliest case refraction at the boundary between two non-absorbing media. In general, light falls on the boundary at an angle θ_0. Part of the light reflects back into the medium from which light is incident and the remaining portion passes to a different medium. Moreover, reflection and refraction of light is different for different polarizations. Let's consider coefficients of reflection R_s, R_p and transmission T_s, T_p depending on the incidence angle θ_0.

$$r_{if}^s = \frac{n_i \cos(\theta_i) - n_f \cos(\theta_f)}{n_i \cos(\theta_i) + n_f \cos(\theta_f)}, \quad t_{if}^s = \frac{2n_i \cos(\theta_i)}{n_i \cos(\theta_i) + n_f \cos(\theta_f)} \tag{3}$$

$$r_{if}^p = \frac{\frac{1}{n_i} \cos(\theta_i) - \frac{1}{n_f} \cos(\theta_f)}{\frac{1}{n_i} \cos(\theta_i) + \frac{1}{n_f} \cos(\theta_f)}, \quad t_{if}^p = \frac{\frac{2}{n_i} \cos(\theta_i)}{\frac{1}{n_i} \cos(\theta_i) + \frac{1}{n_f} \cos(\theta_f)} \tag{4}$$

$$R_s = |r_{01}^s|^2 = \left(\frac{n_0 \cos(\theta_0) - n_1 \cos(\theta_1)}{n_0 \cos(\theta_0) + n_1 \cos(\theta_1)} \right)^2, \quad T_s = \frac{n_1 \cos(\theta_1)}{n_0 \cos(\theta_0)} |t_{01}^s|^2 \tag{5}$$

$$R_p = |r_{01}^p|^2 = \left(\frac{n_0 \cos(\theta_1) - n_1 \cos(\theta_0)}{n_0 \cos(\theta_1) + n_1 \cos(\theta_0)} \right)^2, \quad T_p = \frac{\frac{1}{n_1} \cos(\theta_1)}{\frac{1}{n_0} cos(\theta_0)} |t_{01}^p|^2 \tag{6}$$

And besides the incidence and refraction angles are related by Snell's law $n_0 \sin(\theta_0) = n_1 \sin(\theta_1)$. If the medium is not absorbing, the transmission coefficients associated with the reflection ones as $T = 1 - R$. Averaging over possible polarizations, you can get the general reflection and transmission coefficients

$$R = \frac{1}{2}(R_s + R_p), \quad T = \frac{1}{2}(T_s + T_p) \tag{7}$$

Three media with a thin layer without absorption

Consider now a more complex system consisting of three media, the middle of which is a thin membrane with thickness d_2, where the interference of light is possible. Then reflection and transmission amplitudes are

$$r = \frac{r_{12} + r_{23}e^{2\imath\beta}}{1 + r_{12}r_{23}e^{2\imath\beta}}, \quad t = \frac{t_{12}t_{23}e^{\imath\beta}}{1 + r_{12}r_{23}e^{2\imath\beta}}, \quad \beta = \frac{2\pi}{\lambda} d_2 \cdot n_2 \cos(\theta_2) = \eta \cdot n_2 \cos(\theta_2) \tag{8}$$

If we parameterize the amplitudes as follows

$$r = \rho \exp(\imath\phi), \quad t = \tau \exp(\imath\chi), \tag{9}$$

the expressions for the total amplitudes will look like

$$r = \frac{\rho_{12}e^{\imath\phi_{12}} + \rho_{23}e^{\imath\phi_{23}}e^{2\imath\eta \cdot n_2 \cos(\theta_2)}}{1 + \rho_{12}\rho_{23}e^{\imath(\phi_{12}+\phi_{23})}e^{2\imath\eta \cdot n_2 \cos(\theta_2)}}, \quad t = \frac{\tau_{12}\tau_{23}e^{\imath(\chi_{12}+\chi_{23})}e^{\imath\eta \cdot n_2 \cos(\theta_2)}}{1 + \rho_{12}\rho_{23}e^{\imath(\phi_{12}+\phi_{23})}e^{2\imath\eta \cdot n_2 \cos(\theta_2)}} \tag{10}$$

And then formulas for coefficients are

$$R = |r|^2 = \frac{\rho_{12}^2 + \rho_{23}^2 + 2\rho_{12}\rho_{23}\cos(\phi_{23} - \phi_{12} + 2\eta \cdot n_2\cos(\theta_2))}{1 + \rho_{12}^2\rho_{23}^2 + 2\rho_{12}\rho_{23}\cos(\phi_{12} + \phi_{23} + 2\eta \cdot n_2\cos(\theta_2))} \tag{11}$$

$$T = C_t|t|^2 = \frac{\tau_{12}^2\tau_{23}^2}{1 + \rho_{12}^2\rho_{23}^2 + 2\rho_{12}\rho_{23}\cos(\phi_{12} + \phi_{23} + 2\eta \cdot n_2\cos(\theta_2))} \tag{12}$$

$$C_t = \frac{n_3\cos(\theta_3)}{n_1\cos(\theta_1)} \quad \text{for s-wave and} \quad C_t = \frac{\frac{1}{n_3}\cos(\theta_3)}{\frac{1}{n_1}\cos(\theta_1)} \quad \text{for p-wave} \tag{13}$$

Three media with an absorbed thin layer

Now we introduce the absorption index of the this layer, $n_2 \to n_2(1 + \imath k_2)$. Formulas change somewhat, and now the refraction angle in the second layer is a complex value, which will affect the final result. Following the parametrization $n_2(1 + \imath k_2) \cdot \cos(\theta_2) = u_2 + \imath v_2$ we obtain

$$R = |r|^2 = \frac{\rho_{12}^2 e^{-2\Im(\phi_{12})} + \rho_{23}^2 e^{-2\Im(\phi_{23})}e^{-4v_2\eta} + 2\Re(\rho_{12}\rho_{23}^* e^{\imath(\phi_{12} - \phi_{23}^* - 2u_2\eta)}e^{-2v_2\eta})}{1 + \rho_{12}^2\rho_{23}^2 e^{-2\Im(\phi_{12} + \phi_{23})}e^{-4v_2\eta} + 2\Re(\rho_{12}\rho_{23}e^{\imath(\phi_{12} + \phi_{23} + 2u_2\eta)}e^{-2v_2\eta})} \tag{14}$$

$$T = C_t|t|^2 = C_t\frac{\tau_{12}^2\tau_{23}^2 e^{-2\Im(\chi_{12} + \chi_{23})}e^{-4v_2\eta}}{1 + \rho_{12}^2\rho_{23}^2 e^{-2\Im(\phi_{12} + \phi_{23})}e^{-4v_2\eta} + 2\Re(\rho_{12}\rho_{23}e^{\imath(\phi_{12} + \phi_{23} + 2u_2\eta)}e^{-2v_2\eta})} \tag{15}$$

Logically, if the system has a medium with absorption, the reflection and transmission coefficients in the sum will not give 1. There will be some absorption coefficient, which is calculated as $A = 1 - R - T$. It is simple to add any number of thin media in the system discussed earlier.

Four media with an absorbed thin layer

Finally, consider the four media system, e.g. air-glass photocathode-vacuum system that is the PMT. Glass in this case has a thickness much greater than the length of the incident light, so there is no interference of light in it, and the effect of the air-glass interface is reduced to a purely energy calculation of multiple reflections in the glass.

$$R_{03} = R_{01} + \frac{R_{13}T_{01}^2}{1 - R_{10}R_{13}} \tag{16}$$

$$T_{03} = \frac{T_{01}T_{13}}{1 - R_{10}R_{13}} \tag{17}$$

$$A_{03} = 1 - R_{03} - T_{03} \tag{18}$$

Results

Below you can see the graphs of the reflection, transmission and absorption coefficients with wavelength of light $\lambda = 440nm$ and Sb-Cs photocathode thickness $d_{ph} = 5nm$. Dash lines are for s-wave, dot lines are for p-wave and solid lines are for average.
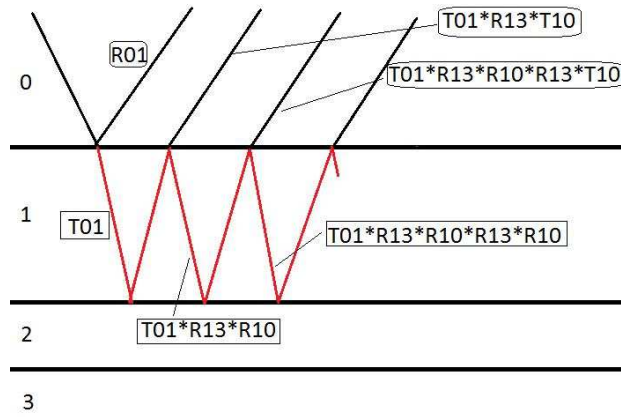
Figure 1: Scheme for coefficients calculation
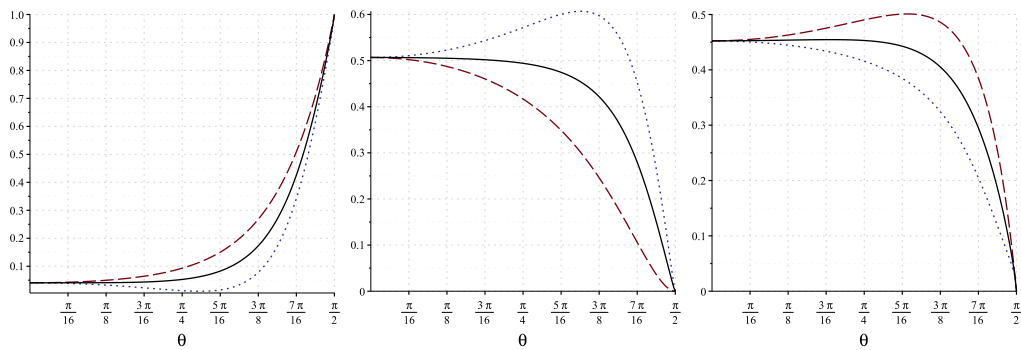
Figure 2: Air-glass-photocathode-air system: reflection 2a, transmission2b, absorption2c.
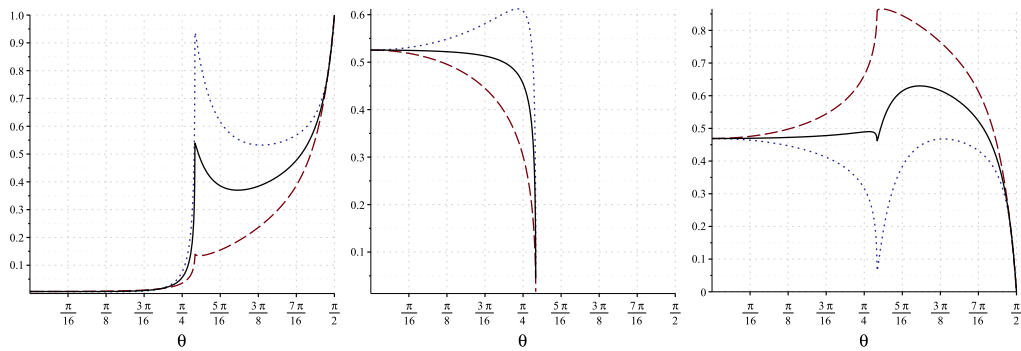
Figure 3: Water-glass-photocathode-air system: reflection 2a; transmission2b; absorption2c.

The reflectance behavior after the peak in Fig.3a and Fig.4a is due to two processes. On the one hand, since the light can not escape from the photocathode into a vacuum, it is reflected many times by the two surfaces of the photocathode, and at final case, due to the absorption it does not go back into the glass. Moreover, the larger is the incidence angle of light, the greater will be light's path in the photocathode and the greater will be the probability of its absorption. On the other hand, increasing the incidence angle the amount of light reflected from the glass/photocathode boundary increases.

161
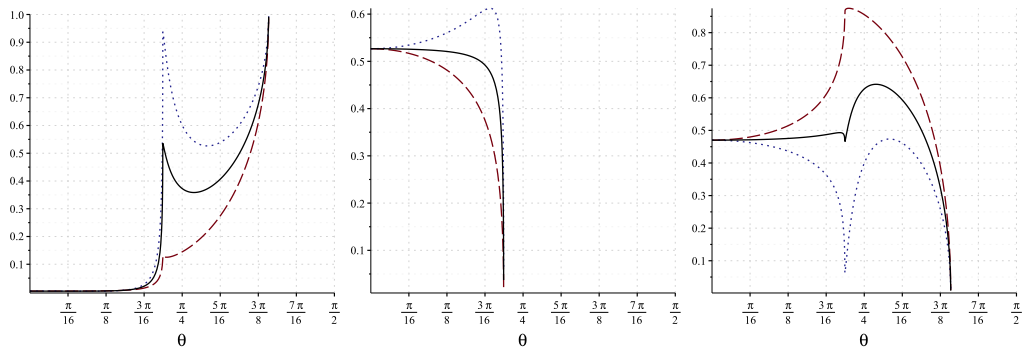
Figure 4: Scintillator-glass-photocathode-air system: reflection 2a; transmission2b; absorption2c.

References

[1] M. Born and E. Wolf, *Principles of Optics*, (Pergamon press, 1970., 808 p).

ANALYZING POWER OF INVERSE DIPROTON PHOTODISINTEGRATION AT INTERMEDIATE ENERGIES

B. Baimurzinova*

Joint Institute for Nuclear Research, Dubna, Russia

Annotation

The reaction $\gamma + \{pp\}_s \to p + p$, where diproton $\{pp\}_s$ is a proton pair in $^1S_0$ state, is a spin-isospin partner of the fundamental reaction of deuteron photodisintegration. The inverse reaction, the hard bremsstrahlung $p + p \to \gamma + \{pp\}_s$, has been observed with the ANKE spectometer at COSY-Jülich. In addition to differential cross section measured earlier, in this work it's analyzing power has been measured at forward angles at several energies in the region of $\Delta(1232)$ isobar exictation.

Introduction

The formation of a so-called "diproton", i.e. a proton pair $\{pp\}_s$ in $^1S_0$ state, is being researched at ANKE collaboration in various processes: $pd \to \{pp\}_s n$, $pp \to \{pp\}_s \pi^0$, $pp \to \{pp\}_s \gamma$ [1–5]. Such reactions are of interest for several reasons. Firstly, they are the elementary inelastic processes in few-nucleon systems which could give valuable information on dynamics of nucleon-nucleon interaction. Secondly, restriction to only one partial wave (S-wave) in the final state considerably simplifies the reactions theoretical consideration in comparison to other reactions of this kind, for example deuteron photodisintegration $\gamma d \to pn$. The diproton photodisintegration $\gamma\{pp\}_s \to pp$ is kinematicly very similar to $\gamma d \to pn$, however dynamically they significantly differ from each other. The matter is that the quantum numbers of a diproton state ($I = 1$, $S = 0$, $L = 0$) differ from the corresponding quantum numbers of a deuteron ($I = 0$, $S = 1$, $L = 0, 2$). As a result multipole contributions will also be significantly different. Therefore the data received for these two reactions mutually supplement each other, indicating that we should study such processes more carefully.

In absence of a free bound diproton, $\gamma\{pp\}_s \to pp$ is traditionally investigated for diproton which bound within a nucleus. At ANKE an alternative approach was applied for the first time — the study of the inverse reaction $pp \to \gamma\{pp\}_s$ [4], free from background created by the deuteron photoabsorption. Particulary, the goal of this work is to find analyzing power of this reaction.

Measurements and analysis

The experiment was carried out in Germany using ANKE facility of the synchroton storage ring COSY-Jülich [6]. A hydrogen cluster-jet target was positioned in the proton beam and secondary particles were detected with wire chambers and scintillation hodoscope. The proton beam was transversely polarized with it's polarization direction varying from up to down. The trajectories and three-momenta of the particles were reconstructed.

---

*baymurzinova@jinr.ru, for the ANKE Collaboration

The first step in the identification of our reaction was the selection of two coincident protons among all the detected pairs of positively charged particles. The scintillation hodoscope allowed measurement of the difference between the times of flight from the target to detector for two recorded particles. If we assume the masses of the particles, we can also calculate this time of difference, using the measured momenta and trajectories. If our assumption was correct then these two values would coincide. With time resolution better than 2 ns, the comparison of this value with that calculated from the measured particle momenta and trajectories led to a very good identification of proton pairs.

At low excitation energy $E_{pp} < 3$ MeV the diproton is predominantely in the $^1S_0$ state. The resolution of the ANKE setup $\sigma(E_{pp}) < 0.6$ MeV allowed reliable selection of $E_{pp} < 3$ MeV diprotons.

As the next step, histograms for missing mass squared were created at $T_p = 0.500$, 0.550, 0.700 GeV (Fig. 1). There is a clear visible γ peak that could be separated from the pion peak associated with the $pp \rightarrow pp\pi^0$ reaction. The peak shapes were obtained by a detailed Monte Carlo simulation at each energy, which took into account all the known features of the setup. The free parameters of interest used to fit the missing-mass spectra were the number of events in the γ peak and the number of events in the pion peak. In order to compensate for the lack of knowledge of the beam spatial distribution, additional parameters were inserted into the fits: a shift of the pion peak position and correction factors for the γ and pion peak widths. The results of the fit can be seen in Fig. 1 as well.
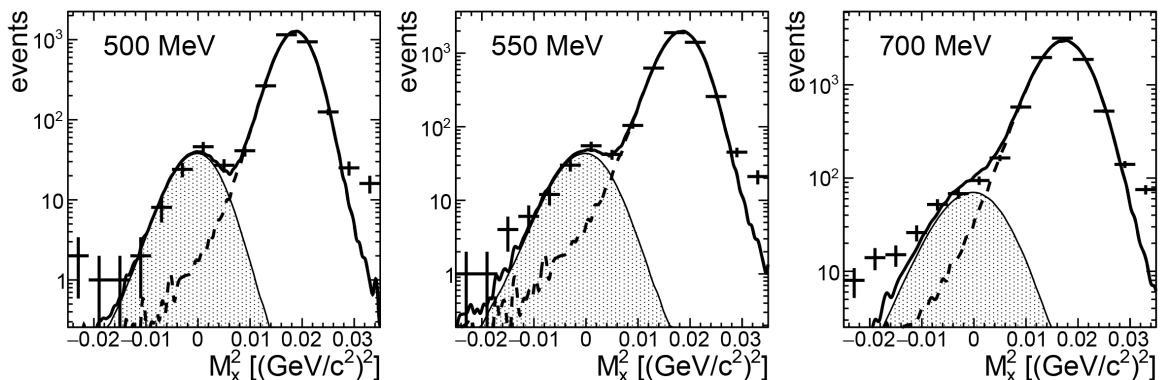
Figure 1: **Distribution of the missing mass squared in the** $p + p \rightarrow \{pp\}_s + X$

To estimate the angular dependence of the analyzing power, the events were divided into two θ_{pp} intervals $5 - 13°, 13 - 30°$ and separate fits were made for each of these ranges. Firstly, we had to find polarization assymetry given by equation (1).

$$\varepsilon = \frac{N_\uparrow/L_\uparrow - N_\downarrow/L_\downarrow}{N_\uparrow/L_\uparrow + N_\downarrow/L_\downarrow}, \tag{1}$$

where $N_\uparrow$ and $N_\downarrow$ are the numbers of events with beam proton spin up and down, and $L_\uparrow$ and $L_\downarrow$ are the corresponding luminosities. It is needed to calculate the analyzing power using equation (2).

$$A_y = \frac{\varepsilon}{P\langle\cos\phi_{pp}\rangle}, \tag{2}$$

where P is the transverse polarisation of the beam and $\langle\cos\phi_{pp}\rangle$ the average over the diproton azimuthal angular distribution. Different approaches were applied to obtain the

Table 1: Numerical values of analyzing power with systematical and statistical errors, preliminary results.

	500	550	700
$5 - 13°$	$1.02 \pm 1.80 \pm 0.02$	$0.14 \pm 1.03 \pm 0.67$	$0.51 \pm 1.23 \pm 0.014$
$13 - 30°$	$0.72 \pm 1.45 \pm 0.03$	$0.77 \pm 0.99 \pm 0.01$	$0.62 \pm 0.92 \pm 0.002$

analyzing power. The numbers of events can be determined either by fitting separately $N_\uparrow$ and $N_\downarrow$, or directly $N_\uparrow - N_\downarrow$ and $N_\uparrow + N_\downarrow$ histograms. Concerning $\cos\phi_{pp}$ there are two possibilities, either to divide by the average value of $\cos\phi_{pp}$ distribution or to correct by $\cos\phi_{pp}$ event-by-event. Hence, four approaches were applied, each repeated for fine and gross histogram binning. These 8 values with errors were averaged. The dispersion of the values was considered as a systematic error. Polarization P was estimated using the known values of A_y for elastic pp and $pp \to d\pi^+$ reactions, registered in parallel with our reaction.

Results and outlook

In Fig. 2 and Table 1 the preliminary results are shown for analyzing power of the $pp \to \gamma\{pp\}_s$ reaction at $T_p = 0.500, 0.550, 0.700$ GeV.
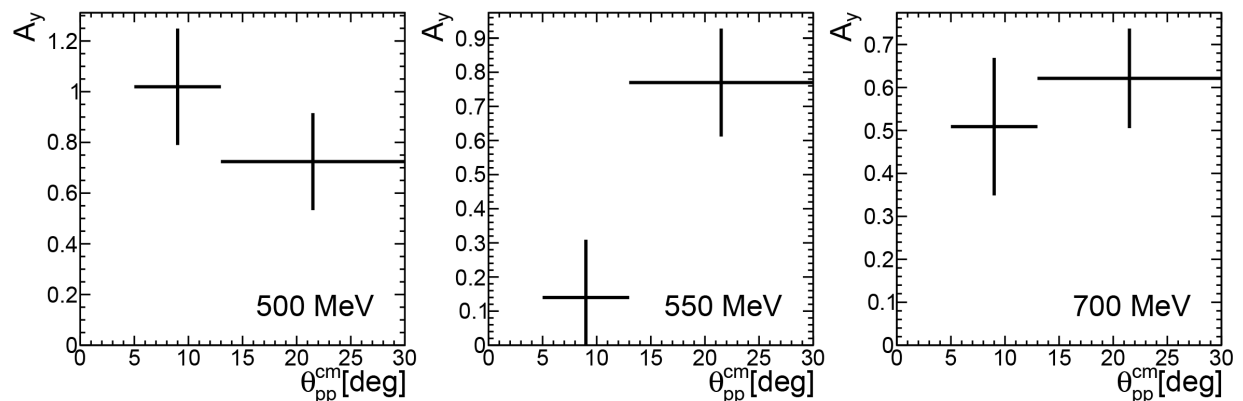
Figure 2: Analyzing power for reaction $p + p \to \gamma + \{pp\}_s$, preliminary results.

Since multipole contributions $M1$ and non-spin-flip part of $E1$ are forbidden, it might be sufficient to retain only $E2$, $M2$ and spin-flip part of $E1$. The qualitative estimate of the results [7] suggests that there may be significant contribution of the $M2$ multipole contrary to the predictions of [8]. The numerical evaluation of $E1$, $E2$, $M2$ multipole contributions to the data is in progress.

References

[1] S. Dymov *et al.*, Phys. Rev. C 81 (2010) 044001.

[2] V. Kurbatov *et al.*, Phys. Lett. B 661 (2008) 22.

[3] D. Tsirkov *et al.*, Phys. Lett. B 712 (2012) 370.

[4] V. Komarov *et al.*, Phys. Rev. Lett. 101 (2008) 102501.

[5] D. Tsirkov *et al.*, J. Phys. G: Nucl. Part. Phys. 37 (2010) 105005.

[6] S. Barsov *et al.*, Nucl. Instrum. Methods. Phys. Res. A 462 (2001) 354.

[7] P. Wilhelm *et al.*, Nucl. Phys. A 597 (1996) 613.

[8] P. Wilhelm *et al.*, Phys. Lett. C 51 (1995) 2841.

JINR LIT COMPUTING RESOURCES FOR NOνA EXPERIMENT

N. A. Balashov*, A. V. Baranov, A. E. Bolshakova, L. D. Kolupaeva, O. B. Samoylov, A. S. Sheshukov, O. N. Petrova
Joint Institute for Nuclear Research. Dubna, Russia

Annotation

This paper represents some application use-cases of JINR LIT computing resources for NOνA experiment. Running NOνA Art framework (used by the experiment) on cloud service and batch system is shown. It also depicts some pros and cons of these two approaches as well as performance comparison.

Introduction

NOνA [1] is a large neutrino experiment based in Fermi National Accelerator Laboratory (FNAL) and it needs a huge amount of computing resources to process all of its data. It requires almost a million of CPUh per week in its peak. Part of it it gets from the local fermilab's computing infrastructure - Fermigrid, part - from Open Science Grid (OSG). It is obvious that any additional contribution would really help, no matter what size. As a part of participation of JINR in the experiment we started working on contributing to the experiment with computing resources.

Computing resources

All the computing resources are located at the Laboratory of Information Technology (LIT). It has different computing facilities: a Tier-1 cluster, combined Tier-2 and local batch-processing cluster, hybrid cluster (Hybrilit) aimed on usage of GPUs and coprocessors; cloud-cluster [2].

Tier-1 cluster is contributing its resources to the CMS experiment at Large Hadron Collider (LHC). Tier-2 cluster contributes mostly to LHC experiments (ALICE, ATLAS, CMS and LHCb), NICA-project experiments, some other experiments like BES-III and also processes jobs from local JINR users. Cloud service is mostly used by local JINR users. Right now only T2-cluster and Cloud service are used by NOνA.

Batch System

A batch-system is basically a set of servers processing jobs from many users. JINR LIT batch-cluster processes jobs both from local users and global infrastructures like grid contributing computing-power to different international experiments. The Fig. 1 shows a simplified scheme of T2-cluster based on a Torque batch system.

This model of computing is perfect but has a couple of obvious drawbacks:
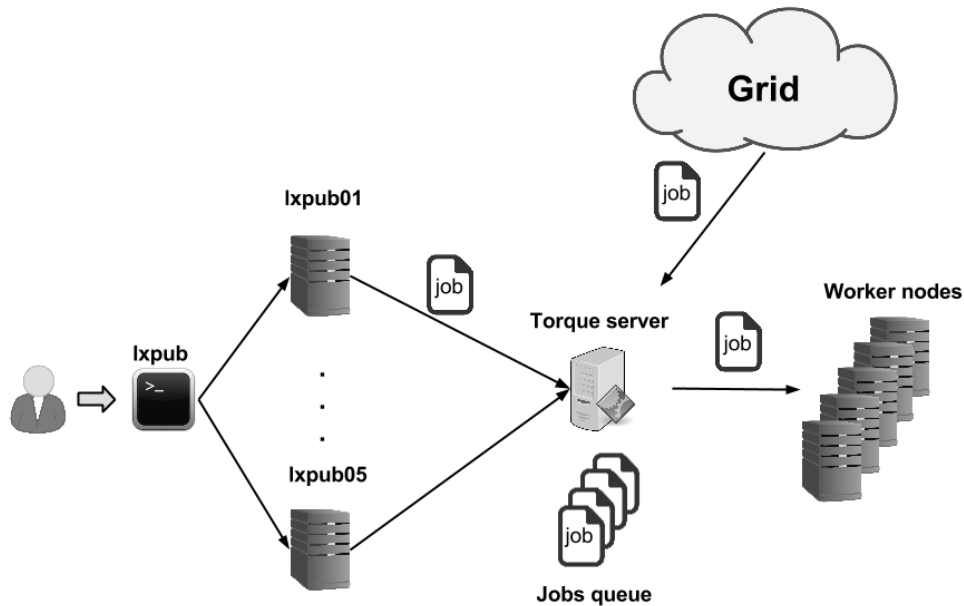
Figure 1: Simplified scheme of T2-cluster.

1. First of all, it has fixed environment: at T2-cluster it is Scientific Linux with a fixed set of libraries.
2. A job can spend significant time in the queue, because there are many users and jobs.

But it still seems to be the perfect model for processing lots of tasks from lots of users.

Cloud service

The end product of JINR Cloud service is a virtual machine (VM) that is basically the same thing as an ordinary PC. So, cloud users can setup any required environment in their VMs - they can have any operating systems (OS), install any applications and libraries and store any data in it.

There is some specifics about JINR Cloud service - it provides 2 types of virtualization: Kernel Virtual Machines (KVM) and OpenVZ-containers (OVZ). The reason we support 2 types of virtualization systems is that in some cases OVZ outperforms KVM due to lower overhead on virtualization, but it has limitation on using only Linux-based OS and all the containers share the same kernel of the host-system.

Simplified scheme of JINR Cloud service is shown on Fig. 2.

There are, of course, some drawbacks of using the Cloud service: it requires extra knowledge to create and setup a virtual machine; users have to manage the whole environment in their machines like installing all the software and libraries; and there are not many resources in the JINR cloud so far.

The JINR Cloud service seems to be best for research, development and hosting IT-services, but have to be combined with a batch system to efficiently process large amounts of production data.
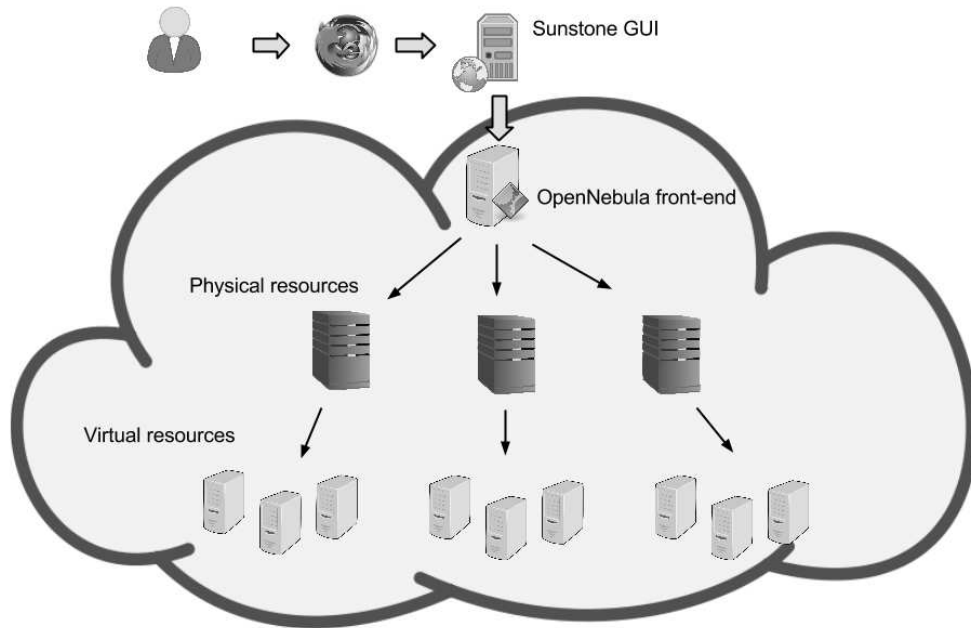
Figure 2: Scheme of JINR Cloud Service.

NO*ν*A cloud cluster

Hardware

Specially for NO*ν*A experiment 5 new Dell servers of the following configuration were purchased: Dell PowerEdge R430 2xE5-2650v3, 6x8GB, 2x2TB NL SAS. These servers were integrated into JINR Cloud service and will become the basis for the virtual batch cluster that will process jobs from both local JINR NO*ν*A team and NO*ν*A-jobs coming from OSG contributing directly to NO*ν*A collaboration. This cluster will be extended by 5 more servers of slightly better configuration which are currently in process of purchase.

*NO*ν*A Cluster Software*

HTCondor will be used as a batch system for the NO*ν*A cluster. This system will be used directly by local NO*ν*A-team users for submitting their jobs to the cluster and to process grid-jobs. Worker nodes of the system will be virtual machines (KVM). Using the JINR Cloud service's virtual machines gives the opportunity to dynamically resize the batch cluster size to add up opportunistic resources to the batch system or to give out some resources to supplement general-use virtual machines in accordance with current needs and workload.

To allow grid users run their jobs on this cluster so called OSG-site (containing HTCondor Computing Element) will be deployed.

In order to keep NO*ν*A software up-to-date CernVM-filesystem is used. NO*ν*A-software is based on the art Event-Processing Framework [3] and is stored in the central repository, that is mounted on all the worker-nodes of our T2 cluster making it possible to run NO*ν*A jobs and will also be used on virtual NO*ν*A cluster. Also this reposi-

tory can be manually mounted on any PC or a virtual machine since it is publicly available.

Performance comparison of Hypervisors

As was mentioned above JINR Cloud service provides 2 types of virtualization systems (also known as hypervisors): KVM and OpenVZ. To make a better decision of choosing an underlying system for the NOνA virtual cluster we made a performance comparison of these 2 hypervisors on a real computing task and also compared them with bare-metal server and T2 batch system worker-nodes. As a test job we used cross section computation of neutrino with energies up to 10 GeV on matter nuclei of the nova detector using GENIE package. Two similar servers were picked up and a KVM virtual machine was deployed on one of them, and an OVZ container on the other one. Bar-chart showing the time they spend on processing the same task is shown on Fig. 3. Additionally 10 similar copies of the same task were submitted to the T2 batch-system - the fourth bar-set on Fig.3 indicates the average time of processing on the worker-nodes of the batch system. The result shows that KVM and containers slightly outperform the server itself and it needs further investigation and may be some kind of misconfiguration of the bare-metal servers' operating systems. And batch-system worker-nodes perform almost 2-times slower than these NOνA-dedicated servers, probably indicating that these servers are pretty much outdated.
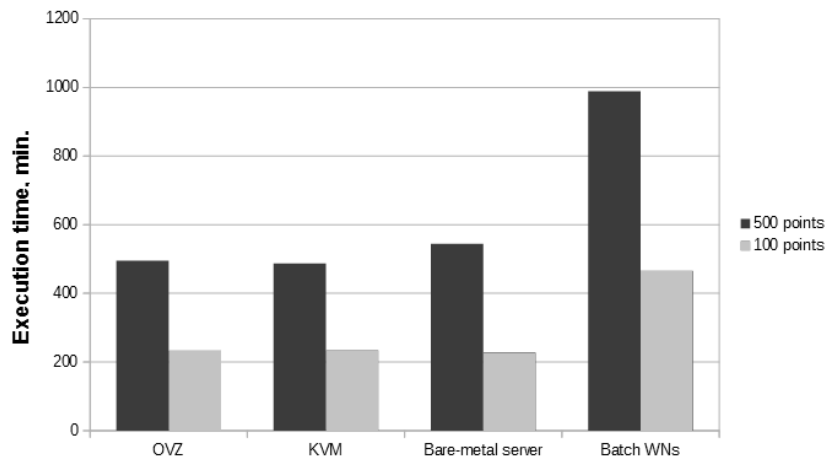
Figure 3: Performance comparison of hypervisors, bare-metal servers and batch system workernodes.

Conclusions

Conducted work showed that both batch systems and clouds can be successfully used for proccessing experimental date by the example of NOνA experiment. It was also shown that overhead on virtualization of modern hypervisors is low enough to try moving computations into virtual machines. At the same time combining batch systems with clouds can help better utilize computing resources.

References

[1] Site of the NOνA experiment.
URL: https://www-nova.fnal.gov/ [accessed on: 05/13/16]

[2] *Site of the "Multifunctional Information and Computing Complex"*:
URL: https://miccom.jinr.ru/en/ [accessed on: 05/13/16]

[3] *The Art Event-Processing Framework home page*:
URL: https://web.fnal.gov/project/ArtDoc/Pages/home.aspx [accessed on: 05/13/16]

EXCLUSIVE PHOTOPRODUCTION OF a$_2$(1320) AT THE COMPASS EXPERIMENT

A. Gridin

Moscow Institute of Physics and Technology, Moscow, Russia
Joint Institute for Nuclear Research, Dubna, Russia

Annotation

The charge exchange reactions at high energies are the object of lively interest. In the proposed talk we discuss the study of exclusive photoproduction of the charged $a_2(1320)$ meson off the target nucleon using data of the COMPASS experiment. COMPASS is a high energy physics experiment at the Super Proton Synchrotron (SPS) at CRN designed to study of hadron structure and spectroscopy with high intensity muon and hadron beams. The cross section of the process $\gamma N \to a_2(1320)N'$ is estimated in the energy range from 10 GeV to 120 GeV. The obtained preliminary results are in agreement with the existing theoretical predictions.

Introduction

QCD is the true theory of strong interactions. But at low energies the constant of strong interaction α_s is about 1. It is significantly greater than the constant of electromagnetic or weak interactions. So, one can't use the perturbation approach in QCD. That's why at low energies phenomenological models like Regge theory [1], One boson exchange Potential Model [2], One pion exchange Potential Model [3] and are popular. These theories are approximate, but able to produce reasonable numerical predictions.

The pomeron exchange is the main mechanism of hadronic interactions at high energies while contribution of the charged exchange is small and not well-known. The interest to the charged exchange processes at high energies has grown in recent years due to relation of this mechanism with the production of exotic charmonia. Photoproduction of the $a_2(1320)$ meson in the reaction $\gamma N \to a_2(1320)N'$ (Fig. 1) could be a promising instrument for study of the charged exchange at high energies. Existing experimental results [4–8] on the measurement of the cross section of the $\gamma p \to a_2^+(1320)n$ at low energies consistent with the theoretical models [9].

The COMPASS experiment

CMPSS (Common Muon and Proton Apparatus for Structure and Spectroscopy) [10] is a high energy physics experiment at the Super Proton Synchrotron (SPS) at CERN designed to study of hadron structure and spectroscopy with high intensity muon and hadron beams. In particular, COMPASS studies the structure of nucleon spin in muon deep inelastic scattering off polarized ^{6}LiD and NH$_3$ targets.

The COMPASS setup could be logically divided into 3 parts along the beam axis. The first part includes tracking detectors located upstream the target, which measure parameters of the beam. The second part is the Large Angle Spectrometer. It consists of the spectrometric magnet, the tracking detectors, the ring-imaging Cherenkov detector, the
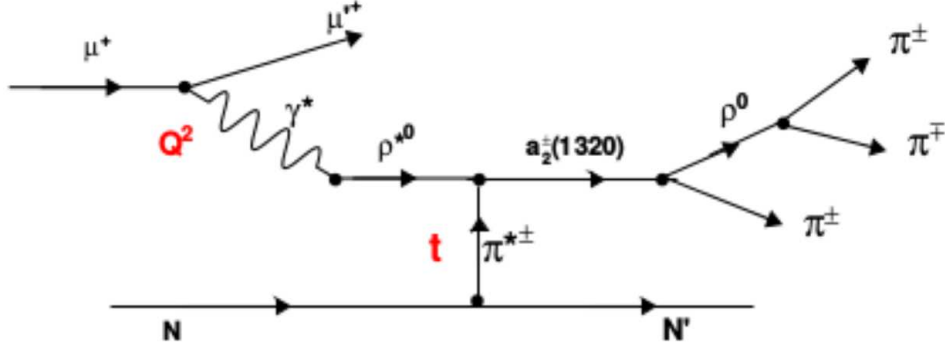
Figure 1: The diagram of the charge exchange process $\gamma N \to a_2 N'$.

set of electromagnetic and hadron calorimeters and the muon identification system. The last part is the Small Angle Spectrometer which is built around the second magnet and also includes the tracking detectors, the electromagnetic and hadron calorimeters and the muon identification system.

Data analysis

The analysis was performed using COMPASS data collected in 20011 with the ammonia target. To select candidate events of exclusive photoproduction of $a_2(1320)$ the next selection criteria were applied:

- the best primary vertex in the target;
- 4 outgoing particles in the best primary vertex: the scattered muon and three pions with the momentum above 5 GeV/c;
- absence of neutral clusters in electromagnetic calorimeters is required to suppress possible background from events with π^0 in the final state;
- no tracks with measured momentum and the difference between the track time and the trigger time > 15ns;
- the sum of the energies of the final state particles matches the energy of the beam muon except for a small recoil energy to the target within the accuracy ± 10 GeV.

The invariant mass spectrum of three pions (Fig. 2) demonstrates a visible peak at M=1320 MeV/c², which corresponds to the production and decay of $a_2^{\pm}(1320)$. The sum of the Breit-Wigner function, which describes the $a_2^{\pm}(1320)$ signal, and the Landau function, describing the background events under the $a_2^{\pm}(1320)$ peak, is fitted to the mass spectrum in the range 0.9-1.8 GeV/c² . Free parameters of the fit M and Γ can vary in the ranges from 1.29 to 1.35 and from 0.102 to 0.112 GeV/c² respectively.

The reaction $\mu^+ N \to N' \mu^+ \pi^{\pm} \pi^{\pm} \pi^{\mp} \pi^{\mp}$ with one pion lost is the main background process. Contribution of this background is estimated by variation of the energy balance cut to be about 30%. The cross section of the process $\gamma p \to a_2^+(1320)n$ is roughly estimated in the photon energy range from 10 GeV to 130 GeV to be about $2 \pm 1_{stat}$ nb. Estimation is done using comparison of yields of $a_2(1320)$ events and the events of the exclusive production of J/ψ-meson with known cross section. The obtained result is basically in agreement with theoretical expectation (see Fig. 3).

The mass spectrum of 3 pions (++-)
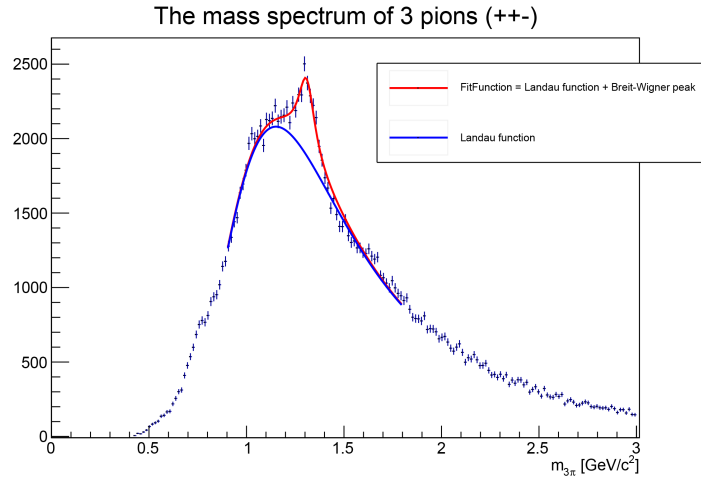
Figure 2: The invariant mass distribution for $\pi^+\pi^-\pi^+$ events.
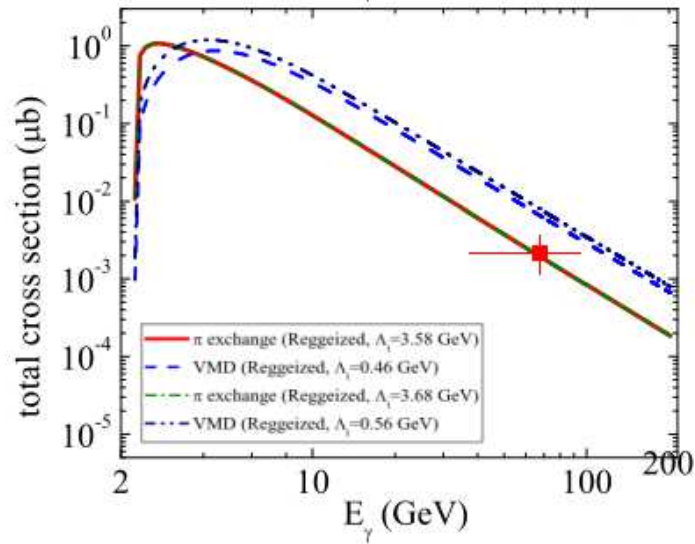
Figure 3: The theoretical predictions for the cross section of the reaction $\gamma N \rightarrow a_2(1320)N'$ for different models [9]. The obtained result is shown by the red point.

Summary

The photoproduction of $a_2(1320)$ is studied using the data of the COMPASS experiment. Reasonable selection criteria are proposed and tested. It is found that the reaction with 4 pions in the final state, going via pomeron exchange, is the main background process. The cross section of the process $\gamma p \rightarrow a_2^+(1320)n$, estimated in the energy range from 10 to 130 GeV is 2 ± 1 nb. The obtained result is in agreement with theoretical expectations.

References

[1] Kaidalov arXiv:hep-ph/0103011

[2] J. J. de Swart, P. M. M. Maessen, T. H. A. Rijken arXiv:nucl-th/9405008

174

[3] K. Bongardt, H. Pilkuhn, H.G. Schlaile, Phys. Lett. B, 52, (1974) 271-274.

[4] W. Struczinski *et al.* (Aachen-Hamburg-Heidelberg-Munich Collaboration), Nucl.Phys. B 108 (1976) 45.

[5] Y. Eisenberg *et al.*, Phys. Rev. D 5 (1972) 15.

[6] M. Nozar *et al.* (CLAS Collaboration), Phys. Rev. Lett. 102 (2009) 102002.

[7] Y. Eisenberg *et al.*, Phys. Rev. Lett. 23 (1969) 1322.

[8] G. T. Condo, Phys. Rev. D 48 (1993) 3045.

[9] W. Xiao-Yun, A. Guskov, Phys.Rev. D 93 (2016) 7, 074016; arXiv:1510.00898 [hep-ph]

[10] P. Abbon *et al.* (CPSS Collaboration), Nucl. Instrum. Meth. A 577 (2007) 455; [arXiv:0703049 [hep-ex]].

COMPUTATION OF PROCESS NOISE MATRIX FOR TRACK FITTING WITH KALMAN FILTER

B. Kolahal*, B. Sudeshna, Naba K. Mondal
INO Cell, TIFR, Homi Bhabha Road, Colaba, Mumbai, India

Annotation

We derive the functional form of the elements of the random process noise matrix (to be used in a Kalman filter) in the problems of track fitting through dense, thick materials and magnetic field in modern high energy physics experiments. The resulting rigorous formula is valid for the tracks curved in the magnetic field and is complementary to the simple solution obtained by Mankel [2] in case of straight tracks in the absence of magnetic field.

Motivation of the study

In the problem of track fitting in a high energy physics experiment, one often has to work on the proper treatment of the multiple Coulomb scattering and energy loss fluctuations which affect the motion of the particle significantly. They introduce random uncertainties to the track parameters like position, direction or momentum and cannot be quantified *apriori*, due to its random nature. These are taken into account in terms of a random process noise matrix in the framework of Kalman filter. If the particle traverses small amount of scattering material, it is sufficient to assume that the scatterings happen in a single layer of very small thickness dl. In this case, one can perform error propagation across the layer in a single step: $\tilde{C} = F\hat{C}F^T + Q$, where F denotes the Kalman propagator matrix that propagates the uncertainties $\hat{C}$ at the plane l to the plane $l + dl$, deterministically. Elements of F depend on magnetic field and average loss of energy. On the other hand, Q denotes the random uncertainties introduced between l and $l + dl$. The total projected error matrix is denoted by $\tilde{C}$.

However, when the scattering material is rather thick, the error propagation must be performed in small steps of thickness dl. The uncertainties $\tilde{C}$ projected from $F_j\hat{C}F_j^T + Q_j$ at the jth step serves as $\hat{C}$ for the error propagation for the next step $j + 1$. Hence, the random uncertainties of jth step is also propagated by propagator of the $j + 1^{th}$ step. This restricts the functional form of the elements of the random process noise matrix, which must be determined. This exercise was performed by Mankel [2, Appendix B], for the development of *ranger*-the pattern recognition program in HERA B experiment. The state vector $\left(x, y, t_x \equiv \frac{dx}{dz}, t_y \equiv \frac{dy}{dz}, \frac{q}{p}\right)^T$ was used and the desired process noise matrix was derived using a simple 4×4 propagator matrix for the position and angular coordinates. The propagator matrix and the corresponding process noise matrix were given as:

$$F = I + \begin{pmatrix} 0 & 0 & 1 & 0 \\ 0 & 0 & 0 & 1 \\ 0 & 0 & 0 & 0 \\ 0 & 0 & 0 & 0 \end{pmatrix} dl \qquad Q(l) = \begin{pmatrix} c(t_x, t_x)\frac{l^3}{3} & c(t_x, t_y)\frac{l^3}{3} & c(t_x, t_x)s\frac{l^2}{2} & c(t_x, t_y)s\frac{l^2}{2} \\ \dots & c(t_y, t_y)\frac{l^3}{3} & c(t_x, t_y)s\frac{l^2}{2} & c(t_y, t_y)s\frac{l^2}{2} \\ \dots & \dots & c(t_x, t_x)l & c(t_x, t_y)l \\ \dots & \dots & \dots & c(t_y, t_y)l \end{pmatrix}$$

*Corresponding author: kolahalb@gmail.com

Clearly, this solution is true when the curvature of the track within magnetic field is neglected or when there is no magnetic field. However, in the presence of strong magnetic field, one has to account for the track curvature. Uncertainties in the track parameters must be propagated through the magnetic field which requires that the elements of the propagator matrix F be nonzero. This situation arises in case of track fitting in the upcoming Iron CALorimeter (ICAL) experiment under the India-based Neutrino Observatory (INO) project [4]. ICAL will employ a 50 kiloton magnetized iron calorimeter (Fig. 1, left
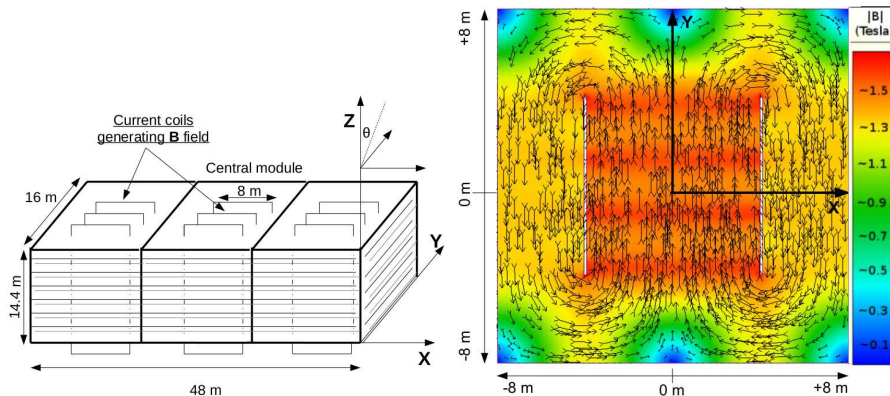
Figure 1: Left panel: ICAL detector geometry. Right panel: Magnetic field map shown in central module. The same field pattern exists in side modules as well.

panel) to detect atmospheric neutrinos and will try to resolve neutrino mass hierarchy problem [6]. It will be mostly sensitive to the detection of muon neutrinos which generate muons after charged current weak interactions. Because of the magnetic field (Fig. 1, right panel), ICAL will also be able to measure the charge of the muons. The thickness of the horizontally placed irons plates in ICAL will be 5.6 cm. Hence, the muons coming from all possible directions will travel across large amount of iron, where they will not only be deflected by the magnetic field, but will also suffer from multiple scattering. ICAL will receive a large flux of atmospheric neutrinos at lower energy [5] and they suffer more from multiple scattering. Therefore, it is important to treat the random effects in a proper fashion.

In the track reconstruction program for ICAL, the formulae developed in [2] were used. However, it is noticed that the propagator matrix F which is used in ICAL has a much more complicated form compared to that used in [2]. Therefore, it is a matter of great interest to check if the solution for the random process noise matrix inside iron influences the track fitting performances in ICAL. This sets the motivation of the present work which endeavours to obtain the expression of the process noise matrix, applicable inside strong magnetic field.

Formulation of the problem

If the process noise contribution to the total track parameter uncertainties between track length l and $l + dl$ is represented by δQ, then we can write:

$$Q(l + dl) = FQ(l)F^T + \delta Q \tag{1}$$

The propagator F can be expressed as ([3], Eq.(24)):

$$F = I + s \ F'dl = I + s \begin{pmatrix} \cdots & \cdots \\ \cdots & \cdots \end{pmatrix} dl \tag{2}$$

where $s = +1(-1)$ when the direction of propagation increases (decreases) the z coordinate while the tracking is carried out and I denotes the identity matrix. Thus, From Eq.(1) and Eq.(2), the differential equation of the process noise matrix Q is given as:

$$\frac{dQ}{dl} = s \left((F' \ Q(l) + (F' \ Q(l))^T \right) + \delta Q/dl \tag{3}$$

The 15 independent elements of the process noise matrix (real symmetric matrix) are the solutions to the matrix valued equation. They can be compiled into a single state $\mathbf{q}$:

$$\mathbf{q} = (Q_{11}, Q_{12}, Q_{13}, Q_{14}, Q_{15}, Q_{22}, Q_{23}, Q_{24}, Q_{25}, Q_{33}, Q_{34}, Q_{35}, Q_{44}, Q_{45}, Q_{55})^T \tag{4}$$

The corresponding independent elements of $\delta Q/dl$ is given by:

$$\delta\mathbf{q} = (0, 0, 0, 0, 0, 0, 0, 0, 0, c(t_x, t_x), c(t_x, t_y), 0, c(t_y, t_y), 0, c(q/p, q/p))^T \tag{5}$$

where $c(., .)$ are covariance among various track parameters, whose values are known ([2], pp. 10), ([3], pp. 25). In this notation, Eq.(3) becomes:

$$\frac{d\mathbf{q}}{dl} = s\mathbf{A}\mathbf{q} + \delta\mathbf{q} \tag{6}$$

where $\mathbf{A}$ is a 15×15 matrix [7, Appendix A].

Solution technique

In the event where $\mathbf{A}$ is diagonalizable (which always happens inside the iron due to large values of the elements) with an invertible matrix P, then the coupled differential equation can be decoupled by $\mathbf{A} = PDP^{-1}$ and $\mathbf{q} = P\mathbf{u}$. It can be shown that the final form of the process noise matrix elements becomes ([7], Eq.(19)):

$$q_i(l) = \sum_{j=1}^{15} P_{ij} \frac{(P^{-1}\delta\mathbf{q})_j}{s\lambda_j} (e^{s\lambda_j l} - 1) \tag{7}$$

where λ_j denotes the set of complex eigenvalues of $\mathbf{A}$. Since $\mathbf{A}$ is real, but asymmetric, the occurrence of complex numbers are inevitable. However, only the real parts of the solutions are taken to construct the elements of the process noise matrix inside the magnetic field.

Application to track reconstruction in ICAL

For track fitting purposes in ICAL, Eq. (7) was used only within iron plate for computing the 15 independent elements of $Q(l)$ matrix. Using the real symmetric property of the covariance matrix, all elements were filled. The diagonalization and the computation of the eigenvalues were performed using a `C++` based mathematical library, called `it++`. The

library uses known computational libraries like `LAPACK` or `BLAS` and the accuracy of the computations is comparable to Wolfram Mathematica. However, outside the iron, it was not possible to carry out the diagonalization of $\mathbf{A}$ (because $Det(\mathbf{A}) = 0$ there). Thus, Mankel's form of the process noise matrix was used.

The standard analysis tool in high energy physics experiments, ROOT, could not be used because of a convention followed by ROOT, that the eigenvalues and eigenvector matrix are kept real.

Reconstruction performance

It is observed that the introduction of the corrected elements of the process noise matrix inside the iron plates does not influence the track fitting performances in ICAL significantly. This can be seen from the following reconstructed momentum and direction ($\cos\theta$) plots in figures 2, left panel, and 2, right panel. Corrections to the reconstructed values are found to appear only at the second or third decimal places.
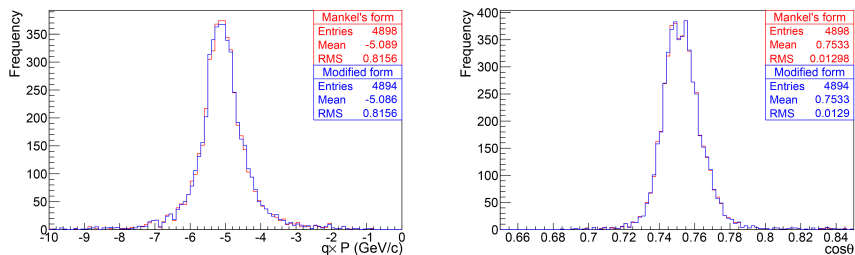
Figure 2: Reconstruction performance comparison between two Kalman filters with different process noise treatment for 5000 μ^- tracks with $P_\mu = 5$ GeV/c and $\cos\theta = 0.75$: (a) Momentum and (b) $\cos\theta$ plots.

It is concluded that the process noise matrix derived by Mankel ([2],[Appendix B]) under various approximations is good enough. Use of a more general set of elements of the process noise matrix inside magnetized iron plates in ICAL does not improve reconstruction significantly.

References

[1] B. Kolahal *et al.*, Computer Physics Communications, 185 (2014) 3259.

[2] R. Mankel, HERA-B note, 97-082 (1997).

[3] A. Fontana, P. Genova, L. Lavezzi, A. Rotondi, PANDA Report PVI01-07, (2007) 3-6; 19-28.

[4] Naba K. Mondal (INO collaboration and others), Pramana, 79 (2012) 1003.

[5] M. Athar *et al.*, Phys. Lett., B 718 (2013) 1375.

[6] S. Abhijit, Phys.Lett., B 673 (2009) 37; hep-ph/0610196.

[7] B. Kolahal, B. Sudeshna, Naba K. Mondal, arXiv: 1509.1234v2.

ANISOTROPIC FLOW FLUCTUATIONS IN Pb-Pb COLLISIONS AT THE LHC ENERGY IN HYDJET++ MODEL

E. N. Nazarova[1][*][†] , L. V Bravina[2,3], E. S. Fotina[1], V. L. Korotkikh[1], I. P. Lokhtin[1], L. V. Malinina[1,4], S. V. Petrushanko[1], A. M. Snigirev[1] and E.E. Zabrodin[1,2,3]

[1] *Skobeltsyn Institute of Nuclear Physics, Moscow State University, Moscow, Russia*
[2] *Department of Physics, University of Oslo, Oslo, Norway*
[3] *Frankfurt Institute for Advanced Studies, Frankfurt a.M., Germany*
[4] *Joint Institute for Nuclear Researches, Dubna, Russia*

Annotation

The LHC data on event-by-event harmonic flow coefficients measured in PbPb collisions at center-of-mass energy 2.76 TeV per nucleon pair are analysed and interpreted within the HYDJET++ model. To compare the model results with the experimental data the unfolding procedure is employed. The essentially dynamical origin of the flow fluctuations in hydro-inspired freeze-out approach has been established. It is shown that the simple modification of the model via introducing the distribution over spatial anisotropy parameters permits HYDJET++ to reproduce both elliptic and triangular flow fluctuations and related to it eccentricity fluctuations of the initial state at the LHC energy.

Introduction

Up to this point studies of heavy ion collisions have reached an enormous efficiency [1–7]. Starting at RHIC and then continuing at LHC, these studies opened a lot of questions for scientific community as well as solved quite a few problems arising with the development of relativistic colliders. One of such discoveries was the evidence of collective behaviour in heavy ion collisions, and one of observables for this behaviour is anisotropic flow. This discovery was the indication of the creation of strongly interacting nuclear matter in a heavy ion collision.

As research in this area was developing, it became possible to study quantities not only averaged by the number of events in the collision, but to calculate them even-by-event. By this studies one can get the probability density distributions of flow coefficients, as well as investigate such phenomena as event-by-event flow fluctuations. There can be several reasons for fluctuations to exist. First of all, it can be due to statistical reasons (finite number of particles in the event). Secondly, non-flow contributions, such as jets and resonance decays can have an impact. Finally, there can be pure dynamical flow fluctuations, which are coming from the asymmetry in the initial state of the system. The very last type of fluctuations is the most important for our analysis, as they can provide direct information to the properties of the initial system. In 2013 ATLAS collaboration

---

introduced an analysis method which can get rid of the statistical and non-flow fluctuations, and leaves dynamical flow fluctuations for direct studies.

HYDJET++ event generator

HYDJET++ is an event generator for simulation of relativistic heavy ion collisions. Detailed information about the generator can be found in [9, 10]. In order to simulate the collision, generation is made as a superposition of two components: soft (hydro-type state with preset freeze-out conditions) and hard (results from the in-medium multi-parton fragmentation with taking into account jet quenching effect). The observable of interest in this research, anisotropic flow, was interpreted by HYDJET++ previously as average by all the events in a collision starting from elliptic flow v_2 up to hexagonal flow v_6.

Elliptic flow is governed by two parameters, which represent the direction and strength of v_2: $\epsilon(b)$ (the spatial anisotropy) and $\delta(b)$ (the momentum anisotropy). The relation between $\delta(b)$ and $\epsilon(b)$ has the following form:

$$\delta = \frac{\sqrt{1 + 4B(\epsilon + B)} - 1}{2B}, \; B = C(1 - \epsilon^2)\epsilon, \; \epsilon = k\epsilon_0 \tag{1}$$

To describe triangular flow, parameter $\epsilon_3(b)$ was introduced.

As study was made first for standard setup of HYDJET++, it was found that the generator does not have enough dynamical flow fluctuations to reproduce the data. Therefore, the modification of the generator was implied by introducing event-by-event Gaussian smearing of spatial anisotropy parameters $\epsilon(b)$ and $\epsilon_3(b)$ with the widths proportional to its "unmeasured" values. The coefficients of this proportionality are tuned to fit the data. In following sections results before and after the unfolding will be shown to be adequate.

Unfolding procedure

The goal of the analysis is to exclude statistical and non-flow contributions on an event-by-event basis, and get the dynamical flow fluctuations. This can be done by using the unfolding procedure. In order to implement the EbyE unfolding procedure for simulated events, the analysis method from [8] was utilized. This method extracts the true flow vector from the observed one on an iterative basis. As it was done in reference [8], in the analysis were used distributions of charged particles produced in a Pb-Pb event with $p_T > 0.5$ GeV/c and $|\eta| < 2.5$. The method consists of several stages. At first, one needs to construct event-by-event single-particle distributions of flow harmonics from a Fourier decomposition of the azimuthal distribution:

$$\frac{dN}{d\varphi} \propto 1 + 2\sum_{n=1}^{\infty} V_n^{obs} \cos\left(n(\varphi - \Psi_n^{obs})\right) = 1 + 2\sum_{n=1}^{\infty} (V_{n,x}^{obs} \cos n\varphi + V_{n,y}^{obs} \sin n\varphi) \tag{2}$$

where V_n^{obs} is the magnitude of the observed per-particle flow vector and Ψ_n^{obs} is the event plane angle, and the flow vector is defined as:

$$V_n^{obs} = \sqrt{(V_{n,x}^{obs})^2 + (V_{n,y}^{obs})^2},$$
$$V_{n,x}^{obs} = V_n^{obs} \cos n\Psi_n^{obs} = \langle \cos n\varphi \rangle, V_{n,y}^{obs} = V_n^{obs} \sin n\Psi_n^{obs} = \langle \sin n\varphi \rangle$$

In the last two equations average is performed over all hadrons in a single event. The single-particle method alone can be used for our study because it was shown, that the distributions obtained after the unfolding procedure do not depend on the method applied to obtain flow coefficients.

Then response function is constructed from distributions of flow vectors' difference $p_{sub}((\overrightarrow{v_n^{obs}})^a - (\overrightarrow{v_n^{obs}})^b)$, get δ_{2SE}:

$$p(v_n^{obs}|v_n) \propto v_n^{obs} \exp(-\frac{(v_n^{obs})^2 + v_n^2}{2\delta^2})I_0(\frac{v_n^{obs}v_n}{\delta^2}), \ \delta = \begin{cases} \delta_{2SE}/\sqrt{2}, & \text{for half} - \text{event} \\ \delta_{2SE}/2, & \text{for full} - \text{event} \end{cases} \tag{3}$$

Here half-event describes the case when only half of the event is used to construct the V_n^{obs} distribution (either with $\eta > 0$ or with $\eta < 0$). Full-event case is used when the distribution is constructed from the whole range of $|\eta| < 2.5$. The constructed function is used to fill unfolding matrix, and then the Bayesian unfolding procedure is performed by means of the RooUnfold package [11].

It should be noted, that before our work [12] there was no direct comparison of model results of probability density distributions of V_2 and V_3 obtained via unfolding event-by-event procedure with ATLAS study [8] performed in the same way.

Results and Conclusions

The simulations and analysis were performed for three centrality intervals, namely, 5 - 10%, 20 - 25% and 35 - 40%, and for two settings of the HYDJET++ model: without and with the additional smearing of spatial distribution of anisotropy parameters $\epsilon(b)$ and $\epsilon_3(b)$. In Fig.1 (Fig.2) the probability density distributions of elliptic flow V_2 (V_3) in three centrality intervals are shown. Dashed and solid histograms present the results for simulated HYDJET++ events before and after the unfolding procedure, respectively. The top/bottom row shows the model results with/without the additional smearing of spatial anisotropy parameters. The closed points are ATLAS data from [8]. As can be seen from the figures, event generator does not have enough flow fluctuations in its original setup to reproduce data. However, a simple modification of spatial anisotropy parameters is sufficient to successfully include dynamical flow fluctuation in the model.

Acknowledgments

References

[1] I. Arsene *et al.*, (BRAHMS Collaboration), Nucl. Phys. A 757, (2005) 1.

[2] B.B. Back *et al.*, (PHOBOS Collaboration), Nucl. Phys. A 757, (2005) 28.

[3] J. Adams *et al.*, (STAR Collaboration), Nucl. Phys. A 757, (2005) 102.
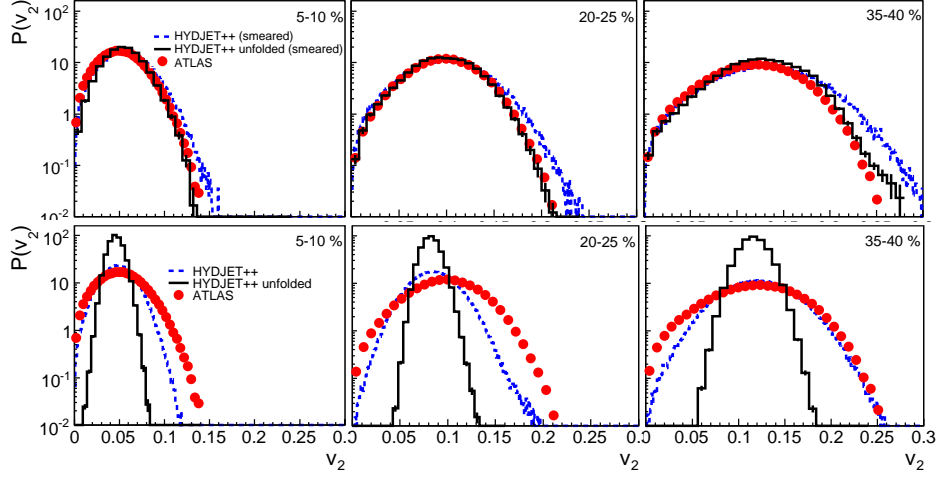
Figure 1: The probability density distributions of elliptic flow V_2 in three centrality intervals 5 - 10 % (left), 20 - 25 % (middle) and 35 - 40 % (right). Dashed and solid histograms present the results for simulated HYDJET++ events before and after the unfolding procedure, respectively. The top/bottom row shows the model results with/without the additional smearing of spatial anisotropy parameters. The closed points are ATLAS data from [8].
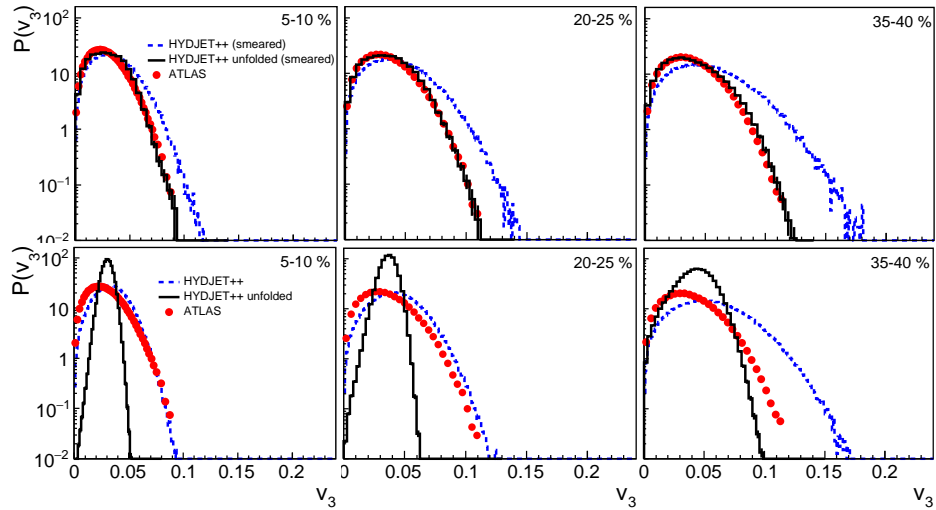
Figure 2: The probability density distributions of triangular flow V_3 in three centrality intervals 5 - 10 % (left), 20 - 25 % (middle) and 35 - 40 % (right).

[4] K. Adcox *et al.*, (PHENIX Collaboration), Nucl. Phys. A 757, (2005) 184.

[5] K. Aamodt *et al.*, (ALICE Collaboration), Phys. Rev. Lett. 105, (2010) 252302.

[6] K. Aamodt *et al.*, (ALICE Collaboration), Phys. Rev. Lett. 107, (2011) 032301.

[7] B. Abelev *et al.*, (ALICE Collaboration), Phys. Lett. B 719, (2013) 18.

[8] G. Aad *et al.*, (ATLAS Collaboration), JHEP 11, (2013) 183.

[9] L. V. Bravina, *et al.* Eur. Phys. J. C 74, (2014) 2807.

[10] I. P. Lokhtin, L. V Malinina, S. V. Petrushanko, A. M. Snigirev, I. Arsene, K. Tywoniuk, Comput. Phys. Commun. 180, (2009) 779.

[11] T. Adye, arXiv:1105.1160 [physics.data-an].

[12] L. V. Bravina, *et al.* Eur.Phys.J. C 75 (2015) 588.

STUDY OF PRODUCTION THE DIRECT PHOTONS AT NICA SPD

A. Rymbekova

Joint Institute for Nuclear Research, Dubna, Russia

Moscow Institute of Physics and Technology, Dolgoprudny, Russia

Annotation

Photons produced in the hard scattering of partons, named the direct photons, provide information about the internal structure of hadrons. This talk will present the preliminary results for possibility to study the production of the direct photons in the proton-proton collisions at the NICA collider. Possibility to extract the signal of the direct photons among background photons from other sources will be discussed. The obtained results can be used for development and optimization of the SPD detector.

Spin physics at NICA

NICA (Nuclotron-based Ion Collider fAility) is a new accelerator complex constructing at the Joint Institute for Nuclear Research (Dubna, Russia). The collider will have two universal detectors: MPD (Multi-Purpose Detector) for heavy ion physics and SPD [1] (Spin Physics Detector) planned for nucleon spin structure studies. Unpolarized and polarized proton and deutron beams will be available for spin physics with energy up to 27 GeV an 14 GeV/nucleon, respectively. Both longitudinal and transverse polarizations of the beams are planned. The expected luminosities are for 10^{32} cm^{-1} s^{-1} for p-p collisions at 27 GeV and 10^{32} cm^{-1} s^{-1} for p-p collisions at 14 GeV/nucleon. The SPD setup will be equipped with the sub-detectors covering 4π angular region around the beam intersection point. SPD will consist of the next subsystems:
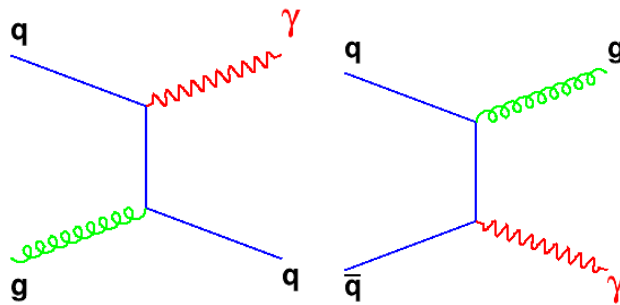
Figure 1: Feynman diagrams for the gluon-quark Compton scattering (left panel) and quark-antiquark annihilation (right panel).

- vertex detectors for reconstruction of the primary and secondary vertices;
- tracking detectors for the measurement of momenta of secondary particles;
- electromagnetic calorimeter for registration of photons and identification of electrons.
- hadron, muon and electron identification systems in the energy range up to 15 GeV.

The main part of the SPD physics program is study of polarized structure functions of the proton and neutron via Drell-Yann process and J/Ψ production. But gluon distributions can be accessed also via production of the direct photons.

Photons at SPD

Direct photons are photons directly produced in hard scattering of partons - quarks and gluons. The main contribution to the direct photons production at the discussed energies comes from the gluon-quark Compton scattering (Fig. 1, left panel) and quark-antiquark annihilation into gluon and photon (Fig. 1, right panel). Only the first one is interesting for investigation of the gluon stuff inside the proton. The cross section of these processes is much smaller than the section of proton-proton collisions. For proton energy 13 GeV the cross section is 1220 nb for the first subprocess and 240 nb for the second while the total proton-proton cross section is about 40 mb.
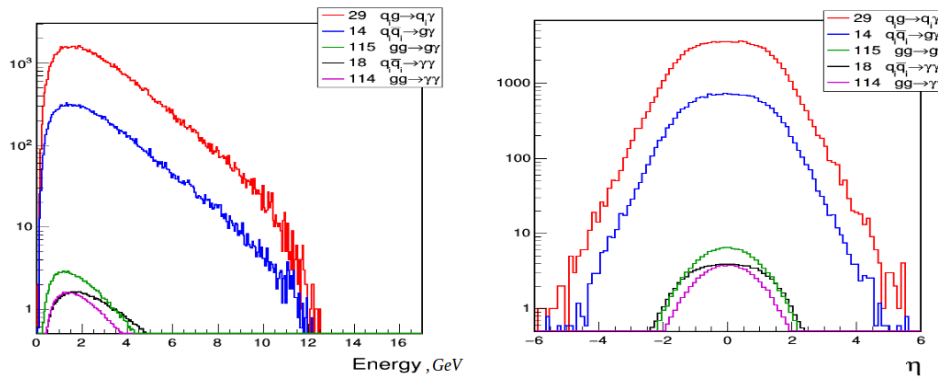
Figure 2: **Kinematic distributions for energy and pseudorapidity of direct photons**
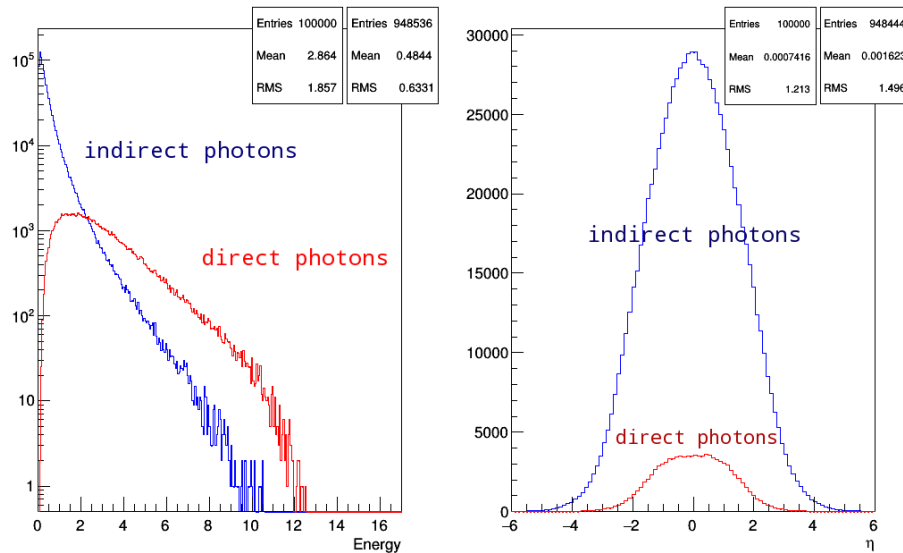
Figure 3: **Energy distribution and distribution of pseudorapidity for direct photons from the reaction of the scattering of a quark gluon.**

The main problem of the measurements with direct photons source of photons in the proton-proton collisions is huge background from production and decay to photons of secondary hadrons - mainly neutral pions. The UA6 experiment at CERN, performed the

186

Table 1: The main sources of photons in proton-proton collisions at 27 GeV

	Photons in 10^6 pp-collisions
π_0	$8.7{\cdot}10^6$
η	400000
$\omega 0$	59500
η'	46200
Σ^0	34500
Δ^+	1610
Δ^0	1130
ρ^0	74
K^{*0}	600
ρ^{+0}	570
ϕ	540
Λ	470
K^{*+}	370

study of direct photons at 24.3 GeV [2], has shown that even use of a nice electromagnetic calorimeter cannot make signal-to-background to be above 1. Similar problem is expected for the measurements at SPD. For preliminary estimation of the photon background at SPD the Pythia6 Monte-Carlo simulation program was used. Kinematic distributions for energy and pseudorapidity of the direct photons produced in proton-proton collisions at 27 GeV (separately for each hard process) are shown in Fig. 2.

One can conclude that direct photons have typically larger energy than the background photons. In Fig. 3 these distributions are compared with the corresponding distributions for background photons. The yields of the background photons from different mother particles per 106 collisions are presented in the Table 1. The main sources of photons are the π_0 and η-meson decays. The significant part of this background can be suppressed by π_0 and η-meson decays reconstruction in the electromagnetic calorimeter. Nice electromagnetic calorimeter with almost 4π geometry is absolutely needed for such kind of measurements.

References

[1] I.A. Savin *et al.* https://arxiv.org/abs/1408.3959

[2] G. Sozzi *et al.* (UA6 collaboration), Phys. Lett. B 317 (1993) 243.

REMOTE OPERATION CENTER AT DUBNA FOR NOVA EXPERIMENT

N. Anfimov, A. Antoshkin, N. Balashov, A. Bolshakova, L. Kolupaeva, Ch. Kullenberg, O. Petrova, O. Samoylov*†, I. Shandrov, A. Sheshukov
Joint Institute for Nuclear Research, Dubna, Russia

Annotation

The ROC-Dubna, Remote Operation Center at Joint Institute for Nuclear Research (Dubna, Russia), supports the NOvA experiment located 14000 km away in Fermilab (Batavia, Illinois, USA) and Ash River (Minnesota, USA). The ROC allows Russian physicists to operate the NOvA detector and monitor the NuMI neutrino beam complex. ROC-Dubna for NOvA is the first fully operational ROC outside USA.

Introduction

The NOvA experiment [1] is one of the new concept experiment in particle physics with remote control of the detectors' operations. This idea came from LHC experiments' era to control large detectors from different scientific research centers and institutes. While each of those experiments (ATLAS, CMS, ALICE, LHCb) controls and operates just one detector from over the World, NOvA has two distant detectors as well a beam machine which the gaol is to control and operate all the remote systems from one place – Remote Operation Center (ROC).

NOvA experiment

The NOvA experiment is a new generation neutrino experiment to study neutrino oscillation properties from muon (anti)neutrino beam to both appearance of electron (anti)neutrino and disapearance of the muon ones. For this research it was built two identical detectors 810 km away in USA. The Near Detector (ND) is located in about 1 km from the beam source at FNAL, Illinois, the Far Detector (FD) is at Ash River, Minnesota. Both detectors are designed to have segmented structure and filled with liquid scintillator into PVC cells 4×6 cm^2 to detect pure signals from electron showers and muon tracks produced in neutrino-nucleon interactions. Total detectors' masses are FD – 14 kT and ND – 0.3 kT. The beam production at NuMI complex used off-axis approach allows to have a narrow spectrum around 2 GeV neutrino energy.

NOvA ROCs

The NOvA experiment at both sites have storage and file transfer systems to accumulate good quality data. While collecting online data safely recorded into local storage, it is more efficient monitoring for the system to use one (Remote) Operation Center for both places in the same time. Now all the NuMI experiments are developing ROCs. The Main Remote

Figure 1: ROC-West view.

Operation Center ROC-West located inside Wilson Hall (FNAL). Currently ten ROCs are operating for the NOvA. There is a ROC-Dubna in JINR, the first non-US ROC started to operate in October, 2015. Figures 1,2 show ROC-West and ROC-Dubna.

ROC-Dubna

History

The NOvA detecrors are operation since 2013 from ROC-West at FNAL. On this stage NOvA collaboration discussed and developed an approach to run remote operation centers out of FNAL. It was first ROC-UMN at Minnesota University started to control and operate from non-Fermilab area at November, 2014. And JINR collaborators initiated ROC question at Dubna.

Constructions

There is a list of key dates and important tasks done at JINR:
1. First ROC-(UMN) out of FNAL started Nov-2014.

Figure 2: ROC-Dubna view.

2. Started to discuss the idea ROC-Dubna, Nov-2014.
3. Checked connection from JINR to FNAL, Dec-2014.
4. Estimated costs of the ROC-Dubna, then buying the equipment, March-July-2015.
5. Installing the Hardware, July-2015.
6. Setting up the Software, August-2015.
7. Took FNAL certification, Sept-2015.
8. We are taking Shift-credits since Oct-2015.
9. Out Colleagues from INR, Moscow took shift at Apr-2016.
10. And also stay tuned our local System.

Operating

The NOvA experiment is operationg 24/7 days a week over the years (at least till 2020, project plan). All the ROCs together ensure continuous processing detectors' systems on both sites as well monitor beam status. Three run coordinators changing every two weeks communicate with Shifters, ROC contacts, Systems' experts, FNAL and Ash river crews. That allows to work together experts and shifters, to monitor beam, detector's electronics, file transfer to take goor quality DATA.

NOvA data storage and transfer software based on Linux-nodes collect information from NOvA DAQ system. ROCs connect to control and operation nodes on both FD/ND sites via VNC-tunneling under secure protocols. Basic idea is that a VNC server transfer a VNC session to many VNC viewers at ROCs with control. In total there are 5 active Scientific Linux based VNC-sessions are connected directly to Near/Far Detectors nodes at FNAL and through GateWays to another World. System includes 1 Linux node for Web-monitoring of the operated systems (Beam, ND/FD Cameras, Data transfer control, Ganglia, Nearline) and 1 Windows node for communication (NOvA electronic loogbook, latest version of expert contact and Bulletin board, Polycom via Vidyo, Slack-chat, Skype).

ROC-Dubna in JINR has developed infrastructure to 8 hours (a shift period) continues work (stable internet, international land-line, kitchen, this is also public JINR area). Computing monitoring system on Nagios controls local Linux-nodes, internet connection, server conditions and notifies JINR experts in case of troubles.

In this way ROC-Dubna while it is 14000 km distance from FNAL allows close collaboration of the JINR scientists and enables smooth operation of the detectors and, given the large time difference between Dubna and Fermilab, relieves some of the burden of around-the-clock shift staffing in the US.

Summary

ROC-Dubna is one of ten NOvA Remote Operation Centers and was the first located outside the USA. The center could serve as a valuable model for participation in other experiments at FNAL including Mu2e, Muon g-2 and DUNE. ROC-Dubna has been visited by Nigel Lockyer (director of FNAL) and Sergei Nagaitsev (head of Accelerator Division) on February 19, 2016.

References

[1] http://www-nova.fnal.gov

FEMTOSCOPIC MEASUREMENTS IN MPD

D. Wielanek[1],[*], P. Batyuk, O. Rogachevsky[2], L. Malinina[3]

[1] *Warsaw University of Technology, Faculty of Physics, Warsaw, Poland*

[2] *Joint Institute for Nuclear Research, Dubna, Russia*

[3] *M.V. Lomonosov Moscow State University, D.V. Skobeltsyn Institute of Nuclear Physics, Moscow, Russia; JINR, Dubna, Russia*

Annotation

Multi-Purpose Detector (MPD) is an experiment to be located on future accelerator complex NICA that is building in JINR. The main goal of the experiment is a study of properties of hot and dense matter created in collisions of heavy ions. One of the methods used for studying of those properties is two-particle correlations. This technique is used to extract information on space-time sizes of a system that emits particles. In this paper we shortly describe current status of preparations for femtoscopic measurements in the MPD.

Introduction

Femtoscopy (also called HBT) is a method used for getting information on space-time sizes of a source that emits particles. The HBT is based on fact that in case of identical particles their function must be symmetrized (for bosons) or antisymmetrized (for fermions). This effect changes probability of pair detection and depends on relative momentum and relative position of emission of particles. Due to this, it is possible to extract information on space-time size of a source that emits particles. A basic tool for the extraction is called a correlation function defined by (1).

$$CF(q) = \frac{N_{correlated\ pairs}(q)}{N_{uncorrelated\ pairs}(q)} \tag{1}$$

Using this definition an experimental correlation function is constructed. Another function is used to fit this data. The fit gives, at least, two types of information. The first one is an average size of the source described by a parameter that corresponds to a femtoscopic radius. The second one is a quality of the fit: if shape of the source used for theoretical function is close to the real one, then quality of the fit is considered to be good. However, not only one dimensional size can be extracted. In the LCMS (Longitudinally Co-Moving System) momentum difference is expanded into three parts. **Long** is a momentum difference along the beam axis, this component contains information on longitudinal size of the source and lifetime of the system. **Side** component is perpendicular to the **long** and gives information on transverse size of the source, **out** gives additional information on emission duration.

It is supposed that below some energy of collision (that corresponds to the Critical Point (CP) location) phase transition (PT) from Quark-Gluon Plasma (QGP) to hadrons is changed from crossover to 1st order phase transition. It means that emission duration and lifetime of system should rapidly increase in some energy range [1]. Step in R_{out}/R_{side}

---

ratio was proposed as a signature of changes in the PT type. Such measurements have been performed by previous experiments and results are presented in Fig. 1. No clear signature of the CP has been found. Only some maximum in the R_{out}/R_{side} ratio around $\sqrt{s_{NN}} = 20$ GeV exists, but it is not a conclusive signature.
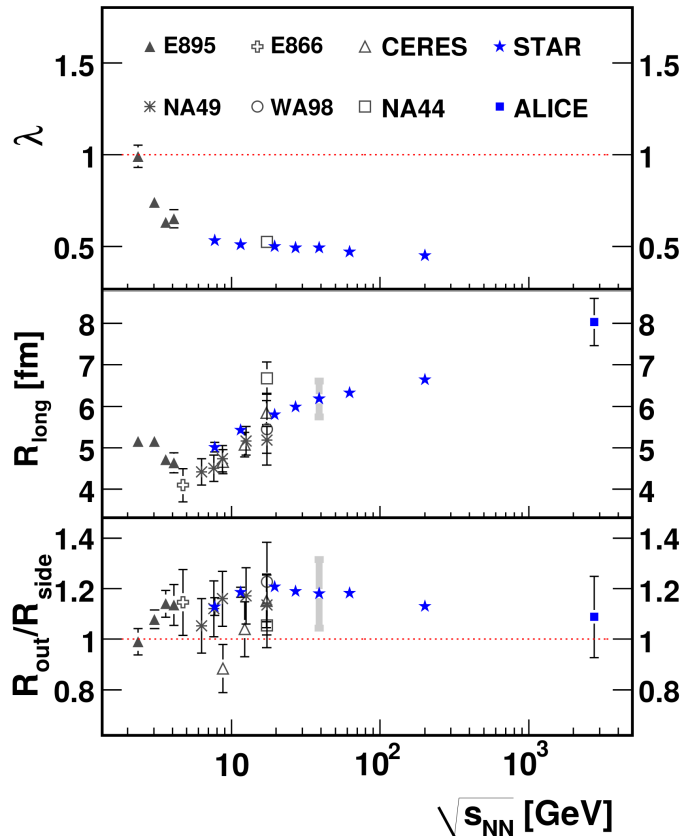
Figure 1: Compilation of the performed femtoscopic measurements. No clear signal of the CP has been found.

The MPD is designed as a tool to study properties of hot and dense matter, part of those research is a study of the PT phenomena [2]. The experiment will provide data with a better quality and accuracy than previous experiments dealing with low energies. It gives possibilities to use more sophisticated types of analysis that require a better precision of measurements and/or bigger statistics. Our studies are dedicated to answer three questions:
- Can we find out, using femtoscopy measurements, what kind of the PT takes place at the NICA energies?
- What are the best methods to answer the question above?
- Can we use those methods to study data from the MPD?

Conclusions

The first step of our studies was a preparation of software. As a result, the NicaFemto package has been developed. The package has been designed for performing femtoscopic analysis. However, there are also classes to perform other simple analysis like spectra or

flow one. The NicaFemto can be also used as a base for developing own type of analysis because contains a system that manages cuts and cut monitors.

The NicaFemto is based on FairROOT and supports many formats of data. It makes it a powerful tool that can be used not only by the MPD collaboration and not only for analysis of data from the MC generators. There are also some features that are not presented in the current software, like system of representation of results of analysis in form of a nicely-formatted web-page instead of text logs. It is necessary to develop not only useful, but also a user-friendly framework. The current version can be obtained from [9]. This package is a candidate for femtoscopic software in three future experiments - BM@N, CBM and MPD. However, due to its flexiblity, it can be also used as a tool for checking how models describe data obtained by femtoscopic analysis. Some parts of the framework can be also useful for other collaborations. After the software has been developed and tested, one has to look for an adequate MC model to be used within the software. Such model should be relatively fast, quite well reproduce available data and have an option of using, at least, two Equations of State (EoS) representing two types of the PT. To perform a test, two hybrid models (UrQMD [3] and vHLLE+UrQMD [4]) were chosen. The obtained results were compared with the NA49 data [5], [6] and the STAR data [7]. Both models quite well describe spectra, however, the vHLLE+UrQMD describes femtoscopic radii better, the model is also faster, so, the vHLLE+UrQMD was chosen as a candidate for analysis. It is important to notice that the UrQMD data description might be better due to fact that a lot of parameters can be used for the model tuning. The next step of the analysis was concentrated on influence of the PT type on standard femtoscopic observables. Simulations with two types of EoS corresponding to two types of the PT were performed. Results of the performed pion-pion analysis for a few energies are presented in Fig. 2.
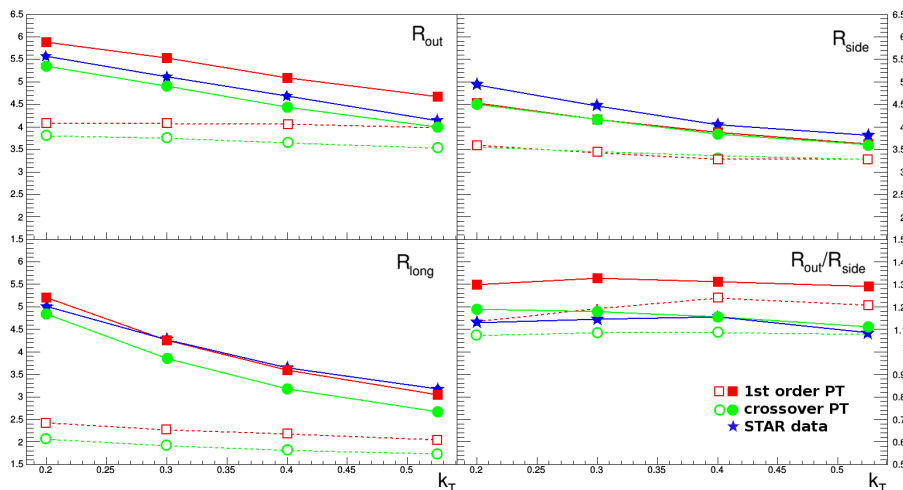
Figure 2: Result of the analysis obtained with the vHLLE+UrQMD data with two EoS's for pairs of identical charged pions. There are also data from the STAR experiment. Full markers represent full simulation, whereas open markers represent simulation without rescatterings and resonance decays.

The obtained results clearly demonstrate that the PT affects femtoscopic observables. As it was predicted, R_{out} and R_{long} are changed by the EoS type, whereas R_{side} seems to be persistent. However, those differences are small. It means that the standard HBT

techniques are not sufficient to clarify what kind of the PT takes place at the given energy range, especially if the detector effects limiting precision of measurements are taken into account. In Fig. 2 there are also dotted lines and open markers. Those data represent results of simulations without taking into account resonances decay and rescatterings. Some theoreticians suppose that for lower energies the mentioned effects might hide some signatures of processes taking place at earlier stages, like the PT from the QGP to hadrons [8]. Such theories can not explain why observation of a clear signal of the CP is not possible. However, our results show that such processes can't completely smear differences caused by the PT even if femtoscopic radii are strongly modified at the latest stages of collision.

Summary

It was studied how the PT type affects femtoscopic observables. Also, it was shown that the HBT might be used as a tool for studying the PT type, however, it will not be an easy task. It is necessary to perform a more sophisticated analysis to find methods that will be more sensitive to this effect. One of the proposed types of analysis is a study of kaon-kaon correlation functions. Kaons are heavier and should be less affected by resonance decays. A limited resolution of the MPD detector is also should be taken into account.

References

[1] D. H. Rischke, M. Gyulassy, arXiv:nucl-th/9606039.

[2] *MPD Collaboration, The MultiPurpose Detector MPD to study Heavy Ion Collisions at NICA* (Conceptual Design Report), http://mpd.jinr.ru/.

[3] H. Petersen, J. Steinheimer, G. Burau, M. Bleicher and H. Stcker, Phys. Rev. C 78 (2008) 044901.

[4] Iu. Karpenko, M. Bleicher, P. Huovinen, H. Petersen, arXiv:1601.00800v1[nucl-th], 2016.

[5] (Na49 collaboration) arXiv:nucl-ex/0208014.

[6] (Na49 collaboration) arXiv:0709.4507 [nucl-ex].

[7] (STAR Collaboration), Phys.Rev. C 92 (2015) 014904 (2015-07-10).

[8] R. Lednicky, Nucl. Phys. B (Proc. Suppl.) 198 (2010) 4345

[9] https://git.jinr.ru/Wielanek/nicafemto NicaFemto repository

Condensed Matter Physics

THE METHODOLOGY OF ELECTRODE MANUFACTURING FOR SPECIAL DESIGNED LITHIUM-ION CELLS

O. Yu. Ivanshina[1,2*], I. A. Bobrikov[1], S. V. Sumnikov[1], and A. M. Balagurov[1]

[1] *Joint Institute for Nuclear Research, Dubna, Russia*
[2] *Department for Nuclear Research, SINP MSU, Dubna, Russia*

Annotation

The methodology of cathode and anode manufacturing for special designed Li-ion electrochemical cells was developed. These cells were designed for in-situ neutron structural analysis of the processes during of lithium-ion batteries operation. Electrochemical characteristics of commercial-like electrodes ($LiFePO_4$, $LiNi_{0.5}Mn_{1.5}O_4$ and etc) and electrodes prepared in our laboratory using the same electrode materials are approximately equal. It allows making the electrochemical cells based on studied electrode materials in laboratory conditions in the absence of hardly accessible factory equipment.

Introduction

At present, lithium-ion batteries (LIB) are considered to be one of the most perspective energy storage systems. The main advantages of LIB compared to other types of power cells include a high specific stored energy and larger number of reversible charge-discharge cycles [1]. Advantages of LIB are determined by the properties of the electrode materials, especially, cathode materials. Improvement of the performance characteristics of LIB requires understanding of the nature of the structural processes occurring on the electrodes. In this instance crystal chemical studies are the most important. Necessary structural data (redistribution of cations with close atomic number, position and occupation of light elements (Li, O)) can be obtained only in the neutron diffraction experiments.

Critical results were obtained in in-situ neutron diffraction studying of the charge-discharge processes in commercial LIB in Frank Laboratory of Neutron Physics (FLNP) [2]. The problem is that commercial power cell consists of many components. Its diffraction patterns contains a lot of reflections not related to electrode materials. Investigation of commercial battery does not allow to study new electrode materials. In FLNP electrochemical cells for neutron diffraction experiments were designed and produced (Fig. 1). The design allows obtaining diffraction patterns with very small number of impurity diffraction peaks during the cell operation (its charge-discharge). Electrodes for the special designed cell can be manufactured from powder materials which are needed for studying. Preparation of such electrodes is a challenge because it requires more skills from researcher, special equipment and additional substances. Moreover a recipe of electrode preparation depends on type of original electrode material and type of electrochemical cell. Our scientific work is devoted to the problem of cathode preparation.

---

*ioyu@nf.jinr.ru
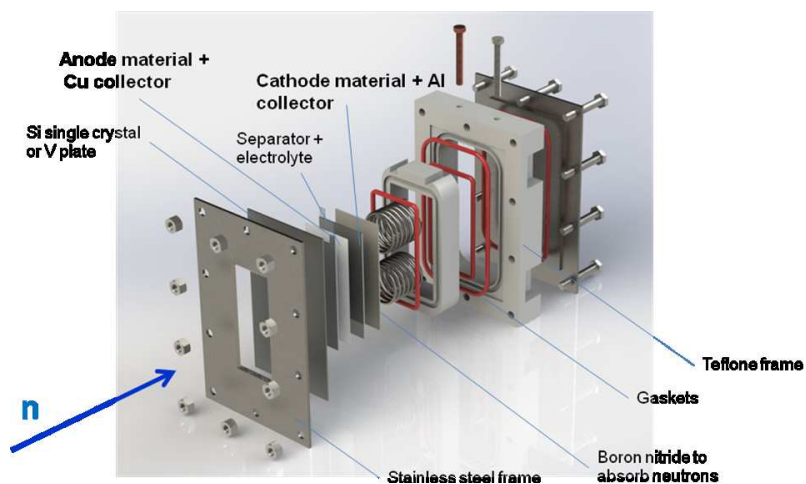
Figure 1: Experimental electrochemical cell.

Experimental part

Purpose of this work was to make the anodes and cathodes similar to commercial ones. The main requirements: values of thickness and density of electrodes have to be not less than 80 μm and $6.25 \cdot 10^{-4}$ g/mm^3 respectively; electrodes must be mechanically stable, without cracks and defects; electrochemical characteristics of commercial and "lab-made" electrodes prepared from the same electrode powder must be similar. Synthesized electrode powder has to be mixed with carbon black to increase of electronic conductivity of electrode material. The next necessary component of electrode is the binder. Polyvinylidene fluoride (PVDF) was selected as one of the most accepted binders [3]. The electrode powder, carbon black are mixed with previously prepared solution of PVDF dissolved in N-methyl pyrrolidone (NMP), and then stirred. To reach good performance of electrode all components should be mixed in certain proportion which was experimentally selected. Further electrode preparation requires additional equipment.

Fig. 2 illustrates the steps from the electrodes manufacturing to the neutron diffraction study. Vacuum mixer (Fig. 2-1) produces electrode mixture by mixing electrode powder, PVDF, carbon black and NMP under vacuum to remove gas bubble and protect sample from oxidation. Film coater (Fig.2-2) with a heating cover was used to produce electrode films with specified thickness on Al or Cu current collectors. It allows drying the electrode film at the specified temperature in the low vacuum. Other variable parameters as the film thickness, rate of the coating films on the foil, time of drying, number of layers are very important too. Electric hot rolling press (Fig. 2-3) is used for pressing electrodes. One can change distance between rolls, speed of rolling, temperature of rolling. Than electrode films should be additionally dried in vacuum. After that the electrodes can be installed in the electrochemical cell. This procedure has to be done in glove box with argon atmosphere. After cell assembly electrode materials are ready for charge-discharge process and neutron diffraction experiment.
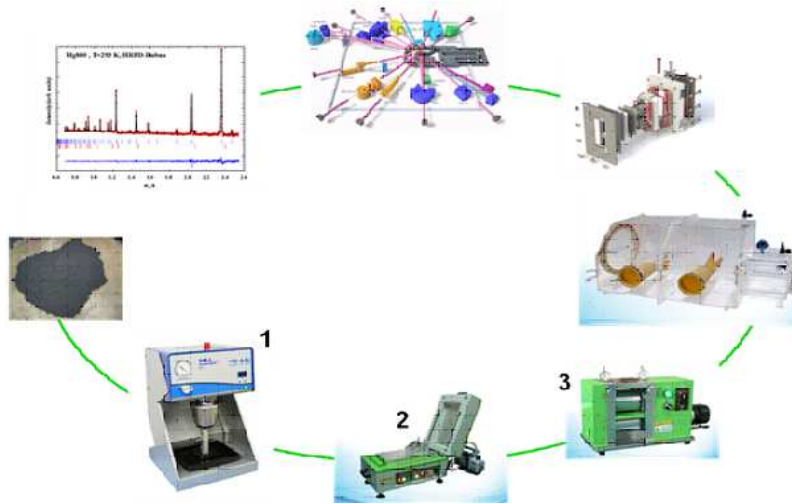
Figure 2: A schematic view "From the powder to understanding of the structural processes". The electrode powder, the mixer (1), the coating machine (2), the roll machine (3), the glove box, the electrochemical cell, the neutron source and the neutron diffraction pattern of the electrode material are shown.

Table 1: Bounds of variation of several parameters and chosen conditions

Parameter	Minimum	Maximum	Chosen
Content of carbon black	0	10	5
Content of PVDF	5	15	10
Drying conditions	50 without vacuum	120 with vacuum	120 without vacuum

Experimental results

One can see there are a lot of parameters which that may presumably affect on the electrode characteristics. Adjustment parameters are shown in Table 1. Some parameters of electrode preparation were fixed: rate of the coating films on the foil and speed of rolling. Our first experiments failed: electrodes cracked and exfoliated from aluminum collector. Table 1 indicates limits of changing of variable parameters and as a result chosen conditions.

Most of electrode materials have low conductivity. It leads to poor electrochemical properties of cells without carbon black in the electrodes. But too high content of carbon black reduces quality of the neutron diffraction spectra (strong incoherent neutron scattering). The final electrode has to be flexible and it strongly depends on quantity of PVDF binder in electrode mixture. When binder content increases the mechanical properties of electrodes improve, but electrochemical characteristics decrease and undesirable incoherent neutron scattering rises. Sufficiently thick electrodes (with thickness about 80 μm and mass content 8-9 mg of electrode material/cm^2) were successfully made when PVDF content was 10 mass %. Film drying temperature was chosen 120°C, and the drying time - 2.5 h. As result capacity and stability of the prepared electrodes were similar to commercial-like electrode properties. For example charge-discharge characteristics of LiNi$_{0.5}$Mn$_{1.5}$O$_4$-type cathode prepared under such conditions were similar to LiNi$_{0.5}$Mn$_{1.5}$O$_4$-type cathode pre-

199
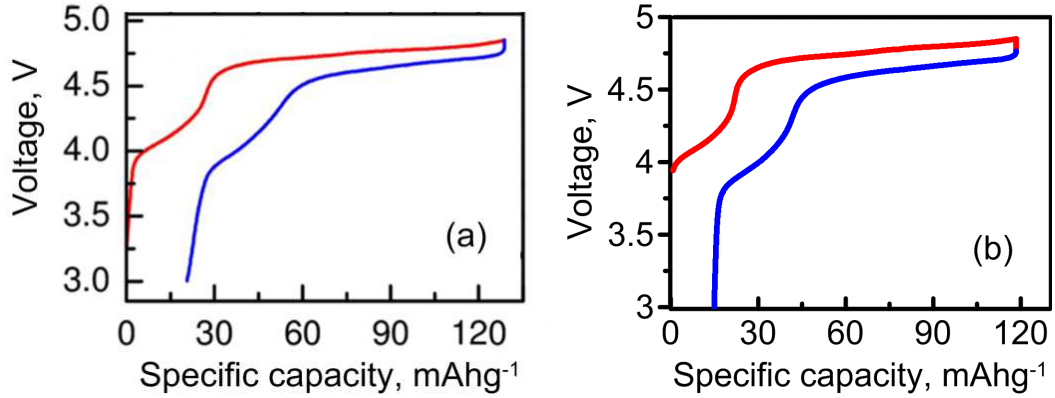
Figure 3: Charge-discharge profiles of LiNi$_{0.5}$Mn$_{1.5}$O$_4$-type electrode material prepared by commercial-like way and tested in a coin cell (left panel) [4], and LiNi$_{0.5}$Mn$_{1.5}$O$_4$-type electrode prepared in FLNP and tested in the special design electrochemical cell (right panel).
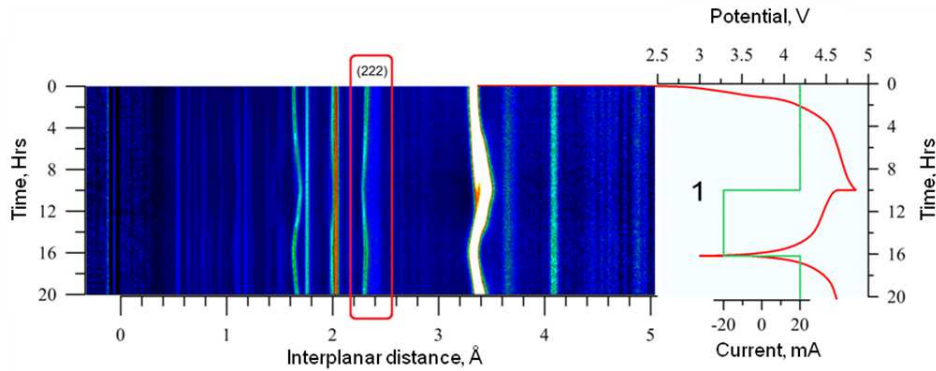
Figure 4: Evolution of the neutron diffraction patterns from spinel cathode material LiNi$_{0.5-x}$Mg$_{x+y}$Mn$_{1.5-y}$O$_4$, measured during charge - discharge cycle.

pared by commercial-like way (Fig. 3). Using this methodology we manufacture electrodes with several novel materials. Example of in-situ neutron diffraction study of doped spinel cathode material LiNi$_{0.5-x}$Mg$_{x+y}$Mn$_{1.5-y}$O$_4$ is presented on the Figure 4. The sample was prepared by mechanochemically assisted solid state synthesis in Institute of Solid State Chemistry and Mechanochemistry SB RAS, Novosibirsk, Russia. Crystalline powders LiNi$_{0.5-x}$Mn$_{1.5-y}$M$_{x+y}$O$_4$ (M =Co, Cr, Ti; $x + y = 0.05$) have promised electrochemical properties as cathode materials for LIB [4]. The experiment has been made on the Real-time Diffractometer (RTD) at the IBR-2 pulsed reactor in JINR (Dubna).

Conclusion

A methodology of the electrode manufacturing for special designed electrochemical cells was developed. Electrochemical characteristics of commercial-like produced electrodes and electrodes prepared in FLNP using the same electrode powder are approximately equal. It allows to produce ready electrodes for neutron scattering experiments on the basis of the laboratory equipment in the absence of hardly accessible factory equipment.

Acknowlegments

References

[1] A. M. Balagurov, I. A. Bobrikov, N. Yu. Samoylova, O. A. Drozhzhin, E. V. Antipov. Russian Chemical Reviews, 83 (12) (2014) 1120.

[2] I. A. Bobrikov, A. M. Balagurov, Ch.-W. Hu, Ch.-H. Lee, T.-Y. Chen, S. Deleg, D. A. Balagurov. Journal of Power Sources, 258 (2014) 356.

[3] M. Yoshio, R. J. Brodd, A. Kozawa. Springer. DOI: 10.1007/978-0-387-34445-4 (2009) c. 185.

[4] N. V. Kosova, I. A. Bobrikov, O.A. Podgornova, A.M. Balagurov, A.K. Gutakovskii. Journal of Solid State Electrochemistry, (2015) DOI: 10.1007/s10008-015-3015-4.

BEYOND LITHIUM-ION BATTERIES: A COMPUTATIONAL STUDY ON NA-S AND NA-O BATTERIES.

M. C. Masedi[1,2, *], P. E. Ngoepe[1], H. M. Sithole[2]

[1]*Materials Modelling Centre, University of Limpopo, School of Physical and Minerals Sciences, Sovenga*

[2]*CSIR, Meraka Institute, Meiring Naude, Brummeria, Pretoria, South Africa.*

Annotation

The first principle pseudopotential calculations based on the Perdew-Burke-Ernzerhof (PBE) form of generalized gradient approximation (GGA) within density functional theory (DFT) has been utilized to investigate the stabilities of insoluble discharge products of oxygen and sulphur in the Na-O and Na-S batteries. Their structural, mechanical and electronic properties were determined. The lattice parameters were well reproduced and agree with the available experimental data. The heats of formation predicts that all structures are generally stable, Na_2S is the most stable structure with the lowest value of heats of formation. The elastic constants suggest that all the structures are mechanically stable which in good agreement with the calculated phonon dispersions.

Introduction

Lithium-air batteries are potentially viable ultrahigh energy density chemical power sources, which could potentially offer specific energy up to 3000 Wh/kg being rechargeable [1]. Although their implementation holds the greatest promise in a number of applications ranging from portable electronics to electric vehicles (EV), there are also impressive challenges in developments of cathode materials and electrolyte system of these batteries. Li-air batteries has a number of difficult problems to overcome, the biggest shortfall exhibited with these systems is the formation of lithium dendrite which raises safety issues [2]. It has been suggested to replace the metallic lithium anode by sodium and operate the sodium-air cell, which could enable the development of a new generation of high specific energy rechargeable batteries. The theoretical specific energy of the sodiumair cell, assuming Na_2O as one of the discharge product and including the weight of oxygen, is 1690 Wh/kg, about four times that of state-of-the-art lithium-ion batteries. The surface tension of the liquid sodium anode is expected to prevent the formation of sodium dendrites on charge. Any sodium dendrites that might be formed would be absorbed into the liquid phase [3]. In the current work we present a comparative study on stability, structural and electronic properties of discharge products of sulphur and oxygen in Na-O and Na-S batteries. Structural properties are schown at Fig. 1.

Structural Properties

Figure 1 shows the crystal structures of Na_2S, Na_2O, Na_2O_2 and NaS_2 to be studied in this work, all have a cubic anti-fluorite structure with Fm-3m symmetry.

---

*cmasedi@csir.co.za
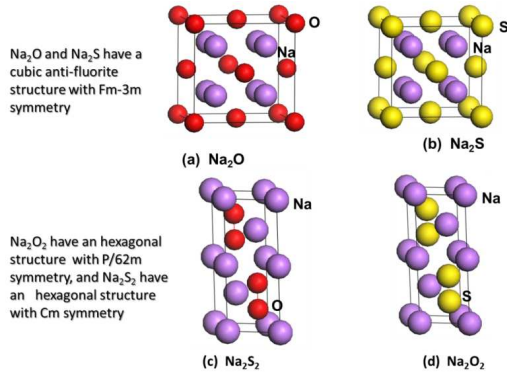
Figure 1: Crystal structures of Na₂S, Na₂O, Na₂O₂ and Na₂S₂, the red atom represent O, yellow atom is S and purple atom is Na.

Methodology

The calculations were carried out using ab initio density functional theory (DFT) formalism as implemented in the VASP total energy package [4] with the projector augmented wave (PAW) [5]. An energy cutoff of 500 eV was used, as it was sufficient to converge the total energy of all the systems. For the exchange-correlation functional, the generalized gradient approximation of Perdew and Wang (GGA-PBE) [6] was choosen. The Brillouin zone integrations were performed for suitably large sets of k points according to Monkhorst and Pack [7]. The phonon dispersion spectra were evaluated using PHONON code [8] as implemented by Materials Design within their MedeA software, VASP code [4]. k-point mesh of 8×8×8 was used. Optimization of structural parameters (atomic positions and lattice parameters) was achieved by minimization of forces and stress tensors.

Results and Discussions

Structural Properties

Table 1: The equilibrium lattice parameters and heats of formation (ΔH_f) of the Na₂O, Na₂S, Na₂O₂ and Na₂S₂ structures.

Structure	Lattice Parameters, (Å)		ΔH_f, (KJ/mol)		Volume (Å³)
	VASP	Exp.	VASP	Exp.	
Na₂O	a = 5.12	a = 5.49 [9]	-318.25		134.29
Na₂S	a = 5.55	a = 5.526 [10]	-298.13		281.50
Na₂O₂	a = 5.26		-145.08		107.06
	c = 4.45				
Na₂S₂	a = 7.66		-14.11		274.26
	c = 5.39				

Table 1 provides structural properties that are in good agreement between the experimental and calculated lattice constants, especially for Na₂S and Na₂O structures. The observed values of heats of formation (ΔH) suggest that all structures are generally stable

which is in good agreement with calculated phonon dispersions. Na_2S is the most stable structure with the lowest heat of formation value.

Phonon Dispersions Calculations

Fig. 2 shows the phonon dispersion calculations (Fig. 2) shows that all the structures are stable due to the absence of soft modes in the negative frequency and is in good agreement with elastic properties values observed.
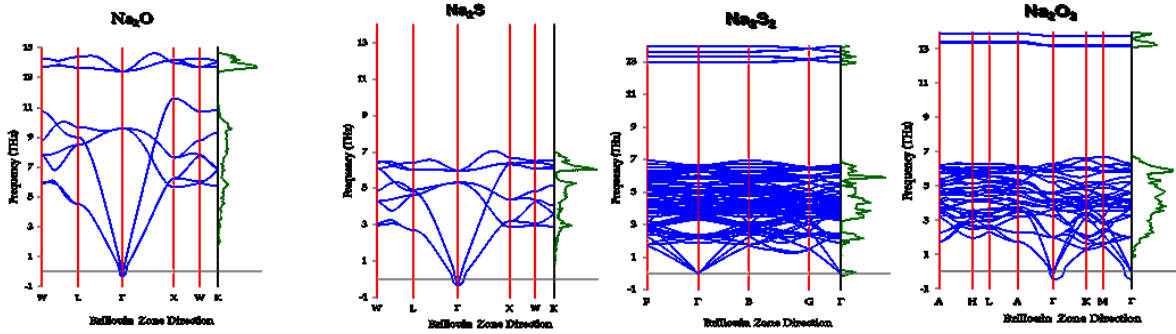
Figure 2: Phonon dispersion curves of Na_2S, Na_2O, Na_2O_2 and Na_2S_2 structures.

Elastic Properties

Table 2: The elastic constants (GPa) for Na_2O, Na_2S, Na_2O_2 and Na_2S_2 structures.

	Na_2O		Na_2S		Na_2O_2	Na_2S_2
	VASP	Exp. [11]	VASP	Exp. [10]	VASP	VASP
C_{11}	127.59	114.00	51.61		220.40	59.35
C_{12}	75.87	34.71	16.25		147.98	16.78
C_{13}					101.21	12.14
C_{33}					263.25	59.88
C_{33}	26.67	27.40	14.56		79.57	9.99

The accurate calculation of elasticity is essential for gaining an insight into the mechanical stability and elastic properties of solids. The mechanical stability criteria of cubic systems as outlined elsewhere [9] are given as follows:

$$C_{44} > 0, \quad C_{11} > C_{44}, \quad C_{11} + 2C_{12} > 0. \tag{1}$$

where C_{11}, C_{12} and C_{44} are the only three independent elastic constants. Table 2 provide elastic constant results which shows that Na_2O, Na_2S, Na_2O_2 and Na_2S_2 are positive, thus satisfying mechanical stability criteria set in equation (1).

Conclusion

All structures are stable because of low values of the heats of formations. The calculated values of lattice parameters and elastic constants are in good agreement with the experimental and theoretical values for both Na_2O and Na_2S. The elastic constants suggest mechanical stability of all discharge products. Our phonon dispersions calculations shows all the structure are stable which is in good agreement with calculated heats of formations values observed.

References

[1] K. M. Abrahamas, Z. Jiang , J. Electrochem. Soc., 143 (1996) 1.

[2] A. R. Armstrong, M. Holzapfel, P. Novák, C. S. Johnson, S. H. Kang, M. M. Thackeray, P. G. Bruce, J. Am Chem Soc., 128 (2006) 26.

[3] E. Peled, J. Electrochem. Soc., 126 (1979) 2047.

[4] P. E. Blöchl, Phys. Rev., B 50 (1994) 17953.

[5] Y. Wang, J. P. Perdew, Phys. Rev. B 45 (1992) 13244.

[6] J. D. Pack, H. J. Monkhorst, Phys. Rev. B 13 (1976) 5188.

[7] K. Parlinski, Z. Q. Li, Y. Kawazoe, Phys. Rev. Lett. 78 (1997) 4063.

[8] S. Kamran, K. Chen, L. Chen, Phys. Rev. B 79 (2009) 024106.

[9] E. Zintl, A. Harder, B. Dauth, Z Elektrochem, 40 (1934) 588, .

[10] H. Khachai, R. Khenata, A. Bouhemadou, H. Reshak Ali, A. Haddou, M. Rabah and B. Soudini, Solid State Commun, 147 (2008) 178.

[11] M. Thomson, X. Shen, B. Allen, Physical Review, B 79 (2009) 113108.

[12] H. R. Chauke, PhD Thesis, University of Limpopo, 2005.

FORMATION OF POLYOXOTUNGSTATES IN AQUEOUS-ORGANIC SOLUTIONS

O. Yu. Poimanova, A. O. Medved, K. Ye Bilousova
Donetsk National University, Donetsk, Ukraine

Annotation

A new synthetic route for polyoxotungstate synthesis was proposed. Novel clusters of decatungstates with organic and inorganic cations were successfully synthesized from aqueous-organic solutions. The thermodynamic aspects of synthesis, chemical composition, crystal structure, surface morphology, thermal decomposition and magnetic properties were investigated by mathematical modeling, chemical, UV-vis., FTIR- and Raman-spectroscopy, X-ray, DTA analysis. These substrates could be used in catalysis, biomedicine, molecular electronics, energy and optical application.

Introduction

Polyoxometallates (POM) belong to the large class of complex metal oxides, which are formed by d-elements like vanadium, molybdenum, niobium, tungsten. The so-called "polyoxometalate periodic table" is presented on the Fig. 1, that shows the diversity of POM compounds. The present work was focused on the tungsten compounds polyoxotungstates.
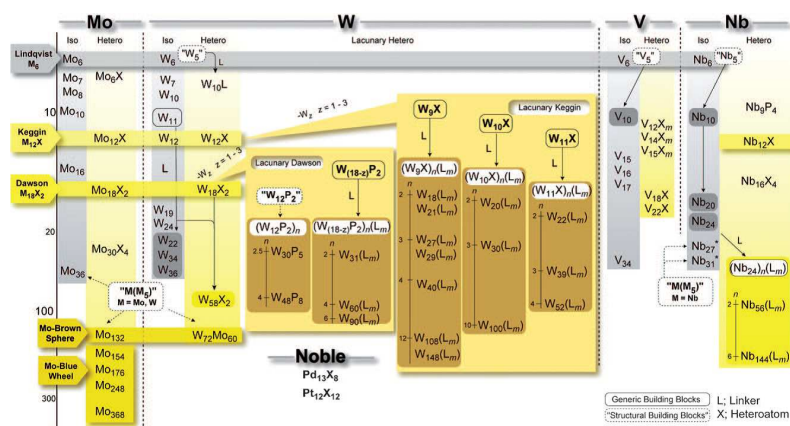
Figure 1: Polyoxometalate periodic table [1]

Due to the self-assembly of POM a diverse range of material structures can be obtained. Such significant characteristics of POMs: stability of complexes (in water, on air, at thermal treatment), big size (diameter 6-25Å), discrete size and discrete structure, anionic nature (charge from -3 t -14), high ionic mass (10^3-10^4), the highest oxidation degree of and reduction ability, photoreduction ability, solubility in water and other solvents, formation of compounds with different elements, diversity of structures lead to the diverse range of their application: catalysis of organic reactions, antitumor, antiviral, antimicrobial agents, anticorrosion covers, analytical chemistry, radioactive waste treatment, sorbents of gases,

sensors, electrooptics, electrochemistry, modifiers for solar cells. The formation of isopoly-tungstates sensitively depends on different factors: the concentration of initial monomer orthometallate, the acidification of the solution, the presence of the reducing agents, het-eroatoms, the temperature and conditions of synthesis, the nature of counter ions and the composition of the solvent. The last two conditions were mostly investigated in the present work.

Experimental

The acidification of the tungstate solution leads to the formation of different forms of IPTA: hexa, hepta, para, meta and decatungstate anions [2]. The hexatungstate with Lindkvist structure and decatungstate are stabilized by aqueous organic organic medium. So the purpose of the work was to develop the synthetic route, synthesise, analyze composition and determine the structure, investigate the properties of salts with IPTA and organic and inorganic cations from aqueous organic medium. Based on previous studies of inter-convertions and transformations of isopolytungstate anions in aqueous dimethylformamide solutions the conditions of synthesis were determined. The system with 40% of DMF at the acidities ($Z = \nu(H^+)/\nu(WO_4^{2-})$) 1.00, 1.14, 1.17, 1.29, 1.42, 1.50, 1.60, 1.67, which correspond to the different reactions of polycondensation, were used. The identification of compounds, determination of composition, structure and properties were conducted by using of the methods of Chemical analysis, UV-vis. spectroscopy, Thermal analysis, FTIR spectroscopy, Scanning electronic (raster) microscopy and EDX analysis, X-Ray analysis and Raman spectroscopy.

Results and Discussions

Isopolytungstates with organic cation - tetrabuthylammonium

The addition of tetrabuthylammonium cation to the acidified to different acidities solu-tions of orthotungstate led to the formation of amorphous mixtures of hepta- and de-catungstates or individual decatungstates. The last anion was identified by the presence of bands 800, 890 and 960 cm^{-1} in the FTIR spectra. On the set of chemical, FTIR and thermal analysis it was concluded that the best systems for tetrabuthylammonium decatungstate ($[(C_4H_9)_4N]_4W_{10}O_{32} \cdot 2C_3H_7ON \cdot H_2O$) formation are those ones with acidity higher than 1.42.

Isopolytungstates with inorganic cations cobalt (II), barium (II)

The difference in influence of inorganic cation was seen from the beginning of the synthesis. Based on the FTIR spectra and chemical analysis of the obtained salts at acidities 1.14-1.29 the following formulae were ascribed: $Co_3W_7O_{24} \cdot xH_2O$ (x=23-19). They are hydrates of cobalt heptatungstate. Increasing of the acidity led to precipitation of powder cobalt paratungstates, which are also hydrates according to the IR-spectra.

The most interesting behavior of the system was at Z=1.60, which corresponds to de-catungstate formation according to the reaction. The necessary conditions were selected: only after evaporating of the part of solution the color from purple turned blue, and after time pink-red transparent crystals of cobalt decatungstate fellout. The Raman, FTIR and
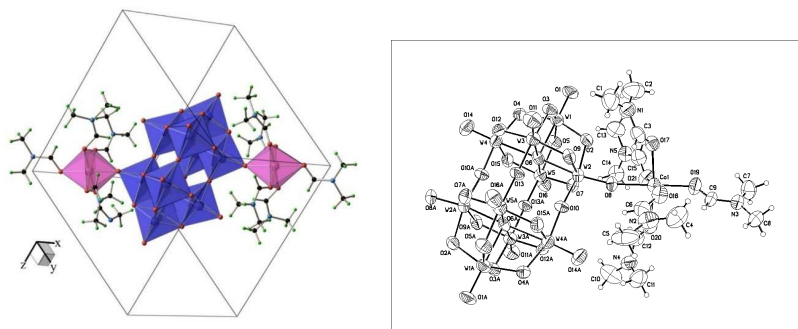
Figure 2: Main structural unit in the crystal structure of $[Co(C_3H_7NO)_5]_2[W_{10}O_{32}]$.

UV spectroscopies indicated the formation of cobalt decatungstate with solvation sheath. The results of EDX analysis, conducted in different areas of the sample, testify to maintenance of the molar ratio Co:W = 1:5, and uniformity of distribution of elements on the surface of the sample confirms the formation of single-phase. 20 000 times magnification shows that the salt surface consists of spherical grains with blurred indistinct edges whose size is in the range of 290-425 nm.

Basic crystallographic data of X-ray analysis of $[Co(C_3H_7NO)_5]_2[W_{10}O_{32}]$, obtained during the imaging of the single crystal, are given in the Table 1. Centrosymmetric anion $W_{10}O_{32}^{4-}$ in the structure has a typical constitution, in which two "square pyramids" consisting of five distorted octahedra WO_6 lacunar derivatives of Lindqvist structure are connected through "bases" at the expense of the common vertices of four octahedra (Fig. 2). The thermal decomposition of the obtained cobalt decatungstate undergoes three stages of consistent loss of mass with destroying of the IPTA structure at temperature higher than 175 degrees Celcius and final crystallization of cobalt orhotungstate and tungsten trioxide that was fixed on the X-ray powder diffraction pattern.
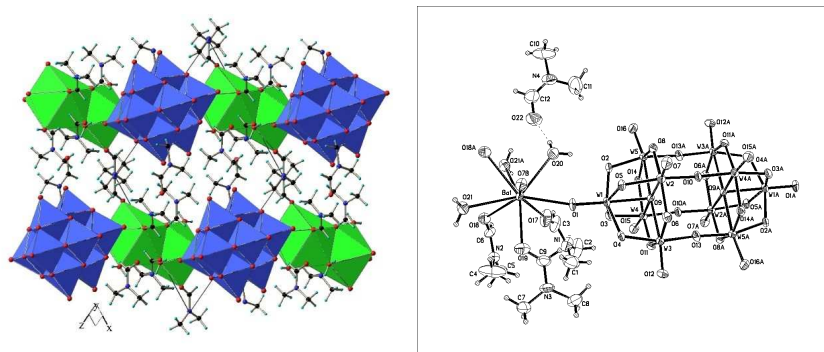
Figure 3: Main structural unit in the crystal structure of $[Ba(H_2O)_2C_3H_7NO_3]_2[W_{10}O_{32}]\cdot 2C_3H_7NO$.

The condensation with another inorganic cation barium at Z=1.60 also did not lead to the immediate formation of decatungstate as it occurs with organic cation. The first two phases were barium heptatungstates on the basis of IR and chemical analysis. The same conditions as in the case of cobalt were created to isolate barium decatungstate $[Ba(H_2O)_2C_3H_7NO_3]_2[W_{10}O_{32}]\cdot 2C_3H_7NO$. The intensities and the positions of bands in FTIR and Raman spectra were characteristic to the decatungstate, which had dimathyl-

Table 1: Basic basic crystallographic data of the novel cobalt (II) and barium (II) decatungstates

Empirical formula	$C_{30}H_{70}Co_2N_{10}O_{42}W_{10}$	$C_{24}H_{64}Ba_2N_8O_{44}W_{10}$
Formula weight	3199.32	3282.01
Temperature ()	293 (2)	
Space group	Triclinic -1	
a [Å]	11.2239(7)	11.899 (3)
b [Å]	12.2221(10)	12.1313 (11)
c [Å]	13.9184(8)	13.341 (2)
[°]	71.380 (6)	70.417 (11)
[°]	89.506(5)	64.254 (18)
[°]	72.144(6)	87.185 (12)
Volume [Å³]	1713.8(2)	1623.75 (5)
Z	1	
Final R indices	$R_F = 0.0488$	$R_F = 0.0435$

formamide in the solvate sheath. The unique structure of decatungstate makes possible to determine it by UV-spectroscopy in the solution the band 320-325 nm indicated decatungstate in the salt composition. By the use of single crystal X-ray analysis the structure of firstly isolated barium decatungstate was decrypted (Fig. 3). The basic crystallographic data are presented in the Table 1.

SEM-images of the triturated crystals of barium decatungstate showed that there are no zones with different surface morphology. 20,000 times magnification shows that the surface is built of spherical granules 220-370 nm in size.

EDX spectral analysis in different zones, averaged for every sample, exhibited no substantial deviation from the molar ratio : W = 1 : 5 according to the empirical formula. The study of thermal behavior of barium decatungstate allowed to determine the stages of the salt decomposition and range of anion stability. It should be noticed, that the obtained decatungstates demonstrated the reversible photosensitivity both in solution and in solid phase.

Conclusions

The presented work is a solution of the new scientific problem, formulated as establishing of the behavior of the IPTA in aqueous organic solutions, investigating of the synthetic conditions and synthesizing of isopolytungstates with organic and inorganic cations, which led to the following conclusions. Salts with IPTA and tetrabuthylammonium were synthesized at different acidities; at all acidities tetrabuthylammonium decatungstate can be obtained, but only at Z¿1,50 from 40% aqueous dimethylformamide solutions individual decatungstate can be isolated; the nature of significantly influences the IPT formation. For the first time from the aqueous dimethylformamide solutions crystal decatungstates $[Ba(H_2O)_2C_3H_7NO_3]_2[W_{10}O_{32}]\cdot 2C_3H_7NO$ and $[Co(C_3H_7NO)_5]_2[W_{10}O_{32}]$ were synthesized and structurally characterized (Tables of atomic coordinates, bond lengths and angles, anisotropic displacement parameters, hydrogen coordinates, and isotropic displacement

parameters were deposited at the Cambridge Crystallographic Data Centre under depository number CCDC 1018995 and 1035468 and can be obtained free of charge by contacting CCDC, 12 Union Road, Cambridge CB2 IEZ, UK (fax: +44-1223-336-033; E-mail: deposit@ccdc.cam.ac.uk or , http://www.ccdc.cam.ac.uk). After the trituration of the crystals the nanoparticles are obtained of size 200-400 nm. The schemes of thermal decomposition of crystals were proposed, which allowed to determine the range of thermal stability of the salts and to suppose the thermal ranges of application the salts, for example, in catalysis of organic reactions of oxidation.

References

[1] D.-L. Long, R. Tsunashima, L. Cronin, Angew. Chem. Int. Ed., 49 (2010) 1736.

[2] M.T. Pope, *Heteropoly and Isopoly Oxometallates* (SpringerVerlag, Berlin, 1983)

Experimental Nuclear Physics

TRIGGER SYSTEM IN THE HYPERNIS PROJECT

A. N. Baeva[*], A. V. Averyanov, D. O. Krivenkov

HyperNIS, LHEP, Joint Institute for Nuclear Research, Dubna, Russia

Annotation

The experimental program of the HyperNIS project contains the investigations of the role which strangeness plays in nucleon and nuclei. The trigger system of HyperNIS project is built on scintillation counters. Methods based on LED sources are used to evaluate the trigger efficiency and the counters calibration.

Introduction

The project is aimed on study of the lightest neutron-rich hypernuclei; in particular, the search for (study of) $^{6}_{\Lambda}$H. Simultaneously, the lifetimes and production crosssections of $^{4}_{\Lambda}$H and $_{\Lambda}{}^{3}$H will be studied in the same experiment. Moreover, productionof $^{4}_{\Lambda}$H and $^{3}_{\Lambda}$H hypernuclei is the precise reference signal to be sure that $^{6}_{\Lambda}$H should beseen or that there are no stable forms of $^{6}_{\Lambda}$H if it is not observed in the same run. Thistask is regarded as the very first experiment because at Frascati experiment [1,2]evidence of only three events was reported and controversial data obtained at J-PARC [3],where no signal was fixed (instead of expected 50 events). On the other hand, before the experiment A.Gal predicted that the possibility to see $^{6}_{\Lambda}$H signal was low in the case because the spectrometer at J-PARC is not suited well for the task - the energy of recoil nuclei is too high.

The Hypernuclear program at Dubna [4] was started in 1988 with the setup based on 2-m streamer chamber. The investigation of the light hypernuclei production and decay [5] was done, namely, the lifetime of $^{4}_{\Lambda}$H and $^{3}_{\Lambda}$H as well as their production cross sections were measured. It was shown that the approach, in which the momentum of hypernuclei produced in the beams of relativistic ions is close to the momentum of the projectiles, was quite effective for measurements of hypernuclei lifetimes and production cross sections. The dedicated and very selective trigger on two body hypernuclei decays with negative pion was the key point of this approach. The accuracy of lifetime measurements was, therefore, restricted only by statistical errors. The values of the experimental cross section were in good agreement with the results of the calculations (refs. [6] of H. Bando, M. Sano, J. Zofka and M. Wakai, see also review [7]) performed using the coalescence model.

Detector Configuration

In the HyperNIS project $^{6}_{\Lambda}$H hypernucleus research will be carried out with the ^{7}Li beam:

$$^{7}_{\square}Li + ^{12}_{\square}C \rightarrow \quad ^{6}_{\square}H \quad + p_{frag} + K^{+} \tag{1}$$
$$\downarrow$$
$$^{6}_{\square}He \quad + \pi^{-},$$
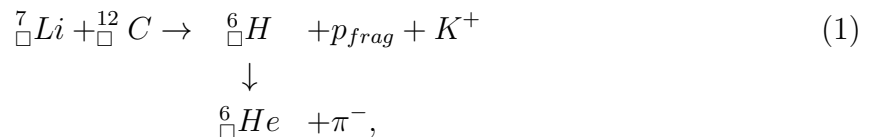
Configuration of the spectrometer is presented in Fig. 1. In the ^{7}Li beam nuclei interactions with carbon target (12 cm along the beam and 3×3 cm^2 cross section, 20.4 g/cm^2), when

---

[*]an.baeva@physics.msu.ru

hypernuclei ($^3_\Lambda$H,$^4_\Lambda$H or $^6_\Lambda$H) are produced, pionic decay $^A_\Lambda H \to \pi^- +^A_\square He$ (A=6,4,3) will occur inside the vacuum vessel with rather high probability.The scintillation counters (trigger detectors B,C) are tuned so as to measure charge difference between hypernucleus and its decay products. Blocks of proportional chambers PC$_1$ (four chambers 38×38 cm^2) and
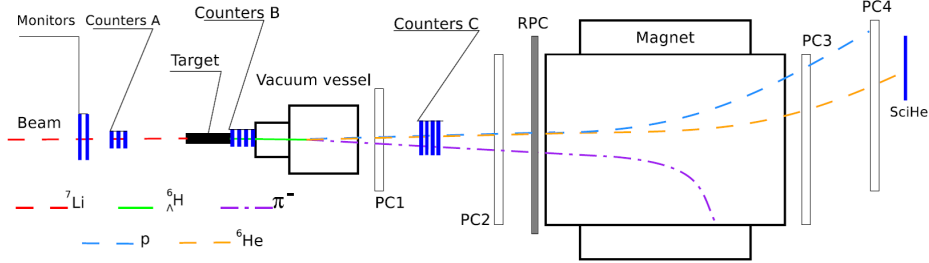
Figure 1: Configuration of the NIS-GIBS spectrometer adapted for the first-stage of the hypernuclear experiments, in particular for the search of $^6_\Lambda$H hypernuclei with the ^{7}Li beam (not in scale). Target - carbon 12×3×3 cm, 20.4 g/cm^2; beam monitors; A,B,C - trigger counters; vacuum decay vessel of 55 cm length; the analyzing magnet of 0.9T; PC$_{1-4}$ - proportional chambers, RPC - TOF stations, SciHe - Scintillation counter to confirm registration of He nuclei.

PC$_2$ (three chambers 130×80 cm^2) register hits from pion and the daughter nucleus (He), allowing the reconstruction of the decay vertex. In addition, the set of all the proportional chambers(PC$_{1-4}$) is used to measure momentum of the He nucleus. The chambers PC$_{3-4}$ are of the same size as the chambers PC$_2$. With the ^{7}Li beam the full set of the chambers allows detection of the secondary proton (p) or another Li fragment and the momentum separation of the hydrogen hypernuclei daughter nuclei - He isotopes. The scintillation counter is used to measure signal amplitude at the location where ^{6}He daughter nuclei are expected to separate them between tritium fragments produced together with $^6_\Lambda$ H hypernuclei. In order to measure momenta of relatively slow pions, emitted at relatively large angles, the time-of-flight method will be used. For this purpose a wall of RPC chambers is installed before the analyzing magnet. The detector is effective for approximately 30% of the full pion spectrum and to determine mass of hypernucleus.

Trigger system

The trigger aimed to detect the pionic decays of hypernuclei was developed and used successfully in the previous experiment in Dubna [4, 5, 8]. The idea of the trigger is as follows. When the $^6_\Lambda$H hypernucleus is produced, the Li nucleus should emit spectatorproton while remaining core ^{6}He nucleus is being changed into the $^6_\Lambda$H. Each of thesetwo particles have charge equal to 1 (total Z = 1 + 1) and hit block of counters B.Since the counter response is proportional to Z^2 of interacting particle, both particles will create in the B counters the signals proportional to U = 12 + 12 = 2. If associated K$^+$ or recoil protons hit counters C$_1$ as well, they increase the signal amplitude and block the hypernuclear trigger. Experience of our previous experiment and simulation estimates show that (generally) these particles avoid the counters and reduction of the trigger rate by this reason is less than 5%. Mesonic decay $^6_\Lambda H \to^6 He + \pi^-$ results into particles of Z = 2 (He) and Z = 1 (π^-). The scintillation counters C of minimal size are used in order to register just the

214

daughter nuclei. Most pions will miss these counters, and such condition provides the best amplitude resolution of counters C. As far as the spectator protons are concerned, it is expected that significant fraction of them will hit the counters. However, it is desirable to have a trigger working at full capacity, and therefore, one should ensure that the trigger works efficiently when the C counters have signal proportional to $U = 2^2 = 4$ (only He hits the CS_2), $U = 2^2 + 1^2 = 5$ (proton or pion also hits the counters), and $U = 2^2 + 1^2 + 1^2 = 6$ (all the particles hit the C). Thus, in the counters C one should register signal proportional to $U \geq 4$ if the hydrogen hypernucleus decay takes place but less than $U = 9$ created by Li beam nuclei.

Finally, we should underline that in the case of pionic decays the signal registered in the counters C is higher than that of the B while for the majority of the background events the signal in the C is lower than in B.

To provide particles with different electric charges for the trigger tests, the ^{12}C beam passed through Al target. The composition of the resulted beam after the target is shown in Fig. 2.
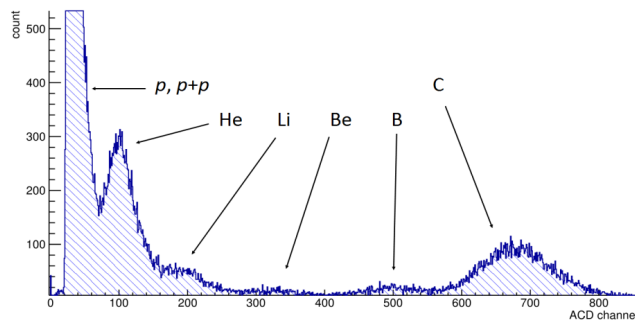
Figure 2: **Amplitude distribution of scintillation counter.**

Trigger efficiency

To evaluate the trigger efficiency simple simulation of each scintillation counters is done. Example of simulation for one of counters is shown on the Fig. 3. Solid histogram is real data, each maximum corresponds to counter's signal for each type of light nuclei. Other distributions are simulation of counter's signal. Using of such simulations, we got the trigger efficiency about 83% at the maximum suppression of the background.
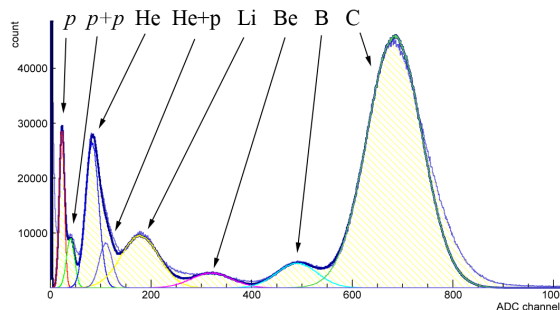
Figure 3: **Example of simulation.**

215

Conclusions

The study of properties of the lightest hypernuclei is actual, has high significance and can be performed in JINR with beams from Nuclotron. Trigger of the HyperNIS spectrometer works perfectly. Installing and commission of the new FEE will allow us to reach high tracking efficiency and to carry out the proposed hypernuclear experiments. Test run of HyperNIS setup is planned at next session of Nuclotron (June-July 2016). Main data set is planned at the end of this year.

References

[1] M. Agnelo *et al.*,Phys.Rev.Lett. 108 (2012) 042501.

[2] E. Botta, Nucl. Phys. A 942 (2013) 119; A. N. Other, "A Very Interesting Paper", (EPAC96, Sitges, June 1996, p. 7984).

[3] H. Sugimura *et al.*, arXiv:1310.6104v2nucl-ex 6 Feb 2014.

[4] A. U. Abdurakhimov *et al.*, NuovoCim. A 102 (1989) 645.

[5] S. Avramenko *et al.*, Nucl. Phys. A 547 (1992) 95.

[6] H. Bando *et al.*, Nucl. Phys. A 501 (1989) 900.

[7] H. Bando, T. Motoba and J. Zofka , Int. J. Mod. Phys. A 5 (1990) 4021.

[8] Yu. A. Batusov, J. Lukstins, L. Majling and A. N. Parfenov, Phys. Elem. Part. Atom. Nucl. 3 (2005) 169.

GAMMA SPECTROSCOPY IN ^{150}SM RARE EARTH NUCLEUS

L. Msebi [1*], S.P Bvumbi[1], L. P. Masiteng[1], S. N. T. Majola[2,4], T. S. Dinoko[2,4], J. F. Sharpey-Schafer[2], E. Lawrie[2], J. J. Lawrie[2].

[1]*University of Johannesburg, Physics Department, Auckland Park, South Africa.*

[2] *iThemba Laboratory for Accelerator Based Sciences, Somerset-West, South Africa.*

[3] *University of Cape Town, Physics Department, Rondebosch, South Africa.*

[4] *University of Western Cape, Physics Department, Bellville, South Africa.*

[5] *Rhodes University, Physics Department, Grahamstown, South Africa.*

[6]*Stellenbosch University, Physics Department, Matieland, South Africa.*

Annotation

Intermediate states of ^{150}Sm, excited through the ^{150}Nd(^{4}He, 4n)^{150}Sm fusion evaporation reaction were studied using the AFRODITE array at iThemba LABS. The gamma-gamma coincidences, DCO ratios and linear polarization measurements were carried out and the previously known level scheme of ^{150}Sm was extended in the intermediate region. In this work we report on the gamma spectroscopy results of the ^{150}Sm nucleus and present experimental evidence to further support octupole correlation in the low lying negative parity states in ^{150}Sm.

Introduction

Gamma spectroscopy is a method used to measure properties of the excited states in nuclei. In this work, gamma spectroscopy was used to study excited states of Samarium -150 (^{150}Sm). ^{150}Sm is one of seventeen rare earth elements that are found on the periodic table. It boasts of isotopes that span the transition region of rare earth between the closed-shell spherical" nuclei, with neutron number 82, and the abrupt deformed region beginning at neutron number 90 [1]. In depth studies have been done on the higher and lower states of ^{150}Sm have been studied [1–6]. The present analysis focuses on the intermediate states of ^{150}Sm, in particular structures built on the first excited 0_2^+ state. In the process, the deformation that exists in these states will be assessed and compared with higher and lower states of ^{150}Sm.

Experimental details and Results

The equipment used to perform the experiment for this work is the AFRODITE spectrometer array at iThemba LABS in Cape Town. A beam of ^{4}He with energy of 45 MeV was used to bombard the target nucleus of ^{150}Nd to populate the intermediate states of ^{150}Sm. Before the start of the experiment, calibration of the clover detectors was performed using the ^{152}Eu source. Nine clover detectors were used and place at 90 degrees and 135 degrees thus making angular distribution measurements possible. The clover detectors detct gamma rays from the ^{150}Nd(^{4}He, 4n)^{150}Sm fusion evaporation reaction. Data is collected using the iThemba LABS Digital Data Acquisition System. It comes in huge sizes ranging from gigabytes to terabytes. MTSort [7] is employed to convert the data into readable

---

*lumkilemsebi@gmail.com

format and it is useful for online and offline data analysis. Radware [8] is used manipulate spectra and to create coincidence spectra.

Discussion
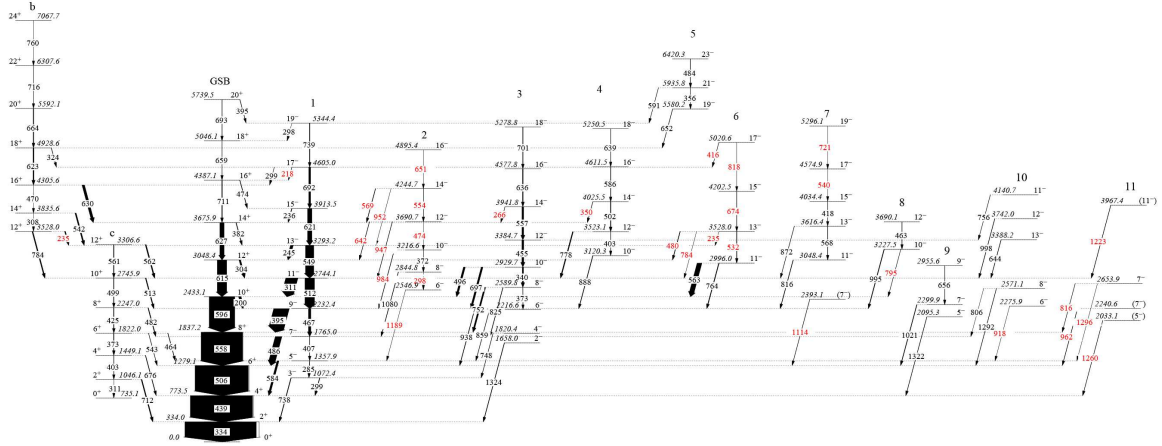
Figure 1: A partial level scheme showing the negative parity bands observed from the ^{150}Nd(^{4}He, 4n)^{150}Sm reaction. The new γ-rays are shown in red.
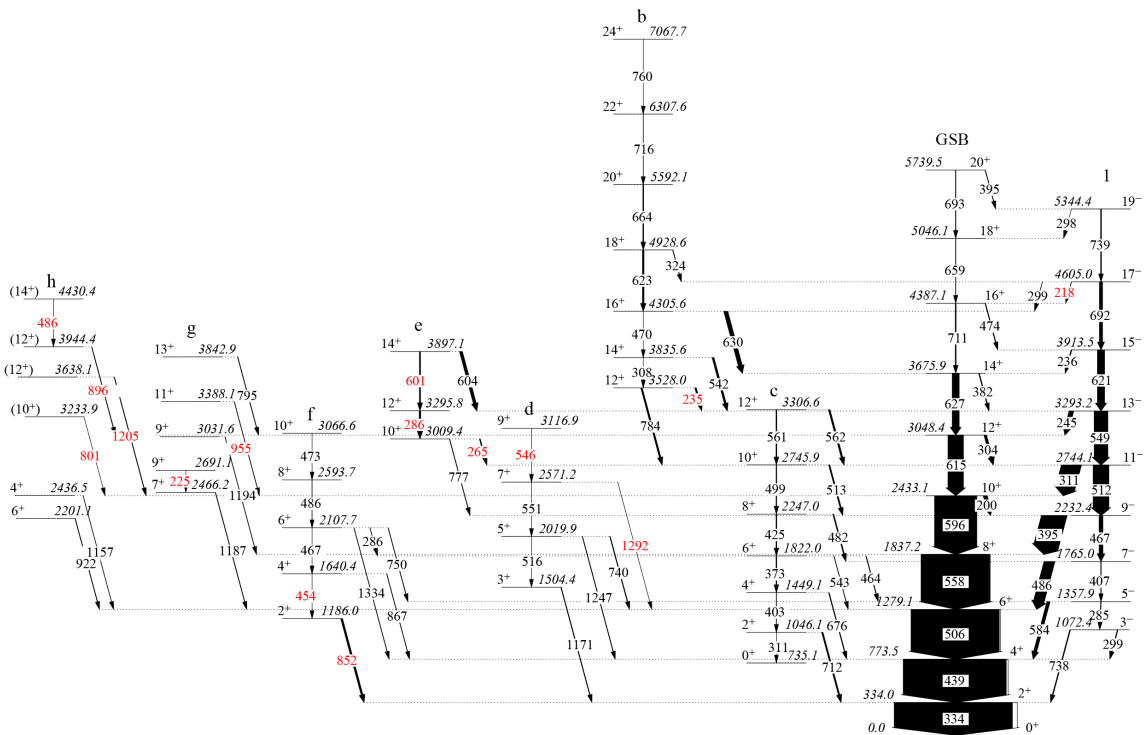
Figure 2: A partial level scheme showing the positive parity bands observed from the ^{150}Nd(^{4}He, 4n)^{150}Sm reaction. The new γ-rays are shown in red.

Newly observed gamma transitions in ^{150}Sm

In this work new gamma transitions have been observed and are shown in figuretggg. Band 2 was established by [2] and was observed up to $I^\pi = 14^-$. Present analysis extends it up to $I^\pi = 16^-$ and established a new band-head at 2546.9 keV, having a spin-parity of $I^\pi = 16^-$. The spectrum showing the new transitions is shown in figure 3. Band 4 has been extended to $I^\pi = 18^-$ with a new 350 keV inter-band transition decaying to the ground state. Band 6 is new band with four rotational levels, it is based on a 2996.0 keV state previously reported by [2] to be $I^\pi = 11^-$. The 3528.0 keV and 4202.5 keV levels have been assigned $I^\pi = 13^-$ and $I^\pi = 15^-$ levels, respectively.

Alignment Properties of Bands

Nuclei tend to exhibit a major Coriolis-induced alignments (breaking of nucleonic pairs by the fictive force in a rotating frame of reference), as the angular momentum is increased [9]. Figure 3 and 4 show energy levels of new band structures in ^{150}Sm plotted as a function of spin. A rotating liquid-drop reference has been subtracted from each structure.
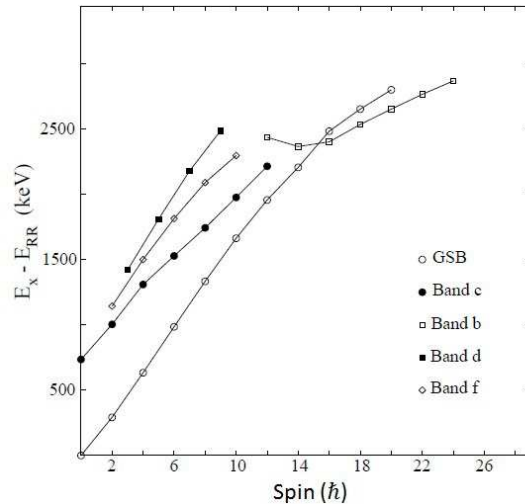
Figure 3: Energies, relative to a rotating liquid-drop reference ($E_{RR} = 0.0715 \times 10^{-3} keV$) **of positive parity bands in** ^{150}**Sm, plotted as a function of spin.**

The observation that the second excited or the first excited 0^+ or the first excited 0_2^+ state prefers to decay to the one-phonon beta vibrational states led to the interpretation of them as having two-phonon beta-vibrational character [10]. Casten and Von Brentano suggested that the lowest 0^+ bands should be understood as phonon excitations [11]. This is due to the fact that 0^+ bands in deformed nuclei decay predominantly to the γ-band rather than to the ground state band. In some cases, however, the first excited 0_2^+ state is not observed to decay to the γ-band and the 0^+ state lies lower in excitation energy than the gamma band. Ref [2] observed E1 transitions decaying from the first excited 0_2^+ state o the ground state. These transitions are suggestive that ^{150}Sm is octupole deformed. The present analysis confirms E1 transitions decaying to the low-lying octupole band as established by [2]. Fig shows Band c or the second vacuum tracking the ground state.
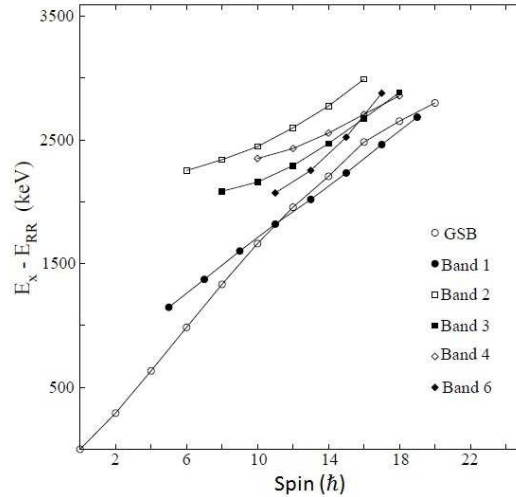
Figure 4: Energies, relative to a rotating liquid-drop reference ($E_{RR} = 0.0715 \times 10^{-3} keV$) of negative parity bands in ^{150}Sm, plotted as a function of spin.

Conclusion

Gamma spectroscopy has made it possible to study the intermediate states of ^{150}Sm. New bands and gamma transitions have established. E1 transitions decaying from the first excited 0_2^+ state to the ground state previously established by Ref. [2] have been confirmed in this work. This serves as a confirmation that the ground state of ^{150}Sm is octupole deformed. Other N= 88 isotones, such as ^{152}Gd and ^{150}Nd, exhibit a similar behaviour of E1 transitions decaying from the 0^+ state to the lowest lying negative parity band.

References

[1] D. J. Buss. Phys. Rev. C 2 (1970) 1513.

[2] S. P. Bvumbi *Investigation of octupole correlations and collective couplings in the rare earth nucleus* (PhD thesis, University of Johannesburg, 2003).

[3] Z. Sujkowski *et al.*, Nucl. Phys., A 291 (1997) 365385.

[4] J. V Thompson, M. W. Johns, J. C. Waddington. Can. J. Phys., 53 (1975) 1229.

[5] W. Urban, J. C. Bacelar, J. Nyberg, Physica Pol. B 32 (2001) 2527.

[6] W. Urban *et al*, Phys. Lett. B 185 (1987) 331.

[7] J. Cresswell, J. Sampson. MTsort manual, 2006.
http://nnst.dl.ac.uk/MIDAS/manual/MTsort/edoc033

[8] D. C. Radford, Nucl. Instr. Methods Phys. Res. Sect. A, 361 (1995) 297.

[9] E. S. Paul *et al.*, Phys. Rev. C 79 (2009) 044324.

[10] D. R. Zolnowski *et al.*, Phys. Rev. C 1 (1980) 2556.

[11] R. F. Casten, P. von Brentano. Phys. Rev. C 50 (1994) R1280.

MEASUREMENT OF SPECIAL MODES OF DOUBLE BETA DECAY IN EXPERIMENTS OBELIX AND TGV

E. Rukhadze[*][†] on behalf of OBELIX and TGV collaborations
Institute of Experimental and Applied Physics CTU in Prague, Czech Republic

Annotation

Investigation of double beta decay processes to excited states of daughter nuclei was performed at the Modane underground laboratory (LSM, France, 4800 m w.e.) using the high sensitivity spectrometer OBELIX in a common activity of JINR Dubna, IEAP CTU in Prague and LSM. The spectrometer is based on the HPGe detector with the sensitive volume of 600 cm^3 and relative efficiency of 160%. Two experimental runs with a large sample (21.7 kg) of nickel containing 68% of ^{58}Ni were carried out at 2014 and 2015. At the same time, a new experimental run of searching for double beta decay of ^{106}Cd was performed using the TGV-2 spectrometer, consisting of 32 planar type HPGe detectors with a total sensitive volume of 400 cm^3. The current results obtained in the TGV-2 experiment with ^{106}Cd and new experimental limits obtained in the measurement of ^{58}Ni using the OBELIX spectrometer are presented.

Introduction

Investigation of double-beta decay processes are of great importance for particle and nuclear physics as a sensitive tool for the study of lepton number conservation and neutrino properties [1]. Up to now more attention has been given to $\beta - \beta$–decay, but there are other channels of double beta decay, in particular the double capture of two bound atomic electrons (EC/EC), capture of the bound electron with emission of a positron (β^+/EC) and decay with emission of two positrons ($\beta^+ beta^+$). Recently, interest in these processes has significantly increased. In contrast to the $\beta^-\beta^-$ - decay, where the two-neutrino mode of the process has been experimentally measured for 11 isotopes [2], other double beta decay processes have never been observed in direct experiments, neither for two-neutrino nor for neutrino-less modes, except the claim of a positive EC/EC signal for Barium isotopes using a geochemical technique [3] and indication of a possible observation of 2νEC/EC decay in ^{78}Kr [4]. ^{106}Cd is one of the most promising candidates for the investigation of two-neutrino double electron capture due to the high decay energy ($Q_{EC/EC} = 2775.39 \pm 0.10$ keV). The 2νEC/EC decay of ^{106}Cd with a transition to the ground state of ^{106}Pd ($0^+ \rightarrow 0^+$, g.s.) is characterized by emission of two Palladium (Pd) X-rays each with an energy of 21 keV. Theoretical predictions of half-lives for this process are ranged between 1.0×10^{20} and 5.5×10^{21} y [2].

For several years ^{106}Cd is the object of studying in experiment TGV-2, which is one of the leaders of investigations of EC/EC process [5]. In the previous run, the best experimental limit on 2νEC/EC decay of ^{106}Cd - $T_{1/2} \geq 4.2 \times 1020$ y (90% CL) [5,6] was obtained

using the TGV-2 spectrometer (Telescope Germanium Vertical) [2] and 13.6 g of ^{106}Cd with enrichment of 75%. The result reached the range of theoretical predictions for this decay. The analysis of KX-KX coincidences showed a small increase in the number of measured events in the region of 21 keV (KXPd), which might be the 2νEC/EC decay of ^{106}Cd. But the statistics was not enough to make any significant claim about the presence of the process searched. A new experimental run was performed at LSM using the TGV-2 spectrometer and highly increased mass of enriched ^{106}Cd (from 13.6 g of ^{106}Cd with enrichment of 75% in the previous run to 23.2 g of ^{106}Cd with enrichment of 99.57% in current measurement) to accumulate larger statistics of KX-KX coincidence events in the region of interest.

In measurement of ^{58}Ni with the OBELIX spectrometer the object of analysis were γ-rays with energies of 511 and 811 keV. The β^+EC decay to the ground 0^+ and first 2^+ excited states of ^{58}Fe will be accompanied by emission of positron, which creates two correlated annihilation γ-quanta with energies of 511 keV. The β^+EC decay to the first 2^+ excited state of ^{58}Fe will be accompanied by additional γ-quantum with energy of 811 keV emitting in de-excitation of this excited state. EC/EC decay of ^{58}Ni to the first 2^+, 811 keV excited state of ^{58}Fe will be accompanied with 811 keV γ-rays. All these γ-quanta can be detected by the high sensitive OBELIX detector [8] with high efficiency.

Description of the OBELIX spectrometer

The low background HPGe detector produced by Canberra is based on P-type crystal with the sensitive volume of 600 cm^3, the mass of approximately 3 kg, and the efficiency of 160%. The crystal was mounted in ultra-low background U-type cryostat with cooled FET. The energy resolution of the detector is 1.2 keV at 122 keV (^{57}Co) and 2 keV at 1332 keV (^{60}Co). To minimize the detector background as low as possible the constructive details of the cryostat were produced from materials with ultra-low radioactive contaminations. The detector part of cryostat (see Fig. 1 (right)) is surrounded by several layers of archaeological lead (12 cm) and low active lead (20 cm) which are made in a ring shape and placed inside stainless steel frame (see Fig. 1 (left)). Two internal layers of archaeological lead with the thickness of 7 cm can be removed to measure big samples in Marinelli beakers and bobbins. The internal part of the passive shielding is flushed by a radon-free air produced by the anti-radon factory installed in LSM. To obtain the detector efficiency for the different geometries of measurements, except "standard" radioactive sources ^{152}Eu and ^{133}Ba, the specially produced low-active samples with known mass and activity were used. The samples were produced from the mixture of some powdery filler and the powder of La$_2$O$_3$. More details of the detector and its efficiency calibration and other parameters were described in [8].

Measurement of ^{58}NI

The investigation of double beta decay processes (β^+EC, EC/EC) of ^{58}Ni was performed at LSM using the OBELIX spectrometer. The sample of natural Ni, containing 68% of ^{58}Ni with a total mass of 21.7 kg was prepared in a shape of a Marinelli beaker. The first run was started at the middle of October 2014 and lasted 47.5 days. The main goal of this measurement was to obtain radioactive contaminations of the investigated sample. This
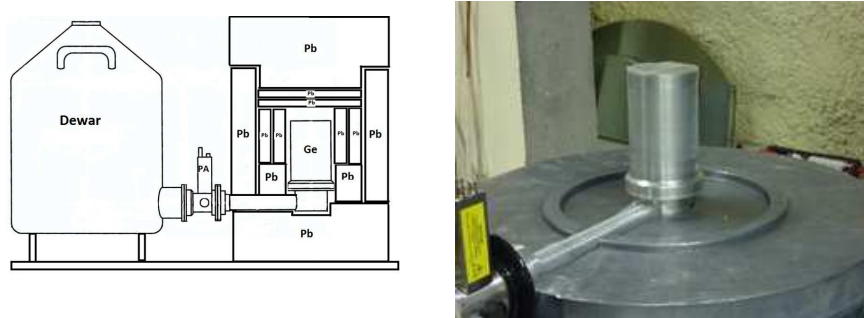
Figure 1: The scheme of the HPGe detector in a passive shielding (left) and the HPGe detector before installation (right).

measurement showed a content of small amount of radioactive isotopes of ^{57}Co and ^{58}Co, which were produced in the sample during its exposure on the Earth's surface (see Fig. **??** (left)). But their activity was found to be high for a long-term measurement of ^{58}Ni.
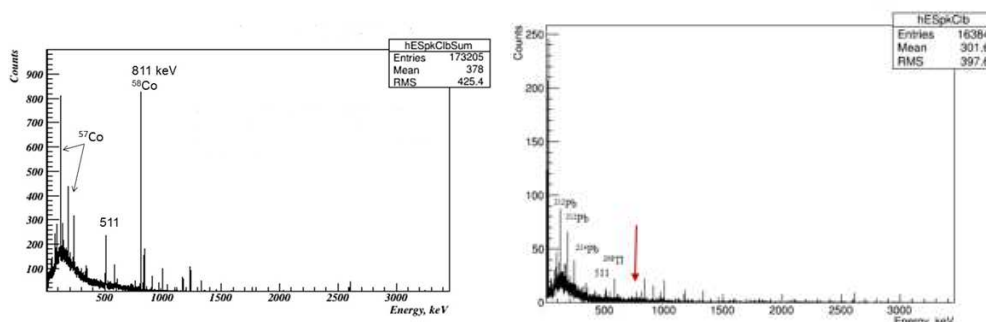
Figure 2: Spectra of ^{58}Ni measured at 20^{14} (left) and 20^{15} (right).

After one year, during which, the sample was placed in the Modane underground laboratory, another experimental run was performed. This test run was started at September 2015 and lasted only 10 days. But the results obtained during this measurement showed the decreasing of the activity of ^{58}Co in the region of interest by about an order of magnitude (see Fig. 2 (right)). Nevertheless, based on the data accumulated in these 2 test measurements new experimental limits on β^+EC decay of ^{58}Ni to the ground 0^+ and excited 2^+, 811 keV excited state of ^{58}Fe, and EC/EC decay of ^{58}Ni to 2^+, 811 keV excited state of ^{58}Fe were obtained.

$$T_{1/2}(\beta^+EC, 0^+ \to 0^+) > 1.2 \times 10^{22} y (90\% CL), \tag{1}$$
$$T_{1/2}(\beta^+EC, 0^+ \to 2^+) > 4.0 \times 10^{21} y (90\% CL),$$
$$T_{1/2}(EC/EC, 0^+ \to 0^+) > 4.6 \times 10^{22} y (90\% CL).$$

The previous experimental limits were improved by approximately two orders of magnitude at high CL [9]. The measurement of ^{58}Ni will be continue at 2016.

Description of TGV-2 spectrometer

The low-background spectrometer TGV-2 was developed for the investigations of rare nuclear processes and was mounted at the Modane underground laboratory. The detector part of the spectrometer is composed of 32 planar type HPGe detectors (see Fig.3). The total sensitive volume of the detectors is about 400 cm^3. The basic detection cell is a sandwich-like pair of face-to-face detectors with a thin foils made of a double beta emitter placed between them. The 16 pairs are mounted one over another in a common cryostat. The detector part of the TGV-2 spectrometer is surrounded by a copper shielding (20 cm), a steel airtight box protecting from radon accumulation near the detectors, a lead shielding (10 cm), and a neutron shielding from borated polyethylene (16 cm thick). The energy calibration of the spectrometer was performed with the help of encapsulated ^{228}Th and ^{241}Am radioactive sources. More details of the spectrometer TGV-2 and its parameters were described in [7].
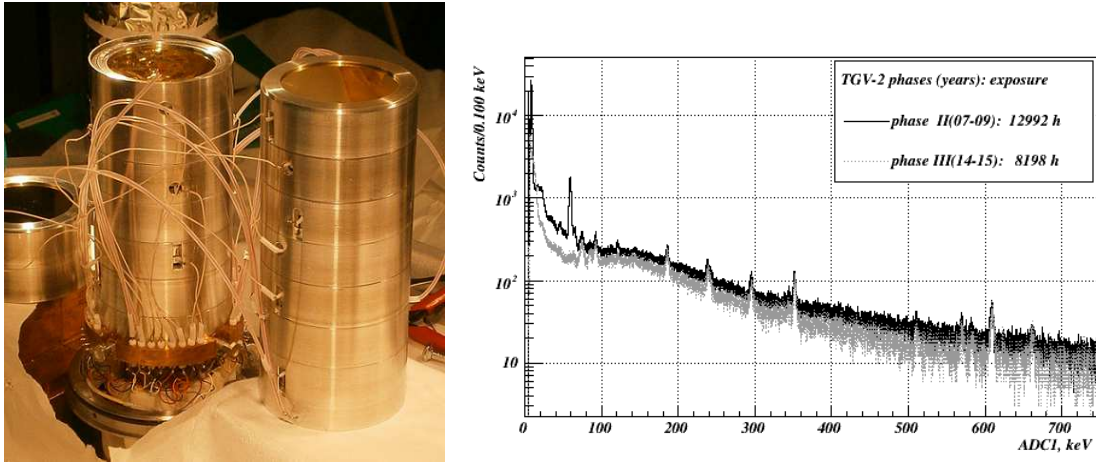
Figure 3: Detector part of TGV-2 spectrometer (left). Spectra obtained at phase II and phase III TGV-2 experiment (right).

Measurement of ^{106}Cd

A new experimental run (phase III) of searching for double electron capture of ^{106}Cd was started at the end of February 2014 using the TGV-2 spectrometer and 16 samples of ^{106}Cd. The investigated samples were prepared in the form of thin metal foils and placed between the entrance windows of each detector pair. The total mass of 16 investigated samples of ^{106}Cd with enrichment of 99.57% is 23.2 g and the thickness foils is 70(10) mm. Double coincidences between two characteristic palladium KX-rays detected in neighboring face-to-face detectors were searched for in order to find the 2νEC/EC decay of ^{106}Cd to the ground 0+ state of ^{106}Pd. The comparison of spectra of single events accumulated for all detectors in Phase III and Phase II are shown on the Fig.3 (right). After 8198 h of measurement in Phase III of experiment the following limit on studied process was obtained: $T_{1/2}(2\nu EC/EC, 0^+ \rightarrow 0^+) > 3.1 \times 10^{20}$ y(90%CL).

Measurements of ^{106}Cd with the TGV-2 spectrometer is in progress. Taking into account theoretical predictions [2] and results obtained in the previous phases of the TGV-2

experiment, the TGV-2 Collaboration expect to detect 2νEC/EC capture in ^{106}Cd decay within the current experimental run. The planning time of the measurement is 3 years.

References

[1] W. C. Haxton. and G. S. Stephenson, Prog. Part. Nucl. Phys. 12 (1984) 409

[2] V. I. Tretyak, Yu. G. Zdesenko, At. Data and Nucl. Data Tables 80 (2002) 83-116.

[3] A. P. Meshik *et al.*, Phys. Rev. C 64 (2001) 035205.

[4] Yu. M. Gavrilyuk *et. al.*, Phys. Rev. C 87 (2013) 035501.

[5] N. I. Rukhadze *et. al.*, Journal of Physics: Conf. Series, 375 (2012) 042020.

[6] N. I. Rukhadze *et al.*, Bul. of Rus. Ac. Sc. : Phys.77 (2013) 379.

[7] P. Beneš *et al.*, Nucl. Instr. Meth. A 569 (2006) 737.

[8] E. Rukhadze *et al.*, AIP Conference Proc. 1549 (2013) 34.

[9] S. I. Vasilev *et al.*, JETP Lett. 57 (1993) 631.

SOFTWARE DEVELOPMENT FOR MULTI-CHANNEL LV/HV SUPPLY SYSTEM BASED ON WIENER MPOD

Ya.T. Skhomenko, A. Yu. Isupov, V. P. Ladygin, S. G. Reznikov
Joint Institute for Nuclear Research, Dubna, Russia

Annotation

The results on the control software development for the multi-channel LV and HV power supply system on the base of Wiener MPod are presented. The application has been developed under Unix-like operating system using the cross-platform software package Qt on the C++ programming language. The main purposes of the application are the power supply modules management, setting, reading, and graphical representation of the control information from their, in particular, channel name, status, voltage, current, etc. There is the possibility to store and retrieve the modules configuration into/from plain files. The threads has been used to improve the application interactive response. The work has been performed within framework of the upgrade of the experimental setup for the study of the light nuclei structure using internal beam of the JINR Nuclotron.

Introduction

The main goal of the DSS (Deuteron Spin Structure) project [1,2] is the measurements of the polarization observables in the deuteron-proton interactions using the internal targets station of the Nuclotron. The detection system of the experimental setup is based on about 80 scintillation counters with the Hamamatsu photomultipliers (PMTs). Wiener MPod LV/HV system is taken as a basic option to provide the online control over the high voltage for PMTs. The Wiener provides the crate settings application under Microsoft Windows OS. However, the conditions of the DSS experiment requires the application for the Unix-like systems. The results of such development are presented in this paper.

Equipment

The development has been performed using crate controller in Wiener MPod minicrate of four slots for LV/HV modules [3]. However the designed program allows us to run in the same way with up to 10 slots of the Wiener MPod crate due to the same controller. Communication is done using the Net-SNMP software package. Three different MPod LV/HV modules were installed for the development and testing of the application, namely: EHS F 030n - 16-channels high-voltage module up to 3kV/3mA; EHS F 210n-F - 16-channels high-voltage module up to 1kV/8mA; OMPV.8008 - 8-channels low-voltage module up to 8V/10A.

Application algorithm

Global algorithm

The algorithm of the application presented in Fig. 1 demonstrates the main blocks of the software. After start the application builds the main window and creates the threads. Next,

the operator must enter in a special area (one-line text box) the IP address of the MPod controller. After pushing of the start button, the application reads modules parameters from crate and generates their per-channel representation. Four possibilities are available to the user: reading parameters from file, interactive setting of the parameters, writing the parameters to the file and the visualization of the MPod parameters.
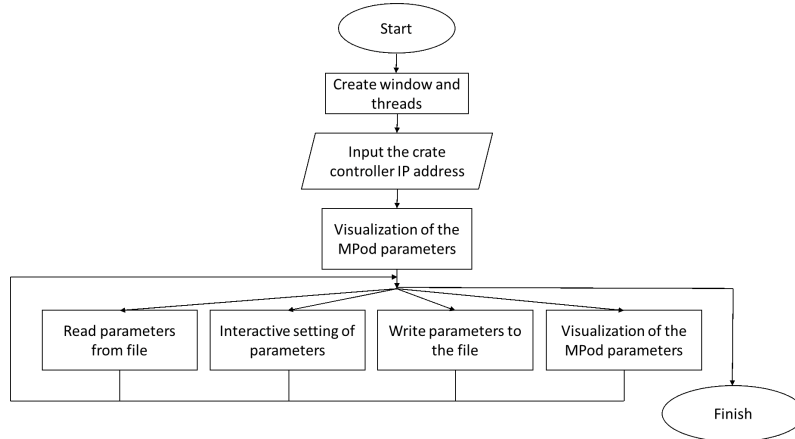
Figure 1: Schematic application algorithm.

QProcess

The computer communication with the MPod crate is made using the Qt library class QProcess. It allows one to run external applications and interact with them. The command line with a specific arguments is used to read or write the data from/to LV/HV module. For example, the following command line requests the channel name:

- snmpget -OQev -v2c -m +WIENER-CRATE-MIB -c guru 192.168.0.10 outputName.u100

Depending on the specified arguments one can obtain information in the well defined output format.

QThread

Since the input and output of the information to/from MPod runs for a long time, the application has been divided by several threads to handle GUI window and QProcess simultaneously. This allows us to improve the interactive response of the application. First of all we should implement a class that contains the functions to be performed by QThread in a separate file. Next, we instantiate the object of this class and the QThread object, and the former is runned by the latter. The interaction between the threads is done by means of signals and slots.

Saving and loading parameters from the plain text file

There is the possibility to store and retrieve the LV/HV modules parameters using plain text files for the user convenience. One needs to save also the position of the modules in the crate, since the change in their positions can lead to incorrect loading of the parameters.

227

The number of channel, voltage, current and rise/fall rates for current and voltage are saved in to the file.

Program window

The Fig. 2 shows the application window. One can see that three modules are situated in the crate, the information for the first one is visible (so called current slot). Also it is seen that in this slot the first three channels only are switched on new. The window consists of several parts. Window menu contains links to the functions for a file reading and writing, and the application termination. The field for the IP input is located below. There is a panel QTabWidget to switch between different modules. The left side displays the information on each channel: name, status, sense voltage, terminal voltage, current, input voltage, input current, voltage rise rate, voltage fall rate, current rise rate, current fall rate. In the center of the window the activate/deactivate channel buttons are located.
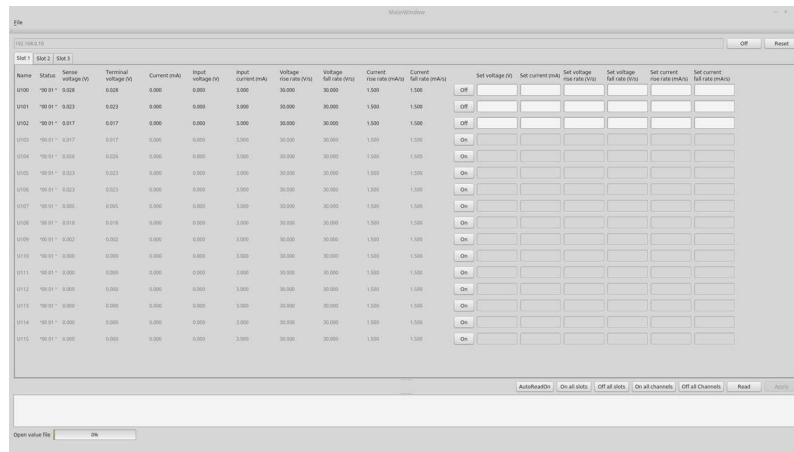
Figure 2: **Application window.**

In the right part of the window there is the parameters input area. Under the per-channel information there are several common buttons: enable of modules parameters auto-read, activate and deactivate all the channels and all the channels of the current slot, read and apply the modules parameters. Also there is a multi-line field to display the error messages. The progress bar is placed at the lower edge.

Conclusion

The software to control the Wiener MPod LV/HV system under Unix- like OS is developed. In the future we plan to create an application to visualize history of the LV/HV modules parameters using the ROOT package [4]. The work has been supported in part by RFBR under grant 16-02-00203a.

References

[1] V. P. Ladygin, Int. J. Mod. Phys.: Conference Series, 40 (2016) 1660074;

[2] V. P. Ladygin, Few Body System, 55 (2014) 709.

[3] MPOD HV& LV Power Supply System Technical Manual. 71 (2014) 8

[4] http://root.cern.ru

HIGH ACCURATE MEASUREMENT OF TEMPERATURE DIFFERENCES AT THE MASSIVE SPALLATION URANIUM TARGET TO DETERMINE THE NEUTRON FLUX

J. Svoboda[1,2*], J. Adam[1,3], A. A. Baldin[1], W. I. Furman[1], K. Katovsky[2], J. Khushvaktov[1], A. A. Solnyshkin[1], P. Tichy[1,3], V. M. Tsoupko-Sitnikov[1], S. I. Tyutyunnikov[1], R. Vespalec[1,4], V. Wagner [3,4], M. Zeman[1,2]

[1] *Joint Institute for Nuclear Research, Dubna, Russia*
[2] *Brno University of Technology, Brno, Czech Republic*
[3] *Nuclear Physics InstitutePI ASCR, Rez, Czech Republic*
[4] *Czech Technical University, Prague, Czech Republic*

Annotation

There are several possibilities of the neutron flux determination inside of the facility. The most using one method is the determination of neutron flux by threshold foils (detectors). This method is complicated to analyzing because irradiated foils need to be measured by gamma spectrometry. It usually takes a few weeks to get results of the neutron flux determination. Other methods are also available. One of them is a determination of neutron flux by measuring of released heat inside of the facility. This method allows online measuring and is greatly variable to measure an unlimited number of positions. The research project of investigation of this type of neutron flux determination is led by Dzhelepov Laboratory of Nuclear Problems (DLNP) at the group of J. Adam. The temperature differences are measured by high accuracy thermocouples. Two experiments took place on 2015 at the massive spallation uranium target QUINTA at facility Phasotron at JINR. Results of these experiments will be discussed at presentation and article. Another 4 experiments are planned on 2016.

Introduction

The electric energy consumption is increasing since the time it started to be firstly used. About 10.6% of all electricity production (2013, World databank) has been produced by nuclear power plant. Therefore, the future of electricity production is connected with the nuclear industry. One of the future nuclear power plant design is based on Accelerator-Driven Systems. There is a long-term research aimed at the behavior of the spallation target which will be actually needy for such system. The group aimed on various problems of ADS operate at the DLNP and Veksler and Baldin Laboratory of High Energy Physics (VBLHEP) in the JINR. The official name of this large group is Energy and Transmutation of RadioActive Waste (E& T RAW). Except of the members from laboratories of JINR, other members come from CPTP Atom energomash, Moscow, Russia; KIPT, Kharkov, Ukraine; Stepanov IP, Minsk, Belarus; JIENR Sosny near Minsk, Belarus; INP, Rez near Prague, Czech Republic; Institute of Nuclear Research and Nuclear Energy, Sofia, Bulgaria; National Centre for Nuclear Research, Otwock-Swerk, Poland; Institute of Nuclear Physics NNC RK, Almaty, Kazakhstan; Aristotle Uni-Thessaloniki, Thessaloniki, Greece;

---

*svoboda@jinr.ru

Gesellschaft for Kernspektrometrie, Germany and the School of Physics, University of Sydney, Australia. The main topics of the group researching are neutron production for heat generation (electric power generation) and transmutation of the spent fuel at deep subcritical ADS. Group also hold an investigation of the core with maximally hard neutron spectrum.

Spallation natural uranium target assemblity quinta

All experiments were set at spallation target QUINTA "QUasi-INfinite TArget" which consists of five hexagonal sections with section length of 114 mm. Completely has the mass of 512 kg natural uranium. Each section with the size of 350 mm high to 114 mm length is composed of natural uranium cylinders with diameter 36 mm, length 104 mm and mass about 1.72 kg. The first section is consist of 54 cylinders with a total mass of uranium about 92 kg. All other sections (from the second to the fifth one) are identified with 61 of cylinders and the total mass of uranium up to 105 kg. All sections are covered by aluminium plate shield with a thickness about 5 mm so the total size of QUINTA is $700\times 350\times 350$ mm^3 with total mass 540 kg [1]. Between each two sections, there is 17 mm of the air gap. About 10 cm thick lead shielding has been provided surrounding the target assembly (TA) QUINTA.
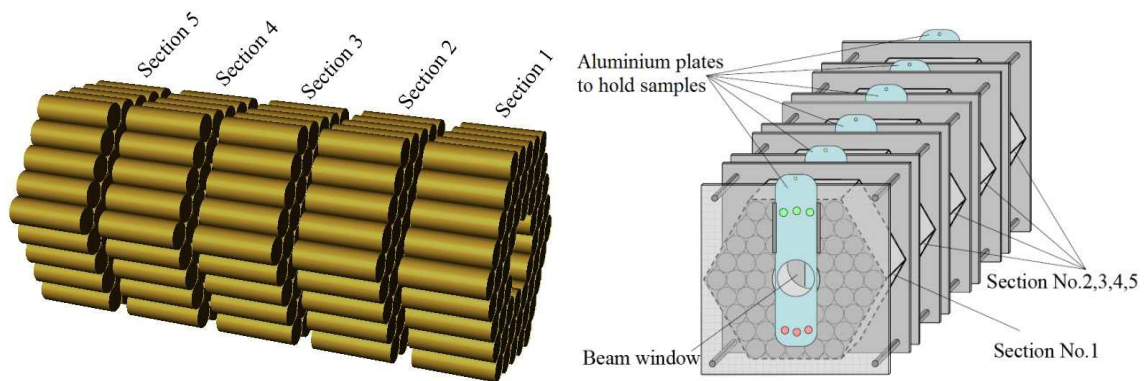
Figure 1: Left panel: Uranium cylinders of TA QUINTA set up. Right panel: TA QUINTA with alumina cover.

Neutron flux determination

The main problem of the neutron flux determination is caused by narrow space inside of TA QUINTA. Only 17 mm air gap between each two sections is available to detect neutron flux. Already utilize technology is based on the activation analysis of various foil samples. This method has a disadvantage in too long time to get sufficient results and difficulty of measurement with analyzation. Due to these facts, a new method of the neutron flux determination has been involving the research group of J. Adam, DLNP, JINR. This method is based on temperature measurement by at various position and then track the neutron flux by the temperature difference. It is measured by high accuracy thermocouples and precious analogue-digital (A/D) converter. Thermocouples type T and converters NI9214 and 9212 were used. Another problem is long distance measurement,

caused by strong gamma radiation and neutron field which complicates the measurement. The distance between A/D converter and QUINTA is about 23 m. Since the research had started, 3 experiments were performed. First, one was so called pre-experiment because the goal of its was to determine temperature difference behind the second section. The result ensures to choose the right one type of thermocouples and A/D convertor for on-coming experiments. The December experiment utilized 15 thermocouples. Thermocouples measured thermally insulated samples of ^{235}U, ^{238}U, and ^{232}Th.
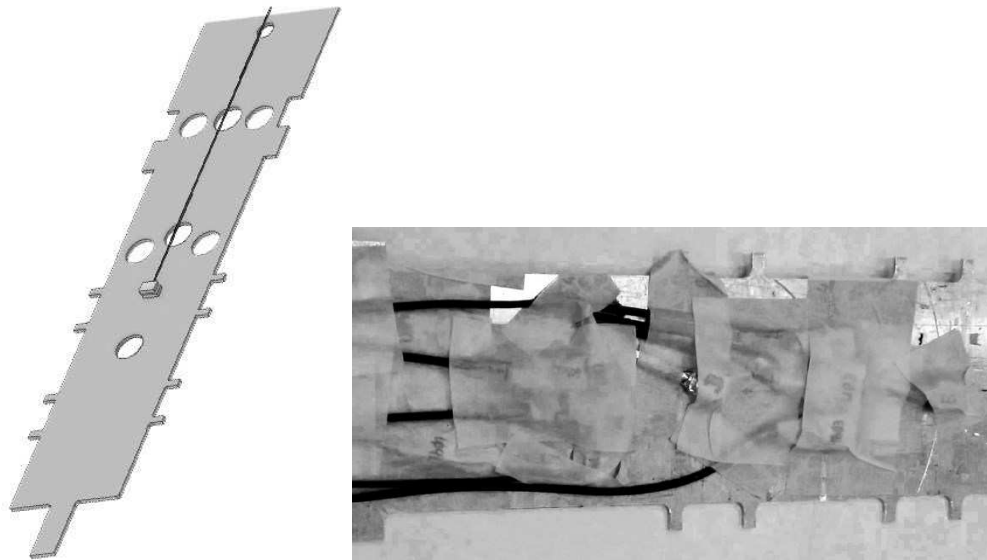
Figure 2: Model and real setup of the measurement

The results from the December experiment shows that thermo-insulation of samples with thermocouples were insufficient and due to that the results are encumbered by systematic uncertainty. Experiment have been performed between second and third section where the most of the neuron are located. Temperature differences between positions 0, +120, -80 mm able to see on. The temperature difference is almost 1°C due to the high neutron flux in this section. These differences need to be recalculated to neutron flux but from the base of determination able to see that the highest neutron flux is in the middle of TA. To compare measuring between the measurement of airgap between 2nd and 3rd section (temperature increase about 15 °C for 6 hours of irradiation) and experiment between 3rd and 4th section where temperature difference was about 2.4 °C for 6 hours of irradiation. So the last experiment was setup in March 2016 and 9 thermocouples were used inside of QUINTA and about 6 thermocouples measured samples outside of QUINTA.

Conclusions

The importance of thermal insulation improvement is necessary for oncoming experiments. Second one possibility is to measure temperature directly on the shell of sections, so at the alumina plate covering the uranium. It was found that for 6 hours irradiation the temperature behind 2nd section increase for 15°C and there is about 1C difference between the center and outer position. For the same performance behind 3rd section temperature
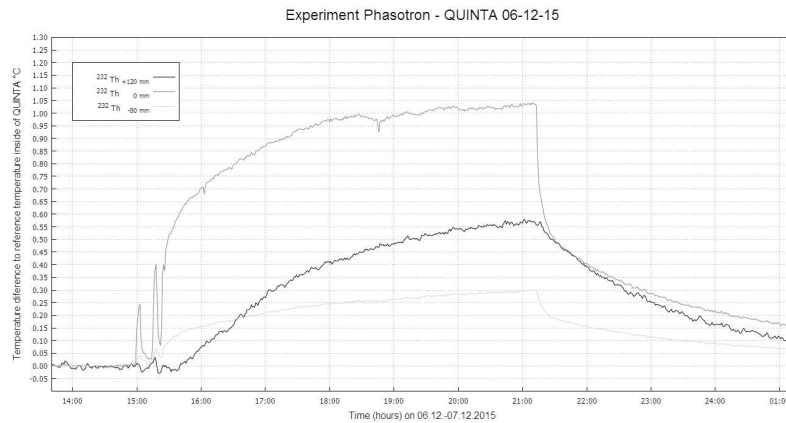
Figure 3: Partial results from the December experiment for ^{232}Th at 3 positions

increase for 2.4°C Obtained results help to estimate the thermal energy, better say temperature distribution inside of QUINTA setup. Oncoming results is planned to be simulated in software Fluent, ANSYS.

References

[1] L. Zavorka, Transmutation of actinides using spallation reactions, 2015, 154 p., dissertation, Czech Technical University in Prague.

[2] W. Furman, Recent results of the study of ADS with 500 kg natural uranium target assembly QUINTA irradiated by deuterons with energies from 1 to 8 GeV at JINR NUCLOTRON, Proceeding of Science. XXI International Baldin Seminar on High Energy Physics Problems September 10-15, 2012 JINR, Dubna, Russia

COMPARISON BETWEEN SIMULATION AND MEASUREMENT OF NEUTRON FLUX USING ^{59}Co AT THE SPALLATION TARGET QUINTA

M. Zeman[1,2,*,†], J. Adam[1,3], A. A. Baldin[1], W.I. Furman[1], K.Katovsky[2], J. Khushvaktov[1], A. A. Solnyshkin[1], M. Suchopar[3,4], V. M. Tsoupko-Sitnikov[1], S. I. Tyutyunnikov[1], R. Vespalec[1,4], J. Vrzalova[3], V. Wagner[3,4], L. Zavorka[1], P. Zhivkov[5]

[1]*Joint Institute for Nuclear Research, Dubna, Russia*
[2]*Brno University of Technology, Brno, Czech Republic*
[3]*Nuclear Physics Institute ASCR, Rez, Czech Republic*
[4]*Czech Technical University, Prague, Czech Republic*
[5]*Institute of Nuclear Research and Nuclear Energy of Bulgarian Academy of Sciences, Sofia, Bulgaria*

Annotation

Experiment with the natural uranium spallation target called QUINTA was performed at the Joint Institute for Nuclear Research (JINR) in December 2013. The mass of the QUINTA setup is 512 kg. It consists of five hexagonal sections. The samples of Co-59 have been irradiated with deuteron beam in the field of secondary neutrons at the Nuclotron accelerator from JINR. Energy of the deuteron beam was 4 AGeV. The total beam integral was 6.1(6)E+12. During the experiment, samples were situated in different position inside the assembly and after irradiation were transported to the spectroscopy laboratory and measured at the high-purity germanium semiconductor detectors. The experimental neutron flux was determined and compared with calculated reaction rates with the MCNPX 2.6 and MCNPX 2.7 codes.

Introduction

Nuclear power plants are based and stable sources of the power energy. The power plants produce thousands tons of radioactive waste and spent fuel per year. The fuel contains more than 90 % of energy, which can be used for produce energy in accelerator driven systems (ADS). One of the leading projects with the use ADS is project MYRRHA in Belgium [1]. An important parameter for ADS is a neutron flux. Several experiments to the determination of the neutron flux were performed with the use of a spallation target QUINTA at the Joint Institute for Nuclear Research (JINR).

Experimental part

This experiment was prepared on behalf of the group of Energy and Transmutation of radioactive waste (E& T RAW). The main part of the experiment was realized with the spallation target QUINTA. The target QUINTA consists 512 kg of natural uranium. The uranium is composed of five hexagonal sections in aluminum rods. Each rod is 104 mm
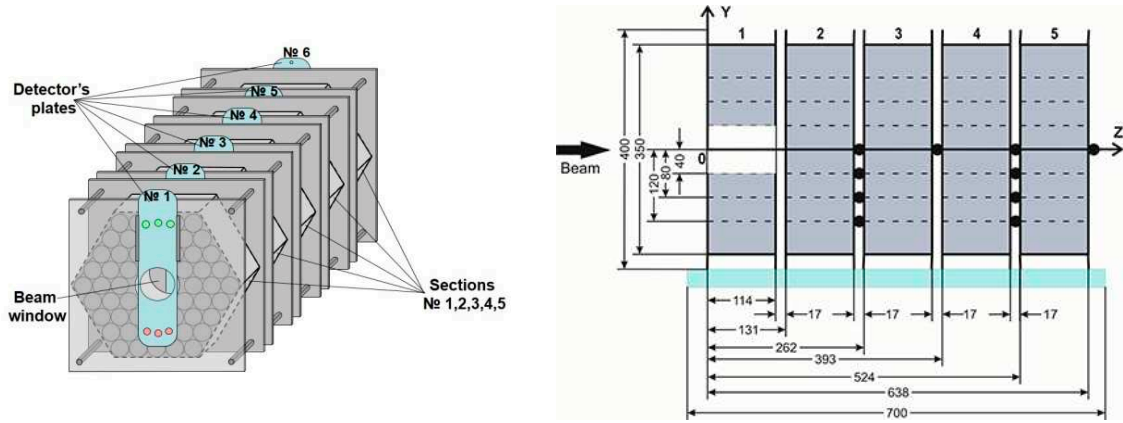
Figure 1: Spallation target QUINTA: front view and side view with samples

long, 36 mm in diameter and its mass is 1.72 kg. Between two sections is 17 mm air gap. The first section consists of 54 rods. Other sections have 61 rods. The length of the setup is 638 mm and a total mass is 538 kg including aluminum container (See Fig. 1). The QUINTA target is surrounded by lead bricks of 100 mm width.

Spallation target QUINTA was irradiated by deuteron beam at the Nuclotron accelerator, which is situated at the Laboratory of High Energy Physics at JINR. Energy of deuteron beam was 4 AGeV. Time of the irradiation was 27 hours and 18 minutes. Samples of ^{59}Co were irradiated in the field of secondary neutrons. The samples had thickness 1 mm, square shape 10×10 mm and mass about 1 g. Positions of samples were situated after sections 2 and 4 at radius 0; 40; 80 and 120 mm from beam axis. After 3rd and 5th sections samples were only at radius 0 mm from beam center (See Fig. 1). The experimental samples were transported to the spectroscopy laboratory after end of irradiation. The irradiated samples were measured with the use of high purity germanium semiconductor detectors. Measured spectra were analyzed with the gamma-spectroscopy software DEIMOS 32 [2].

Calculated of reaction rates and neutron flux

Value of reaction rate is defined as the number of produced residual nuclei per one atom in the sample N_A and one incident deuteron per second N_D. Experimental reaction rate were (Rexp) calculated from following equation:

$$R_{\exp} = \frac{S_p(E_\gamma)C_{\rm abc}(E_\gamma)B_a}{I_\gamma \varepsilon_p(E_\gamma)} \frac{t_{\rm real}}{t_{\rm live}} \frac{1}{N_A} \cdot \frac{1}{N_D} \frac{e^{\lambda t_0}}{1 - e^{-\lambda t_{\rm real}}} \frac{\lambda t_{\rm irr}}{1 - e^{-\lambda t_{\rm irr}}} C_{\rm coisum}, \qquad (1)$$

where S_p is the peak area; $C_{\rm abs}(E)$ the self-absorption correction; B_a the beam intensity correction; I_γ the gamma-line intensity; $\varepsilon_p(E)$ the full-energy peak efficiency; $t_{\rm real}$ the real measurement time; t_{rmlive} the live time of the measurement; λ the decay constant of produce nuclei, $t_{\rm irr}$ the irradiation time, t_0 the time between end of irradiation and begin of counting and $C_{\rm coisum}$ is the correction for true coincidence summing. The experimental neutron flux was determined with the use of equation (2), which represents integral of a reaction rate, where the energetically dependent values are at the right side. The dependent

Table 1: Experimental reaction rates (atom^{-1}·deuteron^{-1}) after the 2nd section

Reaction	Positions of samples in target QUINTA			
	0 mm	40 mm	80 mm	120 mm
^{59}Co(n,γ)^{60}Co	1.36(14)·10^{-26}	1.49(16)·10^{-26}	1.09(11)·10^{-26}	9.31(98)·10^{-27}
^{59}Co(n,p)^{59}Fe	2.19(23)·10^{-27}	1.60(17)·10^{-27}	7.15(77)·10^{-28}	3.87(42)·10^{-28}
^{59}Co(n,2n)^{58}Co	1.87(20)·10^{-26}	1.25(13)·10^{-26}	5.11(55)·10^{-27}	2.57(27)·10^{-27}
^{59}Co(n,3n)^{57}Co	5.60(56)·10^{-27}	3.47(38)·10^{-27}	1.39(16)·10^{-27}	7.19(77)·10^{-28}
^{59}Co(n,2nα)^{54}Mn	3.35(36)·10^{-27}	1.85(21)·10^{-27}	5.98(70)·10^{-28}	-
^{59}Co(n,4n)^{56}Co	1.03(11)·10^{-27}	5.80(65)·10^{-28}	1.64(19)·10^{-28}	8.8(1.3)·10^{-29}
^{59}Co(n,4nα)^{52}Mn	6.85(73)·10^{-28}	3.28(35)·10^{-28}	8.9(10)·10^{-29}	-
^{59}Co(n,2ntα)^{51}Cr	1.98(21)·10^{-27}	9.8(12)·10^{-28}	2.76(40)·10^{-28}	-
^{59}Co(n,4n2α)^{48}V	7.16(76)·10^{-28}	2.80(31)·10^{-28}	6.48(81)·10^{-29}	-
^{59}Co(n,n3α)^{47}Sc	1.68(19)·10^{-28}	6.80(82)·10^{-29}	1.46(27)·10^{-29}	-
^{59}Co(n,2n3α)^{46}Sc	4.30(46)·10^{-28}	1.91(29)·10^{-28}	-	-

values are the cross section $\sigma(E_n)$ and the neutron flux $\varphi(E_n)$.

$$R = \int_{E_{th}}^{\infty} \sigma(E_n)\varphi(E_n)dE_n. \tag{2}$$

The equation follows that the neutron flux in energy area between the energy threshold at (n,xn) reaction a maximum neutron energy constant can be calculated as a ratio of experimental reaction rate and cross section. After calculation of the neutron flux in the above mentioned interval the neutron flux between the energy threshold of (n,(x-1)n) and (n,xn) reaction can be calculated using the neutron flux from the last energy interval. The simulations of the experimental neutron flux at different position inside of the spallation target QUINTA were realized with the use of Monte-Carlo transport code MCNPX version 2.6 (MCNPX 2.6) [3] and version 2.7 (MCNPX 2.7) [4] combining the INCL4 intra-nuclear cascade model [5] with the ABLA fission-evaporation model [6]. The calculated data were used for the comparison of experimental reaction rates and experimental neutron flux. The cross sections were obtained with using program TALYS 1.6 [7] and data library TENDL 2012 [8].

Results of reaction rates and neutron flux

Value of the reaction rates were obtained in ^{59}Co for eleven products ^{46,47}Sc, ^{48}V, ^{51}Cr, ^{52,54}Mn, ^{56,57,58,60}Co and ^{59}Fe. Example of products and their values are showed in Table 1 for all positions at 2ndsection. The highest reaction rates were determined in the center of the target. The lowest reaction rates were determined in 4th section at position 120 mm from the center of target QUINTA.

The experimental neutron flux was calculated with the use of (n,p) and (n,xn) reactions. The experimental neutron fluxes were compared with simulations from MCNPX 2.6 and MCNPX 2.7. Examples of neutron flux for section 2nd and 4th at the center of Target QUINTA were shoved in Fig. 2. The highest neutron flux was determined in the 2nd section at the center of the QUINTA target. The middle value of the neutron flux was calculated to
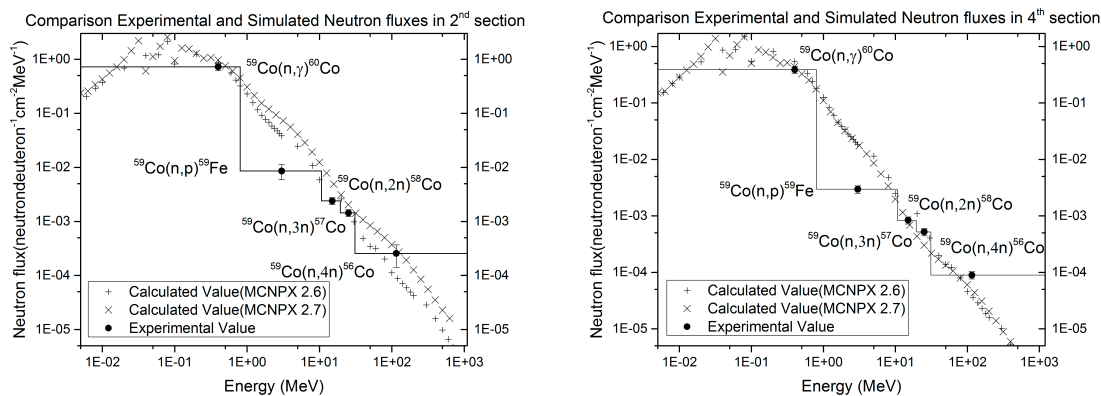
Figure 2: Experimental and calculated neutron flux after the 2nd section (left) and the 4th section (right).

(0.79 ± 0.08) neutron·deuteron^{-1}·cm-2·MeV^{-1}. The comparison the experimental neutron flux and simulation had agreement with two or three standard deviation for MCNPX 2.7. The comparison with MCNPX 2.6 had agreement with four and five standard deviation. The difference between MCNPX 2.7 and MCNPX 2.6 was determined in main causes about 20%.

Conclusion

The experimental reaction rates in ^{59}Co were obtained for 11 products. After 2nd section at diameter 0 mm from the center of QUINTA was determined values of reaction rates in maximum. The lowest values of reaction rates were calculated after 4th section at position 120 mm from the QUINTA center. Reaction rates were decreasing with increasing length and diameter from beam center. The experimental neutron flux was calculated for all positions from the experiment. The neutron flux was obtained from the threshold energy of the first reaction to the threshold energy of the next reaction. The results were medium values of the neutron flux. The highest neutron flux was concentrated at the 0 mm from the center of the QUINTA after the 2nd section. The value of the neutron flux was determined to (0.79 ± 0.08) neutron·deuteron-1·cm-2·MeV-1. The lowest value was calculated after 4th section at positions 120 mm from the center of the QUINTA target. The density of the neutron flux in the center of target decreased of approximately 25 % per section and around 10% per position. Better agreement between experimental and calculated neutron flux was determined for MCNPX 2.7. The disagreement between calculated and experimental neutron flux can be caused by incorrect flux simulation and inaccurate values of cross sections.

References

[1] H. A. Abderrahim, *et al.*, Nuclear Physics News 20 (2010) 24.

[2] J. Frána, Journal of Radioanalytical and Nuclear Chemistry 257 (2003) 583.

[3] D. B. Pelowitz, MCNPX Version 2.6.0, LA-CP-07-1473, 2008.

[4] D. B. Pelowitz, MCNPX Version 2.7.0, LA-CP-11-00438, 2011.

[5] A. Boudard, *et al.*, Phys. Rev. C 66 (2002) 044615.

[6] A. R. Junghans, *et al.*, Nucl. Phys. A 629 (1998) 635.

[7] A. J. Koning, *et al.*, TALYS-1.6. 2013.

[8] TALYS-based evaluated nuclear data library. TALYS [online]. http://www.talys.eu/tendl-2012/

Applied Research

COPPER-YBCO TAPE LOW RESISTIVITY JUNCTIONS

D. Enache[1,2], I. Dobrin[1], A. Chernikov[3]

[1] *National Institute for R & D in Electrical Engineering ICPE-CA, Applied Superconductivity Laboratory, Bucharest, Romania*

[2] *University Politehnica of Bucharest, Romania*

[3] *Joint Institute for Nuclear Research, Frank Laboratory, Dubna, Russia*

Intorduction

The aim of the research is the realization of a superconducting magnet generating 4T magnetic field with high uniformity, for nuclear spectroscopy purposes. The designed magnet will be executed with HTS tape of YBCO type. Both the HTS coils and the connections between them needs high quality junctions with low resistivity in cryogenic range of temperature.

We present here some preliminary results obtained on resistance measurements obtained on junctions made between copper - HTS material and between HTS - HTS tapes in low temperature range. We will present also the obtaining technology of junctions, junctions resistance measuring method and the experimental setup for this.

The HTS magnet consists in two double pancake coils connected together in order to be supplied with D.C. current in 0 - 300 A range. This arrangement was preferred due to the gap existing between the pancakes, useful for neutron access to the sample positioned inside the magnetic "good field zone" [1]. Another device which needs to have copper - HTS junctions, is the HTS current leads who are involved in current carrying from copper current lead to the HTS coils.

The HTS magnet system

The main components of the HTS magnet system are:
- High Temperature Superconducting Helmholtz coils (Fig. 1)
- Conductive Coils Support
- Thermal radiation shield
- Direct cooling system: two stage G-M Cryocooler (4,2K and 50K)
- Cryostat
- HTS current leads

The main parameters of the HTS superconductor magnet system are presented in Table 1.

Experimental arrangement

Fig. 2 (left panel) shows the main components for the experimental setup. The components are: a cryocooler, a cryostat, a temperature controller, a temperature monitor, a voltmeter, a heater, temperature sensors and the HTS sample.

Fig. 2 (right panel) shows from a side view, the experimental setup scheme with the main components. The cryostat has a stainless steel case (nonmagnetic material), a central cylindrical channel at 300 K and it is vacuumed at 10-6 torr. The cryogenic system is an

Figure 1: Left panel: HTS pancake coils - Helmholtz arrangement. Right panel: HTS double pancake coils

Table 1: The main parameters of the HTS superconductor magnet system.

Parameter	Value	Units
Central field	4	T
HTS wire	YBCO	-
Main field coils	2	-
Inner diameter	80	Mm
Outer diameter	310	Mm
Length	35	Mm
Coil turns/pancake	360×2	-
Operating current	280	A
Operating temperature	20	K

Figure 2: Left panel: experimental setup scheme. Right panel: experimental setup, side view (1- Flange, 2-1st cold head of the cryocooler, 3-HTS current lead, 4-2nd cold head of the cryocooler, 5- Heater, 6- Sample support, 7- Temperature sensor)

Figure 3: The cryostat and cooling cryogenic system.
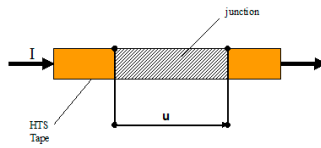
Figure 4: Four points measuring scheme of resistance.

Gifford - McMahon cryocooler with two cooling stages, 1st stage 35W@50K and the 2nd stage 1.5W@4.2K (Fig. 3).

Measuring method

The measuring method used is the four points measurement technique (Fig.4) and the use of Ohm's law.

Devices involved in resistance measurement arrangement:

- Programmable power supply: 0-300A.
- Nanovoltmeter (± 10nV).

Samples Preparation

Sample characteristics (HTS tape YBCO type): 12 mm wide and 0.10 mm thickness, critical current (sf @77K): 300A, copper plated (10 microns), hastelloy substrate. To manufacture the junctions it was used the device seen in Fig. 5.
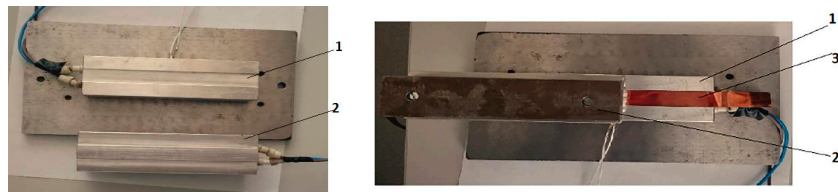
Figure 5: Device for making the junctions (1- lower part, 2- upper part, 3- sample).
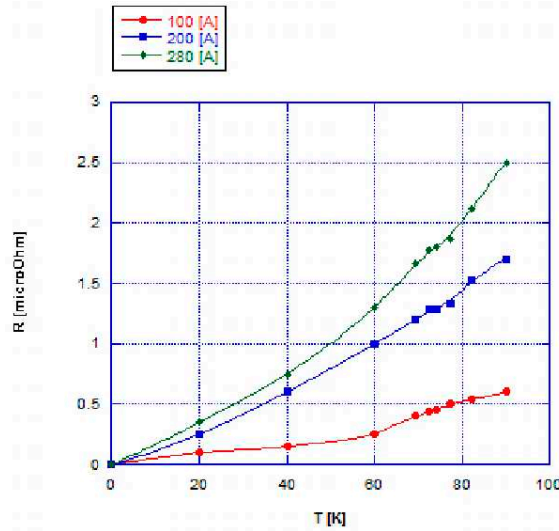
Figure 6: HTS-HTS junction resistance vs. temperature, experimental results.

The two parts (copper/HTS tape) or (HTS tape/HTS tape) are heated in contact with part1 of the soldering device, to 200°C and each part is covered with soldering material. The part 2 of the device, is pressed against the junction just made, and after cooling (150°C), the junction is moved away from the device to be cooled to room temperature. In this way, where performed two types of junctions: 1) with SnPb (60-40%), 2) with In+Ag (97-3%)

Experimental results

Where studied two types of junctions: 1) copper - HTS tape, 2) HTS- HTS tape. The copper-HTS junctions where measured at 77K temperature for both types of soldering materials (Table 2) The HTS-HTS junction made with SnPb was studied vs. temperature in the cryogenic range 10-80K (Fig. 6).

Table 2: Junctions measured at 77K.

Junction/Soldering material	Resistance	Units
Cu-HTS/SnPb	11.50	μohm
Cu-HTS/InAg	5.88	μohm
HTS-HTS(SnPb)	0.44	μohm
HTS-HTS(InAg)	0.55	μohm

Conclusions

Where performed junctions from copper terminals and HTS tape YBCO type, with a special soldering device in order to control the soldering temperature and the pressure on the joints. Where made experimental measurements on the Copper-HTS tape junctions and HTS-HTS junctions, made with two tipes of soldering materials: SnPb (60-40%) and

InAg (97-3%), at liquid nitrogen temperature (77K) and also in the 10-80K range on the HTS-HTS junctions, using SnPb as soldering material. The junctions made with SnPb soldering material show good performance (low resistivity) and a good strenght of the joint compared with the InAg joint. The slight bigger values of the resistance of the joints made with InAg, shows the need for further studies of the conditions for the joints execution (flux, pressure, temperature). The obtained results, show small values (100 nOhms) for the resistance of the joints HTS-HTS at 10K, but these values may be lower, by improving the soldering conditions.

References

[1] SuperOx company, http://www.superox.ru/en/.

[2] I. Dobrin, A. Chernikov, et al., IEEE Transactions on Applied Superconductivity January 2016, DOI: 10.1109/TASC.2016.2520086

[3] T. Lécrevisse, J. M Ghellera, O. Loucharta, J. M Reya, P. Tixadorb, Physics Procedia 36 (2012) 681, Superconductivity Centennal Conference 2011

[4] D. Enache, I. Dobrin, A. Morega, S. Apostol, *Proceedings of the 10th international conference on electromechanical and power systems*, (Chishinev 2015, ISBN 978-606-567-284-0, pps. 351-355).

SYNTHESIS OF NANO-Pb/PVA REINFORCED IN POLYPROPYLENE THROUGH BALL MILLING AND ITS GAMMA SHIELDING PROPERTY

Z. M. Shakfa[1*], A. E. Hannora[2†], M. M. Sherif[1‡]

[1]*Faculty of science, Cairo University, Giza, Egipt*

[2]*Faculty of petroleum and mining engineering, Suez University, Suez, Egipt*

Annotation

Preparation of nano-Pb by ordinary chemical methods is relatively expensive and gives poor yields. Mechanical methods to prepare nanomaterials ended up with reversal results for pure Pb due its high ductility. In this research, nano-Pb was prepared through ball milling using a polymeric surfactant. Elemental Pb and Polyvinyl alcohol (PVA) as the surfactant were milled for different milling times and characterized each time with XRD. According to XRD results, the optimum milling time to get the finest size of Pb (68 nm) was 60 min. The milled Pb-PVA mixture for 60 min was characterized by field emission scanning electron microscope (FE-SEM) and high resolution-transmission electron microscope (HR-TEM) to study the progress in the size and morphology of the nano-Pb particles. Then, nano-Pb/PVA was mixed with Polypropylene for different mass ratios and processed by hot compression. The new composites were tested against the 0.662 MeV gamma rays from Cs-137 source. The experimental mass attenuation coefficient of each sample was compared to the value reported for its normally sized counterpart in Nist-XCOM database. The comparison showed enhancement in the gamma attenuation properties of nano-Pb by 70.8%. The new composite can substitute conventional gamma shielders with great mass and cost savings in addition to its easy production in bulk amounts.

Introduction

Nuclear radiation in large doses is very harmful for human health. Accumulated doses from nuclear particles like neutrons or from high energy ionizing radiation like gamma rays can cause cancer, DNA mutations, sterility, etc. The protection from ionizing radiation depends on increasing the distance from the source of radiation, shortening the time of exposure and shielding the body by an absorbing material to attenuate the energy and the flux of the radiation. In our research, we focused on shielding gamma because of its high penetrating power and domestic effects on humans. Traditionally, gamma is attenuated by shielders made of heavy metals like Lead (Pb) bricks, steel plates and high density concrete. These traditional shielders have some shortcomings like being expensive, heavy, rigid and poorly portable beside their ability to produce secondary ionizing radiation which requires additional shielding. Many research efforts were done to design more efficient shielding materials that are potentially capable of attenuating gamma and neutrons in addition to being light weight, cost effective, easily portable and flexible. Polymer composites are a suitable candidate to solve the traditional shielders problems. Polymer composites are

---

*zshakfa@sci.cu.edu.eg

†ahmed.hannora@suezuniv.edu.eg

‡mmsherif@sci.cu.edu.eg

dual-purpose shielders as they combine the Hydrogen-rich polymer which is effective in absorbing neutrons and metallic additives which are effective for gamma shielding. Also, Polymer composites are light, commercially available and able to be processed into complex shapes. The multifunctionality of polymer composites assigned them to be used in many applications like shielding space crafts and making protective enclosures for humans and devices in hospitals and nuclear power plants [1]. On the other hand, Nano sized materials are increasingly attracting the scientists attention in many fields due to their distinguished physical and chemical properties. Polymer nanocomposites acquire higher mechanical, thermal, electrical and optical properties comparing to their counterparts in micro scale [2]. Our research will study how the usage of nanoparticles can enhance the nuclear shielding properties of the ordinary polymer composites.

Matherials and methods

Nano Pb was prepared with ball milling using PVA as a process control agent. The role of PVA is to impede the clean metal-to-metal surfaces of Pb and thereby prevent cold welding and particle growth. The milled powder was characterized by XRD through milling at different milling times 0, 30, 60 and 90 min. The morphology of the powder milled for 60 min was characterized by FE-SEM and HR-TEM. Bulk nano-Pb/PVA powder milled for 60 min was mixed with Polypropylene by different mass ratios as 1, 5, 10 and 20% of nano-Pb/PVA. These mixtures in addition to a neat PP sample were molded by hot compression to form solid disks with few discontinuous voids appeared. Narrow beam gamma attenuation setup was used to measure the linear attenuation coefficient of the samples. The used gamma energy was 0.662 MeV from 137Cs source. The densities and linear attenuation coefficients were corrected according to the voids volume in each sample and then used to calculate the mass attenuation coefficients. The mass attenuation coefficient of each sample was compared with its counterpart gotten from Nist-XCOM dataset that calculated for the same compositions in regular sizes.

Results and discussion

XRD showed that the grain size of Pb decreased with milling till reaching about 68 nm at milling time 60 min and with further milling increases again as shown in Table 1.

Table 1: Average grain size of Pb for each milling time.

Milling Time (min)	Grain Size (nm)
0	721.2
30	100.8
60	68.6
90	115.0

According to XRD, the suggested milling time to get the finest grain size is 60 min. The morphology of the powder milled for 60 min was characterized by FE-SEM and HR-TEM. FE-SEM image showed irregular shapes of raw Pb before milling as shown in Fig.1, left
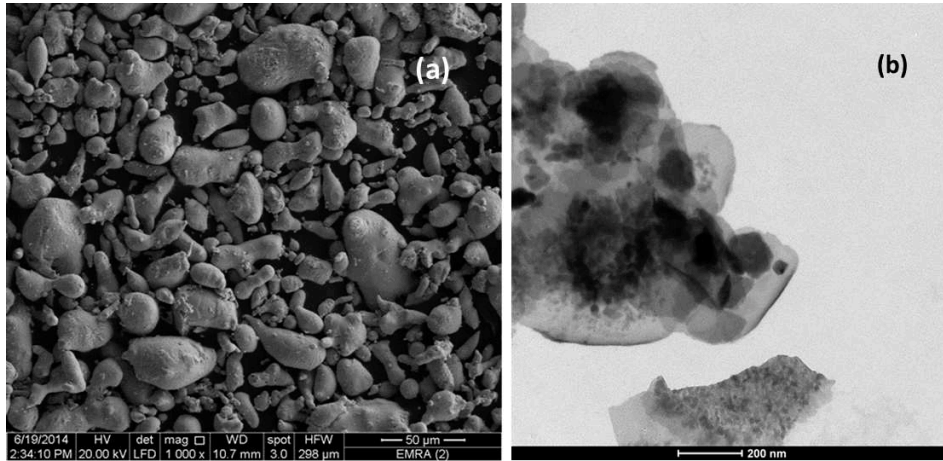
Figure 1: Left panel: HR-SEM of as received Pb. Right panel: HR-TEM of impeded nano-Pb in PVA.

panel. HR-TEM was performed on the milled Pb with PVA and the image confirmed the nanometric size of Pb and the complete capping of them by PVA see Fig.1, right panel.

The mass attenuation coefficient of nano-Pb alone was calculated for different samples and compared with the theoretical value for normal Pb at 0.662 MeV (0.1101 cm^2/gm) [1]. The mass attenuation coefficients of nano-Pb were approximately the same for all samples and averaged to be 0.1884 cm2/gm with 70.8 % improvement compared with regular Pb. This improvement was explained by the high surface area provided by nano-Pb for interaction. The nanometric size of Pb was suggested to highly promote the photoelectric interaction in the material and thereby shielding efficiency. The mass attenuation coefficients of the sample containing 1, 5, 10 and 20% of nano-Pb were calculated and compared to the mass attenuation coefficient of normal pure Pb as shown in Fig. 2. The efficiency
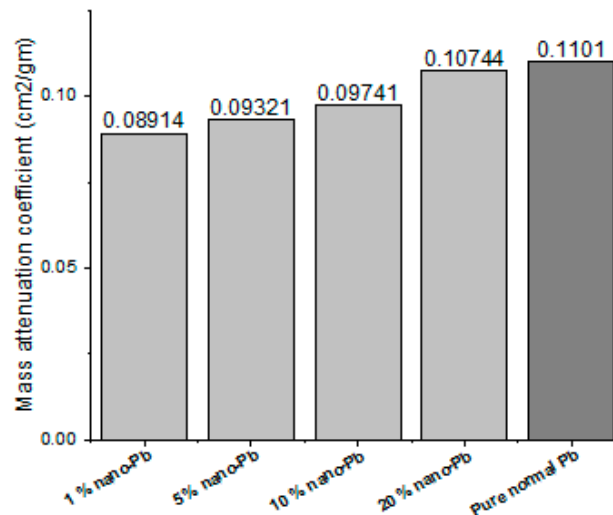
Figure 2: Mass attenuation coefficients for samples with nano-Pb ratios of 1, 5, 10 and 20% with the pure normal Pb.

of sample against gamma increased with the ratios of nano-Pb till approaching the efficiency of normal Pb. According to these results, the sample which has 25% of nano-Pb acquired high mass attenuation coefficient (97.58 % of Pb) and relatively low density. This Pb-polymer nanocomposite can replace many of the commonly used metals for gamma shielding with the same efficiency and lighter weight.

References

[1] S. Thomas, K. Joseph, S. K. Malhotra, K. Goda, M. S. Sreekala, "Polymer Composites", Macro- and Microcomposites, Weinheim : Willey.VCH Verlag & Co. KGaA, 2012, p. 3-4..

[2] T. Hanemann, D. V. Szabó, "Polymer-Nanoparticle Composites: From Synthesis to Modern Applications", Materials - MDPI, 2010, p. 3468-3517.

[3] N S. Hubbell, Nist - XCOM. [Online] 2015. http://physics.nist.gov/PhysRefData/Xcom/html/xcom1.html.

TESTING OF REACTOR ANTINEUTRINO DETECTOR S-CUBE

M. Špavorová[1] [*], V. Belov[2], H. Burešová[3], V. Egorov[2], L. Fajt[1], R. Hodk[1], M. Fomina[2],
R. Pjatkan[3], P. Pidal[1], I. Rozova[2], E. Rukhadze[1], I. Štekl[1], J. Vlášek[1], I. Zhitnikov[2]

[1] *Institute of Experimental and Applied Physics, CTU in Prague, Czech Republic*
[2] *Joint Institute for Nuclear Research, Dubna, Russia*
[3] *NUVIA a. s., Třebč, Czech Republic*

Annotation

The project of the construction of the experimental setup for detection of reactor antineutrinos, which is realized within common project between the Institute of Experimental and Applied Physics of Czech Technical University (IEAP CTU) in Prague and Joint Institute for Nuclear Research, is presented. The testing prototype of detector of reactor antineutrinos, which consists of 18 polystyrene based scintillating plates, has been tested. The background measurement with complex shielding (100-years old lead, polyethylene and borated polyethylene) as well as background measurement without shielding is shown in order to demonstrate the influence of shielding on background suppression. Testing of neutron conversion layers proposed by IEAP CTU and manufactured by the Institute of Macromolecular Chemistry (IMC) of the Czech Academy of Sciences is also shown. A first prototype of the detector of reactor antineutrinos ($40 \times 40 \times 40$ cm^3), called S-cube, which will consist of polystyrene based plastic scintillators (80 pieces, $40 \times 20 \times 1$ cm^3), is under construction. Such detector can be used for the detection of reactor antineutrinos, as well as measurement of their energy spectra and possibly investigation of short-range neutrino oscillations. Moreover, such detector should be able to measure reactor power, estimate isotopic composition of the reactor fuel and so prevent illegal production of plutonium used for the construction of nuclear weapons.

Introduction

Neutrinos are extremely penetrating elementary subatomic particles. They are not detectable by the conventional detectors; therefore, more complicated methods have to be used [1]. One of these methods is based on detection of positron and neutron from the Inverse Beta-Decay (IBD) process (($\bar{\nu}_e + p \rightarrow e^+ + n$) caused by neutrino interacting with matter. Positron loses its energy in short range and then annihilates emitting two 511 keV photons. Neutrons are generally detected through nuclear reactions such as (n, γ) taking place on nuclei (e. g. ^{155}Gd, ^{157}Gd) with the high neutron capture cross-section. Therefore, it is necessary to apply gadolinium isotopes in some way into the detector volume. The signature of the IBD process is the occurrence of prompt signal generated by positron interaction and delayed signal generated by neutron. The time interval between these two events is 20 μs. One of the detectors based on the IBD principle, is the high-segmented polystyrene based scintillating detector DANSS (1 m^3, 2 500 scintillators) [2,3], which was constructed by the group of RCHL DLNP (JINR) and has been installed under the 3 GW$_{th}$ industrial power reactor of the Kalinin Nuclear Power Plant (KNPP) in Udomlya, Russia. Detector S-cube inspired by detector DANSS is under construction in

---

[*]maria.spavorova@utef.cvut.cz

collaboration between IEAP CTU and RCHL DLNP (JINR). It will be installed under the nuclear power reactor in Udomlya NPP and used for online monitoring of the reactor power. Improvement of scintillating plates The basic element of the S-cube detector is a polystyrene-based scintillating plate ($40 \times 20 \times 1$ cm^3) manufactured by polymerization technique in the company NUVIA, Kralupy n. V. In order to improve the light yield and thus the energy resolution of scintillators, optimized scintillating plates with 2% of pTP and 0.025% (50% of standard concentration) of POPOP were selected as the construction material of the S-cube detector. The light yield of S-cube scintillators is 1.5 times higher than scintillators with concentration standardly manufactured by NUVIA ($0.6\%_{wt}$ of pTP, $0.025\%_{wt}$ of POPOP). Each scintillating plate is wrapped into Teflon, which ensures 1.6 higher light yield in comparison with bare scintillator and good homogeneity (80%) of the light collection along the plate. The light collection from the scintillator is done via 19 Wave-Length Shifting (WLS) optical fibers, which are glued into groves along the plate. The WLS fibers are connected to the photomultiplier or SiPM. In order to measure the light yield and the energy resolution of scintillators, the monoenergetic electron source installed in the light-tight box is used. This source has been produced by the IEAP CTU and is installed in the laboratory of the NUVIA Company. The big advantage of the source is the possibility of its remote movability, thus the light yield at any place of the scintillator can be measured without opening the box. The example of detailed measurement of the light yield in transverse direction of the scintillating plate is in Fig. 1. Zero is assigned to the center of the scintillating plate, 4 cm from the side where WLS fibers leave the scintillator. The light yield and the energy resolution were measured every 5 mm in the middle of the scintillator and then every 1 cm up to the edge of the scintillator. The values are normalized to the light yield of the first measured point. As shown in Fig. 1, the
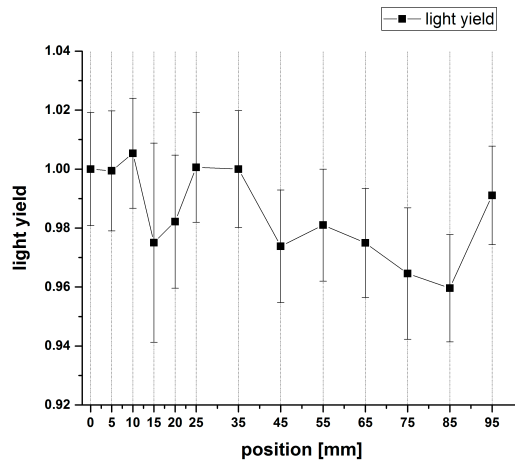
Figure 1: The light yield measured in transverse direction of the scintillating plate.

maximum difference between the highest and the lowest light yield is 4%. A worse case is for the light yield in longitudinal orientation. The maximum difference between points with the highest and the lowest light yield is 19%. However, this situation can be solved using a combination of two wrapping materials with different reflectivity, e.g. Teflon + Mylar.

251

Description of testing protype

The testing prototype consists of 18 scintillating plates. Ten WLS fibers are used for the light collection from each scintillator. Scintillating plates are alternately connected to two photomultipliers to form two individual channels. Additionally, between every layer of scintillators there is a gadolinium neutron conversion layer produced by IEAP CTU. In order to check the influence of shielding on the background radiation, the benchmark tests were carried out using the testing prototype. The complex shielding consists of 10 cm of hundred years old lead working as -shielding, 8 cm of polyethylene working as shielding from thermal neutrons and 8 cm of borated polyethylene working as shielding from fast neutrons. The stepwise installation of individual layers of shielding is shown in Fig. 2.

Figure 2: A stepwise installation of complex shielding.

The background radiation has been measured in each phase, i. e. without shielding, with bottom layer of both types of polyethylene and bottom lead layer, with bottom shielding of both types of polyethylene and all complete lead shielding, with total polyethylene and lead shielding. The LeCroy digital oscilloscope was used for data collection. The measured background up to 3 MeV (mainly γ-background) for one energy channel in each stage of shielding installation is shown in Fig. 3. A significant decrease of the background radiation
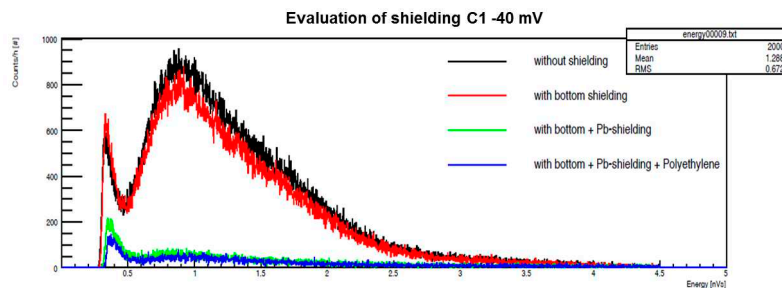
Figure 3: The suppression of the background radiation using the complex shielding. A stepwise decrease of the background radiation with the installation of shielding is visible.

in particular stages of shielding installation is visible in the energy spectrum. The results proved the effectiveness of shielding used to the background suppression.

Gadolinium layer

For detection of neutrons from the IBD reaction it is necessary to apply the neutron conversion layers into the sensitive volume of the detector. The hand-made foils, which

contain the Gd_2O_3, are used in the testing prototype of the detector S-cube [?, 4]. They have been prepared by applying of the Gd_2O_3 powder on the scotch tape surface. Such method is very simple and cheap solution in comparison with commercially manufactured Gd-foils. However, it is not possible to ensure the constant amount as well as homogeneity of the Gd_2O_3 on the scotch tape surface. Therefore, another method was investigated. Based on results of previous tests carried out by IEAP CTU, the IMC manufactured Gd-foils by doping of Gd_2O_3 into the polymer material. The comparative measurements were performed to compare two types of these foils ($10\%_{wt}$ of Gd) with the hand-made foils, DANSS scintillators with Gd-surface made by co-extrusion and white paint containing Gd made by NUVIA. The scintillating plate with the tested Gd-layer was irradiated by neutrons from the AmBe neutron source. A 1 Ci AmBe neutron source was surrounded by paraffin in order to moderate fast neutrons to thermal energies. The gamma radiation emitted after the capture of thermal neutron on the Gd nuclei was detected by the HPGe detector. The peak area of the 181.9 keV line from the (n, γ)-reaction was investigated for each Gd-layer. The results are shown in Fig. 4.
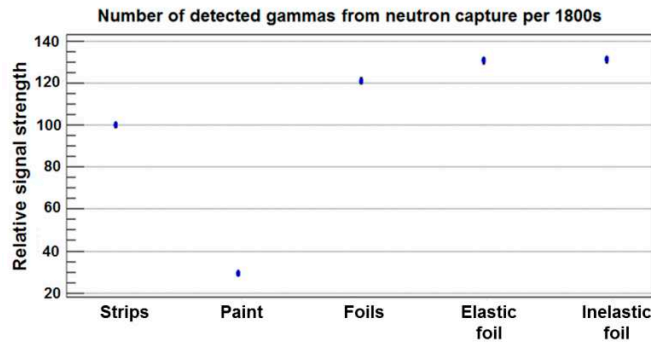
Figure 4: A relative signal strength normalized to the value obtained in measurement of DANSS scintillators. Errors are smaller than the size of markers and are not visible.

Results are normalized to DANSS scintillators, which are considered as the reference scintillators. The hand-made foils are about 20% more efficient than DANSS scintillators and both types of foils made by IMC are about 30% more efficient in comparison with DANSS scintillators. A further R& D of these Gd-foils will be done.

Summary

Present research provided a basis for the construction of first prototype of the S-cube detector (80 scintillating plates, 40 $\times$40 $\times$ 40 cm^3), which will be installed under the 3 GW$_{th}$ reactor of the KNPP in Udomlya in order to monitor the reactor power. A detailed measurement of the light yield and the energy resolution of the scintillating plate in transverse and longitudinal direction was done and showed very good homogeneity. Currently, the intensive R& D of special Gd-foils is being done and their applicability for the S-cube experiment will be tested soon. The complex shielding against the background radiation has been designed and its effectiveness has been also verified.

References

[1] C. L. Cowan, *et al.*, Confirmation. Science. 124 (1956) 103.

[2] I. Alekseev, *et al.*, Phys. Part. Nucl. Lett. 11 (2014) 473.

[3] M. Danilov, *Sensitivity of the DANSS detector to short range neutrino oscillations*, Proceedings of Science. 2013.

[4] H. Burešová *et al.*, *Detektor antineutrin na bázi plastového scintilátoru* , PV 2015-359 and PV 2015-360 Czech Republic, 2015.

ELECTROMAGNETIC COMPATIBILITY FULFILMENT - AN IMPORTANT ASPECT OF MEASURING EQUIPMENT

A. Światek*, K. Sieczkarek, T. Warzyński
Institute of Logistics and Warehousing, Poznań, Poland

Introduction

Sensitive measuring equipment used in scientific research may be susceptible to phenomena originating from an electromagnetic environment. These phenomena are of pulsed or continuous nature. Electromagnetic compatibility (EMC) tests are carried out in order to analyse the ability of electric or electronic devices to proper operation in given electromagnetic environment and to reduce the emission of electromagnetic field disturbances interfering with the operation of other devices in this environment [1]. They are performed in order to recognize and quantify levels of those disturbances. EMC is divided into two basic areas - emission and immunity aspects. Electromagnetic Compatibility is achieved when electronic equipment do not disrupt their environment (emission) and when the environment does not interfere with the operation of electronic equipment (immunity). One of the leading Polish institutions performing EMC tests is Laboratory of Electronic Devices of the Institute of Logistics and Warehousing in Poznań. Some EMC phenomena will be presented along with the methods used to test them in this paper. The ability of measuring devices to withstand electromagnetic disturbances will be assessed. Specifically the information about the continuous electromagnetic field immunity test of exemplary measuring apparatus in Semi-Anechoic Chamber (SAC) according to standard EN 61000-4-3 will be shown.

Types of tests

Electromagnetic emission is the generation of electromagnetic energy by a piece of equipment and its release into the environment. All electronic and electrical equipment produce uncontrolled emissions. Unwanted emissions appear in wide frequency range - from few Hz up to several GHz. Disturbances can be transmitted both through empty space - by electromagnetic waves and via metallic conductors - by direct conduction. Electromagnetic emissions can origin from an AC power cord, a metallic casing containing a subsystem, a cable connecting subsystems or from an electronic component. They need to be reduced below certain acceptable limits in order to ensure that they will not cause any disruption to other equipment. During emission test the analysed factors are radiated and conducted emission, harmonic current emissions, voltage changes fluctuations and flickers [2]. Immunity is the ability of a device, equipment or system to function correctly without performance degradation in the presence of an electromagnetic disturbance. The basic signal for all radio frequency (RF) immunity tests is sinusoidal signal, which is modulated in several ways. The immunity level of a circuit or a device is defined by an electromagnetic environment in which the equipment can operate satisfactorily - without degradation and with a defined safety margin. During immunity test the equipment under test is subjected to different types of electromagnetic disturbances. Examples of pulsed disturbances are

---

*agnieszka.swiatek@ilim.poznan.pl

electrostatic discharges (ESD), electrical fast transients/bursts, pulse magnetic field, voltage dips, short interruptions, voltage variations and surge tests. Examples of continuous disturbances are power frequency magnetic field, radiated RF electromagnetic field and conducted disturbances induced by RF fields [2]. Some of the phenomena applying during tests are presented in Fig. 1. The operation of the equipment is being analysed during the EMC testing. Government agencies and regulatory bodies have imposed EMC regulations
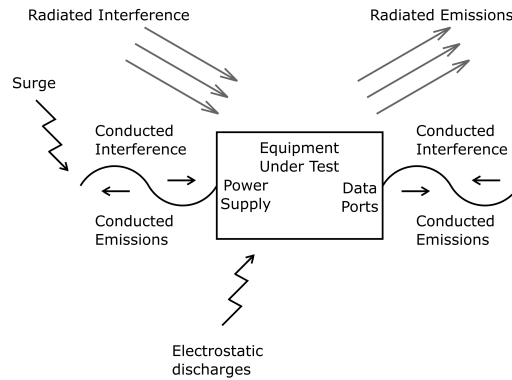
Figure 1: **Different kinds of phenomena implemented during EMC testing.**

which an electronic devices must meet before it can be marked. These regulations control allowable emissions and, in some cases, define the required degree of immunity.

Semi-anechoic chamber

Some of these tests, such as disturbance field strength test and radiated RF electromagnetic field immunity, have to be carried out in a special electromagnetic environment such as semi-anechoic chamber (SAC). Semi-anechoic chamber is a shielded room, in which all the internal surfaces, except the floor, are fully covered with non-reflective material (Fig. 2). Semi-anechoic chamber contains: antenna mast, receiving or generating antennas, turn table, RF absorbers as well as video and audio monitoring system. Measuring receiver and control software are located outside the chamber in order to ensure that no unwanted external signal will get in.

Radio disturbance characteristics

Radiated emission is the emission of electromagnetic waves, which can interfere with the operation of the equipment. The frequency range for radiated emissions begins conventionally at 30 MHz and ends at several GHz. The compliance is verified by measuring the radiated electric fields emitted by the equipment either in a semi-anechoic chamber or at an open - field area test site. The parameters of the test should be set as specified in the standard [2]. An example of test setup in semi-anechoic chamber according to standard EN 55022 - Information technology equipment - Radio disturbance characteristics - Limits and methods of measurement is shown in Fig. 3. EUT (equipment under test) is located on a rotating table and a receiving antenna is placed on the mast allowing to change the height of antenna above the ground plane. Field strength is measured at a distance of 3 m

Figure 2: Semi-anechoic chamber in Laboratory of Electronic Devices of the Institute of Logistics and Warehousing.

from the EUT by measuring receiver. The maximum field strength of the EUT has to be found for each frequency by rotating turn table, scanning antenna height and changing its polarization. As a result of the emission measurement, it is possible to find out whether the level of field strength exceeds the maximum level. An example of result of the test is shown in Fig. 3. In the diagram the dependence of strength of electric field versus frequency is shown. The limits of the field strength are given in dBµV/m. The limit is exceeded for class B, which means the EUT cannot be used in a household environment defined by the standard. When the emissions are below the required limit the EUT is deemed to be compliant [3].
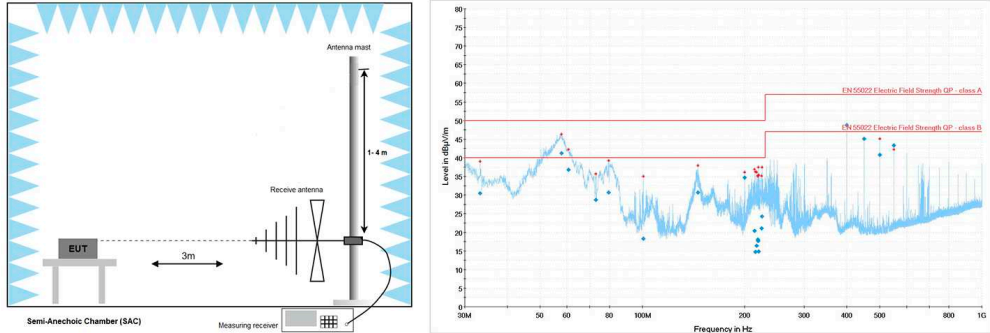
Figure 3: Left - test setup of the electrical disturbance field strength in SAC, right - the example of results.

Electromagnetic field immunity

In the case of radiated RF electromagnetic field immunity test an EUT is subjected to an electric field with a specified amplitude (measured in V/m) in the frequency range defined by the standard. The operation of the EUT is observed in order to determine whether it was disrupted. The extent of the disruption is monitored and it is checked if it is acceptable. An example of test setup according to standard EN 61000-4-3 - Electromagnetic compatibility (EMC). Part 4-3: Testing and measurement techniques - Radiated, radio-frequency, electromagnetic field immunity test is shown in Fig. 5. Standard RF field

immunity test is carried out in the frequency range from 80 MHz up to 6 GHz. The standard describes test procedure and defines test levels of the field strength [4]. A good example presenting the idea of EMC testing is the operation of an electronic scale subjected to radiated electromagnetic field in the frequency range from 80 MHz up to 1 GHz. An EUT is the electronic scale placed inside a semi-anechoic chamber, according to test procedure included in the standard, as shown in Fig 5. EUT was subjected to field strength of 10 V/m, which amplitude was modulated by 1 kHz sinusoidal wave with a modulation depth of 80% by a RF signal generator. The weight of 3 kg was placed on the scale which was subjected to electromagnetic field, as shown in Fig. 5. Readings of the electronic balance were changing from "-1,15kg" to "+2,61kg" instead of displaying the value of "3kg" as shown in Fig. 5. The result was correct again after turning off the field.
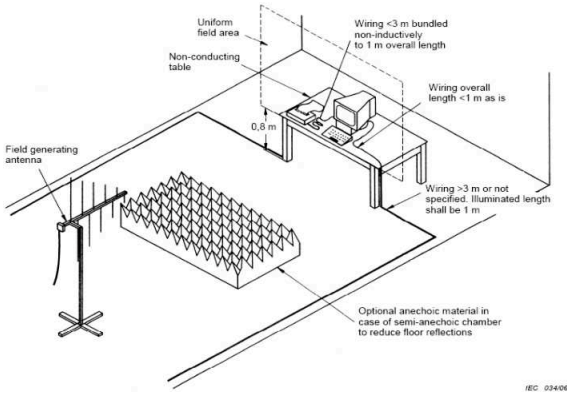
Figure 4: Example of test setup - radiated radio-frequency electromagnetic field immunity in SAC [4].

Figure 5: Left - an example of electromagnetic field immunity test of the electronic scale in semi-anechoic chamber, right - the impact of radiated RF electromagnetic field on the operation of the electronic scale.

Conclusions

Electromagnetic Compatibility tests are an important aspect for measuring equipment as they provide the means to assess and improve reliability of sensitive scientific devices. They prove the ability of an electric or electronic devices for proper operation in a given

electromagnetic environment. Additionally, they allow to recognize and quantify level of disturbances and also help to seek solutions to possible problems resulting from an unexpected loss of function of a measuring equipment.

References

[1] Ch. Kathalay, *A practical approach to electromagnetic compatibility (with an introduction to CE marking)*, (EMC Publications, Pune, 2014).

[2] R. P. Clayton, *Introduction to Electromagnetic Compatibility*, (John Wiley & Sons, Inc., Hoboken, New Jersey, 2006).

[3] EN 55022:2010 - Information technology equipment - Radio disturbance characteristics - Limits and methods of measurement

[4] EN 61000-4-3:2006 - Electromagnetic compatibility (EMC). Part 4-3: Testing and measurement techniques - Radiated, radio-frequency, electromagnetic field immunity test.

ASSESSMENT OF BASIC PHYSICAL AND DOSIMETRICAL PARAMETERS OF PTW MICRO-DIAMOND TYPE 60019 DETECTOR AND ITS APPLICATION IN SMALL FIELD DOSIMETRY

V. Paštyková[1,2,3] *, J. Novotný Jr.[1,2,4], T. Veselský[1,2,4]

[1] *CTU in Prague, Faculty of Nuclear Sciences and Physical Engineering, Department of Dosimetry and Application of Ionising Radiation, Prague, Czech Republic*
[2]*Na Homolce Hospital, Prague, Czech Republic*
[3]*Na Bulovce Hospital, Prague, Czech Republic*
[4] *University Hospital in Motol, Prague, Czech Republic*

Abstract

This paper deals with the dosimetry of small photon fields that becomes currently very relevant in radiotherapy because of the new technologies such as stereotactic radiother-apy and radiosurgery. The new single crystal diamond detector PTW 60019 microDi-amond is introduced in this paper as well as the results of basic physical parameters measurements. Also the relative output factors measurements for Stereotactic linear accelerator, Leksell Gamma Knife and CyberKnife are shown in this paper.

Introduction

In relation with the development of stereotactic radiotherapy and radiosurgery, the methods how to irradiate very small target volumes with better conformity and protection of organs at risk are getting better. The sizes of the radiation fields are often reduced to less than $3\times 3\ cm^2$ and in general those are being called the small fields. Dosimetry in small fields faces several challenges - at first there is the issue of nonequilibrium conditions in small and non-standard fields that are caused by greater lateral range of secondary electrons than is the field size. The new formalism for small and nonstandard fields deals with this issue by using two types of new calibration fields and possible correction factors for both absolute and relative dosimetry [1]. The second issue of small field dosimetry is to find an appropriate detector with a sufficiently small sensitive volume so this detector itself doesn't influent the radiation beam. The new commercially available synthetic single crystal diamond detector PTW 60019 microDiamond (PTW Freiburg, Germany) appears to be a potentially useful tool for this task. Detector with the sensitive volume of 0.004 mm^3 is by the manufacturer especially recommended for relative dosimetry such as measurements of relative out-put factors (ROF) and the depth dose curves for photon fields with sizes from 1×1 to 40×40 cm^2 [2]. In this paper the results of dosimetrical measurements with this detector are introduced. The detector was also used for ROF measurements for all clinically used field sizes of Stereotactic linear accelerator Varian 600C with BrainLAB system (Uni-versity hospital in Motol, Prague), Leksell Gamma Knife Perfexion (Na Homolce Hos-pital, Prague) and CyberKnife (University hospital in Ostrava).

---

*veronika.pastykova@gmail.com

Methods and materials

The measurements of basic physical parameters were performed by using the clinical linear accelerator Varian 600C. For those measurements were used a large water phan-tom Scanditronix/Wellhöfer (at present time IBA Dosimetry, Schwarzenbruck, Ger-many) and a small water phantom miniRAD (miniRAD dosimeteric systems, Czech Republic). For the measurements of ROF for Stereotactic linear accelerator and Cyber- Knife was used the large water phantom PTW MP3-M (PTW Freiburg, Germany), meanwhile for the measurements performed in Leksell Gamma Knife (LGN) was used the standard ABS plastic phantom Elekta. The measurements of ROF in LGN Perfexion were performed in the two different geometries - detector positioned longitudinally and transversely relative to the axis of the table. To determine the dependence of the detector at the chosen parameters the difference of maximum and minimum of the measured response in proportion to the mean of these responses was used.

Results and discussion

Short-term stability

For the measurement of short-term stability of the detector response, at first the detector was pre-irradiated by manufacturer declared dose of 5 Gy [3] and then irradiated with a dose of 0-90 Gy. The reading of detector response was performed in integral mode of UNIDOS electrometer by the time of 1 min. The stability was evaluated in every 5 consecutive measurements (radiation dose of 15 Gy). The required stability of the response was ¡ 0.1%. This stability was reached after the irradiation of detector with the dose of 60 Gy. This high dose necessary for stabilization of the detector response was then measured repeatedly during following measurements and it has to be evaluated as disadvantage of the detector for clinical use.

Dose-rate dependence

The dose-rate dependence of the detector response was evaluated in the range of 100 - 600 cGy / min. The result of the dose-rate dependence was determined as $Delta = (0.24 \pm 0.09)$ %. The manufacturer [3] indicates the dose-rate detector dependence as $\Delta = \pm 0.6\%$, so our result seems to be in very good agreement with this value. The total doserate dependence can be objectively evaluated as being very small. Temperature dependence The temperature dependence of the detector response was measured for 6 different temperatures of the water in small water phantom from 16.2 to 34.4 °C. The overall temperature dependence of response was determined as $\Delta = (0.5 \pm 0.2)$ %, thus ¡0.3 %/K. The value of the temperature dependence determined by manufacturer [3] is 0.08 %/K, but this value is determined for the beam energy range 100 keV - 60Co, which were not available for our measurements. For applied photon beam of the linear accelerator with the energy 6 MV the detector, however, showed an even lower temperature dependence of the response. Under clinical conditions, moreover, the temperature typically ranges from 18 to 25 ° C and for the measurements in this temperature range (from 18.35 to 24.30 °C) the detector showed the dependence $\Delta = (0.031 \pm 0.005)$ %, or 0.005 %/K.

Angular dependence

The dependence of the detector response on the direction from which it is irradiated was measured while placing detector in the air at static positioning in linear accelerator isocenter. The direction of irradiation was given by gantry rotation angle θ. The measured angular dependence was $\Delta = (0.9 \pm 0.3)$ %, while the manufacturer sets the angular dependence 1% for $\theta = \pm 40°$. The positions of the measured maximal and minimal response (minimal for $\theta = 35$ and $215°$ and maximal for $\theta = 115$ and $310°$) show a slight directional dependence of the detector. The extreme measured responses repeated periodically after the intervals of approximately $90°$. At the same time, this result confirms the correct positioning of the detector to the linear accelerator isocenter.

Energy dependence

For the photon beams with energies of 6 MV and 18 MV was measured total dependence of $\Delta = 0.03\%$. For electron beams with energies of 6, 9, 12, 16 and 20 MeV was measured the response dependence of $\Delta = (2.4 \pm 0.9)$ %. All the measurements were performed in the reference depths in the water for the beam energy. For photon beam measurement our result can be evaluated as very satisfactory. Despite the energy dependence of the electron beams higher than for the photon beam, it is necessary to consider that the clinical use of the detector is assumed mainly for the relative dosimetry in photon fields.

Relative output factors

For stereotactic linear accelerator were measured ROF with the diamond detector PTW 60019 microDiamond and PTW Diode E. The resulting values are showed in Tab. 1. The data were compared with reference values measured with the ionization chamber IBA CC01, which are currently used for the planning system in the University hospital in Motol. While deviation from the reference values reached by both used detectors especially for the

Table 1: **ROF measured for Stereotactic linear accelerator; Δ_1 resp. Δ_2 = deviation ROF$_{\text{Diamond}}$ resp. ROF$_{\text{Diode}}$ from the reference value, Δ_{12} = deviation ROD$_{\text{Diamond}}$ and ROF$_{\text{Diode}}$**

A [mm^2]	ROF$_{\text{Diamond}}$ [-]	ROF$_{\text{Diode}}$ [-]	ROF$_{\text{Ref}}$ [-]	Δ_1 [%]	Δ_2 [%]	Δ_{12} [%]
100×100	1,000	1,000	1,000	0,000	0,000	0,000
80×80	0,963	0,960	0,947	1,710	1,319	0,385
60×60	0,915	0,902	0,889	2,887	1,440	1,427
42×42	0,862	0,845	0,832	3,569	1,613	1,925
18×18	0,766	0,747	0,737	3,846	1,283	2,531
12×12	0,733	0,717	0,689	6,317	3,997	2,231
6×6	0,619	0,619	0,487	27,129	27,045	0,066

smallest fields relatively high levels, the relative deviation of both detectors comparing to each other did not exceed 2.6 %. In this place the issue of the right choice of a suitable reference detector is well introduced. In this case especially for the smallest size fields the

Table 2: ROF measured for LGN Perfexion for different collimators sizes (Δ shows the deviation ROF$_{\mathrm{Meas}}$ form ROF$_{rmRef}$ - Reference Elekta value)

Detector position	r [mm]	ROF$_{\mathrm{Meas}}$ [-]	ROF$_{\mathrm{Ref}}$ [-]	Δ [%]
Longitudinal	16	1,000	1,000	0,00
	8	0,900	0,900	-0,05
	4	0,831	0,814	2,12
Transversal	16	1,000	1,000	0,00
	8	0,900	0,903	0,32
	4	0,830	0,814	1,99

currently used ionization chamber IBA CC01 is probably not the best choice of the used detector.

ROF measured for Leksell Gamma Knife Perfexion were compared with the reference Elekta values, which are currently used in the planning system of the device. The total measured deviation for available sizes of collimators are given in the Tab. 2. ROF measured for the CyberKnife were compared with composite data from the planning system used at the University hospital Ostrava. Composite data are the results of statistical processing of the ROF obtained from the measurements performed with various detectors at different workplaces. For static collimators of CyberKnife all the measured deviations were lower

Table 3: ROF measured for CyberKnife for different collimator sizes; Δ = deviation of the measured ROF, resp. ROF$_{\mathrm{Norm}}$ from the reference ROF$_{\mathrm{Ref}}$

r [mm]	Static collimator			Iris collimator		
	ROF [-]	ROF$_{\mathrm{Ref}}$ [-]	Δ [%]	ROF$_{\mathrm{Norm}}$ [-]	ROF$_{\mathrm{Ref}}$ [-]	Δ [%]
60,0	1,000	1,000	0,000	1,000	0,999	0,120
50,0	0,996	0,994	0,251	0,996	0,994	0,181
40,0	0,991	0,988	0,327	0,989	0,988	0,132
35,0	0,988	0,985	0,330	0,985	0,984	0,061
30,0	0,984	0,980	0,395	0,981	0,980	0,143
25,0	0,979	0,974	0,473	0,975	0,975	-0,010
20,0	0,967	0,964	0,351	0,965	0,965	-0,041
15,0	0,946	0,944	0,174	0,941	0,944	-0,275
12,5	0,924	0,924	0,027	0,918	0,924	-0,660
10,0	0,888	0,890	-0,250	0,879	0,890	-1,270
7,5	0,841	0,848	-0,768	0,793	0,812	-2,377
5,0	0,691	0,705	-1,930	0,513	0,557	-7,882

than 2%, so the tolerance usually used in clinical dose measurements was fulfilled and the measurements can be considered as satisfactory. For dynamic Iris collimators were first normalized measured ROF relatively to the field of circular shape. Measured deviations were higher than the permissible tolerance for the collimators 7.5 and 5 mm. The issue of precise measurements in such as small field we content also by using different detectors so usually for this small fields are used the static collimators (in other cases of larger fields

almost unused).

Conclusions

Detector PTW 60019 microDiamond showed very good results while measuring ROF for photon fields of the stereotactic linear accelerator, Leksell Gamma Knife and CyberKnife Very satisfactory results of the basic physical parameters measurements were also obtained - in particular, very small temperature, dose-rate and energy dependence of response for photon beam. Measurements showed a slight angular and energy dependence of the response for the electron beams. Clearly the worst result is high dose (¿ 60 Gy) necessary to achieve stability of the response with the required accuracy. This can be a problem particularly for clinical use of the detector. Overall, however, this detector is regarded as a promising tool that especially in relative dosimetry of small photon fields could be used as one of the usable dosimeters.

References

[1] I. J. Das, G. X. Ding, A. Ahnesjö, Medical Physics 35 (2008) 206.

[2] PTW: microDiamond Type 60019. D930.219.00/02 Effective 2013-09.

[3] PTW: microDiamond: Synthetic Diamond Detector for High-Precision Dosimetry. D252.139.05/02 2014-11.

UMASS LOWELL RESEARCH REACTOR IRRADIATION CHANNEL ANALYSIS

J. Varmuza[1][*][†], S. Agara[2], S. Foral[1], J. Jirickova[3], K. Katovsky[1], M. Ptacek[1], S. Sriprisan[2]
[1] *Brno University of Technology, Brno, Czech Republic*
[2] *University of Massachusetts Lowell, Lowell, United States*
[3] *University of West Bohemia, Pilsen, Czech Republic*

Annotation

This paper gives preliminary information about selected spectral indices which were measured on beam port and thermal column facilities of UMASS Lowell research reactor. The spectral indices were measured using a set of activation detectors from an alloy of copper, manganese and nickel, a molybdenum and last detectors were made from an alloy of tin and antimony. Activation foils were irradiated with and without cover. Foils were shielded by covers which were made from gadolinium, cadmium, hafnium and boron carbide. This paper brings preliminary results about spectral indices of first sort of activation detectors which were made from the alloy of copper, manganese and nickel.

Introduction

Pilot measurement of cooperation project between Brno University of Technology and University of Massachusetts Lowell was carried out by joint group of students and faculty members on the UMASS Lowell research reactor in summer 2014. The main goal of the measurement was to analyze neutron field in horizontal channels for further research studies of BUT students - thermal column and beam port facilities.

This paper gives preliminary information about selected spectral indices. The UMASS Lowell research reactor is a GE designed open pool reactor cooled and moderated by a light water surrounded by a graphite reflector and an output thermal power is 1 MW. It has two thermal beam ports, pneumatic irradiation ports for a neutron activation analysis, multiple in-core irradiation baskets, a center flux trap and a fast neutron irradiation facility. It uses 4 large boron control blades and 1 regulating rod for shutdown and power adjustment purposes.

It has 19 full and 2 partial fuel assemblies in its core. Fuel assemblies are fabricated from uranium-silicide fuel with 19.75 % enrichment. The UMLRR fuel elements are made up of 16 fuel plates with two aluminum side plates at each end. It uses a dispersion fuel type. Each fuel assembly contains 200g of 235U. The maximal thermal flux is 1.4E13 $n.cm^{-2}.s^{-1}$ and the maximal fast neutron flux 9.2E12 $n.cm^{-2}.s^{-1}$.
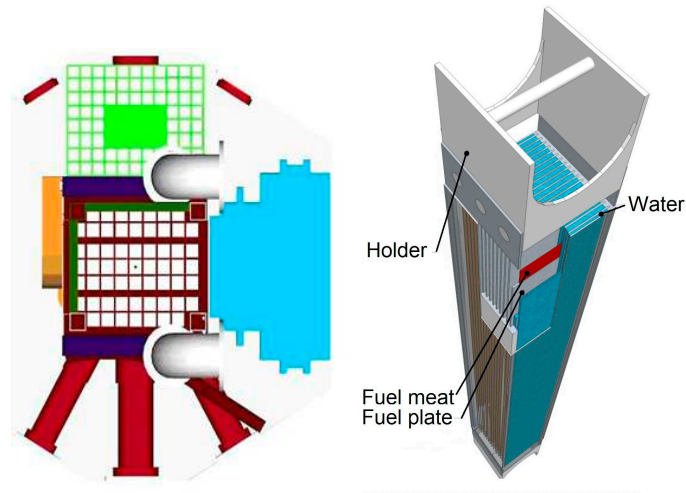
Figure 1: The UMASS Lowell research reactor and the fuel assembly [1]
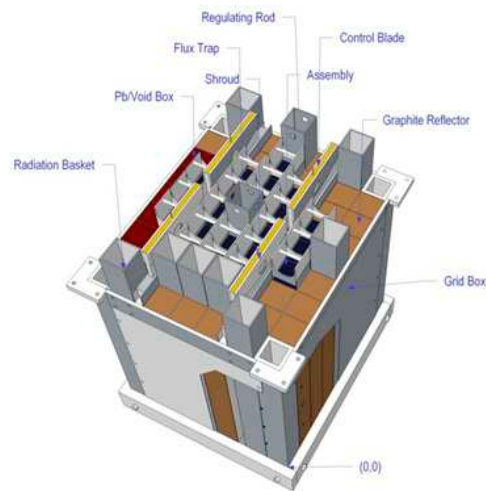
Figure 2: UMASS Lowel reactor core [1]

Experiment description

Three types of activation foils from an alloy of copper (86 %), manganese (12 %) and nickel (2 %), molybdenum (100 %) and an alloy of tin (97.5 %) and antimony (2.5 %) were used for the beam port and thermal column neutron field analyses. Activation foils were irradiated with and without various covers. Foils were put between two covering plates which were fabricated from gadolinium, cadmium, hafnium and boron carbide during irradiation with the cover. Foils were stuck to a holder and centered in the beam port facility and thermal column respectively. Foils were irradiated for 1800 s. Reactor was operated at 1 MW power level. Regarding previously published calculations [1]. Foils were moved to a gamma spectrometry laboratory and there were measured using HPGe detector with almost 90 % relative efficiency.

Figure 3: Foils positioning, dose measurement and uncovering

Reaction rate and spectral index

Neutron activation method is often used for analyzing of reactor neutron field for reactor dosimetry purposes. Reaction rates should be determined according following equation [3]:

$$R_R = \frac{S(E_\gamma)\lambda\frac{t_{\text{real}}}{t_{\text{live}}}}{N_0(1 - e^{-\lambda t_{\text{irr}}})e^{-\lambda t_{\text{cool}}}(1 - e^{-\lambda t_{\text{real}}})\varepsilon_{\text{FEP}}^{\gamma}(E_\gamma)I_\gamma(E_\gamma)}, \tag{1}$$

where R_R is the reaction rate, S the number of counts in a full energy peak (FEP), λ the decay constant of product radionuclide, t_{real} the real time of measurement, t_{live} the live time of measurement, N_0 the number of target nuclei inside activation detector, t_{irr} the irradiation time, t_{cool} the time between end of irradiation and start of measurement, $\varepsilon_{\text{FEP}}^{\gamma}$ the absolute detection effectivity for full energy peak and I_γ the intensity per decay. A spectral index is assessed as a ratio of reaction rate without cover to reaction rate with cover [3].

$$r_i = \frac{R_R^{(n,\gamma)}}{R_{R,i}^{(n,\gamma)}}. \tag{2}$$

Results of copper and manganese reaction rates and spectral indices are available. Due to very low induced activity, just copper and manganese activation products were detectable using the HPGe detector for used reactor power (flux density) and selected real time of measurement. Reaction rates with and without defined cover were calculated for these materials which were placed in beam port and thermal column (Table 1 and 2 respectively).

Table 1: Reaction rate of activation detectors in beam port.

Foil	Cover	$R_R(s^{-1})$	Err (%)	r_i	Foil	Cover	$R_R(s^{-1})$	Err (%)	r_i
Cu	B4C	1.91E-18	5.6	24.35	Mn	B4C	1.79E-18	21	51.64
Cu	Hf	2.56E-17	4.4	1.819	Mn	Hf	5.54E-17	4.0	1.668
Cu	Gd	3.58E-18	5.6	13.00	Mn	Gd	2.15E-18	20	42.85
Cu	N/A	4.65E-17	8.3	1.00	Mn	N/A	9.23E-17	6.1	1.00

Table 2: Reaction rate of activation detectors in thermal column.

Foil	Cover	$R_R(s^{-1})$	Err (%)	r_i	Foil	Cover	$R_R(s^{-1})$	Err (%)	r_i
Cu	B4C	8.40E-19	5.2	2.902	Mn	B4C	1.67E-19	16.3	34.96
Cu	Hf	9.86E-19	6.0	2.4715	Mn	Hf	4.43E-18	5.5	1.313
Cu	Gd	9.43E-19	5.0	2.586	Mn	Gd	1.04E-19	24	55.84
Cu	Cd	8.43E-19	4.7	2.891	Mn	Cd	1.29E-19	19.8	45.26
Cu	N/A	2.44E-18	4.5	1.00	Mn	N/A	5.82E-18	3.7	1.00

Thickness was 0.5 mm of all covers except boron carbide. Thickness of boron carbide cover was 1 mm. Following figures show target materials and coves cross section comparisons.
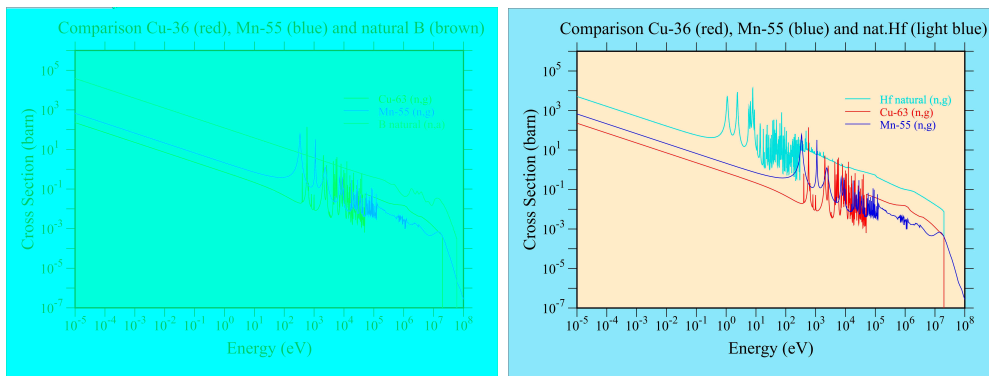
Figure 4: Target materials and cover (B, Hf) cross sections comparisons.
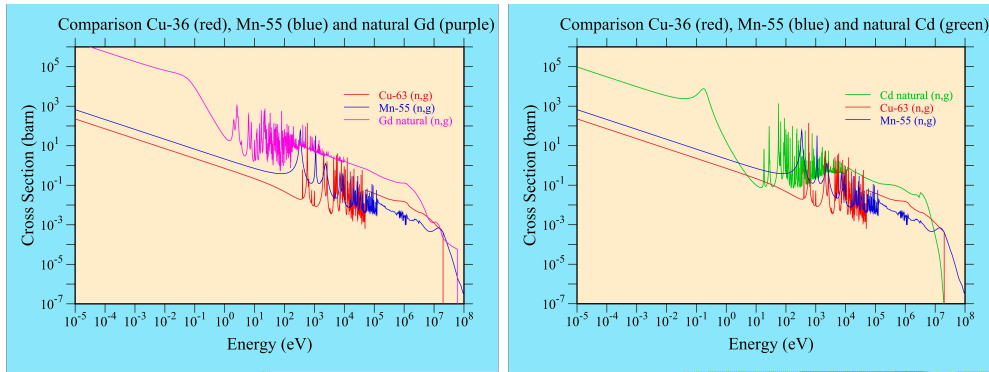
Figure 5: Target materials and cover (Gd, Cd) cross sections comparisons.

Conclusions

The higher spectral indeces were measured using foils covered by the boron carbide and gadolinium. Taking into account higher boron carbide thickness these results show quite hard neutron spectrum in beam port facility. Results given by spectral indices in thermal column are surprising, thermal facility should be characterized by much higher index,

especially for cadmium and gadolinium. Results should be verified by calculations and definitely by further measurements using thermal neutrons sensitive materials like indium, gold, or lutetium. Manganese as well as copper has resonant almost in keV region which might influence. The difference between boron and manganese cross section is almost two orders of magnitude. But the difference is almost one half lower for copper and manganese cross section in the epithermal and the fast neutron region. It leads to more than twice higher spectral index for manganese. Gadolinium as the best natural thermal neutron absorber gives three times higher cross section for manganese than copper in beam port, which show significant thermal neutron fraction in beam port spectrum (supported by hafnium index results). On the other hand, just twice higher spectral indices measured in thermal column than in beam port show reasonably high fraction of resonant neutron in thermal column, which sounds unlikely. Presented results together with other reaction rates measured by joint UMass-BUT group will be used as input data for neutron spectra unfolding procedure to find answer to this challenging question.

References

[1] S. Aghara, O. Dim, *UMLRR Reactor Details and Flux Characterization and UMLRR Reactor Details and Flux Characterization* [online]. 2014 [cit. 2015-02-10].

[2] IAEA Research reactors database. 2015. 2015-02-10. ¡http://nucleus.iaea.org/RRDB¿

[3] M. Stefanik, K. Katovsky, M. Vins, *et al.* Rad. Phys. Chem., 104 (2014) 302.

Life Science

ESTIMATION OF THE ABSORBED DOSE AND RADIOLYTIC YIELDS IN DENTATE GRANULE NEURONS WITH SPINES UNDER EXPOSURE TO ^{56}Fe PARTICLES

M. Batmunkh[1,2], O. V. Belov[1], L. Bayarchimeg[1], O. Lhagva[2], E.A. Krasavin[1]

[1]*Laboratory of Radiation Biology, JINR, Dubna, Russia*
[2] *Natural Science Division, NUM, Ulaanbaatar, Mongolia*

Introduction

Acute and late central nervous system (CNS) risks from space radiation are of concern for exploration missions to the Moon and Mars. The acute CNS risks include: altered cognitive function, reduced motor function and behavioral changes, all of which may affect performance and human health. The late CNS risks are possible neurological disorders such as Alzheimer's disease, dementia or premature aging [1]. These risks are stipulated mainly by space-born protons and HZE (heavy-charged and high-energy) nuclei. Protons are more prevalent and have relatively low linear energy transfer (LET), whereas HZE nuclei (i.e. ^{56}Fe) are relatively rarer, but due to their high LET [2] can be particularly damaging to biological tissues [3]. The hippocampus mediates several higher brain functions, such as learning, memory, and spatial coding. The input region of the hippocampus, the dentate gyrus, plays a critical role in these processes. The granule cells (or granule neurons) of dentate gyrus receive excitatory neuron input from the entorhinal cortex and send excitatory output to the hippocampal other regions via the mossy fibers [4]. But it has been shown to be highly vulnerable to HZE particle exposure [5]. Due to different pattern of energy depositions and ionization track structures, irradiation with protons and ^{56}Fe particles may have different effects on cells and the overall neurological outcomes [6]. Last years, just a few track structure studies of HZE damage to CNS were made [7, 8]. In the present work, we develop an approach to study the indirect radiation damage to the hippocampal neurons exposed to 2.5 Gy of 600 MeV/u ^{56}Fe particles by reconstructing the dentate granule cells with the structures as soma, dendrites, axons and dendritic spines. The chemical reactions and diffusion of the basic water radiolysis species as well as the charged particle energy deposition inside and outside the neuronal structure were simulated with the GEANT4 Monte-Carlo simulation toolkit [9].

Materials and methods

Two granule neurons with dendritic spines in dentate gyrus region of the Thy1-GFP mouse brain hippocampus were selected for the analysis [10]. According to our calculations, individual components of the neuron structure are simulated by elliptical, spherical and cylindrical volumes. The shape of the soma was represented by a single ellipsoid solid and the tracing points of the dendritic branches and axons were represented by combinations of small cylindrical segments. Three-dimensional models of hippocampal fascia dentata granule cells of Thy1-GFP mice were integrated into the Geant4 toolkit and the irradiation by 600 MeV/u ^{56}Fe particles (172.5 keV/μm) was simulated. In the proposed approach, the parallel computing with multiple processors was used. For this purpose, the JINR Central

273

Computing Complex (CICC) was utilized. The special classes, G4PVParameterisation and G4Multi-Threading, were introduced to build neuron morphology and to simulate many-event physical and chemical processes in the case of high dose of radiation.

Results

Traversal of a single particle-track

In this study, the fluence dose of a single particle-track is 3.43×10^{-4} Gy. Fig.1 depicts the 600 MeV/u ^{56}Fe particle track traversing the simulation volume which includes the neuron structure.
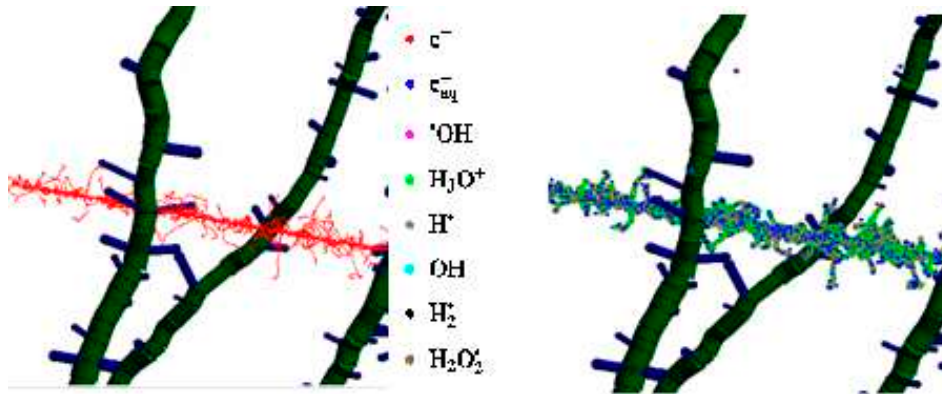
Figure 1: A segment of 600 MeV/u ^{56}Fe particle track traversing spined dendritic branches of a hippocampal granule neuron. The physical processes (left panel) and chemical reactions (right panel) of a single particle track are depicted at the times of 1 fs and 1 ps. The secondary products of incident particle are indicated as the colorbar.

The entrance point of the each particle beam is read randomly from the XY plane of water box and directed along the +Z direction. The physical and chemical processes occur randomly along the path of the incident particle, the number of that occurs within the defined volume is also random. The high energy and high-LET ^{56}Fe particle create numerous and most-energetic secondary electrons denoted as δ-rays. Fig. 2 depicts plots of dose distribution in a single beam penetrating the neuron structure. The first peak is observed in the δ-ray area and the second peak is observed within the so-called "track core" of ^{56}Fe particle beam. In the case of δ-rays, a lower dose deposition and more frequently hits to neuron structures are observed. In this case, the first peak is at 1.02×10^{-4} Gy. In the track core area of the beam, hits with a large dose deposition are observed. The second peak was detected at 3.04×10^{-3} Gy. The total fluence dose of 600 MeV/u ^{56}Fe particle was 2.5 Gy, which is equivalent to about 7300 particle tracks. The dose distribution of a single particle-track obtained with 7300 tracks is represented in Fig.2. The targeting probability, P_{targ} (%), is calculated as the number of particles traversing the neuron to the total number of incident particles (7300, respectively), that's presented in Table 1. For segments of each neuron structure we evaluated the hits percentage P_{vol}, which is described as the number of segments hit by stochastic energy depositions to total number of neuronal segments (14860), that's also described in Table 1. The total energy deposition and absorbed dose in a single neuron structure are considered in Table 1. The soma with a large volume

($938.77 \pm 360.29 \ \mu m^3$) is occurring large energy deposition (9984.31 ± 1488.58 keV), but the absorbed dose to the soma is 1.78 ± 0.41 Gy.
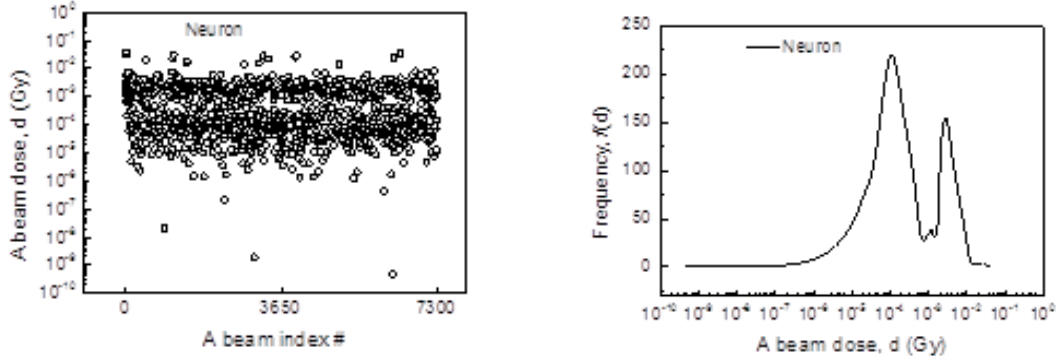
Figure 2: The dose distributions of a single particle-track penetrating the neuron structure at each beam of 7300 tracks (left panel). Frequency distributions of dose deposits within a neuron (right panel) at a beam of 600 MeV/u ^{56}Fe particle.

Table 1: A summary of simulation results related to particles traversing the neuron structures. The incident particle is the 600 MeV/u ^{56}Fe nuclei with radiation dose of 2.5 Gy.

Neuron structure	Targeting probability P_{targ} (%)	Hit percentage P_{vol} (%)	Total energy deposit E_{neuron} (keV)	Mean dose $D_{compartment}$ (Gy)	Total dose D_{neuron} (Gy)
Soma	0.72 ± 0.16	100.0 ± 0.0	9984.31 ± 1488.58	1.78 ± 0.21	1.78 ± 0.21
Dendrite	16.35 ± 1.47	46.76 ± 8.14	14238.69 ± 1231.21	24.84 ± 13.65	1.65 ± 0.24
Axon	0.61 ± 0.35	11.95 ± 19.02	896.86 ± 568.62	27.63 ± 16.89	5.89 ± 1.97
Spine	9.35 ± 1.33	13.01 ± 4.61	1.53 ± 0.41	119.36 ± 43.97	2.73 ± 1.16
Neuron	19.07 ± 1.66	27.16 ± 5.90	42179.17 ± 2187.127	37.75 ± 35.74	1.71 ± 0.32

Water radiolysis in neuron structures

Fig. 3 depicts the yields of water radiolysis products (G-values) in different neuron structures at the end of the chemical stage. At 10^{-6} s, the soma is greatly damaged by free radicals than other structures. In the case of dihydrogen radicals (H_2) and hydrogen peroxide radicals (H_2O_2), G-values are greater.

Conclusions

The proposed approach allows building the different types of neuronal structures and enables studying direct and indirect effects of radiation in neuronal cells. It is based on stochastic computational model of physical and chemical processes. The proposed approach is adapted for the Geant4 Monte-Carlo simulation code, which provides detailed information on properties of the interactions such as spatial distribution of energy depositions, interaction types, and free radicals produced in the water radiolysis in neuron
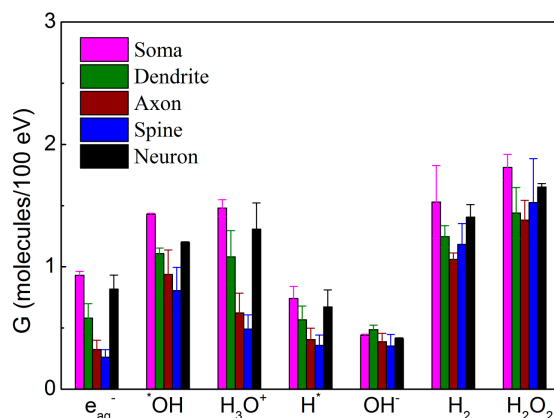
Figure 3: The average yields of water radiolysis products in the neuron structures under exposure to 600 MeV/u ^{56}Fe particles at 1 μs.

structures. The present work uses real and complete anatomical tracing data of the dentate granule neurons of Thy1-GFP mouse hippocampus. The neuron structure includes the soma, dendrites, axon and several thousands of spines. Small segments of these structures are represented by ellipsoid solids, spherical and cylindrical solids parameterized with the GEANT4. The stochastic events of HZE particle energy depositions inside and outside neuronal segments are simulated to determine dose deposition and the initial yields of primary free radicals within the given neuron structures. The results provided are of particular importance for the problems of hadron therapy. They may also contribute to the going studies on space radiation risk assessment.

References

[1] F. A. Cucinotta, *et al. Risk of acute or late central nervous system effects from radiation exposure. In: Mcphee J.C., Charles J.B., editors. The Human Health and Performance Risks for Space Explorations* (Houston, Texas: NASA Human Research Program. pp. 191-212) (2009).

[2] E. A. Blakely, P. Y. Chang, Advances in Space Research 40 (2007) 1307-1319.

[3] R. Vikolinsky *et al.* Radiation Research 173(3)(2010) 342-352.

[4] P. Jonas, J. Lisman. Front Neural Circuits 8 (2014) 107, doi: (2014).10.3389/fncir.2014.00107.

[5] R. Rola, *et al.* Radiation Research, 164 (2005) 556-560.

[6] V. N. Marty, *et al.* Radiation research, 182 (2014) 653-665.

[7] M. Alp, *et al.* PLoS Comput Biol. 7 (2015) 11(8):e1004428.

[8] M. Batmunkh, *et al.* Journ. Rad. Res. Appl. Scie. 8 (2015) 498-507.

[9] S. Agostinelli. *et al.* Nucl. Instr. Meth. A, 506 (2003) 250-303.

[10] G. A. Ascoli, PLoS Biol. 8 (2015) 13(10).

EFFECT OF NOS-INHIBITOR NS23 ON RADIATION-INDUCED ALTERATION IN HEMAPOIESIS AND SURVIVAL OF IRRADIATED ANIMALS

V. M. Makarchuk [*], M. V. Filimonova, L. I. Shevchenko, O. S. Izmesteva, E. A. Chesnakova, T. S. Korneeva, A. S. Samsonova, A. S. Filimonov
A. Tsyb Medical Radiological Research Center - branch of the National Medical Research Radiological Center of the Ministry of Health of the Russian Federation, Obninsk, Russia

Annotation

Due to the wide use of sources of ionizing radiation in various areas of human activity there is a high probability of radiological emergencies and possibility of hitting people with radiation. A significant problem is the development of radiation damage in cancer patients who receive radiation therapy [1, 2]. Often, these patients' life expectancy is determined by the development of radiation complications but not the development of tumor. Most of the existing radioprotectors are effective only when used at doses close to maximum portability [3,4]. It makes them difficult to use, particularly in cancer patients. There are a considerable number of publications about the important role of endogenous nitric oxide in radiobiological reactions. These data formed the basis for searching of new radioprotective agents among the compounds possessing NOS-inhibitory activity [5].

Previously we have shown a statistically significant correlation between NOS-inhibitory and radioprotective properties of S-monosubstituted derivatives of ITU. At the same time, aminothiols amifostine and cystamine, effective radioprotectors showed weak NOS-inhibitory activity [6]. So, NOS-inhibitory activity of ITU derivatives plays a fundamental role in the development of their radioprotective action. And searching of new effective radioprotectors among NOS-inhibitors is of current interest.

It is known that NOS-inhibitors induce the increase in vascular tone and thus can cause hypoxia. According to the sources of literature and our own experimental data induction of hypoxia is one of the leading mechanisms of radioprotective action of NOS-inhibitors [7,8].

Matherials and methods

In this research we used substance NS23, an N,S-substituted derivative of isothiourea. Male F1 ($CBA \times C_{57}Bl_{6j}$) mice were exposed to gamma-radiation with dose rate 10 mGy/s. To investigate radioprotective activity of new substance we used standard radiobiological tests: 30-days survival of mice and survival of their bone marrow clonogenic cells by methods of splenic endo- and exogenous colony formation. Also we estimated the quantity of cells in bone marrow and peripheral blood using the automatic hematology analyzer Abacus Junior Vet (Diatron, Austria). The significance of differences between groups was assessed by paired comparison -using the Mann-Uhitney test; by multiple - using Dunnett and Dunn criteria. The differences considered statistically significant when $p < 0.05$.

---

[*]amnea@mail.ru

Results

Using the test of splenic exogenous colony formation after irradiation at a dose of 5 Gy we revealed a clear radioprotective effect of NS23. Minimal radioprotective dose was estimated as 1/8 LD16 (40 mg / kg) and optimal - as 1/4 LD16 (75 mg / kg). So in our further studies we used NS23 at dose of 75 mg / kg. Time dependence of radioprotective effect of NS23 was studied using splenic endogenous colony formation test after irradiation at a dose of 6 Gy. Radioprotective effect achieved maximum from 15 th to 60 th minute after injection of NS23 with a statistically significant peak on the 30th minute after injection (Fig. 1). Such dynamics of radioprotective efficacy of the compound NS23 was largely correlated with hemodynamic changes. This correlation can be the evidence of hypoxic mechanism of radioprotective action of NS23. The results suggest that the NS23 largely contributes to maintaining the viability of hematopoietic stem cells in irradiated animals. Studying its viability we estimated that dose change factor of NS23 was 1.5-1.8.
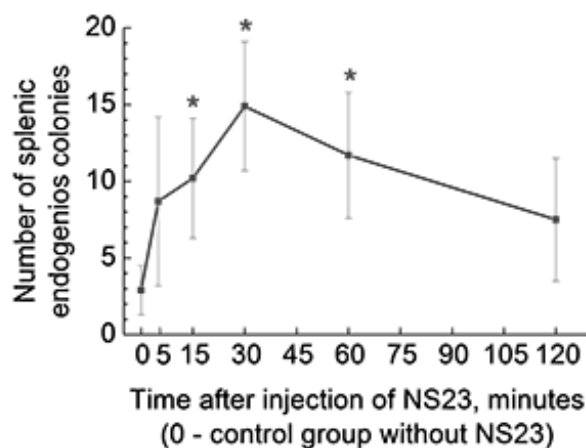
Figure 1: Number of splenic endogenios colonies in F1 (CBA×C$_{57}$BL$_{6j}$) mice, 8 days after administration of 75 mg/kg of NS23 and irradiation at 6 Gy. *Statistically significant differences with indicators of control group.

Trough such an effect there is an evidence that compound NS23 can influence the course of bone marrow syndrome of acute radiation sickness. And we showed that mice who received NS23 had accelerated recovery of the quantity of bone marrow cells after irradiation. Especially it was expressed in the period from 2 till 8 days after irradiation (Fig. 2a.). Accelerating the recovery of bone marrow hematopoiesis NS23 influenced on the dynamics of peripheral blood parameters. On the 8th day after irradiation intensity of the devastation of the population of granulocytes was decreased twofold (Fig. 2f.), and by the end of the experiment the accelerated recovery in blood of population of different types of leukocytes was indicated (Fig. 2d, e, f.). Intensity of devastation of red blood cells (Fig. 2b.) and especially platelets (Fig. 2c.) was also significantly decreased and accelerated recovery of their population was observed. For bone marrow syndrome the most important clinical significance has the depletion in the blood of the population of neutrophils and platelets. It causes the development of infectious, inflammatory and hemorrhagic complications of acute radiation syndrome [9]. Impact of NS23 on bone marrow and peripheral blood of

278
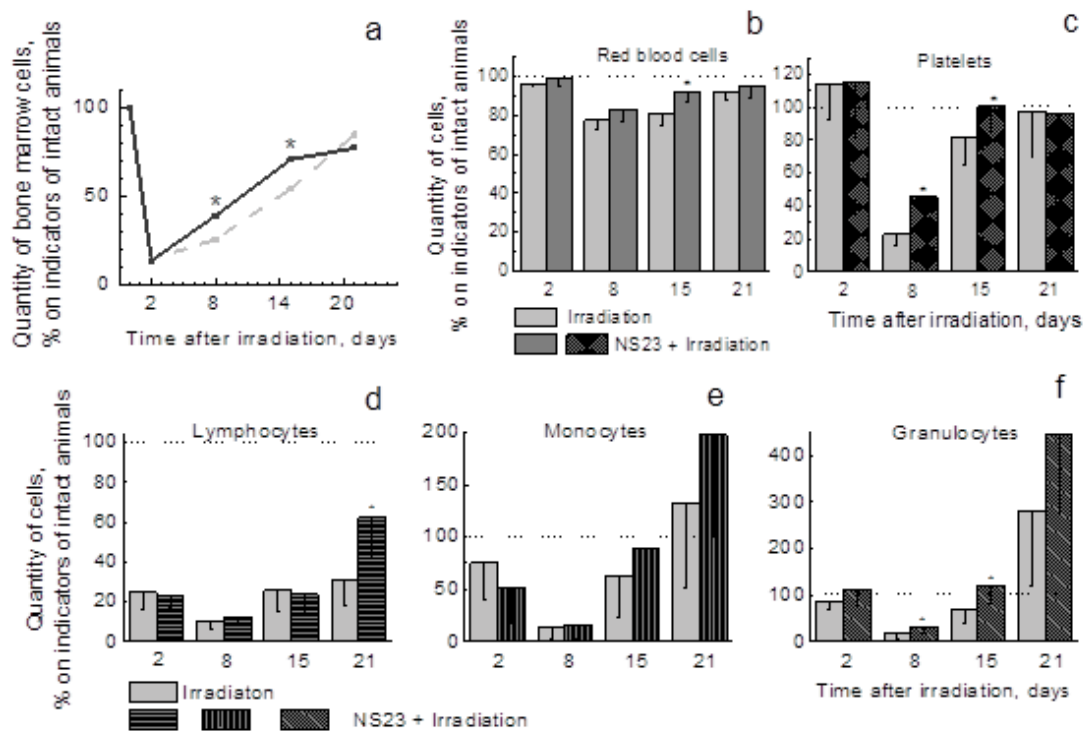
Figure 2: Effect of NS23 on quantity of bone marrow cells (a), red blood cells (b), platelets (c), lymphocytes (d), monocytes (e) and granulocytes (f) of irradiated at 6 Gy animals. Statistically significant differences with indicators of irradiated animals.

irradiated animals explain the ability of this compound to improve significantly survival of this animals. NS23 increased LD50 of -radiation from 7.1 to 10.2 Gy. Apparently the effect of NS23 on hematopoiesis was not limited by an increase in radioresistance. It is known that NOS-inhibitors promote the mobilization of mature cells in bone marrow and stimulate their output in peripheral blood [10, 11]. We noted lack of influence of NS23 on content of bone marrow cells on the 2nd day after irradiation (Fig. 2a.). At the same time on the 4th hour after administration of NS23 we observed statistically significant decrease in cellularity of bone marrow in nonirradiated mice (Fig. 3a.). This effect can not be associated with the death of bone marrow cells because cytotoxic effect of NS23 appears at significantly higher concentrations. Apparently, it does reflect a forced exit from the bone marrow in peripheral blood of mature white blood cells - granulocytes and, to a lesser extent, monocytes. After 4 hours after administration of NS23 in the blood was observed a 3-fold increase in the content of granulocytes and on the 2 day - 2-fold increase of granulocytes and monocytes (Fig. 3b.). To the 7th day the number of these cells remained one and a half fold higher than in intact animals and potentially it could reduce the extent of the devastation of white blood after radiation exposure.

Conclusions

NS23 promotes the accelerated restoration of bone marrow cells population, significantly reduces the depletion of the population of granulocytes and platelets, and accelerates the
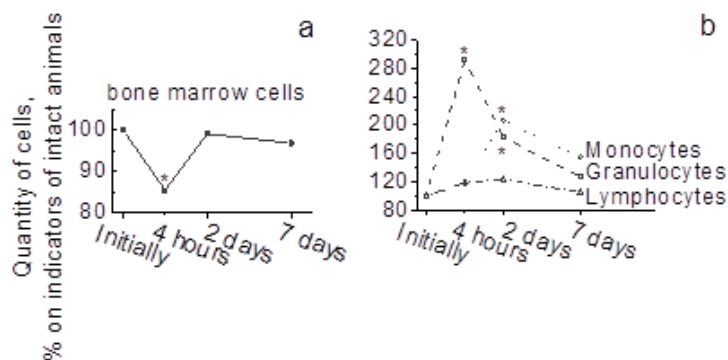
Figure 3: Effect of NS23 on quantity of bone marrow cells (a), lymphocytes, monocytes and granulocytes (b) of intact animals (nonirradiated). Statistically significant differences with indicators of intact animals.

recovery of most of blood cells populations. It reflects the greater safety of the stem cell pool. In nonirradiated animals NS23 causes expressed mobilization of ripening granulocytes and monocytes in the blood. It can potentially influence on the progress of bone marrow syndrome. These effects of NS23 allows to decrease radiation-induced hematopoietic disorders, largely ensuring survival of animals irradiated in medullary dose range. Further studying of NS23 is promising because creates opportunities for the development of new radioprotectors and drugs for treatment of early stages of acute radiation sickness.

References

[1] E. F. Loushnikov, *A.Yu. Abrosimov, Actual human radiation pathology: problems of research methodology, etiology, pathogenesis and classification*, (Obninsk, 2012, 236 p., ISBN 978-5-901968-22-2).

[2] A. V. Akleev, Radiats Biol Radioecol., 54(3) (2014) 241.

[3] M. V. Vasin, *Antiradiation medicines*, (oscow, 2010, 180 p., ISBN 978-5-7249-1411-6).

[4] L. M. Rozhdestvensriyi, Radiat. Biol. Radioecol., 53 (2013)) 513-520 .

[5] J. Liebmann, Cancer Res., 54 (1994) 3365.

[6] M. V. Filimonova, S. Ya. Proskouriakov, L. I. Shevchenko *et al.*, Radiat. Biol. Radioecol., 52(6) (2012) 593.

[7] A. Quillon, B. Fromy, R. Debret, Nitric Oxide, 45 (2015) 20.

[8] M. V. Filimonova, L. I. Shevchenko, T. P. Trofimova *et al.*, Radiat. Biol. Radioecol., 54(5) (2014) 500.

[9] A. F. Tsyb, R.S. Budagov, I.A. Zamulaeva *et al.*,*Radiation and pathology*, (Moscow, 2005, 341 p., ISBN 5-06-005520-5).

[10] T. Michurina, P. Krasnov, A. Balaz *et al.*, Mol. Ther., 10(2) (2004) 241.

[11] B. Ozuyaman, P. Ebner, U. Niesler *et al.*, Thromb. Haemost., 94(4) (2005) 770.

TRACE METAL CONTAMINATION OF SURFACE SOIL AND RECYCLED BUILDING MATERIALS IN PARTS OF THE SINAI PENINSULA AND GAZA STRIP

M. Mahmoud*[†], M. M. Sherif
Physics department, Faculty of science, Cairo University, Giza, Egypt

Annotation

This work aims to assess the contamination levels of trace elements found in soils and recycled demolition debris located in parts of the Gaza Strip and North Sinai Peninsula, and to identify the main anthropogenic pollutants affecting trace metal contents. Due to the excessive siege and aggression in Gaza, residents are in critical need to acquire currently scarce resource of building materials in an attempt to rebuild their homes along with necessary infrastructure and thus, are being forced to utilize the contaminated debris as recycled building materials. Sixty eight samples were collected to represent soil, raw building materials (Ex. cement, Gypsum, and concrete), and recycled demolition debris from the recycling plants in the Gaza strip. Contamination levels of soils were assessed on the basis of geoaccumulation index and enrichment factor. Anomalous contamination levels of some trace metals in heavily bombed areas of the Gaza strip are an indicator for being the bombing one of the main pollution sources there. Cluster and correlation analysis revealed that trace metal contamination in soils are of anthropogenic origin.

Introduction

Trace metals in the soil are either naturally occurring due to the weathering of the parent materials or from anthropogenic sources. The main anthropogenic inputs to the environment are metallurgy (mining, smelting, metalliferous industry) , industrial activities, agricultural activities (frequent use of fertilizers, pesticides and fungicides), sewage sludge, petroleum or fossil fuel consumption, waste disposal, military activities and nuclear power stations [1]. In the last decades, human activities have led to the accumulation of trace metals that may reach toxic levels in some polluted regions. Few previous studies were done to assess trace metal levels in the North Sinai Peninsula and Gaza strip. Other studies in relation to the effect of neighboring regions to the source areas of contamination proved the high probability of shared contamination in both regions, due to long-range atmospheric transport [2], thus confirming importance to study the Gaza strip and parts of the North of Sinai Peninsula. Although in 2005, one of the main studies were carried out to assess trace metal distributions in different soils of the Gaza strip, and to identify the anthropogenic input sources that contaminated the soil [3], a lot of changes happened in the Gaza strip which created a changed situation that necessitated further studies. This "changed situation" was confirmed by the presence of an anomalous concentration of some trace and toxic elements in soils from craters bombed in 2006 and 2009 [4].

Study area

The present work was carried out in Parts of the Sinai Peninsula and the Gaza strip. The initial plan was to study the area starting from El Arish in North of Sinai peninsula till the Gaza strip, but it was difficult to collect samples from some regions such as Rafah and ELSheikh Zowied due to the existing unstable conditions. It was decided to divide our study areas into two regions (some of the north Sinai villages "Ramanah -Qateya and Nigella" and the Gaza strip) (Fig.1).

Figure 1: Location map of the studied areas.

Materials and methods

*Sampling and analysis**

All samples were dried at 80° C, sieved and put in polyethylene bags. They were then digested to be analyzed by inductively coupled plasma optical emission spectrometry (ICAP6500 DUO, Thermo-scientific, England) and the standard 1000 mg/L multi element certified standard solution, Merk, Germany was used for calibration. Contamination levels of Gaza soils were assessed on the basis of the geo-accumulation index and enrichment factor.

Index of geo-accumulation

This index enables us to assess the metal contamination by comparing the recent and the preindustrial concentrations. It is computed from the following equation:

$$I_{geo} = \log_2(C_n/1.5B_n),\tag{1}$$

where C_n is the measured concentration of the examined element in the soil sample and B_n is the geochemical background reference value in the Earth's crust for the same element. Müller has classified the index of geoaccumulation into seven classes [5].

---

*Special thanks for Islamic university staff In Gaza who helped us in collection of samples

Enrichment factor (EF)

The enrichment factor is used to measure the enrichment of the top soils with trace metals and is based on the standardization of an element tested against a reference element. The most common reference elements are Sc, Mn, Ti, Al and Fe [6]. It is calculated from the modified equation:

$$EF = (C_i/C_{\text{ref}})_{\text{sample}}/(B_i/B_{\text{ref}})_{\text{background}}, \qquad (2)$$

where $C_{i(\text{sample})}$ is the concentration of the measured element in the measured sample, $C_{\text{ref(sample)}}$ is the concentration of the reference element in the measured sample, $B_{\text{n}}(\text{background})$ is the concentration of the measured element in the reference environment; and $B_{\text{ref(background)}}$ is the concentration of the reference element in the reference environment. In this work, we selected Al as a reference element and the reference environment is an average concentration of the Earth's crust. The enrichment factor is classified into five categories [7].

Results and discussion

Most of the elements showed a wide range of variations in concentrations, for example, Pb concentrations varied from 19 to 1538mg/kg with a median of 265.30 mg/kg, and a significantly higher mean of 513.62 mg/kg. A clear increase in the average concentration of trace metals were found for example, The average concentration of As, Pb, Cd, Cr, Mn were 31, 51 , 84, 18, 62 times respectively higher than the benchmarked average value recorded in 2003 [3]. Anomalous concentrations of As, Pb, Cd, Hg, Mn ,Ti and Cr was recorded especially in heavily bombed areas in the Gaza strip. Geoaccumulation index and enrichment factor of the measured trace metals for soil samples from the Gaza strip is shown in Figs. 2.
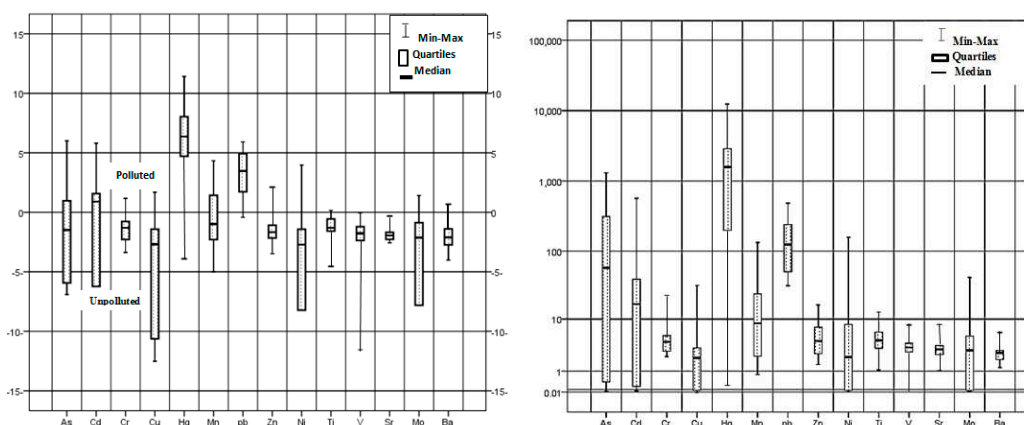
Figure 2: Left panel: . Indexes of geo-accumulation for trace metals in soil of the Gaza strip. Right panel: Enrichment factors for trace metals in the soil of the Gaza strip.

Based on pollution indices, some sites are classified as heavily contaminated with Pb, As, Hg, Cd, Ni, Mn. Referring to concrete samples of the destroyed buildings and crushed demolition debris, they showed contamination with (Al, As, Ba, Cd, Cr, Ni, Mo, Mn, Hg, Pb, Ti, and Zn) compared to the reference concrete samples. On other hand, trace

metal concentration of plaster samples collected from the crushers were close to trace metal concentration in cement samples which were collected from local suppliers . This is due to some components such as; limestone, clay stone, sand, and the additives that may be used in cement production. To recognize distinct groups of trace metals as tracers of natural or anthropgenic source, a hierarchical cluster analysis was carried out using single linkage method and pearson's correlation coefficients. Cluster analysis results were illustrated with dendrogram (Fig. 3) . Based on CA, it is rational to conclude that Cr, Ni and Cd are affected by some anthropogenic inputs such as foundry. Meanwhile, elements of the second branch Co, Ti, V, Al, Fe, Sr, Ba, Zn, Mn, Pb, Cu and Hg are influenced by common anthropogenic sources. Other Previous studies reported presence of these metals in the measured biopsies of victims from the Gaza strip with concentrations higher than the control samples [8, 9].
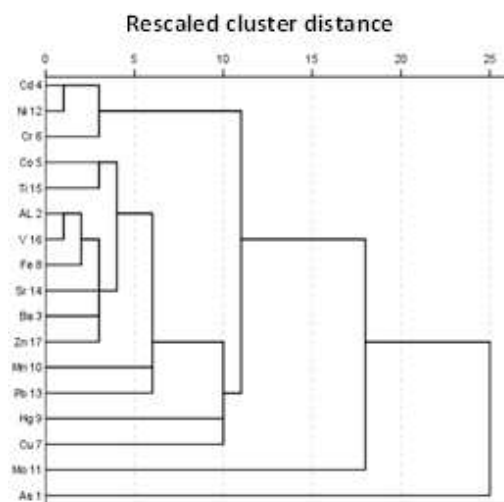
Figure 3: Dendrogram using single linkage for trace metals in soil samples of the Gaza strip.

Conclusions

Soil is a very important constituent of the ecosystem and any pollution of the soil affects human life and health, as they are introduced to the food chain and through it to the human population. Evidence has shown a clear increase in the mean concentration of trace metals in the Gaza strip in comparison to the recorded means in 2003, with clear pollution of As, Hg, Cd, Pb, Mn, Ti and Cr especially in heavily bombed areas. Bombing of the Gaza strip is one of the main pollution sources in Gaza and fast environmental changes have occurred on Gaza that may result in a dispersion of the pollutants in the different regions of the Gaza Strip. Further, crushed demolition debris and destroyed buildings showed contamination with trace metals (Al, As, Ba, Cd, Cr, Ni, Mo, Mn, Hg, Pb, Ti, and Zn). Workers in crushers must take precautions in working with these contaminated materials to avoid exposure, either through ingestion or inhalation. On the other hand, recycling of the debris is a good solution for the current situation in Gaza when comparing benefits to hazards. Also other studies reported production of adequate concrete blocks using recycled aggregate the debris was reported in other studies [10]. Further studies are

required to determine the current situation in the Gaza Strip as there are many factors increasing the distribution of the trace metals like flooding, sewage sludge problems and the 2014 aggression on the Gaza strip. Remediation techniques such as phytoremediation are needed to decrease pollution [11].

References

[1] D. C. Adriano, Trace Elements in Terrestrial Environments, vol. 32, no. 1. 2001.

[2] C. E. Amunsen, J. E. Hanssen, a. Semb, and E. Steinnes, Atmos. Environ. Part A. Gen. Top., vol. 26, no. 7, pp. 1309-1324, 1992.

[3] B. H. Shomar, G. Mller, and a. Yahya, Environ. Res., vol. 98, no. 3, pp. 372-382, 2005.

[4] P. Manduca, Gaza strip,soil has been contaminated due to bombings: population in danger, 2009.

[5] G. Muller, GeoJournal, vol. 2, no. 3, pp. 108-118, 1969.

[6] C. A.-D. Reimann P., Environ. Sci. Technol. vol. 34, no. 24, pp. 5084-5091, 2000.

[7] R. a. Sutherland, Environ. Geol., vol. 39, no. 6, pp. 611-627, 2000.

[8] S. Skaik, N. Abu-Shaban, N. Abu-Shaban, M. Barbieri, M. Barbieri, U. Giani, and P. Manduca, BMC Int. Health Hum. Rights, vol. 10, p. 17, 2010.

[9] P. Manduca, M. Barbieri, and M. Barbieri, pp. 15-18, 2010.

[10] Y. S. Ghuraiz, M. H. Swellam, G. L. K. Garas, and a M. Ragab, J. Emering Trends Engeneering Appl. Sci., vol. 2, no. 2, pp. 308-313, 2011.

[11] S. P. Mcgrath, F. J. Zhao, and E. Lombi, "Phytoremediation of metals, metalloids, and radionuclides," 75, 2002.

DETERMINATION OF SELENIUM IN VEGETATION SAMPLES FROM POLAND BY REACTOR NEUTRON ACTIVATION ANALYSIS

T. Mróz[1*], M. V. Frontasyeva[2], T. Ostrovnaya[2]

[1]*Pedagogical University in Cracow, Cracow, Poland*
[2] *Joint Institute for Nuclear Research, Dubna, Russia*

Annotation

For living organisms, selenium (Se) is one of the most important trace element. It has many biological functions, mainly in detoxication and antioxidation processes. However, the occurrence of selenium in the Earths crust is very low as well as its bioavailability, so concentration of Se in vegetation samples is very low, too. In our study, we determined concentration of selenium in five species of plants: seeds and fruits from Poland by Instrumental Neutron Activation Analysis at the reactor IBR-2M of FLNP, JINR, in Dubna. Concentration of Se in dry mass of samples ranged from 0.10 ± 0.02 to 0.22 ± 0.03 mg/kg.

Introduction

In recent years we can observe growing interest in Selenium (Se) as a micronutrient not only for animals, but also for plants. Selenium belongs to the VI group elements in the Periodic table. It is usually bonded to metal atoms and forms selenides. In the environment, Se is present as a mineral (e.g. crookesites or tiemmanite). In coal layers Se can be present in pyrite, where due to chemical similarity, can replace sulfur atoms. Due to presence Se in coal, during combustion selenium dioxide is formed. The selenium dioxide can be transformed to methyl form of selenium or to selenium acid, and after absorption by the aerosols particles may deposite into the soil and waters. Concentration of selenium in soils is low. An average concentration is calculated as a 0.4 mg/kg [1]. In Poland, average selenium concentration was found at the level of 0.27 mg/kg [2]. Low concentration of Se in soil is the main factor, limiting accumulation of Se in plants. Also, very important is bioavailability of this element. It depends on chemical form of Se, pH of the soil environment, redox potential, content of organic matter in soil and microbiological activity in soil. Most soils in Poland are classified as a acidic soils. In this conditions, Se is present as a selenite (SeO_3^{2-}). If soil has a strong reducing conditions, selenium can occur as a selenide ion (Se^{2-}) [3]. Plants accumulate selenium in this form also some organic forms of Se can be also absorbed by plants. In animals, humans and plants, Se has many biological functions. In general, biological functions of Se can be described as protective and antioxidant functions, so it is very important to ensure optimal content of Se in human and animal diet. One of the most important enzyme is glutathione peroxidase (GPx) [4,5]. It is general name of enzyme reducing hydrogen peroxide to water. GPx are also very important for hemoglobin protection. GPx, which is not inhibited by by azide or cyanide, has been found as a very effective hemoglobin protective agent. Selenium in GPx can be found as a selenocysteine. Selenocysteine can also be found in deionidase [6,7]. Deionidase is peroxidase class enzyme,

---

*tmrozek@o2.pl

responsible for thyroid hormones activation and deactivation. Se deficiency can result as low biologically active form of thyroid hormones (T_3) in blood and tissues. Se is also present in thioredoxin reductase (TrxR) [8]. TrxR is the only known enzyme group able to reduce thioredoxin in all organisms. As a dietary intake is the only way to provide Se for animals and humans, it is very important to determine Se concentrations is soils and plants. Excess levels of Se in organism can causing three way of toxicity mechanisms [9]. Selenium toxicity can be described as a epidemiological (prostate cancer, cardiovascular disease or diabetes), cytotoxicological (inhibited cell growth and proliferation) and genotoxicological (breaking DNA structure, impair genomic stability). The LD_{50} for sodium selenite in rats by oral exposition was estimated as a 12.7 mg/kg in body weight. Due to very low Se concentration in biological samples Very sensitive measurement approach is required (in practice - most samples requires extremely low detection limits, which can be achieved only by ICP-MS or NAA). The great advantage of NAA (especially Instrumental Neutron Activation Analysis - INAA) is that it is non-destructive, multielemental analytical technique. NAA is based on conversion of stable atomic nuclei to radioactive isotope, by capturing neutron [10]. After neutron capture, atomic nuclei is emitting prompt gamma rays and undergo radioactive decay (for example β- decay). During radioactive decay, nuclei is emitting delayed gamma rays. The gamma ray spectrum is quantitative and qualitative information about measured sample. Neutron source for the REGATA facility is IBR-2M reactor. REGATA facility has two irradiations channels. One of them is cadmium screened to cut off thermal neutrons. The other channel has a full neutrons energy spectrum.

Materials and methods

Samples collecting and preparation

Investigated samples of *Vicia faba*, *Phaseolus coccineus*, *Pisum sativum*, *Phaseolus vulgaris* and *Vaccinum corymbosum* were collected in the south of Poland, near Nowy Scz city. Samples were transported to Sector of Neutron Activation Analysis and Applied Research of FLNP JINR and were prepared to irradiation. First, samples were dried. After drying, samples were homogenized using ball mill (Fig. 1a). After homogenization, about 300 mg of each sample was compressed to form a pill (Fig. 1b). The pills were packed into plastic bags and polyethylene vials (for short irradiation) or in aluminium foil (Fig. 1 c) and aluminium containers (for long irradiation).

Figure 1: Sample preparation.

Irradiation and measurements

Prepared samples were transported to the irradiation channels using pneumatic transport system. After irradiation, gamma ray spectra were measured using high purity germanium detectors (HPGe) and Genie 2k software. Nuclides identification and activities calculations were performed using isotopes libraries (for long or short irradiation). Final elements concentrations were calculated using dedicated software developed in laboratory. For selenium, long lived isotope ^{75}Se ($T_{1/2} = 120$d) was measured by gamma ray line 265 keV. Measurements of short lived ^{77m}Se by Cyclic NAA were not successful due to time fixations problem.

Results and discussion

Obtained results are showed in Table 1. Se concentrations in dry mass of samples are in the range from 0.10 ± 0.02 to 0.22 ± 0.03 mg/kg. Thus, investigated plants can be calssified as a selenium "non-accumulators" (plants accumulating Se less than 25 mg/kg dry weight) [3]. Strong correlation between selenium and arsenic (As) in investigated samples was observed

Table 1: Se concentrations in dry mass of samples.

SAMPLE	Se content [mg/kg]
Vicia faba	0.222 ± 0.028
Phaseolus coccineus	0.102 ± 0.018
Pisum sativum	0.209 ± 0.022
Vaccinum corymbosum	0.167 ± 0.018
Phaseolus vulgaris	0.150 ± 0.023

(fig. 2). Presence of As in soil can be toxic for the plant, by producing oxygen-based radicals in cells. Selenium can reduce oxidative stress caused by arsenic by elevating levels of enzymatic antioxidants like a superoxide dismutase (SOD) or catalase (CAT) [11, 12].
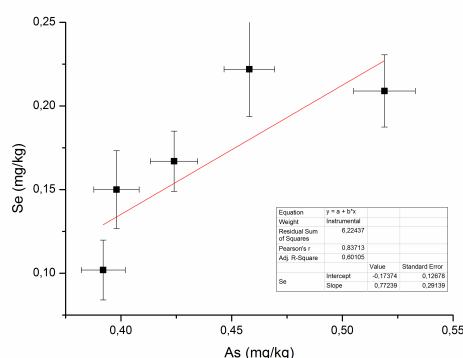
Figure 2: Se-As correlation graph.

Obtained result showed, that INAA is very good technique for determination trace amounts of selenium. But CNAA has a few more advantages. In CNAA the analyti-

cal time is shorter (short irradiations - seconds), detection limits are lower and number of potential spectral interferences than in INAA [13, 14].

Acknowledgements

References

[1] Sherwood Lollar B. *Environmental geochemistry* pp. 46, (2005).

[2] Piotrowska M., Rocz. Glebozn, **36**, 147-149 (1984).

[3] Sierpawska A., Korna A., Filek M., Acta Biologica Cracoviensis, **57**, 9 (2015).

[4] Mills G. C., J. Biol. Chem. **229**, 189, (1959).

[5] Bhabak K. P. , Mugesh G., Acc. Chem. Res., **43**, 1408 (2010).

[6] Sagar G. D., *et al.* Molecular Endocrinology **22** (2008).

[7] Curcio-Morelli C., Gereben B., Zavacki A.M.. Endocrinology, **144**, 937 (2003).

[8] Lillig C. H., Holmgren A., Antioxidants & Redox Signaling, **9**, 25 (2007).

[9] Sun H. J., Rathinasabapathi B., Wu B., Luo J., Pu L. P., Ma L. Q. Environment International, **69**, 148 (2014).

[10] Frontasyeva M. V. Rev. Phys. Part. Nucl. **42**, 332-378 (2011).

[11] Flora S. J., Free radical biology and medicine, **51**, 257-281 (2011).

[12] Malik J. A., Goel S., Kaur N., Sharma S., Singh I., Nayyar H . Env. Exp. Bot., **77**, 242-248, (2012).

[13] Hou X. *Cyclic Activation Analysis*, Encyclopedia of Analytical chemistry (2000).

[14] Zhang H., Chai Z. F., Qing W. Y., Chen H. C., J. Rad. Nucl. Chem., **281**, 23-26 (2009).

GAMMA RADIATION DOSE ASSESSMENT IN YEMENI BUILDINGS

M. M. Sherif, M. Orabi, Safa Y. Abdo

Physics Department, Faculty of Science, Cairo University, Giza 12613, Egypt

Annotation

The indoor gamma radiation dose rates inside Yemeni buildings are estimated using a theoretical model. This model is a development of a previous work, with some of its parameters are being obtained by the MCNP simulation software. It has the advantage that it can be applied on any shape of rooms, with any size, any design, and most importantly with any type of building materials. The obtained results are compared with other studies and other countries. The estimated annual doses from the concrete types are higher than that in developed countries. The granite stone and cement brick annual doses are almost three times higher than those of concrete. Some of the samples are found to give radiation doses that may exceed the dose limit.

Introduction

With the fact that the number of recorded cancer cases due to indoor gamma exposure is not small in some countries, it is important to study and investigate the radioactivity concentrations in the building materials. This should not be taken lightly, since we are exposed to that kind of radiation almost all the time; at home, at office, at shops, etc. It is therefore necessary to study a variety of building materials that are used in different places, with different structures. This cannot be done unless we have a model that can be applied easily on any type of building materials. That model has to be also precise, convenient, and not time consuming. In this research article we propose a developed model that can cope with those challenges. The present model is a modification of a previous work [1–3], with some of the key parameters are being obtained by using the MCNP simulation code (Monte Carlo N-Particle) [4]. The usual difficulty of getting the models parameters was a strong hold back in applying the model extensively on different building materials. This is because the building materials are usually made of a mixture of different elements, and no reference data give their parameters. With simulating the values of those parameters, it is now very easy to get them. All what needed is to know the elemental structure of the material. Once this is provided, the simulation code will work smoothly and give you all the required parameters at any gamma energy. Then these parameters can be used to continue all the calculations in the model. In the following section we briefly mention the main experimental procedures. Section 3 gives an overview of the model. The results are in section 4, where we show the model's application on Yemeni buildings, calculating their indoor exposure rates, and comparing them with other studies and other countries. A conclusion is presented in the last section.

Methods

The applied samples are mostly collected from the two major Yemeni cities Taiz and Hodeida. After collection they are saved in plastic bags, and then crushed by a hammer, and sieved by a 0.8 mm mesh sieve. Each sample is weighed and stored in a sealed beaker

for more than four weeks to reach the secular equilibrium between the parent nuclides and their decay products. Using the High Purity Germanium (HPGe) detector to measure the activity concentrations of the samples, we find that the concentrations range between (0.21 ± 0.16 - 180.95±6.92), (0.29±0.17 - 252.85±3.94) and (2.48±0.96 - 1701.34±59.57) Bq/Kg for ^{226}Ra, ^{232}Th and ^{40}K, respectively. The highest concentrations are in the cement and granite samples.

Overview of the Theoretical Model

The indoor gamma exposure dose rate at a point in a room can be calculated by [1–3][1, 4, 10]

$$x = \frac{kC\rho}{4\pi} \sum_i E_i N(E_i) \mu_a(E_i) \int \frac{B(E_i, s)}{l^2} e^{-d(E_i)} dV, \tag{1}$$

where x is the exposure dose rate, ρ is the density of the material, C is the activity per unit mass, k= 1.462×10^{-5} R.MeV^{-1}.cm^3 is the coefficient to change the exposure into Roentgen unit, E_i is the photon energy, $N(E_i)$ is the number of photons with energy E_i emitted per unit primary disintegration, $\mu_a(E_i)$ is the linear absorption coefficient in air, s is the distance the photon travels in the material, l is the distance from the source point, $B(E_i, s)$ is the dose build-up factor, V is the volume of the material, and $d(E_i)$ is

$$d(E_i) = \mu_m(E_i).s, \tag{2}$$

where $\mu_m(E_i)$ is the linear absorption coefficient in the material. The build-up factor is calculated using the Berger's formula [3]

$$B(E_i, s) = 1 + a.d(E_i).exp(b.d(E_i)) \tag{3}$$

where the two parameters a and b depend on the energy. The μ_m values are calculated by the MCNP simulation code [4]. This is very useful since in many cases, for different materials and different gamma energies, the μ_m data are not available, especially for un-traditional manufactured composite materials. Even for the air, is not known for many gamma energies. Here we simulate the μ_m values for concrete, granite and cement, for which the chemical compositions are shown in Table 1. The μ_m values are calculated by applying the gamma absorption law in the simulated configuration, at different gamma energies. A target of thickness x is designed with uniform shape and homogeneous density, and then a collimated beam of gamma rays with certain energy radiates that target. The gamma energies of interest are shown in Table 2, together with their probabilities $N(E_i)$. The target is made of the required material for which the linear attenuation coefficient is to be calculated. If the incident flux is denoted by $\oslash_0$ and the flux after crossing the target by $\oslash$, then according to the gamma absorption law

$$\oslash = \oslash_0 e^{(-\mu x)}, \tag{4}$$

the linear gamma-attenuation coefficient can be calculated for the target's material, at the given energy. We tested this method first by reproducing some of the known values, and they were successfully and precisely reproduced. We then applied it on concrete, granite stone, and cement brick, at the required gamma energies. Some of the obtained μ_m values, at some of the energies, are shown in Table 3. Those for air are given in Table 2.

Table 1: Chemical composition (%) of ordinary concrete, granite stone and cement brick.

Concrete		Granite stone		Cement brick			
H	1	SiO_2	72.04	SiO_2	59.71	MnO	0.12
O	53.4	Al_2O_3	14.42	Al_2O_3	9.58	Cl	3.18
Mg	0.2	K_2O	4.12	Fe_2O_3	4.30	L.O.I	8.93
Ca	4.45	Na_2O	3.69	CaO	6.630	P_2O_5	0.18
Si	34.4	CaO	1.82	MgO	0.92		
Na	1.7	FeO	1.68	SO_3	0.41		
K	1.3	Fe_2O_3	1.22	Na_2O	2.04		
Al	3.45	MgO	0.71	K_2O	3.65		
C	0.1	TiO_2	0.30	TiO_2	0.35		

Table 2: The energy lines (daughters of ^{238}U, ^{232}Th and ^{40}K) with their probabilities and the corresponding air attenuation coefficients.

Nuclide	E (MeV)	N ($\times 10^{-2}$)	μ_a ($\times 10^{-5}$) (cm^{-1})	Nuclide	E (MeV)	N ($\times 10^{-2}$)	μ_a ($\times 10^{-5}$) (cm^{-1})
^{238}U	0.047	4.0	6.84	^{232}Th	0.038	1.3	9.32
	0.063	3.8	5.68		0.098	2.1	2.92
	.092	7 2.7	3.97		0.120	3.0	3.17
	0.186	3.2	3.39		0.209	4.4	3.48
	0.241	8.2	3.59		0.238	44.6	3.57
	0.295	19.2	3.70		0.277	6.8	3.65
	0.351	35.2	3.78		0.301	3.4	3.70
	0.468	2.0	3.84		0.338	11.4	3.80
	0.609	46.3	3.32		0.509	8.3	3.79
	0.771	7.9	3.73		0.583	84.2	3.82
	0.808	2.2	3.72		0.74	6.9	3.75
	1.12	15.1	3.53		0.779	9.2	3.72
	1.388	9.3	3.41		0.86	12.5	3.69
	1.498	3.1	3.28		0.911	27.7	3.66
	1.650	1.8	3.20		0.967	16.9	3.65
	1.76	15.8	3.17		1.59	6.0	3.27
	1.85	3.1	3.12		1.64	4.4	3.26
	2.121	1.3	3.02		2.623	36.1	2.92
	2.196	5.8	3.04				
	2.44	2.5	2.93	^{40}K	1.464	10.7	3.34

Results and Discussion

As mentioned above, the obtained simulated values for the μ_m parameters at some of the energies are shown in Table 3. The computer run time in obtaining those values is not large, and the relative errors in the outputs from the simulation code are less than 0.1%. It does take a bit of time to describe the modeled geometry in the simulation input file,

and to define the materials' structures, and also to test the code and make sure it's free of any kind of inaccuracy, but after all, that consumed time is way much less than the time taken to search for those parameters, which even if they could be found, they wouldn't be necessarily given at the required energies. The specific exposure dose rate Q is obtained by dividing the exposure rate by the activity concentration C, and hence, according to Eq. (1), is given by

$$Q = \frac{X}{C} = \frac{(k\rho)}{4\pi} \sum_i E_i N(E_i) \mu_a(E_i) \int \frac{B(E_i, s)}{l^2} e^{(-d(E_i))} dV. \qquad (5)$$

To calculate the gamma-flux, at any point in the room, resulting from a volume source (inside the wall for example), the gamma radiation source is supposed as a point Q inside the wall, as shown in Fig.1, and then the contribution from all point sources to the total flux is calculated by the integral form of Eq. (5). That integration is carried out numerically. The geometry used is shown in Fig. 1, where the detection point P is taken to be at the centre of the room. Some of the parameters needed to calculate equation (5) are given in Tables 2 and 3.

Table 3: Attenuation coefficients $\mu_m(cm^{-1})$ for concrete, granite and cement.

E (Mev)	Concrete	Granite	Cement	E (Mev)	Concrete	Granite	Cement
0.063	0.371	0.582	0.081	0.351	0.239	0.317	0.153
0.092	0.279	0.35	0.071	0.583	0.183	0.233	0.067
0.186	0.227	0.257	0.078	0.609	0.188	0.251	0.123
0.209	0.195	0.261	0.128	0.86	0.159	0.196	0.097
0.238	0.222	0.285	0.120	0.911	0.165	0.212	0.117
0.277	0.215	0.280	0.075	0.968	0.166	0.210	0.114
0.295	0.219	0.273	0.123	1.12	0.164	0.171	0.085
0.3	0.238	0.288	0.158	1.464	0.14	0.169	0.087
0.338	0.205	0.260	0.107	1.76	0.142	0.162	0.088
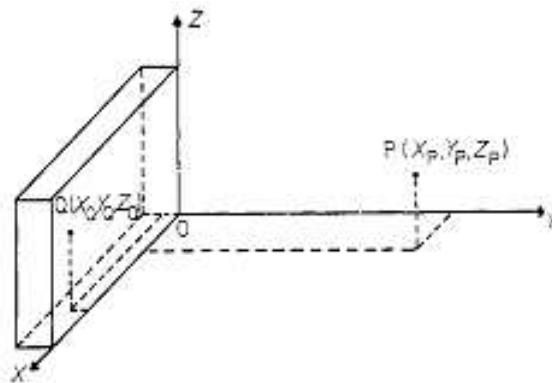
Figure 1: Geometry of calculating the exposure dose rate from a wall.

The specific γ-exposure dose rates due to the radionuclides ^{226}Ra, ^{232}Th and ^{40}K are calculated in the center of rooms constructed from different types of building materials

that are commonly used in Yemen. Many of the previous works that calculated exposure rates applied their models on rooms with dimensions 5×4×2.8 m³ and wall thickness 20 cm, and therefore, in this paper, we do our calculations with similar dimensions, so that we can compare with them. Table 4 shows our results of estimating the specific exposure rate in the center of a room built with concrete, in comparison with some previous studies. It can be noticed in Table 4 that the results here are very close to other studies. This indicates how accurate the model is and how reliable. The granite stone and cement brick results are shown in Table 5, with the same dimensions as used in Table 4. The cement's results are a little bit different from concrete and granite due to its small density compared to them.

Table 4: Specific exposure rates in the centre of rooms built of ordinary concrete.

Reference	Dimensions of the room	Thickness (t) of walls (cm)	Density (g/cm³)	Specific exposure rate (μR/h)/(Bq/Kg) ($\times 10^{-2}$)		
				^{226}Ra	^{232}Th	^{40}K
[5]	5×4×2.8 m³	20	2.35	10.6	11.7	0.895
[2]	5×4×2.8 m³	20	2.35	10.5	12.7	0.892
[6]	5×4×2.8 m³	20	2.35	10.6	12.6	0.927
[7]	6×4×3 m³	20	2.32	10.3	6.9	0.570
This work	5×4×2.8 m³	20	2.35	10.8	12.6	0.933

Table 5: Specific exposure rates in the centre of a 5×4×2.8 m³ room, t=20cm, built of granite or cement.

Material used	Specific exposure rate (μR/h)/(Bq/Kg) ($\times 10^{-2}$)		
	^{226}Ra	^{232}Th	^{40}K
Granite (density = 2.75 g/cm³)	10.7	12.1	0.894
Cement (density = 1.5 g/cm³)	9.4	10.9	0.738

Since concrete is the most commonly used material for constructions in Yemen, it is given more focus by considering its different types in Hodeida and Taiz. There are six types in Hodeida which we label (1), (2), (3), (4), (5) and (6), and two types in Taiz which we label (a) and (b). Details about those types, including their densities and radioactivity concentrations are in ref [3]. The calculated annual effective doses for those concrete types are shown in Table 6. They range between 326.20 and 391.68 Sv/y. Even the lowest of this range is a bit high compared to [8] (309 μSv/γ). The average of that range (360 μSv/γ) is smaller than countries like Jordan (470 μSv/γ) [5], Nigeria (400 μSv/γ) [7], and Cuba (429 μSv/γ) [9]. On the other hand, the annual effective doses calculated for granite and cement as 1184.31 μSv/γ and 1068.93 μSv/γ, respectively, are almost three times higher than the average of the different concrete types.

Table 6: Annual effective doses (μSv/γ) for different types of concrete.

City	Concrete type	Walls	Ceiling and floor	Whole room
Hodeida	(1)	223.05	132.18	355.23
	(2)	245.94	145.74	391.68
	(3)	237.02	140.45	377.47
	(4)	213.83	126.72	340.55
	(5)	236.72	140.28	377.00
	(6)	227.79	134.99	362.78
Taiz	(a)	205.46	121.75	327.21
	(b)	204.83	121.37	326.20

Conclusion

By applying the above explained developed calculation model, it is proved to be efficient, convenient, precise, and time saving. The save of the time is not only with the short run time, but for saving a lot of time and effort trying to search for those parameters in some literature. Upon applying the model on rooms constructed with Yemeni commonly used building materials, and comparing the obtained results with some other countries, it is found that the annual effective doses from the studied concrete types are high compared to developed countries. This indicates that a more elaborated study has to be made for those building material types. Moreover, the annual effective doses from granite and cement are almost three times higher than those of concrete. This means that people in Yemen using granite or cement for constructions should be very careful, because this could cause bad accumulated effects on population's health.

References

[1] Stranden E. Phys. Med. Biol. **24**, 921-930 (1979).

[2] Mustonen R., Radiat. Prot. Dosim. **7**, 235-238 (1984).

[3] Safa Y. Abdo. *Activity concentrations of some building materials in Yemen and simulation of indoor gamma dose rate.* MSc thesis; 2011.

[4] MCNP X-5 Monte Carlo Team. *A General Monte Carlo N-Particle Transport Code.* Version 5:24 April; 2003. Revised 10 March 2005.

[5] Ahmad N., Hussein A. J. A., Aslam., J. Environ. Radioact. **41**, 127-136 (1998).

[6] Ackers J. G., Bosnjakovic B. F. M., Strackee L., Radiat. Prot. Dosim. **7**,413-416 (1984).

[7] Ademola J. A., Farai I. P.. Radiat. Prot. Dosim. **114**, No. 4, 524-526, (2005).

[8] Ettenhuber E., Lehmann R., Health Phys. **50**, 49-56 (1986).

[9] Brgido O. F., Montalván A. E., Rosa R. S., Tomás J Z, Hernández A. P. Journal of Environmental Radioactivity. **99**, 1834-1837 (2008).

[10] Koblinger L., Health Phys. **34**, 459-463 (1978).

RADIOACTIVE AND ELEMENTAL ANALYSIS FOR SOME EYE COSMETICS

M. M. Sherif, M. Orabi, O. R. Abdurahem
Department of Physics, Faculty of science, Cairo University, Giza 12613, Egypt

Abstract

Some types of kohl and other types of eye-cosmetics are investigated concerning their radioactivity and heavy elements concentrations. The radioactivity concentrations are measured by the High Purity Germanium detector (HPGe) investigating the radionuclides ^{238}U, ^{235}U, ^{226}Ra, ^{232}Th, and ^{40}K. The annual radiation dose to the lens of the eye as a result of using kohl is simulated. The simulation model is executed by using the MCNP software. The heavy elements concentrations are measured by the Inductively Coupled Plasma-Optical Emission Spectrometer (ICP-OES) investigating the most toxic elements As, Cd, Hg, and Pb. The annual absorbed amounts of those heavy elements due to daily application of the kohl types are calculated.

Introduction

The study of people's safety from using cosmetics is an important subject since many people all over the world use cosmetics, sometimes on a daily basis. There are different types of cosmetics that are used on different parts of the body. The current study concerns about cosmetics that are used for the eyes and all parts around like eyelash, eyelid, eyebrow, etc. The type of safety we study here is the cosmetics- concentrations of radioactivity and heavy elements. We investigate those concentrations and their possible impact on human's health in some kohl types and other types of eye-cosmetic that are commonly used in Arabic countries.

Kohl is famously related to the Arabic region. It is very commonly used by the Arabic people as a kind of tradition and heritage. Sometimes they deliberately place it inside their eyes, on the conjunctive surface, because of the Arabs' thoughts about kohl that it widens eyes, purifies it from dust and impurities, and protects it from hot sunshine. Kohl is usually sold in Arabic markets in the form of powders and stones (Fig. 1). High concentrations of heavy elements could harm human health. After the intake of those elements, they could accumulate in the internal parts and organs of the body such as bones, livers, kidneys, pancreas, lungs, and so on, and hence might cause damage over time. The most toxic elements are As, Cd, Hg, and Pb [1]. The allowable level of lead in cosmetics is 10 ppm as given in the Canadian health ref. [1], and 20 ppm as given in the US-FDA ref. [2]. On the other hand, the allowable levels of As, Cd, and Hg are 3 ppm in Canadian health [1], and 5 ppm, 5 ppm and 1 ppm, respectively in US-FDA [2]. As for radiation, its effect on the eye is in particular by causing a cataract, which might happen if the radiation dose exceeds 15 mSv [3].
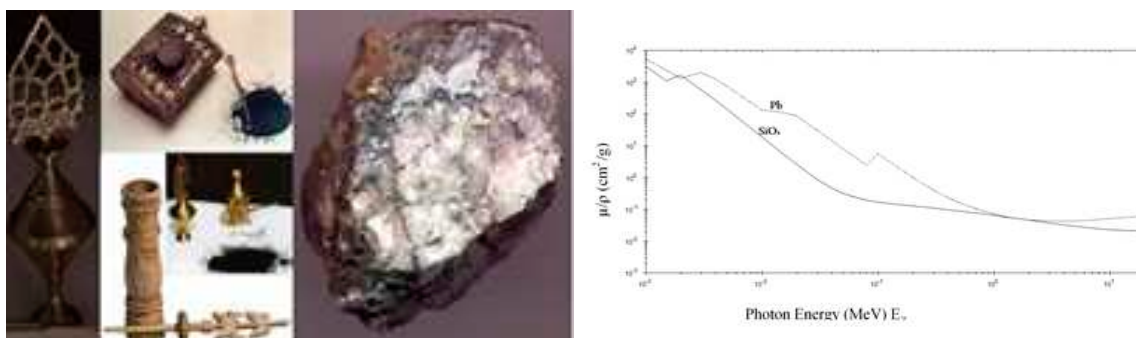
Figure 1: Left panel: Powder and stone kohl. Right panel: mass attenuation coefficient of SiO$_2$ and Pb as a function E$_\gamma$

Experimental work

Samples Collection

The samples are purchased from various markets in different Arabic countries. The samples include varieties like eyeliner, mascara, eye-shadow, powder kohl and stony kohl.

Elemental Measurements

Sample digestion: A 0.15 gm of each sample, 7 ml high purity HNO$_3$ and 2 ml high purity HF are added to a microwave vessel and the mixture is heated up to 130°C for more than 15 minutes. The mixture is then held at 130°C for three minutes before the temperature is ramped up to 200°C for more than 15 minutes and held at 200°C for 30 minutes. After that, 30 ml of 4% high purity H$_3$BO$_3$ is added to the vessel to neutralize the HF, and then the mixture is heated again in the microwave up to 170°C over 15 minutes and held for 10 minutes at 170°C. The mixture is then diluted to 50 ml using a distilled H$_2$O. The samples are analyzed using the Thermo Scientific ICap 7000 series ICP-OES spectrometer in Laboratories Compound of Desert Research Center of Egyptian Ministry of Agriculture and Land Reclamation.

Radioactivity Measurements

Radioactivity measurements are applied only on samples of kohl stones due to the lack of the suitable standards for the other samples. Using standard sample is necessary to make the efficiency calibration for the HPGe detector.

Sample preparation

Kohl stone is crushed and collected through a 0.85 mm mesh sieve. The sample is then placed in an oven at   90°C until constant weight is achieved. Due to the high density of kohl samples (4gm/cm^3) we use a pure silica powder (SiO$_2$, 2.46 g/cm^3 density) to make the samples of densities comparable to the density of the reference material. Silica has an appropriate mass attenuation coefficient for gamma rays as shown in Fig. 1, right panel. Values of the mass attenuation coefficient (μ/ρ) of SiO$_2$ are obtained according to the

simple sum [4] $\mu/\rho = \sum_i w_i(\mu/rho)_i$, where w_i is the fraction by weight of the ith atomic constituent, and the $(\mu/\rho)_i$ values are obtained from Ref. [4]. In order to check that the use of silica does not affect the rate of self-absorption of the emitted gamma-rays, we use two masses of kohl samples (90 and 180 gm), and then we add the appropriate amount of silica for each mass to fill 240 ml beakers. Silica and kohl are mixed well to get a homogenous sample. Then, the appropriate amounts of samples are put in 240 ml sealed plastic beakers for more than 28 days to reach the secular equilibrium between ^{226}Ra and its short lived products. More about the two masses (90& 180) is given shortly below, in the discussion section. The radioactivity concentrations are measured by using the HPGe detector in the Egyptian Nuclear Authority. The same geometry and size are used for both measured and reference material samples. The measurements are collected for 20 to 24 hours [5].

Results and Discussion

Elemental Analysis

The mean values of heavy elements concentrations are shown in Table 1. According to this table the heavy elements concentrations in the eyeliner and mascara samples are lower than the allowable levels except As which has higher values (3.38 and 3.62 ppm, respectively) than the allowable level (3 ppm) [1]. The concentrations of As, Cd and Hg in the eye-shadow and powdered kohl samples are lower than the allowable levels, while the concentrations of Pb are higher than the allowable levels. However, those concentrations of Pb are so low compared to those in kohl stone samples which have concentrations of the four elements higher than the allowable levels. Al-Ashban et al. [6] shows that the lead concentrations in the imported samples available in KSA range between 40 and 530000 ppm. That reference also, with other earlier studies [7, 8], illustrate the increase of lead level in blood and the reduction of hemoglobin for individuals who use kohl as compared to those who do not. Another study [9] indicates the high level of lead in eye's lenses with cataract in comparison with clear lenses. Al-Ashban et al. [6] provides information to indicate that the Kohl used previously in the Arabic and Islamic history is quite different from the current circulated kohl in the Arabic markets. That reference provides a considerable evidence to support a suggestion that earlier kohl types mainly contained antimony sulphide, which when became scarce, was replaced by lead sulphide and lead oxide.

Many of the Arabia women use kohl at a rate of one to two times a day, with approximately 2 gm each time. Since we cannot estimate the exact amount absorbed into the body from the used kohl, by ingestion or through the tear duct, we can roughly assume that about 50 % of the applied kohl is absorbed into the body and then calculate the amount of As, Cd, Hg, and Pb absorbed per year. Assuming that kohl is used once a day, the obtained results are shown in Table 2. According to this table the values of maximum annual absorbed amounts of As, Cd, and Hg are 38.73, 14.55, and 55.68 mg, respectively. On the other hand the maximum value for Pb is much larger than those for As, Cd, and Hg. That is 273145.76 mg/yr, and so Pb is a main reason to classify kohl as a toxic material [10]. The US-FDA [2] warns not to use the present types of kohl as a color additive to any of the products, and does not allow the entry of these products to the USA because of kohl's contamination with lead. There is no any regulation permitting its use in cosmetics

or any other FDA-regulated products [10].

Table 1: Heavy elements' concentrations (ppm) in kohl and the other eye-cosmetics.

Sample name	Sample code	Country of origin	As	Cd	Hg	Pb
Eye liner	SEL18	unknown	3.38±0.89	<0.0003	Nil	5.33±1.74
Mascara	SMM14	UK	3.62±2.72	<0.0003	0.09±0.05	3.37±1.67
Eye shadow	SESR9.1	China	<0.008	<0.0003	Nil	35.18±1.20
	SESY9.3	China	<0.008	<0.0003	0.04±0.02	13912.47±0.33
	SEB31	unknown	<0.008	<0.0003	0.12±0.06	29.12±1.91
Kohl powder	SKA17	India	<0.008	<0.0003	0.08±0.01	2771.38±0.34
Kohl stone	SKK20	KSA	6.23±1.02	8.00±0.27	Nil	50666.67±0.71
	SKP22	Pakistan	13.55±0.55	39.87±0.34	0.02±0.01	547896.44±1.08
	SKI23	India	4.54±1.51	19.25±0.03	Nil	564369.31±0.38
	SKK24	KSA	11.23±1.05	7.56±0.25	0.06±0.02	527565.89±1.06
	SKA1	KSA	7.1±2.8	7.86±0.53	68.85±0.11	707033.84±1.05
	SKR2	KSA	106.12±0.48	6.39±0.04	67.9±0.12	669993.35±0.66
	SKL3	Iran	4.5±2.62	15.6±0.07	152.55±0.01	748344.54±1.40

Table 2: Annual absorption of the heavy elements from the kohl types and eyeliner.

Sample Code	The amount (mg) of heavy elements absorbed annually			
	As	Cd	Hg	Pb
SEL18	1.23	Nil	Nil	1.95
SKA17	Nil	Nil	0.03	1011.55
SKK20	2.27	2.92	Nil	18493.33
SKP22	4.95	14.55	0.01	199982.20
SKI23	1.66	7.03	Nil	205994.80
SKK24	4.10	2.76	0.02	192561.55
SKA1	2.59	2.87	25.13	258067.35
SKR2	38.73	2.33	24.78	244547.57
SKL3	1.64	5.69	55.68	273145.76

Radioactivity Analysis

The radioactivity concentrations of the natural radionuclides ^{238}U, ^{235}U, ^{226}Ra, ^{232}Th, and ^{40}K in kohl stones are measured, and their risk is assessed. The radiation dose on the eye is estimated by a simulation model using the MCNP software [12]. This is explained in detail in the next subsection. The IAEA Safety Guide RS-G-1.7 [11] suggests that radiation protection control is not necessary if the radioactivity concentration of naturally occurring radionuclides in a material is below the IAEA criteria (10 Bq/Kg for ^{40}K and 1 Bq/Kg for all other natural radionuclides).

The mean values of the measured activity concentrations in kohl stone samples are listed in Table 3. According to this table, the radioactivity concentrations of ^{235}U, ^{232}Th, and ^{40}K in kohl samples are lower than the IAEA critical values, while the activity concentrations of ^{238}U and ^{226}Ra are higher than the critical values [11]. It is known that the activity concentration is independent on the mass of the sample, but during our measurements of the activity concentrations, we notice that the number of counts per second (which is directly proportional to the activity concentration) in the 90 gm kohl sample is larger than its value in the 180 gm sample of the same kohl type. This is due to the high concentration of Pb in kohl (see Table 1), which means that the amount of Pb in the 180 gm kohl sample is larger than that in the 90 gm kohl sample. The large amount of Pb increases the rate of self-absorption of the gamma rays by the sample itself before they reach the detector and be counted. Figures 2, left panel and right panel show the activity concentrations in the 90 gm and 180 gm masses of the SKA1 and SKR2 samples, respectively.
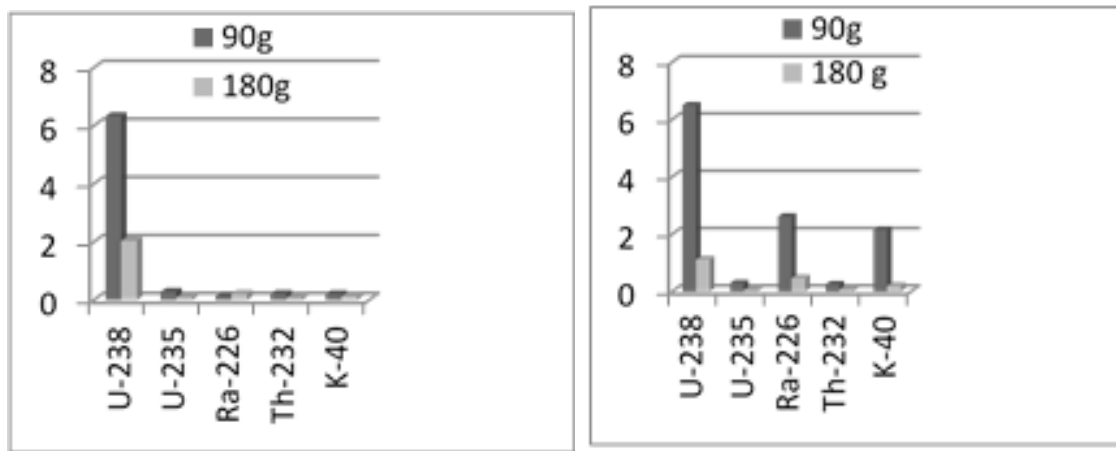
Figure 2: Left panel: Activity concentrations of the radionuclides in the kohl sample SKA1, for the two different masses 90 gm and 180 gm. Right panel: Activity concentrations of the radionuclides in the kohl sample SKR2, for the two different masses 90 gm and 180 gm.

Simulation

From the previous sections we see that the radioactivity concentrations for the natural radionuclides in the kohl samples are low, which can give an indication that the radiation dose on the eye is small. However, in some Arabic areas many women use kohl two or three times a day, and we think that may lead to an appreciable annual dose on the eye. Therefore in this section we develop a simple simulation model, using the MCNP code [12], to estimate the gamma radiation annual dose on the eye's lens. In our simple model we depict the eye as a sphere with radius 1.25 cm, with the medium inside having the structure of the eye [13]. We then put the radioactive source on the surface of the sphere and calculate the gamma flux through the surface of the lens of the eye. This surface is the intersection of a plane with the sphere as shown in Fig.3. We do these calculations for the natural radionuclides ^{238}U, ^{235}U, ^{226}Ra, ^{232}Th, and ^{40}K, for the seven kohl stone samples. The obtained results are shown in Table 4 in units of μSv/yr. The last column in that table gives the total of all nuclei. The relative errors in all the obtained numbers are very small

(¡ 0.1%). As shown in Table 4 the dose rates are small in spite of assuming a frequent use of the kohl. From that table we can also notice that the largest contribution is from ^{40}K and then from ^{238}U.
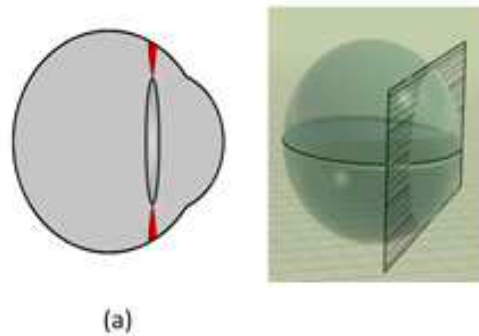
Figure 3: The eye lens geometry; a) the real one, and b) as assumed in the MCNP simulation code.

To convert the calculated particle flux, in the simulation code, to human biological dose equivalent rate, we use the ANSI/ANS-6.1.1-1977 conversion factors (American National Standards Institute, and American Nuclear Society) [13]. This gives the results shown in Table 4. However, it's known that the conversion factor sets are subject to changes based on the actions of various national and international organizations due to the reevaluation of existing data and calculations or the availability of new information, and so, for comparison, we use another set of conversion factors, the ICRP-21 (International Commission on Radiological Protection) [13]. Applying them on the kohl sample SKL3, we get the results shown in the last line in Table 4 (SKL3(I)), with no significant differences from ANSI/ANS.

Table 3: Radioactivity concentrations in kohl stone samples (Bq/kg).

Sample code	^{238}U	^{235}U	^{226}Ra	^{232}Th	^{40}K
SKK20	6.87±1.35	0.29±0.03	1.31±0.04	0.28±0.03	4.35±0.18
SKP22	3.87±0.60	0.14±0.02	1.34±0.04	0.06±0.01	3.35±0.12
SKI23	2.49±0.39	0.11±0.02	0.16±0.01	0.60±0.07	0.85±0.04
SKK24	4.12±0.59	0.20±0.02	1.01±0.03	0.31±0.02	3.18±0.13
SKA1	6.33±0.27	0.28±0.03	0.13±0.01	0.21±0.02	0.20±0.01
SKR2	6.49±1.05	0.29±0.08	2.61±0.05	0.25±0.03	2.15±0.10
SKL3	1.09±0.14	0.05±0.01	0.28±0.01	0.16±0.01	0.45±0.02

Conclusion

After analyzing kohl samples and other eye-cosmetics we find that some of them are not really safe to use. Some eye-shadows contain concentrations of Pb that are higher than the allowable levels. The radioactivity concentrations in kohl samples are low, and so they don't have radiation risk on the eye, as demonstrated by the simulation model. However,

Table 4: Simulated annual γ-radiation doses (μSv/yr) of the eyes lens from natural radionuclides in kohl.

Sample code	238U	235U	226Ra	232Th	40K	Total
SKK20	0.064	0.002	0.024	0.011	0.197	0.298
SKP22	0.036	0.001	0.024	0.002	0.152	0.215
SKI23	0.023	0.001	0.003	0.024	0.039	0.090
SKK24	0.038	0.002	0.018	0.012	0.144	0.214
SKA1	0.059	0.002	0.002	0.008	0.009	0.080
SKR2	0.060	0.002	0.048	0.010	0.097	0.217
SKL3	0.010	0.007	0.0004	0.0003	0.005	0.004
SKL3(I)	0.006	0.006	0.020	0.019	0.041	0.036

those kohl types are contaminated with significant concentrations of the heavy elements As, Cd, Hg, and Pb. Depending on our assumption that 50% of the applied amount of kohl is absorbed, the maximum values of the annually absorbed amount of As, Cd, Hg, and Pb from daily applied kohl (2 gm a day) are 38.73, 14.55, 55.68, and 273145.76 mg, respectively. This means that appreciable amounts of those elements could be absorbed into the body, through skin or drop down to the mouth from the eyes. Finally those elements could move through blood, spread into different organs, where they accumulate and cause damage to those organs. It is worth to mention that many of the Arabia women prefer to use kohl more than eyeliner to decorate their eyes because of cultural heritage, but according to our results here, we see that it's safer for them to use eyeliner because the heavy elements concentrations in the eyeliner are lower than the allowable levels.

References

[1] Health Canada, consumer product safety, Guidance on Heavy Metal Impurities in Cosmetics

[2] U.S. Food and Drug Administration, Color Additives Approved for Use in Cosmetics (http://www.fda.gov/ForIndustry/ColorAdditives/ColorAdditiveInventories/ucm115641.htmtable3A).

[3] International Commission on Radiological Protection (ICRP), 1991. 1990 Recommendations of the International Commission on Radiological Protection. ICRP Publication 60. Ann. ICRP 21 (1-3).

[4] J. H. Hubbell+ and S. M. Seltzer, (1989,1990,1996).Tables of X-Ray Mass Attenuation Coefficients and Mass Energy-Absorption Coefficients from 1 keV to 20 MeV for Elements Z = 1 to 92 and 48 Additional Substances of Dosimetric Interest. U.S. Secretary of Commerce on behalf of the United States of America. http://www.nist.gov/pml/data/xraycoef/index.cfm

[5] Turhan, S. and Gndz, L., (2008), Determination of specific activity of 226Ra, 232Th and 40K for assessment of radiation hazards from Turkish pumice samples, J. Environ. Radioact.99:332-342.

[6] R.M. Al-Ashban, M. Aslam, A.H. Shah. (2004),Kohl (surma): toxic traditional eye cosmetic study in KSA (Public Health118, (292-298).

[7] Aslam M, Healy MA, Davis SS, Ali AR. Surma and blood lead in children. Lancet 1980; 1 (658-9).

[8] Warley MW, Blackledge P, OGorman P. Lead poisoning fromeye cosmetic. BMJ 1968; 13(1)(117).

[9] Nandita Shukla, J.K. Moitra, R.C, 1996. Trivedi. Determination of lead, zinc, potassium, calcium, copper and sodium in human cataract lenses (The Science of the Total Environment 181 (161-165).

[10] U.S. Food and Drug Administration, Cosmetics, Kohl, Kajal, Al-Kahal, or Surma: By Any Name, a Source of Lead Poisoning (http://www.fda.gov/Cosmetics/ProductandIngredientSafety/ProductInformation/ucm137250.htm)

[11] IAEA, 2004. Application of The Concepts of Exclusion Exemption and Clearance. Safety Standards Series No. RS-G-1.7. Vienna.

[12] MCNP - A General Monte Carlo N-Particle Transport Code, Version 5, University of California, Los Alamos National Laboratory.

[13] Manual of the Monte Carlo N-Particle Transport Code, Version 5.

ADAPTIVE RESPONSE OF RETINA TO LOW DOSE OF PROTON IRRADIATION

Yu. V. Vinogradova*, V. A. Tronov
Joint Institute for Nuclear Research, Dubna, Russia

Introduction

The retina consists of terminally differentiated cells that have lost their ability to divide. It is relatively highly resistant to radiation. Nevertheless, a large contingent of people find themselves in a situation where the level of genotoxic exposure exceeds the level of retinal resistance or the type of influence on the retina is not adaptive: in the radiotherapy of brain tumors and melanoma or space flights. The aim of our work was to assess the damaging effect of gamma and proton radiation on the DNA structure in the mouse retina, the functional activity of the retina, and its ability to recover in vivo. The hypothetic cause of retinal radioresistance can be: 1) resistance to apoptosis, which is characteristic of the post-mitotic cells compared to proliferating ones; 2) the limited number of actively transcribed genes, which leads to reduction of the physical size of the target for damage genotoxicants; 3) active DNA repair associated with a limited number of transcribed genes [1]; 4) proteostazis the defective inactive protein removal mechanism in the retinal cells.
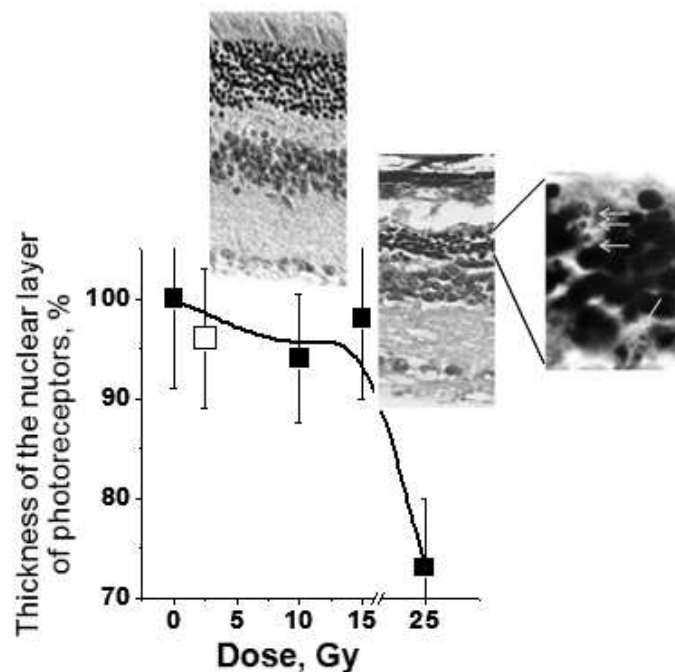
Figure 1: The effect of thickness of the nuclear layer of photoreceptors (%) on graph doseresponse curve with microphotographs of the retina.

---

*vinojv@jinr.ru

Radioresistance of the retina

Morphological and functional changes are not observed after proton and gamma irradiation at a dose of 14 Gy. It has been shown that both radiation (accelerated protons) and chemical (methylnitrosourea) effects are characterized by a non-linear doseresponse curve: there is a radioresistance plateau on the graph dose effect, indicating that retinal repair mechanisms take place (Fig. 1).

Radiation preconditioning of the retina

An adaptive dose (1 Gy, protons) protects the retina from degeneration induced by methylnitrosourea (MNU). The mechanism of protection include suppression of the apoptotic death of photoreceptor cells in the retina. And the mechanism of protection include decrease induction of DNA double-stand breaks in cells of the retina, compare to MNU 70 mg/kg (possibly, their repair activation). We have found possible participation of Mller glial cells in retinal cellular damage repair. This cells play on important role in retina. It is known that these cells help to recovery retina after some stress. Adaptive dose 17 mg/kg decrease number of Muller glial cells in compare with single dose 70 mg/kg.

Spontaneous DNA damage in the retina

A procedure of the visualization of Muller glial cells has been proposed, which made it possible to detect the DNA comets of these cells. The Mller cells have a high level of DNA damage (Fig. 2).
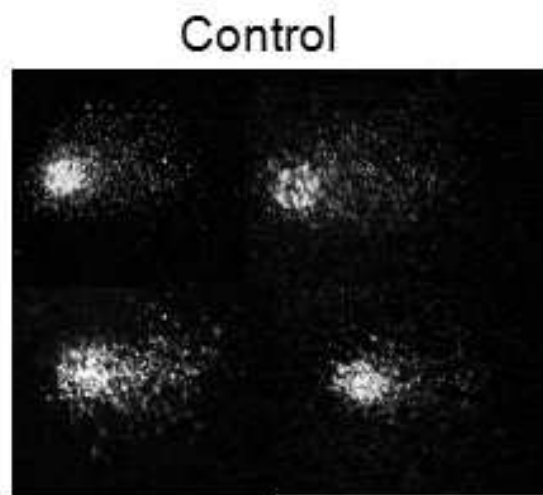
Figure 2: DNA comets of the Mller cells in control.

High spontaneous DNA damage was observed in all retinal cells. Spontaneous DNA damage in the cells of different organs of mice was growing in the same order as the oxygenation degree: leukocytes < liver cells < brain cells < retinal cells (Fig. 3) [2, 3].

The yield of spontaneous DNA damage in the retina corresponds to a radiation dose of 15 Gy [3]. Nevertheless, it does not cause the death of retinal cells and has no effect on its functional activity. It can indicate that in the process of evolution, adaptive mechanisms developed in the retinal cells to ensure their high resistance to light and radiation stress.
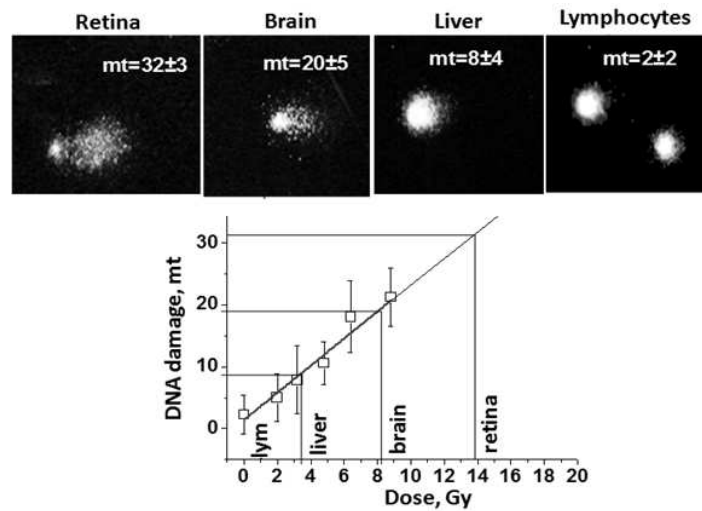
Figure 3: Spontaneous DNA damage (DNA-comets and mt parameter) in the cells of the different mice organs and dose-response curve in a graphic representation of the effect of DNA damage of these cells.

References

[1] Nouspikel T. DNA repair in differentiated cells: some new answers to old questions. Neuroscience. 2007. V.145. P. 213-1221.

[2] Wang A.L., Lukas T.J., Yuan M., Neufeld A.H. Age-related increase in mitochondrial DNA damage and loss of DNA repair capacity in the neural retina. Neurobiol Aging. 2010. V. 31. P. 2002-2010.

[3] Tronov V.A., Vinogradova Iu.V., Loginova M.Iu., Ostrovskii M.A. Mechanisms of radioresistance in terminally differentiated cells of mature retina // Tsitologiia. 2012. 54(3). P. 261-269.

**The XX International Scientific Conference
of Young Scientists and Specialists
dedicated to the 60th anniversary of the Joint Institute for Nuclear Research
(AYSS-2016)**

Proceedings

Responsible for preparation A. V. Friesen, E. I. Krupko

The contributions are reproduced directly from the originals presented by the Organizing Committee.

The Organizing Committee is not responsible for the content of contributions.